Spring 1-1-2017

Modeling and Optimization of Fluid Flows in the Continuum and Slip Regime

Luis F. Negrete
University of Colorado at Boulder, lnegrete90@gmail.com

Modeling and Optimization of Fluid Flows in the Continuum and Slip Regime

by

Luis Fernando Negrete

B.S., Aersopace Engineering, New Mexico State University, 2012

A thesis submitted to the

Faculty of the Graduate School of the

University of Colorado in partial fulfillment

of the requirements for the degree of

Master of Science

Department of Aerospace Engineering Sciences

2017

This thesis entitled:
Modeling and Optimization of Fluid Flows in the Continuum and Slip Regime
written by Luis Fernando Negrete
has been approved for the Department of Aerospace Engineering Sciences

Prof. Kurt Maute

Prof. Georg Pingen

Date

The final copy of this thesis has been examined by the signatories, and we find that both the content and the form meet acceptable presentation standards of scholarly work in the above mentioned discipline.

Negrete, Luis Fernando (M.S., Aerospace Engineering Sciences)

Modeling and Optimization of Fluid Flows in the Continuum and Slip Regime

Thesis directed by Prof. Kurt Maute

Microscale fluid flows have gained increased attention in recent years. As the physical scale of fluidic devices decreases, rarefaction effects governed by the Knudsen number appear and the continuum assumption is invalid. Fluidic devices designed without the consideration of these effects may, in turn, perform sub-optimally. The goal of this thesis is to present two alternative approaches for modeling flows with finite Knudsen numbers. First, a comparison of governing equations derived from a moment method approach to the Boltzmann Transport Equation is considered. The proposed stabilization scheme is found to be overly diffusive for nonlinear equations, which are expected for higher-order moment equations. As an alternative, the incompressible Navier-Stokes equations are used and a slip boundary condition is proposed to model the non-zero fluid velocity near solid walls that occur at finite Knudsen numbers. The explicit Level Set Method (LSM) is adopted to provide the precise location and orientation of the fluid-solid interface and the eXtended Finite Element Method (XFEM) is used to realize the flow. A ghost penalty stabilization method ensured smooth velocity gradients along the interface. The framework is validated with 2D numerical examples. Finally, 2D and 3D topology optimization examples are studied. For some examples, ignoring the slip boundary leads to considerable design differences and sub-optimal performance.

Acknowledgements

I would like to thank my committee members for their time in reviewing this research, Profs Kurt Maute and Georg Pingen for their time and effort in directing the course of research, my colleagues for their contributions to the framework this work is based on, and my family and friends for their support during my pursuit of this thesis.

Contents

Tables

Table

Figures

Figure

Chapter 1

Introduction

The Knudsen number is a nondimensional parameter that characterizes the rarefaction of a gas and is defined as:

$$Kn = \frac{\lambda}{L_r} \approx \frac{\lambda}{\Phi_0} \left| \frac{d\Phi_0}{dL} \right|, \tag{1.1}$$

where λ is the mean-free path of the fluid, L_r is a global reference length, e.g. the spacing between plates or the cylinder diameter, and Φ_0 is any chosen quantity, e.g. the fluid density or pressure [1]. The mean-free path is the average distance a fluid particle travels between collisions with other particles. The first definition in (1.1) represents a global Knudsen number, while the second can be used to represent a local Knudsen value. Larger Knudsen numbers indicate that particles travel further distances between collisions; thus, the fluid is said to be more rarefied.

The regime breakdown based on the Knudsen number was originally proposed by Schaaf and Chambre [2] and revised by Gad-el-Hak [3]. Flows for which $Kn < 10^{-3}$ are said to be in the Hydrodynamic Range, where the Navier-Stokes (NS) equations with traditional no-slip boundary conditions are valid. Flows for which $10^{-3} < Kn < 10^{-1}$ are said to be in the Slip Flow Regime, where the NS equation cannot be used with the traditional no-slip boundary conditions. Instead, velocity and temperature slips begin to occur as the Kn increases, i.e. the velocity and temperature of the fluid at the wall and that of the wall itself are not the same. Flows for which $10^{-1} < Kn < 10$ are said to be in the Transition Regime; here, the NS equations are no longer valid, regardless of boundary conditions. Finally, flows for which $Kn > 10$ are said to be in the Free Molecular Flow Regime, where intermolecular collisions are so rare that they can be ignore; instead, only particle-

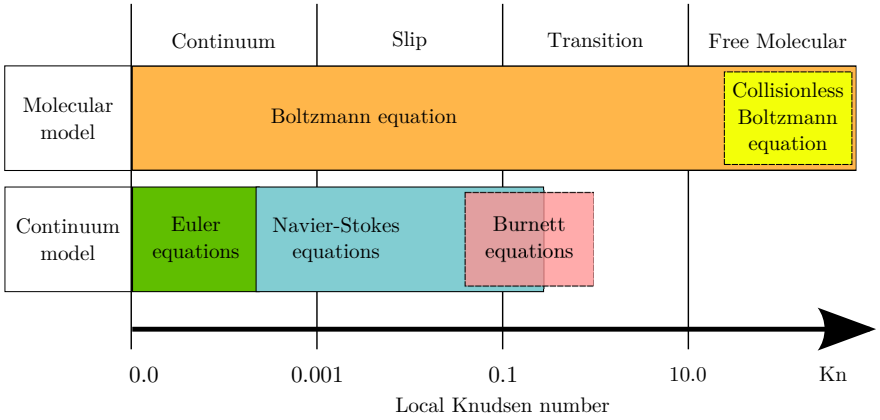

Figure 1.1: Classification of gas flow regimes and governing equations over a range of Knudsen numbers.

wall interactions are important. The Direct Simulation Monte Carlo (DSMC) method proposed by Bird [4] is particularly powerful in this regime, since each particle can be considered independent of other particles in a flow. In contrast to other fluid flow equations, the Boltzmann Transport Equation (BTE) is valid across all regimes, though a collision-less BTE is most appropriate for large Kn number flows [5]. This breakdown is summarized in Fig. 1.1. As the Knudsen number increases, rarefaction effects becomes more obvious and the continuum assumption breaks down. To fully understand the Knudsen effect, it is important to resolve all transport regimes [6]. However, the classification discussed here is somewhat empirical and the boundary between regimes depends on the particular device [7].

The goal of the work presented in this thesis is two-fold: 1. Develop a fluid model to resolve rarefaction effects for low but finite Knudsen numbers. 2. Integrate these model into an existing topology optimization framework to find optimal designs for fluidic devices operating in the microscale.

Chapter 2 considers the moment approach proposed by Tölke [8] and studied previously by Makhija and Maute [9], where the governing equations are linear and thus benefit from the presented stabilization scheme. As higher-order moments are considered, as discussed in that chapter, the governing equations become increasingly non-linear and may be negatively affected by

the stabilization scheme. To study this effect, we derived a new set of governing equations similar and compare its performance to previous work.

As an alternative, Chapter 3 considers an extension of the Navier-Stokes equations by introducing a slip boundary model to the framework proposed by Villanueva and Maute [10]. This extends the applicability of the NS equation to Kn numbers in the Slip Regime. The slip boundary model introduced in this work benefits from smooth velocity gradients, which motivates the use of the ghost-penalty method over other stabilization schemes. We validate the implementation of the slip boundary model with several examples and then study the influence of the ghost-penalty method.

Finally, Chapter 4 studies the influence of the slip boundary model on the optimal design of several fluidic devices. In the simplest example, the device is required to split and redirect an inlet flow. Then, we consider a fixed-valve whose intent is to allow flow in one direction but discourage it in another. It is for this problem that the slip boundary has the greatest influence. These two problems are more heavily discussed in the attached manuscript in Appendix C. Further, we consider two transport problems in 2D and 3D.

Chapter 2

Moment Methods

2.1 Introduction to moment methods

The hydrodynamic Boltzmann transport equation (HBTE) represents a kinetic theory approach to fluid dynamics, whereas the Navier-Stokes equations are derived from the conservation of momentum in a fluid continuum. Likewise, the continuity equation is derived from a conservation of mass. The HBTE has been shown to recover the Navier-Stokes by Grad [5] and is able to resolve finite Knudsen number flows [11]. In this Chapter, we will limit our discussion to Knudsen numbers in the continuum regime and will revisit larger Kn numbers in Chapter 3. The HBTE describes the time-evolution of a particle distribution function, $f(\boldsymbol{x}, \boldsymbol{\xi}, t)$, and is introduced properly in Section 2.2. Traditionally, the majority of research on the HBTE has focused on the explicit finite difference discretization, leading to the lattice Boltzmann method (LBM). A review of the LBM is provided by Yu et al. [12]. As discussed by Makhija and Maute [9], while the LBM offers several numerical advantages, including low computational cost and easy parallelization, it suffers from limitation due to the explicit time integration scheme and from a large number of degrees-of-freedom per node. The LBM also lacks a mathematical formalism for unstructured meshes and local mesh refinement is more complex because the model parameters depend on the mesh spacing, e.g., see [13].

These limitations have been addressed with alternative discretization schemes, include finite difference by Mei and Shyy [14] and, more recently, by Tölke [8], finite volume by Patil and Lakshmisha [15], and finite element techniques. Finite element techniques have gained recent attention, including a characteristic Galerkin finite element method by Lee and Lin [16], a least-

squares finite element method by Li et al. [17] and Li et al. [18], and discontinuous Galerkin schemes by Düster et al. [19] and Min and Lee [20].

Alternatives to the LBM include a wide variety of moment methods, such the Burnett, BGK-Burnett, and super-Burnett models of Zhong et al. [21], Jin and Slemrod [22], and Balakrishnan [23], respectively. As explained by Lockerby et al. [24], three reasons contribute the large number of moment methods: (1) constitutive relations of higher-order than the NS equations have indicated potential in modeling rarefied flows, (2) all these models depend on the numerical and physical instability and (3) no single equation has the ability to predict the important non-equilibrium effects in rarefied gas microflows. In particular, the regularized 13-moment equations (R13),originally proposed by Struchtrup and Torrilhon [25], have becomes a popular choice for the study of non-equilibrium flows. The R13 equations use a Chapman-Enskog expansion on Grad's 13-moment equations. Analytical solutions exist for simple flows, such the flow between parallel plates [26] and the flow around a sphere [27]. They have also been shown to resolve the flow in a driven cavity [28], a heated cavity [29], and the flow through a Knudsen pump [30]. Their reach in application has also been considered by Gu et al. [31]. While the R13 and other higher-order moment methods show promise in resolving non-equilibrium flows, they have not been rigorously studied for very complex geometries, such as those that might arise in the process of topology optimization. Moreover, these models are highly non-linear, which require greater computational power.

Recently, Makhija and Maute [9] applied an immersed boundary approach with a Streamline Upwind Petrov-Galerkin (SUPG) scheme to the HBTE. Further, Makhija and Maute [32] augmented said approach with a scalar advection-diffusion equation and studied mass transport and heat transfer optimization problems. In that work, the immersed boundary approach provides a way to perform topology optimization for various fluid problems and is realized by the eXtended Finite Element Method (XFEM). In this Chapter, we will limit our discussion to fluid analysis and will thus not require the immersed boundary approach. However, we will revisit this approach in Chapter 3.

The remainder of this Chapter is organized as follows: Section 2.2 shows the derivation of the

governing equations from the BTE, Section 2.3 discusses the enforcement of boundary conditions, and Section 2.4 shows the numerical stabilization scheme. Section 2.5 briefly shows the finite element discretization used in this Chapter. Numerical examples are provided in Section 2.6. Conclusions drawn from these examples are discussed in Section 2.7.

2.2 Governing Equations

The Boltzmann Transport Equation (BTE) operates on a probability distribution function, $f(\boldsymbol{x}, \boldsymbol{\xi}, t)$, such that $f(\boldsymbol{x}, \boldsymbol{\xi}, t)\mathrm{d}\boldsymbol{x}\mathrm{d}\boldsymbol{\xi}$ is the probable number of particles within a sphere of radius $\mathrm{d}\boldsymbol{x}$ centered around $\boldsymbol{x}$ having velocities within $\mathrm{d}\boldsymbol{\xi}$ of $\boldsymbol{\xi}$ [5]. Some texts, as in this work, redefine this distribution as a mass distribution instead of a number distribution, such that $f(\boldsymbol{x}, \boldsymbol{\xi}, t)\mathrm{d}\boldsymbol{x}\mathrm{d}\boldsymbol{\xi}$ is the mass of the previously described particles. This redefinition is allowed by:

$$f_{num} = \frac{1}{m} f_{mass}, \tag{2.1}$$

where m is the mass of a single particle. Furthermore, moments of this distribution have physical interpretations [5]. For example, the zeroth moment of the mass distribution is the local density:

$$\rho(\boldsymbol{x}, t) = \int f(\boldsymbol{x}, \boldsymbol{\xi}, t)\mathrm{d}\boldsymbol{\xi}, \tag{2.2}$$

and the first moment is the momentum field:

$$\rho u_i(\boldsymbol{x}, t) = \int \xi_i f(\boldsymbol{x}, \boldsymbol{\xi}, t) d\boldsymbol{\xi}. \tag{2.3}$$

At this is point, it becomes convenient to define the remaining moments with respect to this mean, so we introduce an intrinsic velocity:

$$\boldsymbol{c}(\boldsymbol{\xi}, \boldsymbol{x}, t) = \boldsymbol{\xi} - \boldsymbol{u}(\boldsymbol{x}, t). \tag{2.4}$$

The second moments, i.e. the fluid stresses, are defined as:

$$\sigma_{ij} = \int c_i c_j f(\boldsymbol{x}, \boldsymbol{\xi}, t)\mathrm{d}\boldsymbol{\xi}, \tag{2.5}$$

and so on for larger moments. For a more detailed consideration and for the derivation of the BTE, the reader is referred to Grad [5]. The BTE is written as:

$$\frac{\partial f}{\partial t} + (\boldsymbol{\xi} \cdot \boldsymbol{\nabla}) f = \Omega, \tag{2.6}$$

where Ω is the integral collision operator. The BTE is thus a integro-differential equation in 7 variables (3 spatial, 3 velocities, and time) and presents two primary issues: (i) The integral on the right-hand side is difficult and expensive to evaluate and (ii) the velocity space is infinite, i.e., to apply a numerical scheme, it would have to be truncated. To mitigate these issues, this work follows Tölke [8] and Makhija and Maute [9].

2.2.1 The BGK approximation

To mitigate the difficulty of the right-hand side integral, the Bhatnagar-Gross-Krook (BGK) [33] approximation is adopted:

$$\Omega \approx \Omega_{BGK} = -\tau^{-1} \left(f - f^{eq} \right), \tag{2.7}$$

where τ is called the relaxation time and f^{eq} is the equilibrium distribution:

$$f^{eq} = \frac{\rho}{(2\pi RT)^{D/2}} \exp\left(-\frac{(\boldsymbol{\xi} - \boldsymbol{u})^2}{2RT} \right), \tag{2.8}$$

where D is the dimension of the problem, R is the specific gas constant and T is a reference temperature.

Considering a $\mathrm{d}\boldsymbol{x}\mathrm{d}\boldsymbol{\xi}$ finite volume centered at $(\boldsymbol{x}, \boldsymbol{\xi})$ in the $\boldsymbol{x}\boldsymbol{\xi}$-phase plane, the BGK collision operator approximates the exit rate of particles as proportional to the distribution of particles in said finite volume and the entrance rate of particles as proportional to an equilibrium distribution outside this space, such that intermolecular collisions tend the flow towards equilibrium. The latter approximation is the most critical, since the original collision operator, Ω, required knowing the distribution of all particles outside this finite volume, making it expensive to evaluate. The BGK approximation replaces this requirement with an equilibrium distribution.

2.2.2 Moment approach to the infinite velocity space

To mitigate the difficulty of the infinite velocity space, we take moments of the entire BTE,

$$\int \left(\frac{\partial f}{\partial t} + (\boldsymbol{\xi} \cdot \boldsymbol{\nabla}) f \right) \Psi^{(N)} \mathrm{d}\xi = \int -\tau^{-1} \left(f - f^{eq} \right) \Psi^{(N)} \mathrm{d}\xi, \tag{2.9}$$

$$\frac{\partial}{\partial t} \int f \Psi^{(N)} d\xi + \frac{\partial}{\partial x_i} \int f \xi_i \Psi^{(N)} d\xi = -\tau^{-1} \left(\int \left(f - f^{eq} \right) \Psi^{(N)} d\xi \right), \tag{2.10}$$

where $\Psi^{(N)}$ is 1, ξ_i, $c_i c_j$, as in (2.2), (2.3), (2.5), respectively, and so on for higher-order moments. In the first term on the left-hand side and in both terms on the right-hand side, an N-th order moment, $M^(N)$, appears. However, the second term on the left-hand side has an additional ξ_i, meaning that the resulting moment will necessarily be one order higher. This results in:

$$\frac{\partial}{\partial t} M^{(N)} + \frac{\partial}{\partial x_i} M_i^{(N+1)} = -\tau^{-1} \left(M^{(N)} - M_{eq}^{(N)} \right), \tag{2.11}$$

thus creating a system of equations, i.e. (2.11) written for all orders, N.

While this approach removes the molecular velocities as independent variables, it inevitably creates a new issue: the governing equation for an N-th order moment, appearing in the time derivative and on the right-hand side, generally involves an $(N+1)$-th order moment. In the literature, this is commonly referred to as the closure problem, which has been discussed by Levermore [34], Levermore and Morokoff [35], and Lam and Groth [36]. For a brief review of moment closure approaches, the reader is referred to Kuehn [37]. In principle, the closure problem appears in the NSF equations as well: the governing equation for the density requires the velocity and the governing equations for the velocities require the stresses. It is only until the stresses are related to the gradients of the velocities, e.g. for Newtonian fluids, that the system is closed.

2.2.3 Galerkin expansion of the distribution

To mitigate this new issue for the BTE, we represent the distribution function, f, as a series expansion of Hermite polynomials in the velocity space, such that the need of higher-order moments is truncated depending on how large an expansion is used. Following the work of Tölke [8], a so-

called global expansion is written as:

$$f \approx \hat{f}_{glb} = \frac{1}{(2\pi RT)^{D/2}} \exp\left(-\frac{\boldsymbol{\xi}^2}{2RT}\right) \sum_{k=1}^{n_{D,N}} a_k(\boldsymbol{x},t)\phi_k(\boldsymbol{\xi}). \tag{2.12}$$

For a 2^{nd} order expansion in 2D, $n_{2,2} = 6$. Following the work by Tölke [8], this work chooses ϕ_k as combinations of the first three Hermite polynomials:

$$H_1(\xi) = 1, \quad H_2(\xi) = \xi, \quad H_3(\xi) = \frac{\xi^2 - 1}{\sqrt{2}}, \tag{2.13}$$

such that

$$\begin{aligned}
\phi_1 &= H_1(\xi_1)H_1(\xi_2) = 1 \\
\phi_2 &= H_2(\xi_1)H_1(\xi_2) = \frac{\xi_1}{\sqrt{RT}} \\
\phi_3 &= H_1(\xi_1)H_2(\xi_2) = \frac{\xi_2}{\sqrt{RT}} \\
\phi_4 &= H_2(\xi_1)H_2(\xi_2) = \frac{\xi_1\xi_2}{RT} \\
\phi_5 &= H_3(\xi_1)H_1(\xi_2) = \frac{1}{\sqrt{2}}\left(\frac{\xi_1^2}{RT} - 1\right) \\
\phi_6 &= H_1(\xi_1)H_3(\xi_2) = \frac{1}{\sqrt{2}}\left(\frac{\xi_2^2}{RT} - 1\right).
\end{aligned} \tag{2.14}$$

Substituting f_{glb} in place of f in (2.2), (2.3), and (2.5) gives a relationship between the coefficients, a_k, and the physical moments of the fluids, which can be summarized as:

$$\boldsymbol{U} = \boldsymbol{F}_{glb}(\boldsymbol{a}), \tag{2.15}$$

where

$$\boldsymbol{a} = \begin{pmatrix} a_1 & a_2 & a_3 & a_4 & a_5 & a_6 \end{pmatrix}^T, \tag{2.16}$$

and

$$\boldsymbol{U} = \begin{pmatrix} \rho & v_i & \sigma_{ij} \end{pmatrix}^T, \tag{2.17}$$

such that

$$\begin{aligned}
\rho &= a_1, \\
v_1 &= \frac{a_2}{a_1}\sqrt{RT}, \\
v_2 &= \frac{a_3}{a_1}\sqrt{RT}, \\
\sigma_{12} &= -RT\left(a_4 - \frac{a_2 a_3}{a_1}\right), \\
\sigma_{11} &= -RT\left(\sqrt{2}a_5 - \frac{a_2^2}{a_1}\right), \\
\sigma_{22} &= -RT\left(\sqrt{2}a_6 - \frac{a_3^2}{a_1}\right).
\end{aligned} \tag{2.18}$$

Note that (2.15) is invertible, by solving (2.18), to give expressions for $\boldsymbol{a}$ in terms of $\boldsymbol{U}$:

$$\boldsymbol{a} = \boldsymbol{F}_{glb}^{-1}\left(\boldsymbol{U}\right). \tag{2.19}$$

Substituting ϕ (2.14) and f_{glb} (2.12) in place of $\Psi^{(N)}$ and f, respectively, in (2.10) gives the 2nd-order governing equations for the global expansion coefficients, or rather, the 2^{nd} Global Hermite Form (GHF2), which may be written as:

$$\frac{\partial \boldsymbol{a}}{\partial t} + \left(\boldsymbol{A}\cdot\boldsymbol{\nabla}\right)\boldsymbol{a} + \boldsymbol{C}\left(\boldsymbol{a}\right) = 0, \tag{2.20}$$

where $\boldsymbol{A} = [A_x, A_y]$ are referred to as the coefficient matrices and $\boldsymbol{C}(\boldsymbol{a})$ is the collision vector. These are shown in detail in Appendix A. At this point, one can solve (2.20), e.g. with finite elements, and then use (2.18) to obtain solution for the physical moments of the fluid. This system of equations is considered in Makhija and Maute [9], who used an immersed body method to study the compressibility limit of said system of equations. Note that the system of equations presented here is consistent with the ideal gas law:

$$p = \rho RT. \tag{2.21}$$

Further, the fluid forces, $\boldsymbol{F}$, acting on a surface, Γ, are found from the pressure and stress tensor as:

$$\boldsymbol{F} = \int_{\Gamma}\left(-\boldsymbol{\sigma}\cdot\boldsymbol{n} + p\boldsymbol{n}\right)\mathrm{d}\Gamma. \tag{2.22}$$

Finally, as stated in Tölke [8], the GHF2 equations recover the NS equations with the kinematic viscosity equal to:

$$\mu = \tau RT. \tag{2.23}$$

2.2.4 Direct moment equations

In this work, we introduce an alternative to (2.20), by substituting (2.19) into (2.20). In principle, this would give a system of governing equations for the physical moments directly, eliminating the need for (2.18). This substitution results in:

$$\frac{\partial}{\partial t}\boldsymbol{F}_{glb}^{-1}(\boldsymbol{U}) + (\boldsymbol{A}\cdot\boldsymbol{\nabla})\,\boldsymbol{F}_{glb}^{-1}(\boldsymbol{U}) + \boldsymbol{C}\left(\boldsymbol{F}_{glb}^{-1}(\boldsymbol{U})\right) = 0, \tag{2.24}$$

$$\frac{\partial \boldsymbol{F}_{glb}^{-1}}{\partial \boldsymbol{U}}\frac{\partial \boldsymbol{U}}{\partial t} + \left(\boldsymbol{A}\frac{\partial \boldsymbol{F}_{glb}^{-1}}{\partial \boldsymbol{U}}\cdot\boldsymbol{\nabla}\right)\boldsymbol{U} + \boldsymbol{C}\left(\boldsymbol{F}_{glb}^{-1}(\boldsymbol{U})\right) = 0. \tag{2.25}$$

Denoting

$$\boldsymbol{J}_{glb} = \frac{\partial \boldsymbol{F}_{glb}^{-1}}{\partial \boldsymbol{U}}, \tag{2.26}$$

we can derive the equivalent set of equations for the moments:

$$\frac{\partial \boldsymbol{U}}{\partial t} + \left(\boldsymbol{J}_{glb}^{-1}\boldsymbol{A}\boldsymbol{J}_{glb}\cdot\boldsymbol{\nabla}\right)\boldsymbol{U} + \boldsymbol{J}_{glb}^{-1}\boldsymbol{C}\left(\boldsymbol{F}_{glb}^{-1}(\boldsymbol{U})\right) = 0, \tag{2.27}$$

$$\frac{\partial \boldsymbol{U}}{\partial t} + \left(\hat{\boldsymbol{A}}(\boldsymbol{U})\cdot\boldsymbol{\nabla}\right)\boldsymbol{U} + \hat{\boldsymbol{C}}(\boldsymbol{U}) = 0. \tag{2.28}$$

In this work, we will refer to (2.28) as the 2nd-order Global Moment Form (GMF2). Note that (2.20) and (2.28) represent the *same* physical phenomena and are linked by (2.15). While these two systems of equations govern the same physical phenomena, this work is interested in finding any differences that arise from the use of both of these systems of equations after discretization, since at that point, their numerical forms will be different; for more, see Section 2.6.1.

2.2.5 Expansion about the local equilibrium

An alternative to the global expansion (2.12) is the so-called local expansion, originally suggested by Grad [5]:

$$f \approx \hat{f}_{loc} = \frac{1}{(2\pi RT)^{D/2}}\exp\left(-\frac{(\boldsymbol{\xi}-\boldsymbol{u})^2}{2RT}\right)\sum_{k=1}^{n_{D,N}} a_k(\boldsymbol{x},t)\phi_k(\boldsymbol{\xi}). \tag{2.29}$$

As discussed by Tölke [8], the global expansion is an expansion about an *absolute* equilibrium where the macroscopic velocities are much smaller than the average velocity of particles, which occurs in nearly incompressible flows. The local approximation does not make this assumption and, thus, more closely approximates compressible flows.

Substituting f_{loc} (2.29) in place of f in (2.2), (2.3), and (2.5) gives a different set of expressions for the physical moments, $\boldsymbol{U}$, and the expansion coefficients, a_k, which can be summarized as:

$$\boldsymbol{U} = \boldsymbol{F}_{loc}\left(\boldsymbol{a}\right). \tag{2.30}$$

In this process, (2.3) requires that $a_2 = a_3 = 0$; instead, u and v become the dependent variables. Just as for the GHF2 equations, substituting ϕ (2.14) and f_{loc} (2.29) in place of $\Psi^{(N)}$ and f, respectively, into (2.10) gives the 2nd-order governing equations for the local expansion coefficients (LHF2), which may be written as:

$$\frac{\partial \boldsymbol{a}}{\partial t} + \left(\boldsymbol{B}(\boldsymbol{a}) \cdot \boldsymbol{\nabla}\right) \boldsymbol{a} + \boldsymbol{D}\left(\boldsymbol{a}\right) = 0, \tag{2.31}$$

where $\boldsymbol{B}$ and $\boldsymbol{D}(\boldsymbol{a})$ are shown in Appendix A. Thus, (2.31) is a set of governing equations for a mixture of expansion coefficients and physical moments, i.e. the velocities.

2.2.6 Direct moment equations with the local expansion

Just as for the GMF2 equations, we can substitute (2.30) into (2.31) to arrive at the 2nd-order Local Moment Form (LMF2) equations:

$$\frac{\partial \boldsymbol{U}}{\partial t} + \left(\hat{\boldsymbol{B}}(\boldsymbol{U}) \cdot \boldsymbol{\nabla}\right) \boldsymbol{U} + \hat{\boldsymbol{D}}\left(\boldsymbol{U}\right) = 0, \tag{2.32}$$

where $\hat{\boldsymbol{B}}$ and $\hat{\boldsymbol{D}}\left(\boldsymbol{U}\right)$ are also shown in Appendix A. In the same way that the GHF2 and GMF2 equations are equivalent, as discussed in Section 2.2.4, the LHF2 and LMF2 equations are similarly equivalent. However, as stated by Tölke [8], the GHF2 and GMF2 equations represent nearly incompressible flows, while the LHF2 and LMF2 equations are not limited to the incompressible case.

2.2.7 Summary of Formulations

The derivation of governing equations can be summarized as follows: four sets of governing equations are available, depending on the choice of f_{glb} or f_{loc} and whether or not to substitute the coefficient-to-moment expressions, namely the GHF2, GMF2, LHF2 and LMF2 equations.

Note, again, that the GHF2 and GMF2 equations are derived from the same global expansion, but because different variables will be discretized they will have different finite elements models. Further, while the GMF2 and LMF2 are governing equations on the same variables, meaning that they will have an equal discretization, they are derived from different expansions and thus represent different physical phenomena. Because the LMF2 equations use a local expansion, we expect that they will behave differently as we consider flows further from the incompressible limit. All four forms can be written generally as:

$$\frac{\partial \boldsymbol{a}}{\partial t} + \left(\boldsymbol{A}(\boldsymbol{a}) \cdot \boldsymbol{\nabla}\right) \boldsymbol{a} + \boldsymbol{C}\left(\boldsymbol{a}\right) = 0, \tag{2.33}$$

where $\boldsymbol{a}$ is a_i in the GHF2, $\boldsymbol{U}$ in the GMF2 and LMF2, or a mixture of both in the LHF2; and $\boldsymbol{A}(\boldsymbol{a})$ and $\boldsymbol{C}(\boldsymbol{a})$ take on their respective forms for each set of equations. Note especially that $\boldsymbol{A}$ is constant for the GHF2 equations, which is discussed further by Makhija and Maute [9]; otherwise, it is non-linearly dependent on $\boldsymbol{a}$.

2.2.8 Non-dimensional form

All governing equations derived from the BTE have two numerical parameters, RT and τ. However, in the incompressible limit,

$$\mu = \tau RT, \tag{2.34}$$

where μ is the fluid kinematic viscosity [8]. Further, as shown by Makhija and Maute [9], the GHF2 can be expressed in a nondimensional form:

$$\frac{\partial \hat{\boldsymbol{a}}}{\partial \hat{t}} + \frac{\tau\sqrt{RT}}{L}\left(\hat{\boldsymbol{A}} \cdot \hat{\boldsymbol{\nabla}}_{\hat{\boldsymbol{x}}}\right) \hat{\boldsymbol{a}} = -\hat{\boldsymbol{C}}(\hat{\boldsymbol{a}}), \tag{2.35}$$

where, in this Section, $\hat{(\cdot)}$ denotes non-dimensional quantities. The coefficient of the advective term can be interpreted as:

$$\frac{\tau\sqrt{RT}}{L} = \frac{r\ RT}{\sqrt{RT}L} = \frac{\mu}{\sqrt{RT}L} = \frac{|\bar{\boldsymbol{U}}|\nu}{|\bar{\boldsymbol{U}}|\sqrt{RT}L} = \frac{Ma_{ref}}{Re}, \tag{2.36}$$

where $|\bar{\boldsymbol{U}}|$ is a reference velocity, $Re = \rho|\bar{\boldsymbol{U}}|L/\mu$ is the Reynolds number, and $Ma_{ref} = |\bar{\boldsymbol{U}}|/\sqrt{RT}$ is a reference Mach number. The Reynolds number is determined by the physical fluid problem, assuming a reference velocity is available. The reference Mach number is then a free parameter which determines the compressibility of the fluid; low reference Ma numbers lead to nearly incompressible flows. However, as Ma_{ref} is lowered, the scale of the collision term becomes more significant than the scale of the advection terms; mesh refinement may be necessary to resolve these mismatches scales. This behavior is discussed by Makhija and Maute [9] for the GHF2 equations; in this work, we will further study this effect in the GMF2 equations.

For a chosen reference Mach number, the numerical parameters are computed by:

$$RT = \frac{|\bar{\boldsymbol{U}}|^2}{Ma_{ref}^2}, \tag{2.37}$$

and

$$\tau = \frac{\mu}{RT}. \tag{2.38}$$

The remaining systems of equations presented here likewise depend on the same numerical parameters as the GHF2 equations. The parameters, RT and τ, are computed equally for all four systems of equations.

2.3 Boundary Conditions

In this Section, we will discuss the method of enforcing boundary conditions for all forms of the governing equations in Section 2.2. The approach shown here is a generalization of the approach used by Makhija and Maute [9]. Using a comma notation to indicate time or spatial derivatives, the weak form of (2.33) is written as:

$$R = \int \boldsymbol{w} \cdot (\boldsymbol{a}_{,t} + A_x(\boldsymbol{a})\boldsymbol{a}_{,x} + A_y(\boldsymbol{a})\boldsymbol{a}_{,y} + \boldsymbol{C}(\boldsymbol{a}))\,\mathrm{d}\Omega, \tag{2.39}$$

with trial functions $\boldsymbol{w} = \delta\boldsymbol{a}$. Temporarily grouping the time derivative and the collision terms into R_{rem}, we can write (2.39) as:

$$R = R_{rem} + \int \boldsymbol{w} \cdot (A_x(\boldsymbol{a})\boldsymbol{a}_{,x} + A_y(\boldsymbol{a})\boldsymbol{a}_{,y})\,\mathrm{d}\Omega. \tag{2.40}$$

Because $A\boldsymbol{a}_{,x_i} = (A\boldsymbol{a})_{,x_i} - A_{,x_i}\boldsymbol{a}$,

$$R = R_{rem} + \int \boldsymbol{w} \cdot \left((A_x\boldsymbol{a})_{,x} + (A_y\boldsymbol{a})_{,y}\right)\delta\Omega - \int \boldsymbol{w} \cdot \left((A_x)_{,x} + (A_y)_{,y}\right)\boldsymbol{a}\mathrm{d}\Omega. \tag{2.41}$$

Calling $\boldsymbol{F} = \boldsymbol{A}\boldsymbol{a} = [\boldsymbol{A}_x\boldsymbol{a},\ \boldsymbol{A}_y\boldsymbol{a}]$ and applying the divergence theory on the first integral term gives:

$$\begin{aligned}
R &= R_{rem} + \int \boldsymbol{w} \cdot (\boldsymbol{\nabla} \cdot \boldsymbol{F})\,\mathrm{d}\Omega - \int \boldsymbol{w} \cdot \left((A_x)_{,x} + (A_y)_{,y}\right)\boldsymbol{a}\mathrm{d}\Omega, \\
R &= R_{rem} + \int \boldsymbol{\nabla}\,(\boldsymbol{w} \cdot \boldsymbol{F})\,\mathrm{d}\Omega - \int \boldsymbol{F}\,(\boldsymbol{\nabla} \cdot \boldsymbol{w})\,\mathrm{d}\Omega - \int \boldsymbol{w} \cdot \left((A_x)_{,x} + (A_y)_{,y}\right)\boldsymbol{a}\mathrm{d}\Omega, \\
R &= R_{rem} + \int ((\boldsymbol{w} \cdot \boldsymbol{F}) \cdot \boldsymbol{n})\,\mathrm{d}\Gamma - \int \boldsymbol{F}\,(\boldsymbol{\nabla} \cdot \boldsymbol{w})\,\mathrm{d}\Omega - \int \boldsymbol{w} \cdot \left((A_x)_{,x} + (A_y)_{,y}\right)\boldsymbol{a}\mathrm{d}\Omega.
\end{aligned} \tag{2.42}$$

Here, we declare $\boldsymbol{F}|_\Gamma = \boldsymbol{F}^* = \boldsymbol{A}(\boldsymbol{a}^*)\boldsymbol{a}^*$, where $\boldsymbol{a}^*$ is a vector of values for the free degrees-of-freedom. Recall that $\boldsymbol{a}$ is either the coefficients or the physical moments, at the boundary, i.e., $\boldsymbol{a}^* = \boldsymbol{a}|_\Gamma$. In this way, we can enforce no-slip or pressure Dirichlet boundary conditions directly in the GMF2, LHF2, and LMF2 equations or via (2.18) in the GHF2 equations. Substituting $\boldsymbol{F}^*$ gives:

$$R = R_{rem} + \int ((\boldsymbol{w} \cdot \boldsymbol{F}^*) \cdot \boldsymbol{n})\,\mathrm{d}\Gamma - \int \boldsymbol{F}\,(\boldsymbol{\nabla} \cdot \boldsymbol{w})\,\mathrm{d}\Omega - \int \boldsymbol{w} \cdot \left((A_x)_{,x} + (A_y)_{,y}\right)\boldsymbol{a}\mathrm{d}\Omega. \tag{2.43}$$

Adding and subtracting the boundary integral term gives:

$$\begin{aligned}
R = R_{rem} + \int ((\boldsymbol{w} \cdot \boldsymbol{F}^*) \cdot \boldsymbol{n})\,\mathrm{d}\Gamma - \int ((\boldsymbol{w} \cdot \boldsymbol{F}) \cdot \boldsymbol{n})\,\mathrm{d}\Gamma + \int ((\boldsymbol{w} \cdot \boldsymbol{F}) \cdot \boldsymbol{n})\,\mathrm{d}\Gamma \\
+ \int \boldsymbol{F}\,(\boldsymbol{\nabla} \cdot \boldsymbol{w})\,\mathrm{d}\Omega - \int \boldsymbol{w} \cdot \left((A_x)_{,x} + (A_y)_{,y}\right)\boldsymbol{a}\mathrm{d}\Omega.
\end{aligned} \tag{2.44}$$

Here, we recover all the original terms and, after applying the divergence theory in reverse, can recombine them with R_{rem} into R_{orig}, such that R_{orig} represents the terms that appear in (2.39), which gives:

$$R = R_{orig} + \int \boldsymbol{w} \cdot \left(\left(\boldsymbol{A}\left(\boldsymbol{a}^*\right) \cdot \boldsymbol{n}\right)\boldsymbol{a}^* - \left(\boldsymbol{A}\left(\boldsymbol{a}^h\right) \cdot \boldsymbol{n}\right)\boldsymbol{a}^h\right)\mathrm{d}\Gamma. \tag{2.45}$$

Note that, for the GHF2 equations, where the coefficient matrices are constant, (2.45) simplifies the enforcement shown in [9]:

$$R = R_{orig} + \int \boldsymbol{w} \cdot \left((\boldsymbol{A} \cdot \boldsymbol{n}) \left(\boldsymbol{a}^* - \boldsymbol{a}^h \right) \right) \delta\Gamma. \tag{2.46}$$

2.3.1 Comments on implementation

In practice, (2.45) is applied by first setting $\boldsymbol{a}^* = \boldsymbol{a}^h$, where $\boldsymbol{a}^h$ are the values of the degrees-of-freedom at an integration point. Then, the appropriate values in $\boldsymbol{a}^*$ are overwritten by the desired Dirichlet boundary conditions. For example, for the traditional no-slip condition on the velocity field, $u_i = 0$, we override $a_2^* = a_3^* = 0$.

2.4 Stabilization

This work uses the Streamline Upwind Petrov-Galerkin (SUPG) stabilization scheme used by Makhija and Maute [9], which is itself derived from the work by Brooks and Hughes [38], such that:

$$R = \int \left(\boldsymbol{w} + \boldsymbol{\tau} \left(\boldsymbol{A} \cdot \boldsymbol{\nabla} \right) \boldsymbol{w} \right) \cdot \left(\boldsymbol{a}_{,t} + A_x(\boldsymbol{a}) \boldsymbol{a}_{,x} + A_y(\boldsymbol{a}) \boldsymbol{a}_{,y} + \boldsymbol{C}(\boldsymbol{a}) \right) \delta\Omega, \tag{2.47}$$

where $\boldsymbol{\tau}$ is the stabilization matrix:

$$\boldsymbol{\tau} = \boldsymbol{P} |\boldsymbol{\Lambda}|^{-1/2} \boldsymbol{P}^{-1}, \tag{2.48}$$

and $\boldsymbol{P}$ and $\boldsymbol{\Lambda}$ arise from the eigenvalue decomposition:

$$\boldsymbol{P} \boldsymbol{\Lambda} \boldsymbol{P}^{-1} = 4 \left(h_x^{-2} A_x^T A_x + h_y^{-2} A_y^T A_y \right) + \frac{\partial \boldsymbol{C}^T}{\partial \boldsymbol{a}} \frac{\partial \boldsymbol{C}}{\partial \boldsymbol{a}}, \tag{2.49}$$

where

$$h_i = \frac{2}{\sum_{k=1}^{q} |\boldsymbol{e}_i \cdot \nabla N_k|} \tag{2.50}$$

is the approximate length of a quadrilateral element, $\boldsymbol{e}_i$ is the unit vector in the i-direction, $N_k = N_k(\boldsymbol{x})$ is the nodal basis function for node k, and q is the number of nodes per element. As discussed in [9], for similar first order equations, such as the compressible Euler equations, the eigenvalues

and vectors can be expressed analytically to remove computational cost. However, the collision contribution in the GHF2 and the non-linear nature of the coefficient matrices in the remaining forms, renders this approach prohibitive. Makhija and Maute [9] addressed this issue by removing the non-linear components in $\frac{\partial \boldsymbol{C}}{\partial \boldsymbol{a}}$; however, this approach is not possible for the remaining governing equations and is not considered in this work.

2.5 Discretization

The previous work in [9] uses the XFEM, which introduces additional degrees-of-freedom to allow the immersed boundary method on a uniform background mesh. Because this particular study is not interested in topology optimization, the XFEM is not needed. Instead, state variables are interpolated within an element as:

$$u(\boldsymbol{x}) \approx \tilde{u}(\boldsymbol{x}) = \sum_{i=1}^{N_n} v_i(\boldsymbol{x}) u_i^f, \tag{2.51}$$

where $v_i(\boldsymbol{x})$ are the nodal basis functions and u_i^f are the degrees-of-freedom of node i. The XFEM is a generalization of this approach and is formally introduced in Section 3.7.1.

2.5.1 Remarks regarding the Jacobian

The finite element discretization will require the derivative of the weak form of the governing equations (2.39) with respect to the nodal degrees-of-freedom. Of particular interest as the advective terms, $A_x(\boldsymbol{a})\boldsymbol{a}_{,x}$ and $A_y(\boldsymbol{a})\boldsymbol{a}_{,y}$, which are evaluated at an integration point as:

$$\boldsymbol{R}^g = A_x(\boldsymbol{a}^g)\frac{\partial \boldsymbol{a}^g}{\partial x} + A_y(\boldsymbol{a}^g)\frac{\partial \boldsymbol{a}^g}{\partial y} = A_x(N\hat{\boldsymbol{a}})B_x\hat{\boldsymbol{a}} + A_y(N\hat{\boldsymbol{a}})B_y\hat{\boldsymbol{a}}, \tag{2.52}$$

where $\boldsymbol{a}^g$ are the interpolated values at the integration point, $\hat{\boldsymbol{a}}$ are the nodal degrees-of-freedom, $N = N(\boldsymbol{x}^g)$ are the interpolation functions at the integration point, and B_x and B_y are the corresponding differential operators. The remaining terms in (2.39) are ignored in this discussion. When the coefficient matrices are constant, the derivative of this residual contribution with respect of the nodal degrees-of-freedom is trivially found. However, because the coefficient matrices are not

constant for the GMF2 and LMF2 equations, they are implemented with the following procedure. For brevity, we will limit our discussion to the x-component term in (2.52), but the y-component term is treated similarly. First, consider the differential product rule:

$$\frac{\partial \boldsymbol{R}^g}{\partial \hat{\boldsymbol{a}}} = \frac{\partial (A_x(\boldsymbol{a}^g))}{\partial \hat{\boldsymbol{a}}} B_x \hat{\boldsymbol{a}} + A_x(\boldsymbol{a}^g) B_x. \tag{2.53}$$

When the coefficient matrices are constant, the first term vanishes and only the second remains. For the first term, we now consider the chain rule of differentiation:

$$\frac{\partial \boldsymbol{R}^g}{\partial \hat{\boldsymbol{a}}} = \frac{\partial (A_x(\boldsymbol{a}^g))}{\partial \boldsymbol{a}^g} \frac{\partial \boldsymbol{a}^g}{\partial \hat{\boldsymbol{a}}} B_x \hat{\boldsymbol{a}} + A_x(\boldsymbol{a}^g) B_x, \tag{2.54}$$

where $\frac{\partial (A_x(\boldsymbol{a}^g))}{\partial \boldsymbol{a}^g}$ is a 3^{rd} order tensor. While this does not present a mathematical challenge, as this term has an analytical expression, it does present an implementation challenge in the current framework, as it would require the storage of a rather sparse object and its product operator is computationally expensive. We avoid the need for this tensor by first introducing $\boldsymbol{b}^g = B_x \hat{\boldsymbol{a}}$ and treating it locally as a constant, then the Jacobian becomes:

$$\frac{\partial \boldsymbol{R}^g}{\partial \hat{\boldsymbol{a}}} = \frac{\partial (A_x(\boldsymbol{a}^{\boldsymbol{g}}) \boldsymbol{b}^g)}{\partial \boldsymbol{a}^{\boldsymbol{g}}} \frac{\partial \boldsymbol{a}^g}{\partial \hat{\boldsymbol{a}}} + A_x(\boldsymbol{a}^{\boldsymbol{g}}) B_x, \tag{2.55}$$

and, recognizing that analytical expressions for $\boldsymbol{d}^g = A_x(\boldsymbol{a}^g)\boldsymbol{b}^g$, i.e. the matrix-vector product of A_x and an arbitrary vector, are available, we can write:

$$\frac{\partial \boldsymbol{R}^g}{\partial \hat{\boldsymbol{a}}} = \frac{\partial \boldsymbol{d}^g}{\partial \boldsymbol{a}^{\boldsymbol{g}}} \frac{\partial \boldsymbol{a}^g}{\partial \hat{\boldsymbol{a}}} + A_x(\boldsymbol{a}^g) B_x = J_x(\boldsymbol{a}^g, \boldsymbol{b}^g) N + A_x(\boldsymbol{a}^g) B_x, \tag{2.56}$$

where

$$J_x(\boldsymbol{a}^g, \boldsymbol{b}^g) = \frac{\partial (A_x(\boldsymbol{a}^g)\boldsymbol{b}^g)}{\partial \boldsymbol{a}^g} \tag{2.57}$$

is a matrix that has analytical expressions. We thus avoid the need to have expressions for a 3^{rd} order tensor. The time and collision vectors do not require this type of treatment. Further, we recognize that the stabilization term in (2.47), i.e. $\boldsymbol{\tau}(\boldsymbol{A}\cdot\boldsymbol{\nabla})\boldsymbol{w}$, needs a similar treatment to calculate its derivative with respect to the nodal degrees-of-freedom. While the term $\boldsymbol{\tau}\frac{\partial((\boldsymbol{A}\cdot\boldsymbol{\nabla})\boldsymbol{w})}{\partial \hat{\boldsymbol{a}}}$ could make use of the treatment described in this section, its counterpart would inevitably involve the factor

$\frac{\partial \boldsymbol{\tau}}{\partial \boldsymbol{a}^g}$, which has no analytical expression. As noted by Makhija and Maute [9], the eigenvalues and eigenvectors resulting from the eigenvalue decomposition (2.49) are not known analytically, even for the GHF2 equations. An alternative would be to compute $\frac{\partial \boldsymbol{\tau}}{\partial \boldsymbol{a}^g}$ with finite differences. However, this approach would significantly increase the computational cost, e.g. consider that the each degree-of-freedom would be perturbed twice, each followed by an eigenvalue decomposition. Thus, this finite difference approach would require 12 additional decompositions per integration point. We recourse to ignore the derivative of the stabilization term with respect to the nodal degrees-of-freedom.

2.6 Numerical example for the moment formulations

To resolve higher Knudsen number flows, higher-order moment methods will be required. However, these approaches result in highly non-linear equations that may be negatively impacted by the SUPG stabilization framework presented previously. To this end, we will study the impact of non-linear system of equations by comparing the GHF2 and GMF2 equations. Because these two systems of equations result from the same equilibrium expansion, we expect that their resulting flow solutions to be the same, except for any influence from the non-linearity of the GMF2 coefficient matrices.

We consider the same problem as in [9], namely, the benchmark problem *2D-1* for the flow past a cylinder in [39]. As noted in [9], the governing equations presented here approximate nearly incompressible flows while the benchmark in [39] is presented for purely incompressible flows; further, Makhija and Maute [9] studied the incompressibility error due to the reference Mach number. The study in this work will focus on the influence of the GMF2 and LMF2 equations, when compared to the GHF2 work in [9].

The problem description and boundary conditions are taken from Schafer [39] and are shown in Fig. 2.1. The inlet flow profile is parabolic and the Reynolds number is set to $Re = 20$ and is computed with respect to the mean inlet velocity and the cylinder diameter. While the benchmark problem does not specify outlet boundary conditions, in this work, as in [9], we consider a constant pressure boundary for simplicity. The benchmark problem provides a lower and upper limit on the

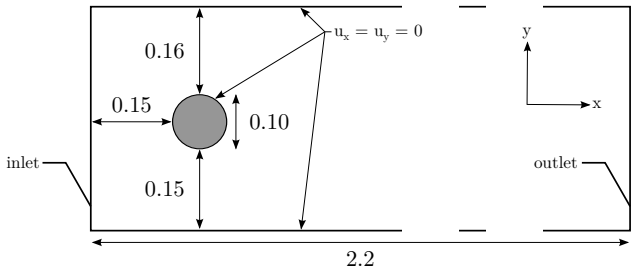

Figure 2.1: Problem description for the flow past a cylinder. All dimensions are in m.

coefficient of drag, which is computed after nondimensionalizing the forces,

$$C_D = \frac{2\boldsymbol{F} \cdot \frac{\bar{\boldsymbol{U}}}{|\bar{\boldsymbol{U}}|}}{\bar{\rho}|\bar{\boldsymbol{U}}|^2 D}, \tag{2.58}$$

where D is the cylinder diameter. As mentioned previously, Makhija and Maute [9] studied this problem for the GHF2 equations presented here and found, among other results, that (i) the GHF2 satisfy the benchmark as the reference Mach number is decreased, (ii) as the reference Mach number is decreased, a more refined mesh is required to accurately resolve the flow, and (iii) the XFEM accurately predicts the cylinder boundary and has similar results to the body-fitted examples considered. In this work, we will focus on the use of body-fitted meshes and study the effect of the proposed systems of governing equations.

The body-fitted meshes used in this study use a constant number of intervals in the radial direction and a higher mesh density near the cylinder to attempt to better capture boundary layer effects. The remaining domain behind the cylinder is meshed uniformly with square elements. The coarsest body-fitted mesh is shown in Fig. 2.2.

2.6.1 Effect of the finite element discretization: GMF2 against the GHF2 equations

First, we wish to compare the GMF2 and GHF2 equations. While Makhija and Maute [9] found that $Ma_{ref} = 0.023$ satisfied the benchmark problem, the results are very close to the upper limit on the coefficient of drag set by Schafer et al. [39]. Instead, the reference Mach number is set to $Ma_{ref} = 0.01$. We will consider the compressibility error in Section 2.6.2. Here, we solve the *2D-1* benchmark problem with the GHF2 and GMF2. For the GHF2 equations, the no-slip

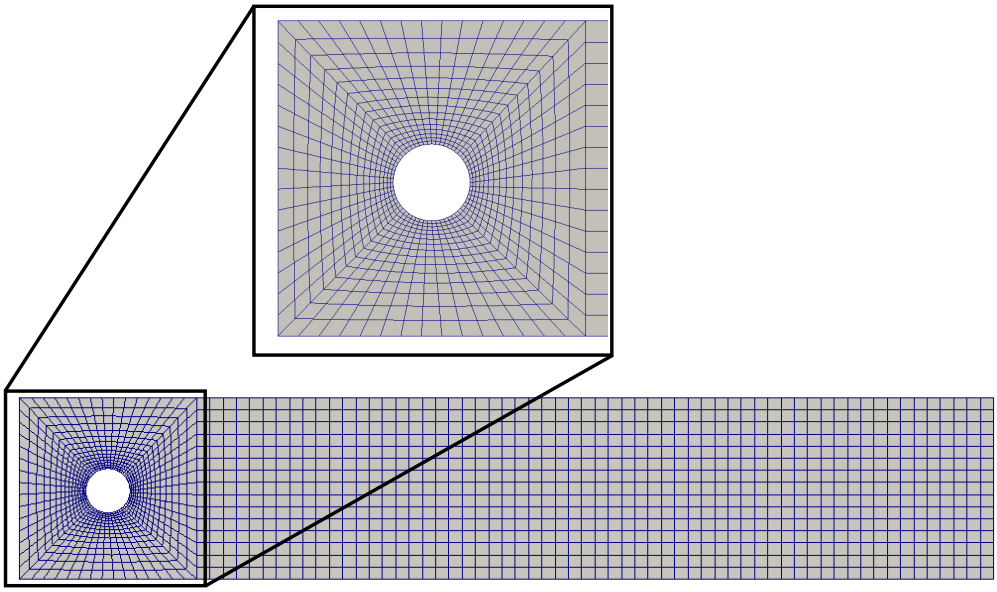

Figure 2.2: Coarsest body-fitted mesh for cylinder problem.

boundary conditions are taken as $a_2 = a_3 = 0$; the GMF2 equations have the velocities as the degrees-of-freedom, so the no-slip boundary conditions are enforced directly.

Fig. 2.3 shows the nondimensionalized velocity magnitude with streamlines for three levels of refinement: 78720, 484800, and 1478400 total degrees-of-freedom, respectively. From this study, we observe that the velocity distribution is rather insensitive to the level of refinement when using the GHF2 equation; in contrast, the level of mesh refinement is critical when using the GMF2 equations. Even for the finest level of refinement, we see a slight disagreement in the velocity solutions; however, this disagreement diminishes with mesh refinement. This suggests that the GMF2 and GHF2 equations are indeed equivalent, i.e. in the limit of mesh refinement, both sets of governing equations converge to the same solution.

To investigate the disagreement between the GHF2 and GMF2 results, we solve the benchmark problem again but without the numerical stabilization, i.e. $\boldsymbol{\tau} = \mathbf{0}$. Because we remove stabilization, we can no longer consider the same levels of refinement as previously; instead, we use a body-fitted mesh with 92400 degrees-of-freedom. Fig. 2.4 shows the velocity magnitude for the GHF2 and GMF2 equations, with and without stabilization. We observe the same phenomena as in Fig. 2.3, the GMF2 results disagree with the GHF2 when an insufficiently refined mesh is used.

Further, we see the effect of omitting the stabilization, oscillations develop for both sets of equations. These oscillations are stronger in finer meshes, which prevents their use. Finally, the disagreement between the GHF2 and GMF2 vanishes when stabilization is removed, i.e. compare Fig. 2.4b and Fig. 2.4d. This suggests that that the disagreement shown in Fig. 2.3 is directly caused by the stabilization. The stabilization presented by Makhija and Maute [9], who show the need for mesh refinement as the reference Mach number decreases, dampens the flow solutions with the GHF2. In this work, we find that the diffusive effect of the stabilization scheme is considerably worse for the GMF2 equations. We suggest that this is due to the highly non-linear nature of the coefficient matrices, $\boldsymbol{A} = [A_x,\ A_y]$.

We consider the coefficient of drag (2.58), shown in Fig. 2.5 for the GHF2 and GMF2 equations and several levels of mesh refinement. The convergence for the GHF2 was previously

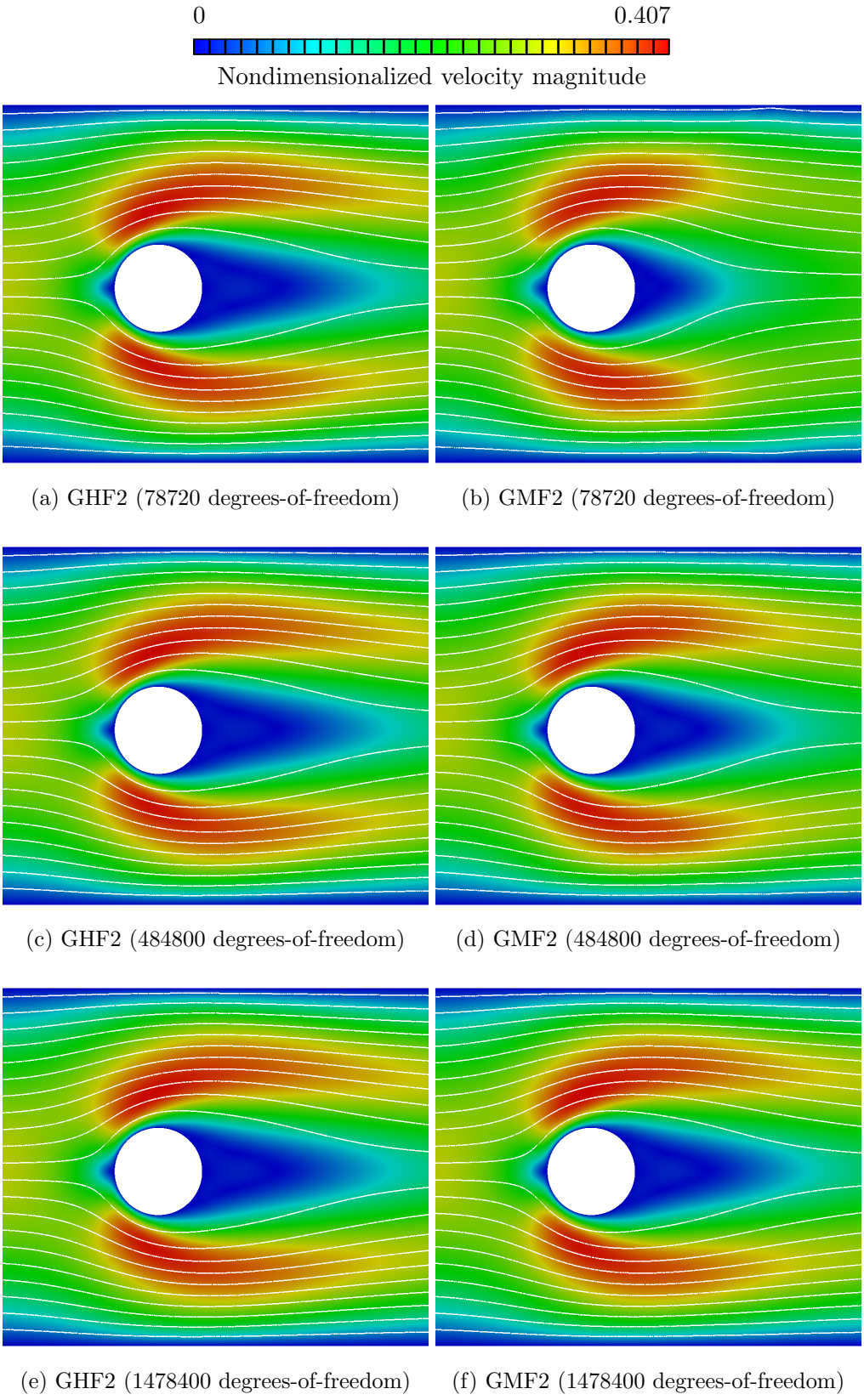

(a) GHF2 (78720 degrees-of-freedom) (b) GMF2 (78720 degrees-of-freedom)

(c) GHF2 (484800 degrees-of-freedom) (d) GMF2 (484800 degrees-of-freedom)

(e) GHF2 (1478400 degrees-of-freedom) (f) GMF2 (1478400 degrees-of-freedom)

Figure 2.3: Velocity magnitude with streamlines for the GHF2 and GMF2 equations for select levels of mesh refinement.

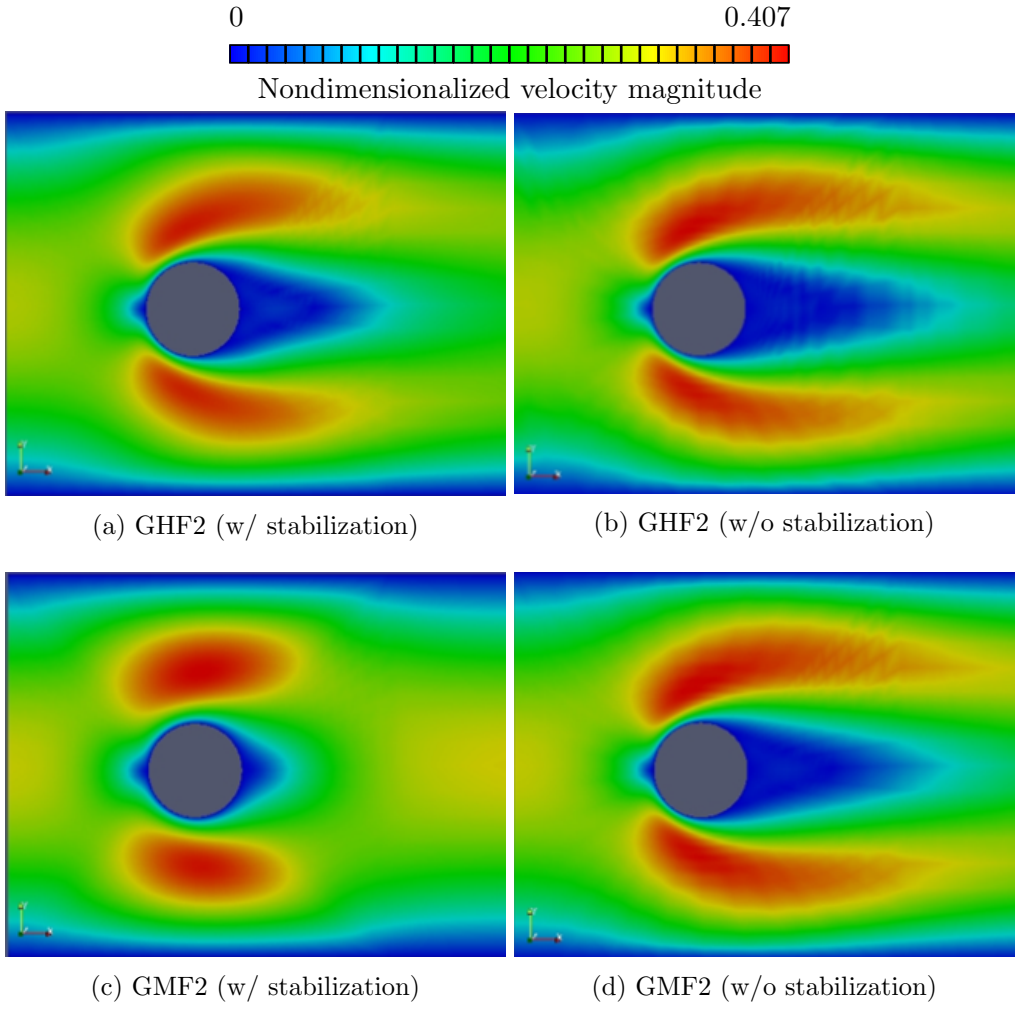

(a) GHF2 (w/ stabilization) (b) GHF2 (w/o stabilization)

(c) GMF2 (w/ stabilization) (d) GMF2 (w/o stabilization)

Figure 2.4: Velocity magnitude for the GHF2 and GMF2 equations with and with stabilization for lowest level of refinement.

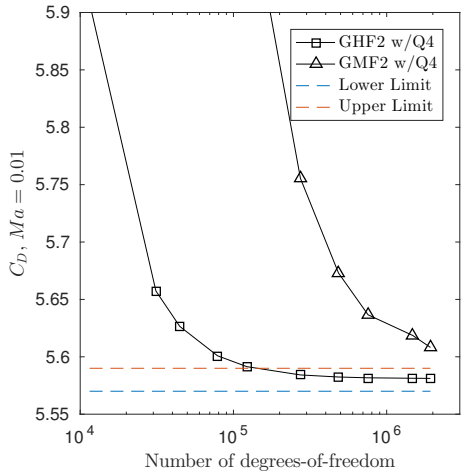

Figure 2.5: Coefficient of drag using the GHF2 and GMF2 equations, $Ma_{ref} = 0.01$, and several levels of mesh refinement.

shown in [9]. In contrast, the GMF2 requires further mesh refinement. In [9], the GHF2 also required significant mesh refinement for smaller reference Mach numbers; this study suggests that the GMF2 equations require further refinement at a larger reference Mach number threshold than the GHF2 equations, i.e. the GHF2 equations require considerable mesh refinement when $Ma_{ref} \leq 0.001$, whereas the GMF2 require it when $Ma_{ref} \leq 0.01$.

Finally, we consider the convergence of the two system of equations. The L^2 error is computed for a chosen solution, $\boldsymbol{u}_{sol}$, against a reference solution, $\boldsymbol{u}_{ref}$, as follows:

$$L^2 \text{ error } = \left(\frac{\int |\boldsymbol{u}_{sol} - \boldsymbol{u}_{ref}|^2 \mathrm{d}\Omega}{\int |\boldsymbol{u}_{ref}|^2 \mathrm{d}\Omega} \right)^{1/2} \tag{2.59}$$

. Fig. 2.6 shows the L2 error of the GHF2 and GMF2 solutions at each level of refinement, where the reference solution uses the GHF2 equations and the finest level of mesh refinement. We observe that the convergence rate of the GMF2 is considerably lower than that of the GHF2 equations; however, we can reasonably expect that the two system of equations converge to the same solution and that the disagreement between the two is caused by the interaction between the stabilization scheme and the non-linear form of the coefficient matrices.

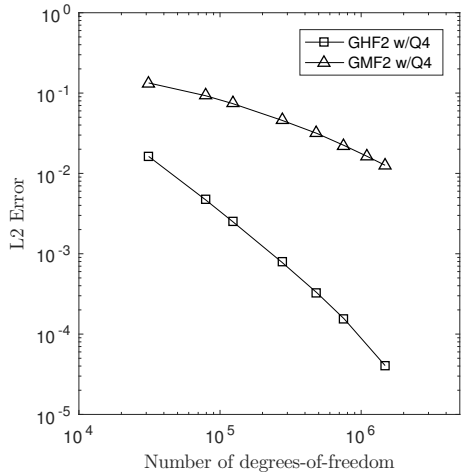

Figure 2.6: L^2 error using the GHF2 and GMF2 equations, $Ma_{ref} = 0.01$, and several levels of mesh refinement. The reference solution uses the GHF2 equations and the finest level of refinement, 1.93×10^6 degrees-of-freedom.

2.6.2 Effect of the reference Mach number

In this study, we consider the effect of the reference Mach number on the numerical results. For the GHF2 equations, lower reference Mach numbers eliminate the compressibility error, they also require increasingly finer meshes to convergence [9]. We seek to understand this effect in the GMF2 equations; as in [9], we consider reference Mach numbers 0.023, 0.04, 0.0577, and 0.1, and repeat the mesh refinement study considered previously.

Fig. 2.7, 2.8, 2.9, 2.10 show the velocity magnitude near the cylinder using the GHF2 and GMF2 equations and two select levels of refinement, for reference Mach numbers 0.023, 0.04, 0.0577, and 0.1, respectively. We observe that as Ma_{ref} is increased, the disagreement between the GHF2 and GMF2 results on a coarse mesh vanishes. The required level of refinement relaxes as larger reference Mach numbers for the GMF2 equations, just as for the GHF2 equations in [9].

The coefficient of drag for same levels of refinement and reference Mach numbers is shown in Fig. 2.11. As the reference Mach number is increased, the convergence rate of the GMF2 equations approaches that of the GHF2 equations. Hardware limitations prohibit further levels of refinement. Fig. 2.12 shows the coefficient of drag at the finest level of refinement available for each reference Mach numbers. This shows the agreement between the GHF2 and GMF2 equations for larger reference Mach numbers and highlights the need for further refinement at the lower reference Mach numbers. Because this level of refinement was not available for this study, the GMF2 only *appear* to diverge from the GHF2 equations. This will be made clear in the next Section, where we consider an alternative to mesh refinement.

2.6.3 Improved performance with quadratic elements

Because finer levels of refinement are not considered due to hardware limitations, we instead consider the use of higher-order 8-node quadratic elements. We expect that the use of a higher-order element will result in smoother solutions and that the diffusive effect of the stabilization scheme presented in Section 2.4 will be reduced. Fig. 2.13 shows an example of the bilinear (Q4) element

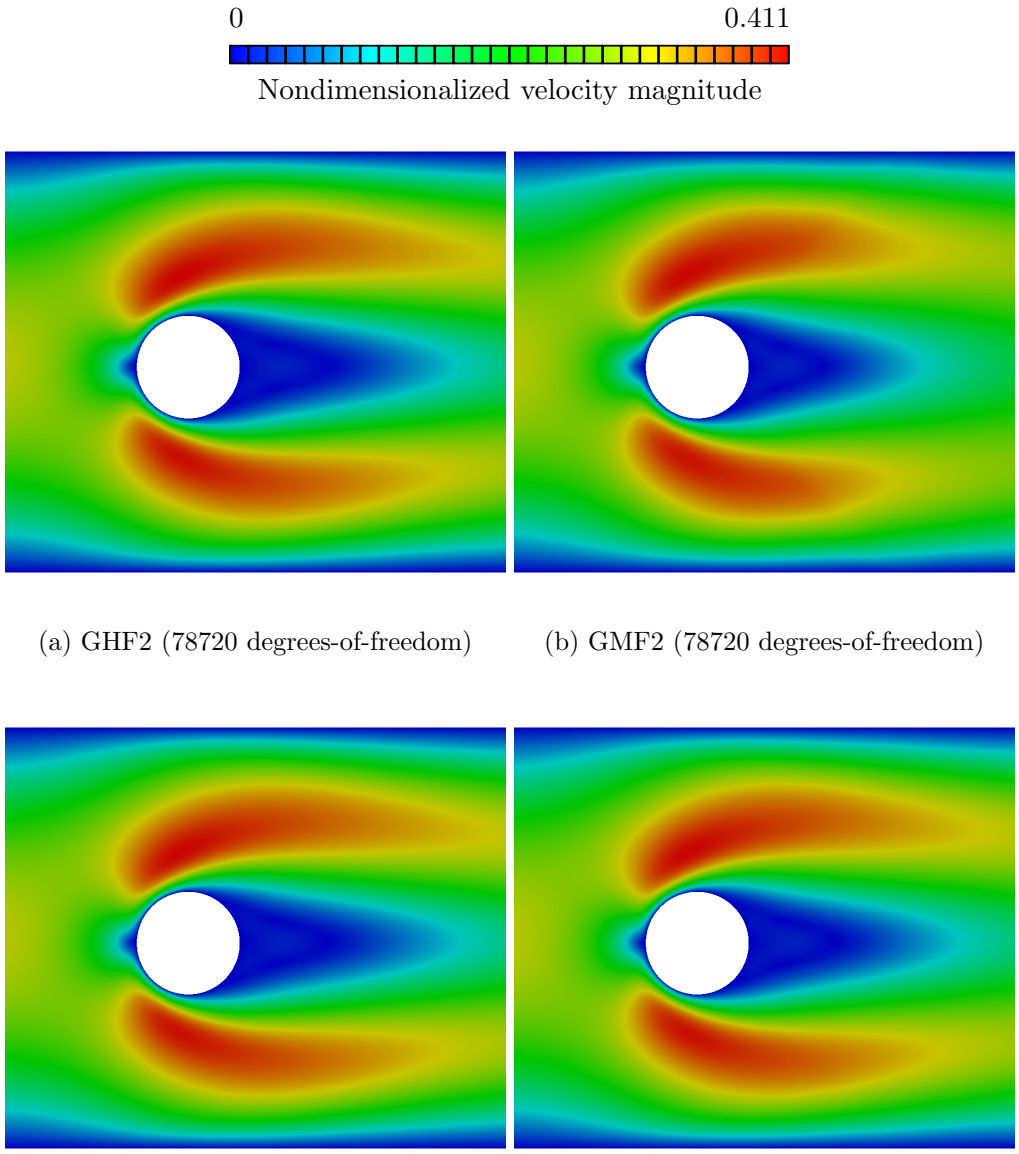

(a) GHF2 (78720 degrees-of-freedom) (b) GMF2 (78720 degrees-of-freedom)

(c) GHF2 (484800 degrees-of-freedom) (d) GMF2 (484800 degrees-of-freedom)

Figure 2.7: Velocity magnitude for the GHF2 and GMF2 equations, for $Ma_{ref} = 0.023$ and two levels of refinement.

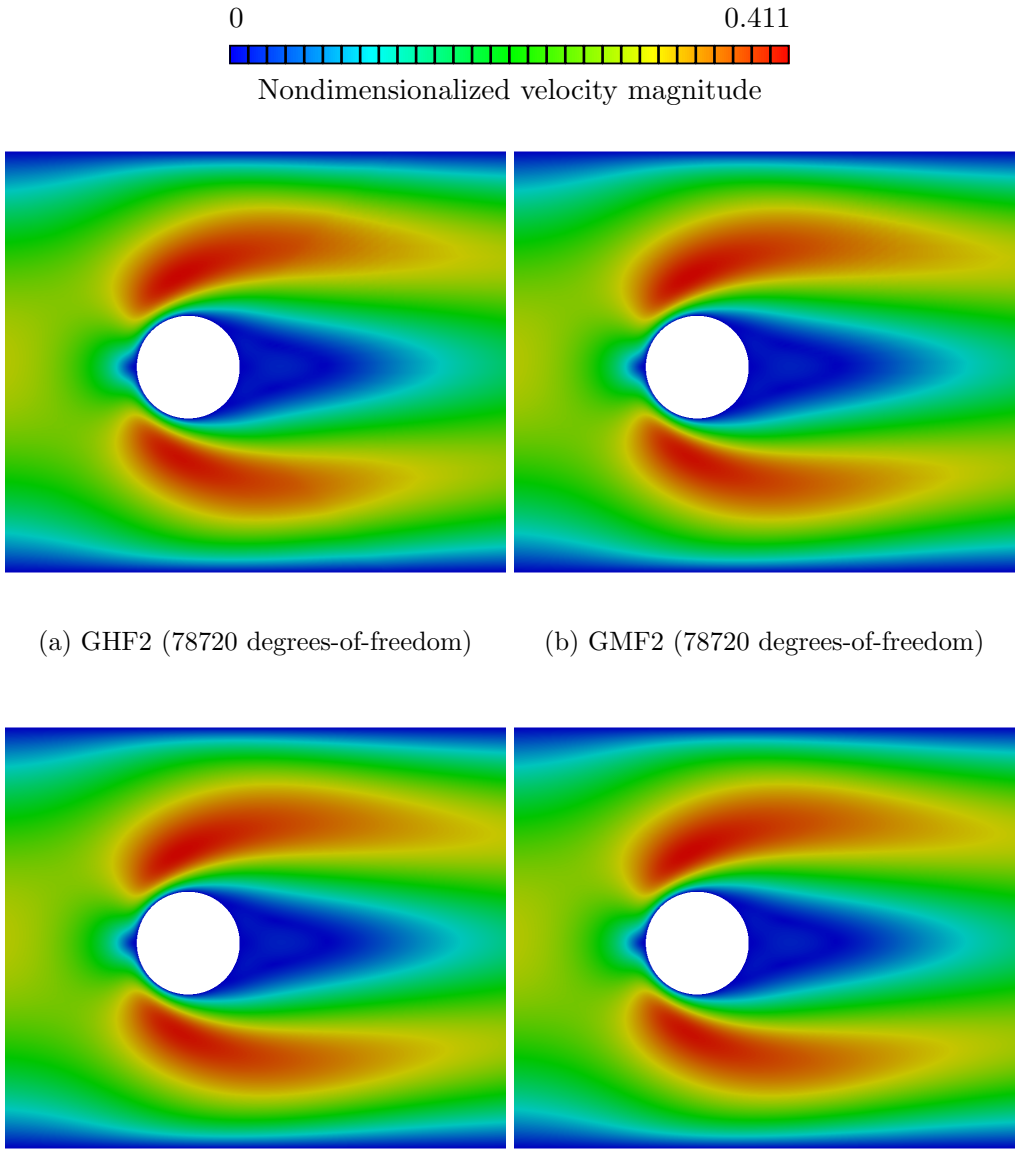

(a) GHF2 (78720 degrees-of-freedom) (b) GMF2 (78720 degrees-of-freedom)

(c) GHF2 (484800 degrees-of-freedom) (d) GMF2 (484800 degrees-of-freedom)

Figure 2.8: Velocity magnitude for the GHF2 and GMF2 equations, for $Ma_{ref} = 0.04$ and two levels of refinement.

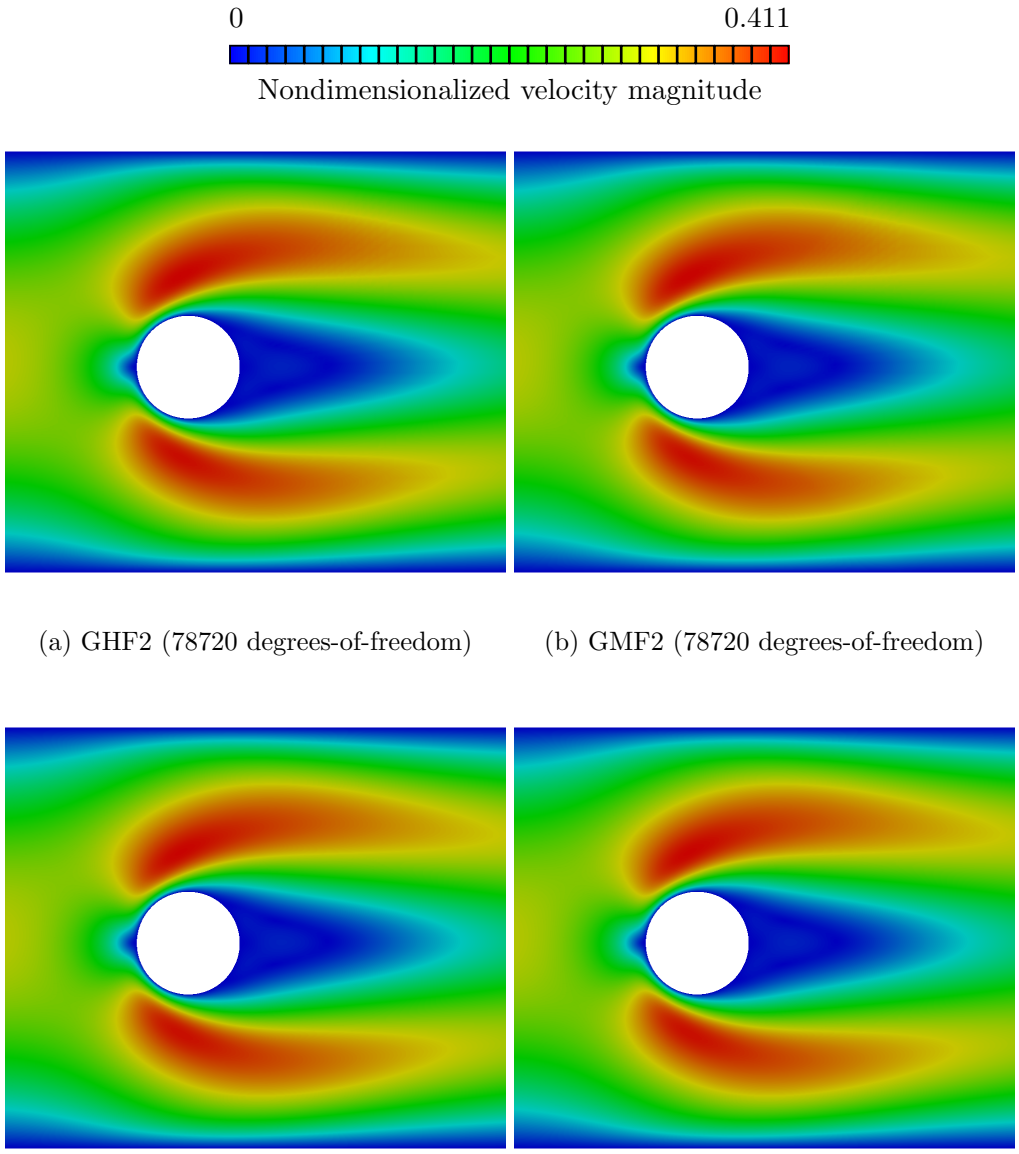

(a) GHF2 (78720 degrees-of-freedom) (b) GMF2 (78720 degrees-of-freedom)

(c) GHF2 (484800 degrees-of-freedom). (d) GMF2 (484800 degrees-of-freedom).

Figure 2.9: Velocity magnitude for the GHF2 and GMF2 equations, for $Ma_{ref} = 0.0577$ and two levels of refinement.

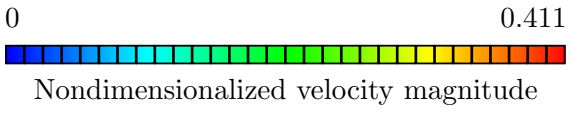

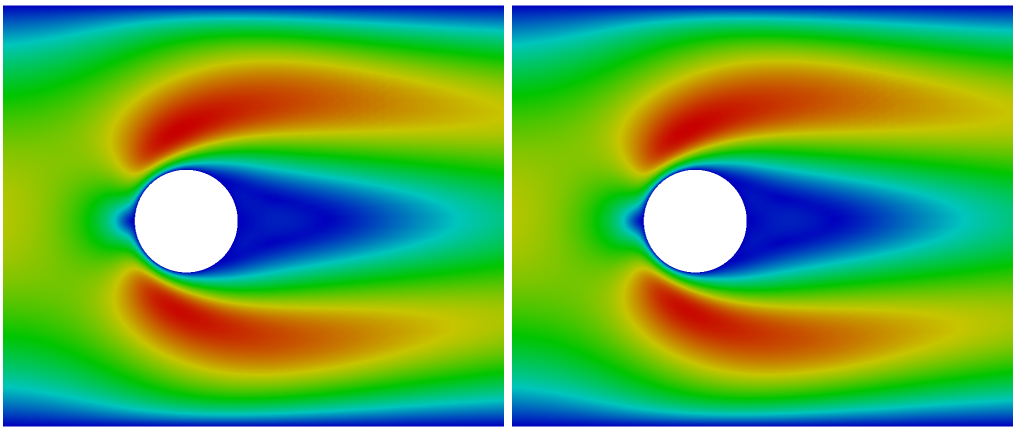

(a) GHF2 (78720 degrees-of-freedom). (b) GMF2 (78720 degrees-of-freedom).

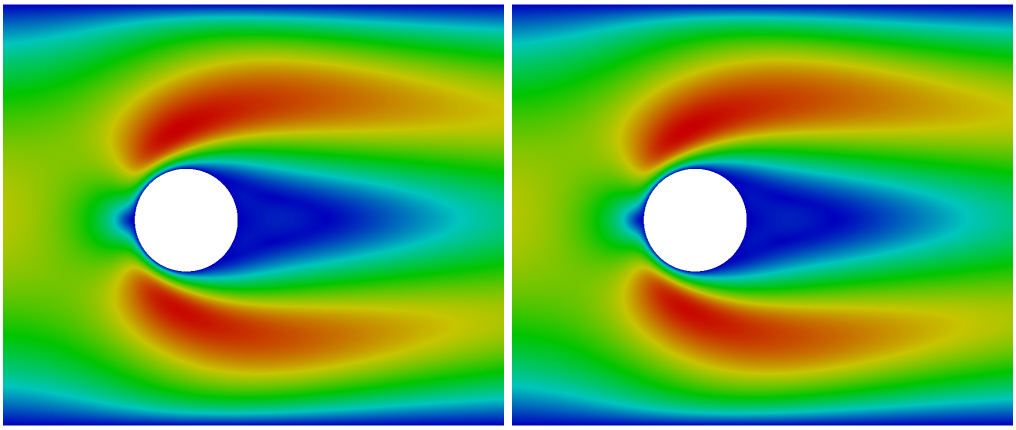

(c) GHF2 (484800 degrees-of-freedom). (d) GMF2 (484800 degrees-of-freedom)

Figure 2.10: Velocity magnitude for the GHF2 and GMF2 equations, for $Ma_{ref} = 0.1$ and two levels of refinement.

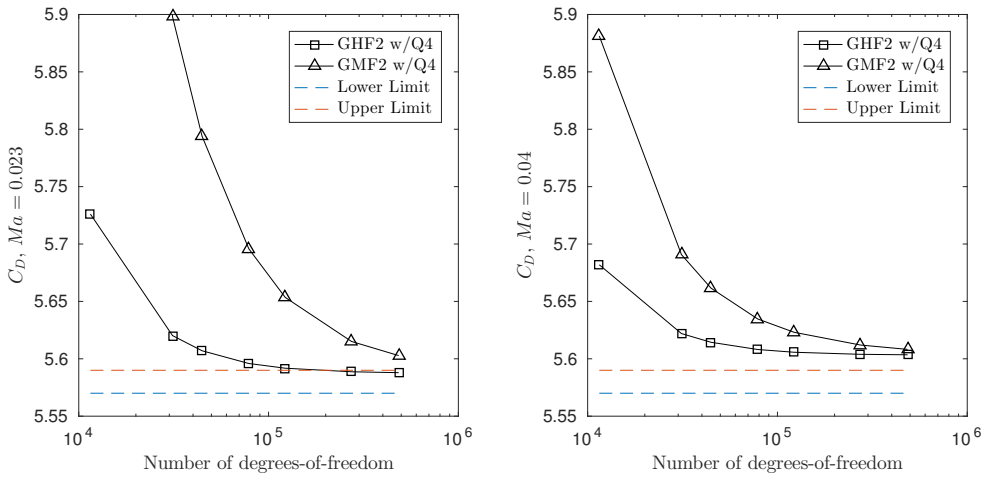

(a) $Ma_{ref} = 0.023$ (b) $Ma_{ref} = 0.04$

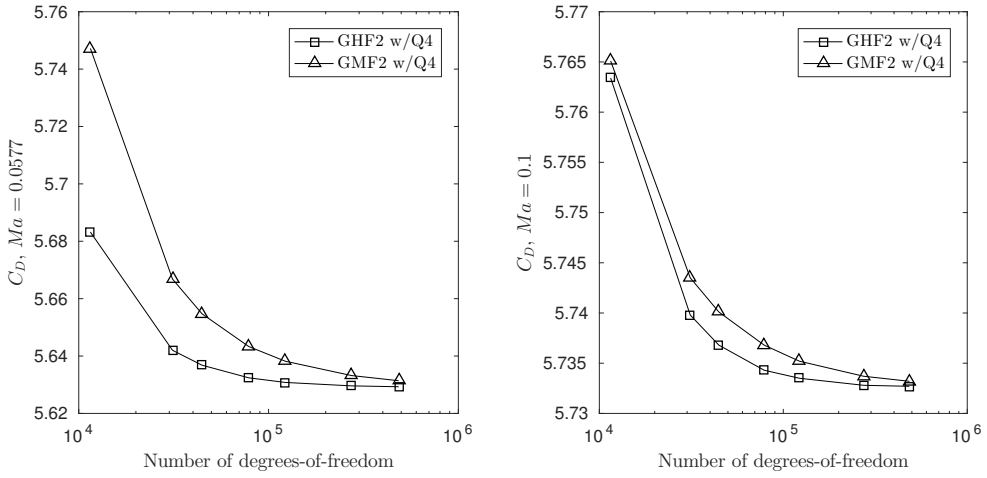

(c) $Ma_{ref} = 0.0577$ (d) $Ma_{ref} = 0.1$

Figure 2.11: Coefficient of drag using the GHF2 and GMF2 equations, for several reference Mach numbers and several levels of mesh refinement.

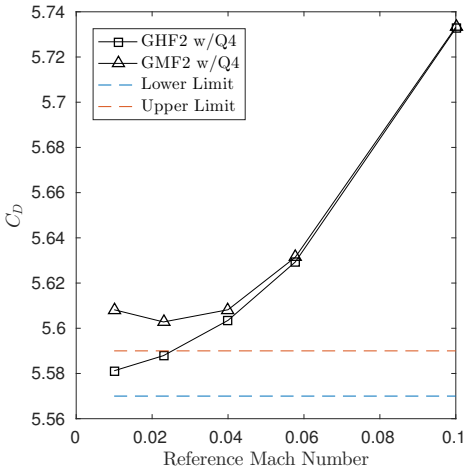

Figure 2.12: Coefficient of drag using the GHF2 and GMF2 equations and the finest level of mesh refinement for several reference Mach numbers.

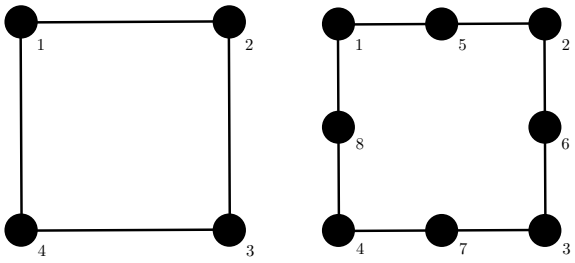

(a) Bilinear (b) Quadratic

Figure 2.13: Example of a bilinear and quadratic element with relative node numbering.

used previously, as well as an example of a quadratic (Q8) element, where each element edge has three nodes, instead of two.

Fig. 2.14 shows the nondimensionalized velocity magnitude with streamlines for two levels of refinement, similar to the refinement used in Fig. 2.3. In contrast with the results using bilinear elements, the results with quadratic elements suggest a considerably better agreement between the GHF2 and GMF2 equations at low levels of refinement. The pronounced diffusive effect of the stabilization scheme when using the GMF2 equations appears to be well-countered by the use of quadratic elements.

We again consider the coefficient of drag, shown in Fig. 2.15 for the GHF2 and GMF2 equations using quadratic elements and several levels of refinement. The GHF2 results using bilinear elements as the same as those shown in Fig. 2.5. We observe the significant improvement in convergence rate for both sets of governing equations; moreover, we note the nearly perfect agreement of the GHF2 and GMF2 equations.

Finally, we again consider the L^2-convergence rate of the GHF2 and GMF2 equations using quadratic elements. Fig. 2.16 shows L^2 error for several levels of refinement. The reference solution is the GHF2 solution using quadratic elements and the finest level of refinement, 1.45×10^6 degrees-of-freedom. Note the remaining error in the GHF2 results using bilinear elements, we reasonably attribute this to the difference in element degree. More importantly, we observe the improved convergence rate of the GMF2 when using quadratic over bilinear elements. This study

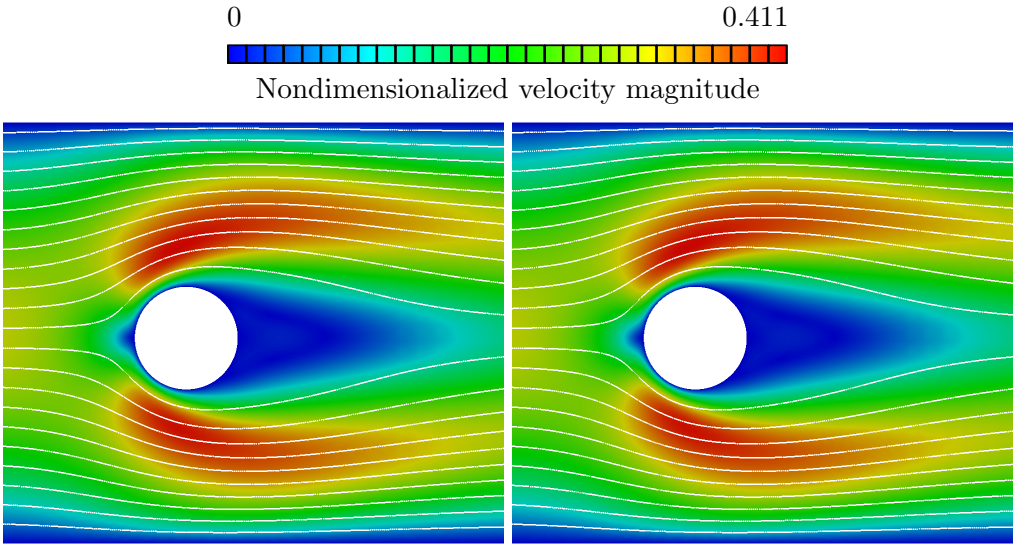

(a) GHF2 (92400 degrees-of-freedom) (b) GMF2 (92400 degrees-of-freedom)

(c) GHF2 (364800 degrees-of-freedom) (d) GMF2 (364800 degrees-of-freedom)

Figure 2.14: Velocity magnitude with streamlines for the GHF2 and GMF2 equations using quadratic elements for select levels of mesh refinement.

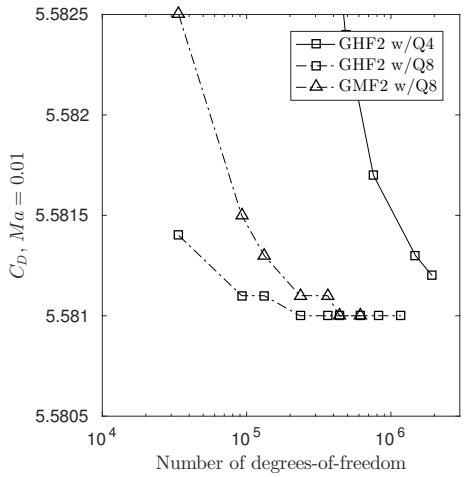

Figure 2.15: Coefficient of drag using the GHF2 and GMF2 equations, $Ma_{ref} = 0.01$, and several levels of mesh refinement.

more strongly suggest that the GMF2 equations are indeed equivalent to the GHF2 equations. The change in discretized variables, i.e. the GHF2 equations discretize the Hermite expansion coefficients, a_i, whereas the GMF2 equations discretize the physical moments directly, does not ultimately change the final flow solution.

2.6.4 Influence of quadratic elements at larger reference Mach numbers

In this section, we study the use of quadratic elements for larger reference Mach numbers, similar to the study in Section 2.6.2. We again consider reference Mach numbers 0.023, 0.04, 0.0577, and 0.1. Here, we do not show the velocity magnitude near the cylinder, as done in Fig. 2.7-2.10, since there are no discernible differences between the GHF2 and GMF2 results.

Rather, Fig. 2.17 shows the coefficient of drag for the same reference Mach numbers and for several levels of refinement. We observe that the coefficients of drag converge using the GMF2 equations converge to those using the GHF2 equations at coarser levels of refinement. The disagreement in Fig. 2.17d is less than 0.002%; note the vertical scale compared to other plots that show the coefficients of drag. The use of quadratic elements greatly improves the convergence rate of the GHF2 and GMF2 equations; because of this, we are able to reach the level of refinement to

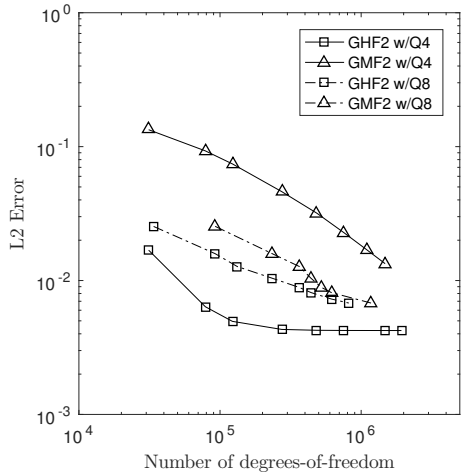

Figure 2.16: L^2 error using the GHF2 and GMF2 equations, $Ma_{ref} = 0.01$, and several levels of mesh refinement. The reference solution uses the GHF2 equations with quadratic elements and the finest level of refinement, 1.45×10^6 degrees-of-freedom.

achieve full convergence.

Fig. 2.18 shows the coefficient of drag for several reference Mach numbers, similar to Fig. 2.12. Here, the available level of mesh refinement allows the GMF2 results to agree with the GHF2 results.

2.6.5 Other Re numbers

Having considered the effect of the reference Mach number previously, we now consider the effect of the Reynolds numbers and its interaction with the use of quadratic elements. We consider only $Ma_{ref} = 0.01$ and Reynolds numbers of 30, 40, 50, and 60. Fig. 2.19 shows the coefficient of drag for the GHF2 and GMF2 equations with bilinear and quadratic elements and several levels of refinement. We again observe the good agreement of the GHF2 and GMF2 equations when quadratic elements are used and that the GMF2 require a greater level of refinement when using bilinear elements. Moreover, requirement threshold decreases as the Reynolds number increases. This suggests that at larger Reynolds numbers, the diffusive effect of the stabilization scheme on the GMF2 is weakened, just as it does for larger Reference Mach numbers.

2.6.6 Concluding remarks on the GMF2 equations

We summarize our findings regarding the GMF2 equations as follows: the GMF2 and GHF2 are indeed equivalent such that they converge to nearly identical solutions. However, the diffusive effect of the stabilization scheme is considerably more pronounced with the GMF2 due to the non-linear coefficient matrices. The GMF2 require a higher level of refinement at each reference Mach number when compared to the GHF2 equations; however, this requirement is considerably reduced when using quadratic elements over bilinear elements. We expect that this is due to the ability of quadratic elements to more smoothly resolve the non-linear nature of the GMF2 equations.

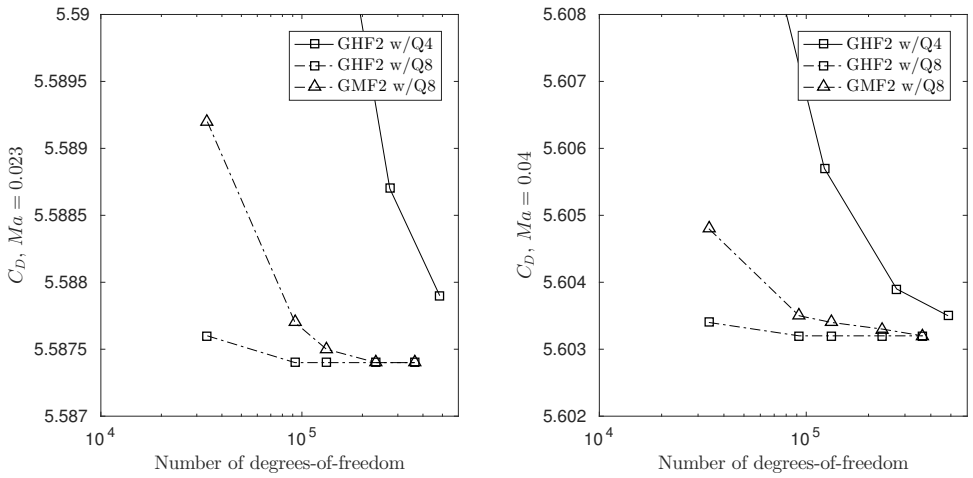

(a) $Ma_{ref} = 0.023$ (b) $Ma_{ref} = 0.04$

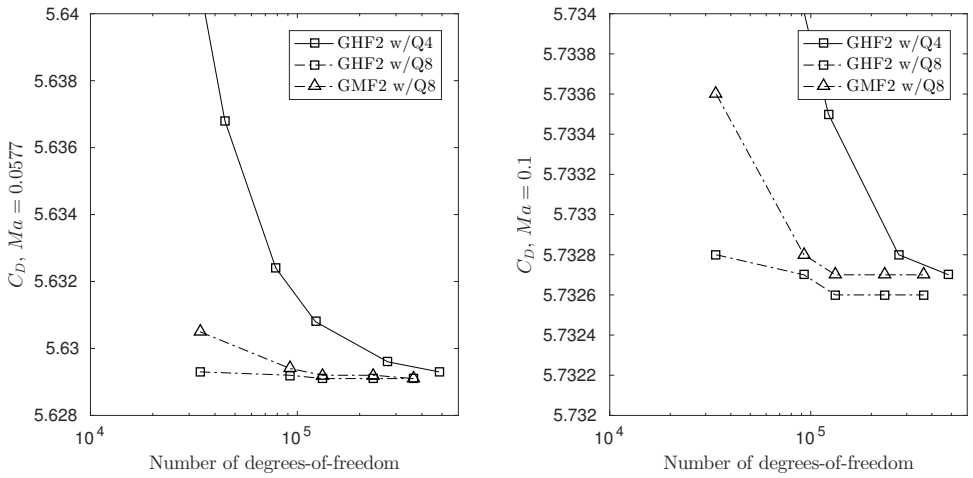

(c) $Ma_{ref} = 0.0577$ (d) $Ma_{ref} = 0.1$

Figure 2.17: Coefficient of drag using the GHF2 and GMF2 equations and quadratic elements, for several reference Mach numbers and several levels of mesh refinement.

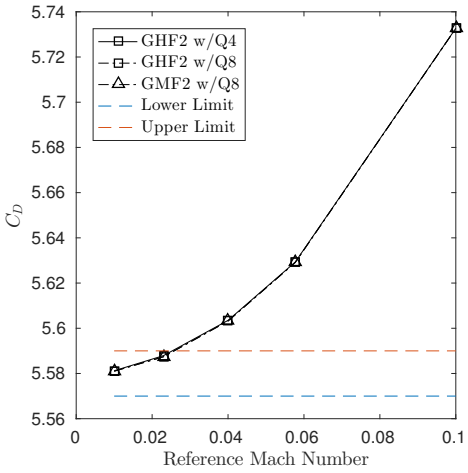

Figure 2.18: Coefficient of drag using the GHF2 and GMF2 equations, quadratic elements, and the finest level of mesh refinement for several reference Mach numbers.

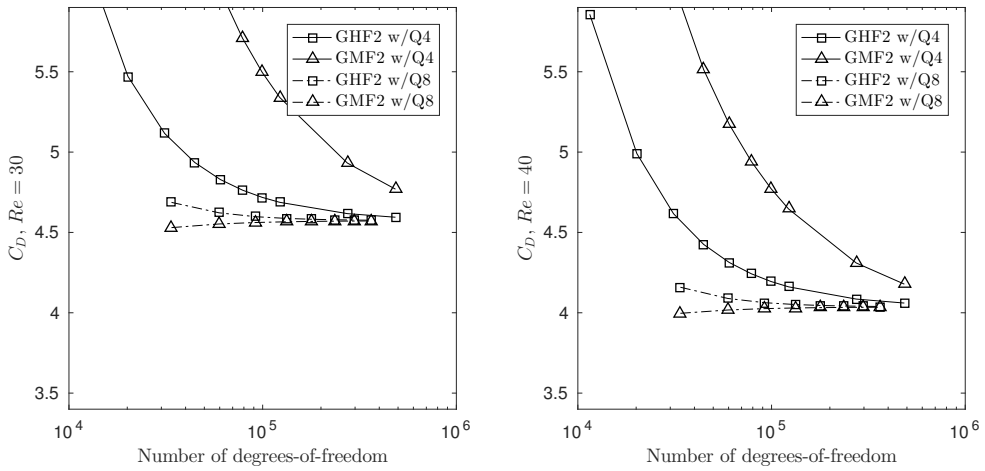

(a) $Re = 30$ (b) $Re = 40$

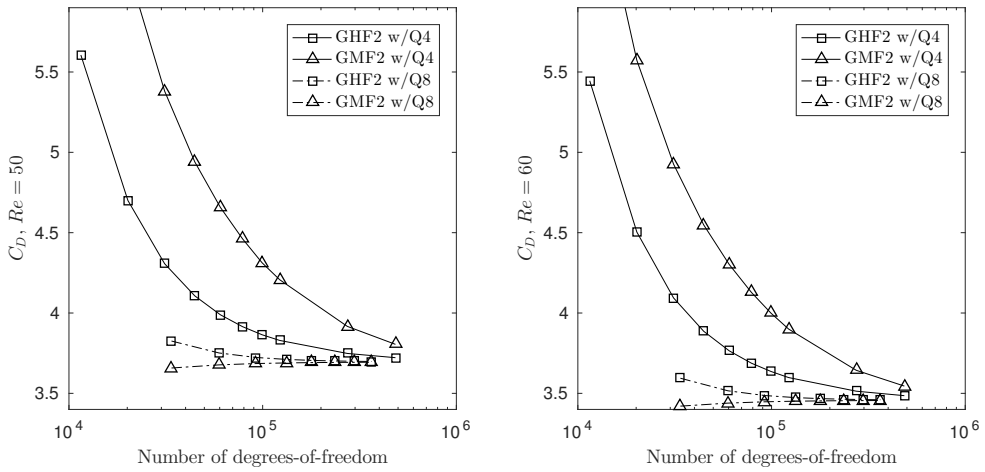

(c) $Re = 50$ (d) $Re = 60$

Figure 2.19: Coefficient of drag using the GHF2 and GMF2 equations, for several Reynolds numbers and several levels of mesh refinement.

2.6.7 Effect of the local expansion: LMF2 against the GMF2 equations

In this Section, we will study the impact of using the local expansion (2.29) over the global expansion (2.12). Recall that the global expansion is an expansion about an *absolute* equilibrium where the macroscopic velocities are much smaller than the average particle velocities, which is true for nearly incompressible flows. The local expansion is instead an expansion about a *local* equilibrium, which is not bound to the nearly incompressible assumption [8]. To this end, we expect that the governing equations resulting from the local expansion, i.e. the LHF2 and LMF2 equations, will behave differently than those resulting from the global expansion for larger reference Mach numbers. We further expect that both expansion will behave similarly as the reference Mach number is decreased.

Because we have already shown that discretizing different variables does not result in different performance, provided that the mesh is sufficiently refined, we will not consider the LHF2 equations in this study. Further, unlike the GHF2, the LHF2 equations are also non-linear; in this way, the LHF2 and LMF2 are more alike than the GHF2 and GMF2 equations are. While we expect that the stabilization scheme will have a similar effect on the LMF2 equations as it did on the GMF2 equations when using bilinear elements, we will refrain from using quadratic elements until Section 2.6.8.

Fig. 2.20 shows the velocity magnitude around the cylinder for the GMF2 and LMF2 equations and several reference Mach numbers. The flow solutions are very similar, but differences begin to emerge at $Ma_{ref} = 0.1$, i.e. the tail ends of the fast-moving fluid (shown in red) and the fluid behind the cylinder (shown in blue) extend slightly further from the cylinder when the LMF2 equations are used.

Fig. 2.21 shows the coefficients of drag for the same reference Mach numbers. Note that the GHF2 and GMF2 results are repeated from the previous section. We observe that the LMF2 equations behave similarly to the GMF2 equations for low reference Mach numbers, but differences arise starting at $Ma_{ref} = 0.0577$. Further, the LMF2 equations suffer from the same lack of

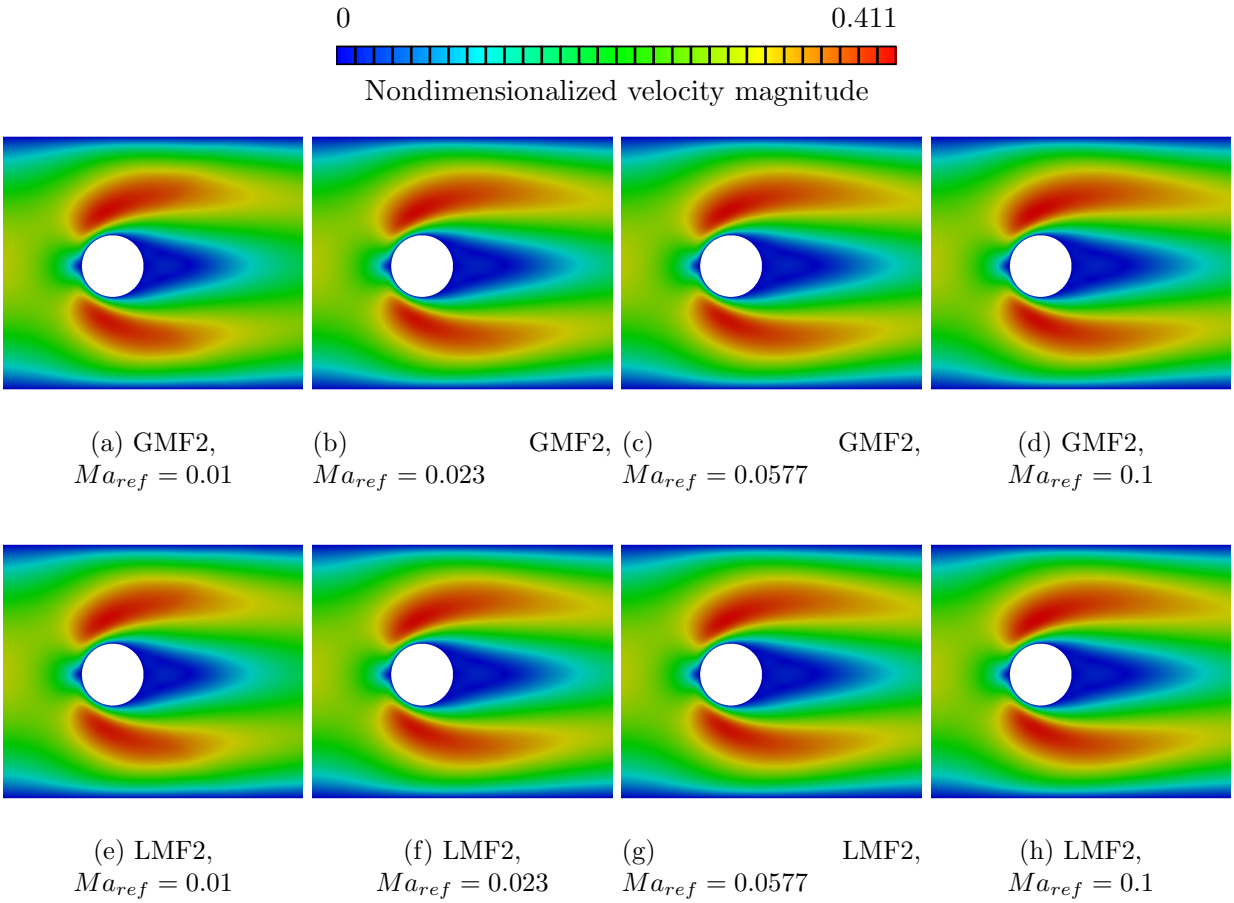

(a) GMF2, $Ma_{ref} = 0.01$ (b) GMF2, $Ma_{ref} = 0.023$ (c) GMF2, $Ma_{ref} = 0.0577$ (d) GMF2, $Ma_{ref} = 0.1$

(e) LMF2, $Ma_{ref} = 0.01$ (f) LMF2, $Ma_{ref} = 0.023$ (g) LMF2, $Ma_{ref} = 0.0577$ (h) LMF2, $Ma_{ref} = 0.1$

Figure 2.20: Velocity magnitude for the GMF2 and LMF2 equations, using bilinear elements and 484800 degrees-of-freedom, for several reference Mach numbers.

convergence as the GMF2 equations when using bilinear elements.

2.6.8 Improvement in performance of the LMF2 equations using quadratic elements

In this Section, we introduce the use of quadratic elements to the LMF2 equations. Fig. 2.22 shows the velocity distribution around the cylinder for several levels of refinement. Fig. 2.23 shows the coefficients for several levels of refinement at each reference Mach numbers. The results using GHF2 and GMF2 are repeated from before; we observe that, with the improved convergence of the quadratic elements, the difference between the LMF2 and GMF2 appear at a lower reference Mach number. Finally, Fig. 2.24 shows the percent relative difference in the coefficient of drag between the GMF2 and LMF2 equations. Even for $Ma_{ref} = 0.1$, the relative difference is only $\approx 0.1\%$; however, we can reasonably expect that this difference will continue to grow for larger reference Mach numbers.

2.6.9 Concluding remarks regarding the LMF2 equations

While this study is not sufficient enough to suggest when compressible effects should be considered in a flow, i.e. we show small differences around $Ma_{ref} = 0.1$, but common consensus says that compressible effects are important for $Ma > 0.3$, we can observe that indeed the LMF2 and GMF2 are different due to the fact that the LMF2 are derived from a local expansion, which does not use the nearly incompressible assumption.

2.7 Conclusion

We have shown, in the study of moment expansions of the BTE, that using the governing equations for the physical moments directly, i.e. the GMF2, does not offer any benefit over the governing equations for the expansion coefficients, i.e. the GHF2. In fact, the required level of mesh refinement for a given reference Mach number, shown for the GHF2 by Makhija and Maute [9], is greater for the GMF2 equations due in part to the interaction between the stabilization scheme

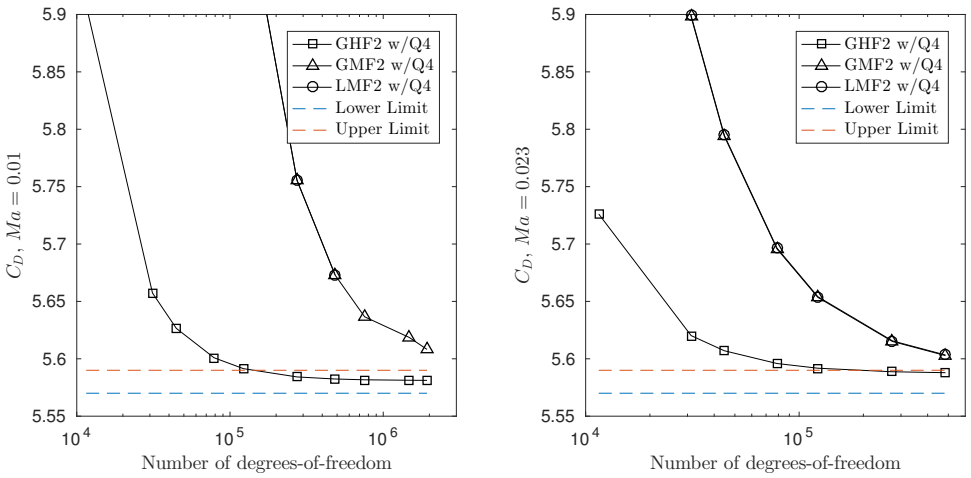

(a) $Ma_{ref} = 0.01$

(b) $Ma_{ref} = 0.023$

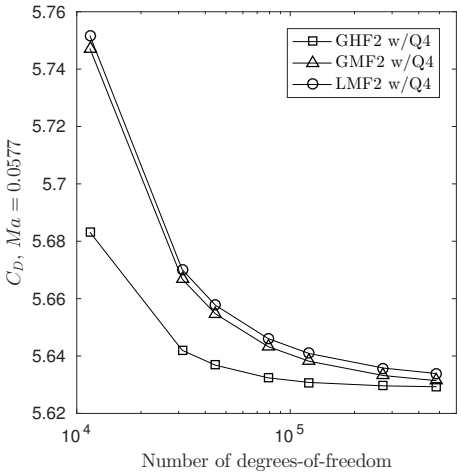

(c) $Ma_{ref} = 0.0577$

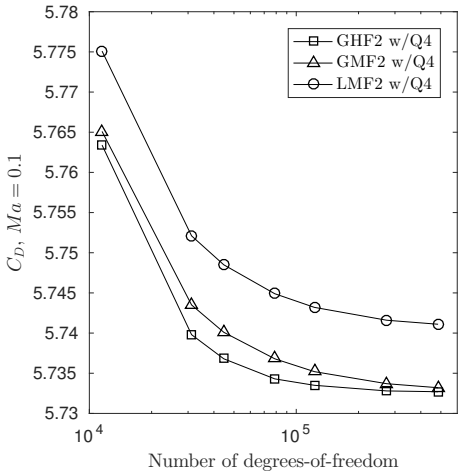

(d) $Ma_{ref} = 0.1$

Figure 2.21: Coefficient of drag using the GHF2, GMF2, and LMF2 equations, for several reference Mach numbers and several levels of mesh refinement.

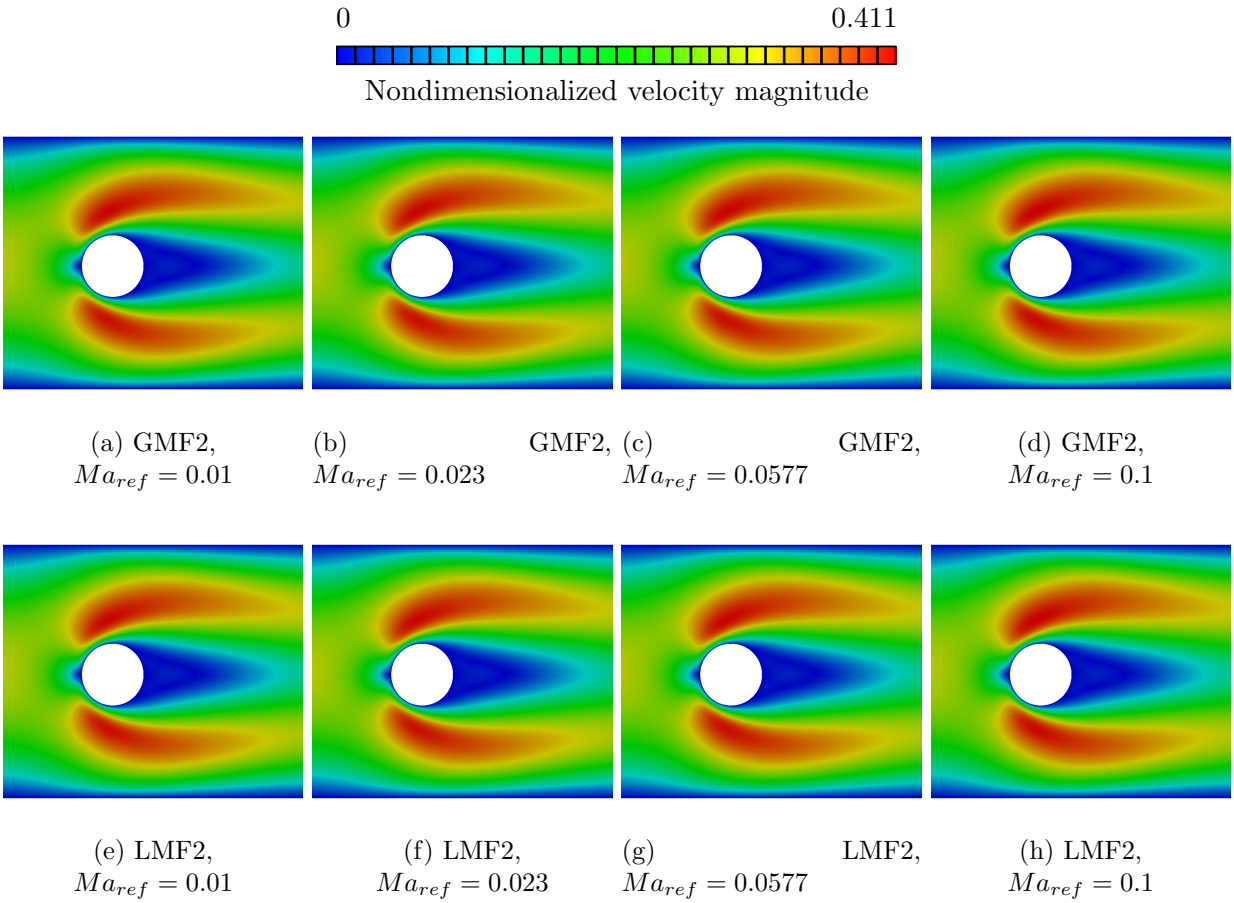

(a) GMF2, $Ma_{ref} = 0.01$ (b) GMF2, $Ma_{ref} = 0.023$ (c) GMF2, $Ma_{ref} = 0.0577$ (d) GMF2, $Ma_{ref} = 0.1$

(e) LMF2, $Ma_{ref} = 0.01$ (f) LMF2, $Ma_{ref} = 0.023$ (g) LMF2, $Ma_{ref} = 0.0577$ (h) LMF2, $Ma_{ref} = 0.1$

Figure 2.22: Velocity magnitude for the GMF2 and LMF2 equations, using quadratic elements and 364800 degrees-of-freedom, for several reference Mach numbers.

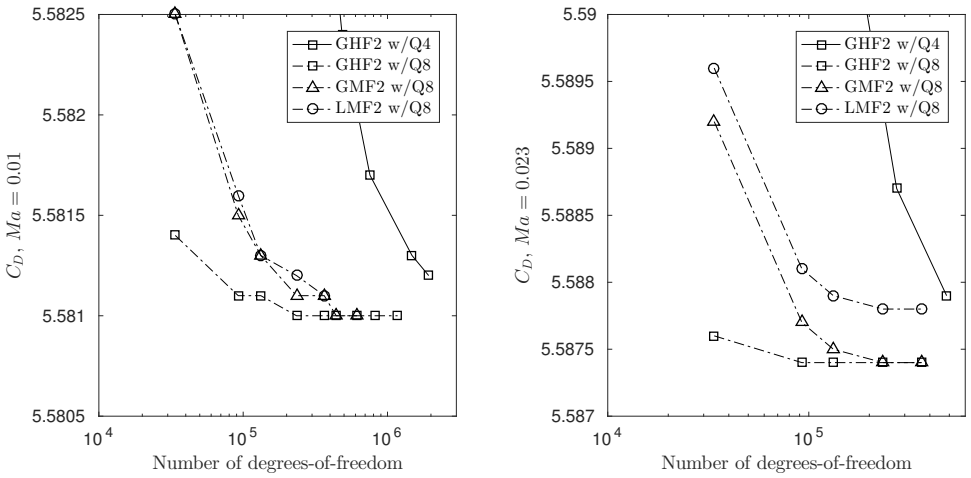

(a) $Ma_{ref} = 0.01$

(b) $Ma_{ref} = 0.023$

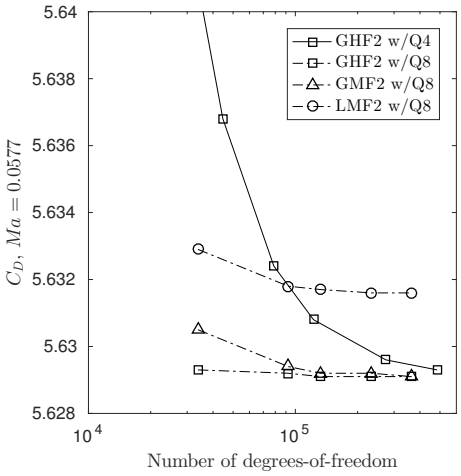

(c) $Ma_{ref} = 0.0577$

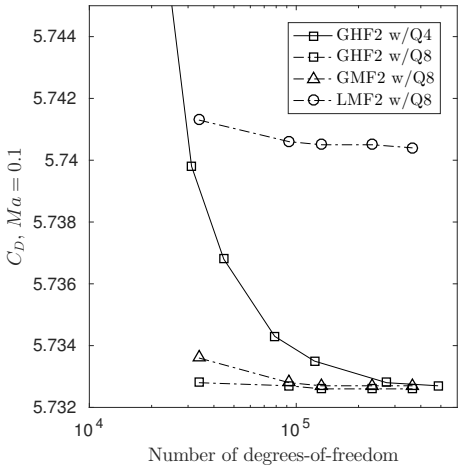

(d) $Ma_{ref} = 0.1$

Figure 2.23: Coefficient of drag using the GHF2, GMF2, and LMF2 equations and quadratic elements, for several reference Mach numbers and several levels of mesh refinement.

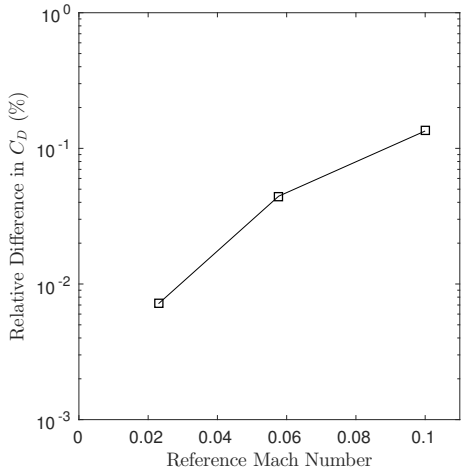

Figure 2.24: Percent relative difference in the coefficient of drag using the GMF2 and LMF2 equations, quadratic elements, and the finest level of mesh refinement for several reference Mach numbers.

and the highly non-linear coefficient matrices. This interaction can be mitigated with the use of quadratic elements; however, both using finer meshes and using quadratic element ultimately make the linear problem larger with more degrees-of-freedom when compared to a coarse mesh or bilinear elements, respectively. Moreover, the GHF2 equations remain superior, though the differences are significantly less when using quadratic elements. The GHF2 equations represent a good alternative to the incompressible Navier-Stokes equations, provided that a sufficiently small reference Mach number is used, while the GMF2 are just as non-linear and difficult to resolve.

Further, we have shown that the use of the LMF2 equations over the GMF2 equations results in small difference in flow performance and in the coefficient of drag. We expect that, just as the GHF2 may be an alternative to the incompressible Navier-Stokes equations, the LMF2 equations may be an alternative for the *compressible* Navier-Stokes equations. However, because the LMF2 suffers from the same diffusive effect of the stabilization scheme as the GMF2 equations, their benefit is not likely as great as that of the GHF2 equations.

Finally, because Makhija and Maute [9] showed that the GHF2 behave similarly using body-fitted meshes and with an immersed boundary with the XFEM, we can expect that the GMF2 and LMF2 will have similar extensions and suffer from the same diffusive effects shown in this work.

Higher-order expansions, such as the 3^{rd} order expansion derived by Grad [5], and other approaches to the closure problem, such as the R13 equations of Struchtrup and Torrilhon [25], are highly non-linear. Most importantly, our comparison of the GHF2 and GMF2 equations suggest that the SUPG stabilization framework will require too fine a level of refinement for adequate flow resolution in the nearly incompressible regime based on the reference Mach number. This required level of refinement will in turn prohibit meaningful topology optimization examples. To this end, in the next Chapter, we will introduce a slip boundary model to be used with the Navier-Stokes equation in the Slip regime.

Chapter 3

Slip boundary conditions for the Navier Stokes equations

3.1 Introduction

The study of optimal designs for fluid flows, through shape and topology optimization, for example, has gained widespread attention for Stokes and Navier-Stokes flow regimes in recent years. In these regimes, gas microflows in microfluidic devices have a broad range of applications, such as extracting biological samples, cooling integrated circuits and actively controlling aerodynamic flows [1,7]. However, as we consider flows with physical scales further in the microscale, e.g. micro-electromechanical systems, rarefaction effects begin to impact the performance of the flow. Flows at the microscale behave different than those in the macroscale [40]. The differences arise with near-wall effects and continue further into the fluid domain as the flow becomes more rarefied. While these effects have been been readily studied for simple geometries [41–44] and, more recently, for fluid-structure-interaction problems with complex geometries [45], their impact on optimal designs has not been fully explored. In this and subsequent Chapters, we will introduce a topology optimization framework for microfluidic flows and will show that the Knudsen-number-dependent slip boundary condition affects the optimal design and should be considered.

Recall that the NS equations cannot be used with the traditional no-slip boundary condition in the Slip Flow Regime. Instead, velocity and temperature slip effects begin to occur as the Kn number increases. Specifically, the tangential velocities and temperatures of the fluid and the solid are no longer the same. For flows in the Slip Flow Regime, there exists a variety of slip models for the tangential velocity at the fluid-solid interface. The wall-function method described the

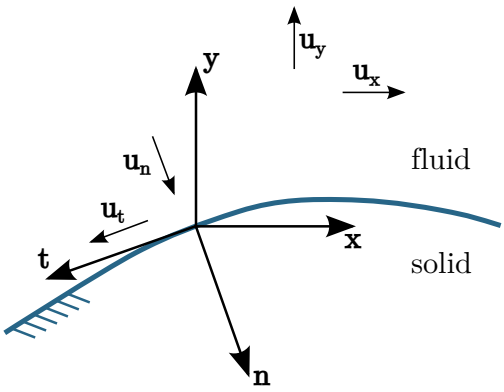

Figure 3.1: Cartesian and local coordinate system at the fluid-solid interface and velocity components.

tangential velocity as a function of the distance from the wall up to $O(\lambda)$, i.e. within the so-called Knudsen layer [41]. Another option is to use higher-order continuum models, including the Burnett, BGK-Burnett, and super-Burnett models, inside the Knudsen layer, e.g. [21–23, 25]. The reader is referred to Zhang et al. [46] for a review of slip models. The boundary condition used in this work is introduced in Section 3.6 and is represented by:

$$u_t - u_t^w + \frac{Kn}{1+Kn}\left(\frac{\partial u_t}{\partial n} + \frac{\partial u_n}{\partial t}\right) = 0, \tag{3.1}$$

where u_t and u_t^w are the fluid and wall tangential velocities, respectively, u_n is the fluid normal velocity, and $\frac{\partial}{\partial n}$ and $\frac{\partial}{\partial t}$ denote derivatives in the normal and tangential directions, respectively. Fig. 3.1 shows the local coordinate system at the fluid-solid interface. Throughout this paper, we will refer to this boundary condition as the Knudsen-slip (or simply, Kn-slip) boundary condition. To adequately model slip, the proposed boundary condition requires accurate near-wall velocity gradients, which will dictate the choice of our boundary representation for topology optimization as discussed in the following.

The majority of fluid topology optimization studies use density methods [47, 48]. Topology optimization in fluids was pioneered by Borrvall and Peterson [49], who adopted the concept of density methods to Stokes flows and modeled the presence of a wall in the fluid flow by representing it as a body force, i.e. a penalization approach. The work on Stokes models has been extended

to the NS equations by several authors, including [50], [51], [52], and [53]. The density method typically describes the interface between different material domains by either using intermediate densities, which lead to ambiguous boundaries, or by discrete material distributions, which could lead to jagged boundaries. For problems that require a precise geometrical description of the interface, density methods will result in an inaccurate enforcement of boundary conditions due to the aforementioned ambiguous or jagged boundaries [54, 55]. Such issues can be mitigated by mesh refinement or by adaptive refinement; however, they do not provide the exact location and orientation of the boundary *a priori*. Thus, unlike the no-slip boundary condition, the Kn-slip boundary condition cannot be enforced with the same penalization approach as is used with density methods.

In response to the shortcomings of density methods, we utilize the Level Set Method (LSM) to represent the geometry. External or internal phase boundaries, where phase may refer to either the fluid or solid domain, are described implicitly by the zero level set isosurfaces of a Level Set Function (LSF), $\phi(\boldsymbol{x})$, where $\boldsymbol{x}$ is the position vector [56–58]. Smooth changes in the LSF lead to smooth changes in the geometry, e.g. the merging or separation of geometric features, making the LSM a good choice for topology optimization.

The LSF is typically discretized on a fixed background mesh and updated during the optimization process by the Hamilton-Jacobi equations. An alternative, used in this paper, is to define the parameters of the LSF as explicit functions of the optimization variables. The resulting optimization problem is solved by standard nonlinear programming (NLP) methods [59]. For a detailed discussion of the LSM, the reader is referred to van Dijk et al. [59] and Gain and Paulino [60].

Further, we utilize the eXtended Finite Element Method (XFEM) to describe the material distribution in the model. The XFEM allows for an immersed boundary technique that does not require a conforming mesh. The XFEM was developed by Babuška and Melenk [61] and was originally used to model crack propagation [62]. Alternatives to the XFEM include an Ersatz's material approach, which suffers from the same problems as density methods, and adaptive remeshing after each LSF update, which is computationally expensive. The XFEM decomposes an

element cut by a zero isosurface of the LSF into several subdomains, such that each subdomain has a distinct phase, i.e. is exclusively fluid or solid. Thus, the LSM and XFEM provide the exact location and orientation of the fluid-solid interface.

The XFEM, however, results in an ill-conditioned system of equations, when an element cut by the zero isosurface of the LSF has a small ratio of volumes, e.g. when the interface moves very close a node. These configurations are unavoidable when using a fixed background mesh. Several approaches have been proposed to avoid this ill-conditioning issue, such as the geometric, Jacobi, and Cholesky decomposition preconditioners of [63], [64], and [65] and [66], respectively, and, more recently, face-oriented ghost-penalty methods [67]. Face-oriented ghost-penalty methods penalize discontinuities in the spatial gradients of the velocities and pressure across the common facets of intersected elements [68]. This presents a clear advantage over preconditioners, since smooth gradients are particularly important for the Kn-slip boundary condition. Smooth velocity gradients in (3.1) result in smooth tangential velocities at the interface. Boundary conditions on the interface are imposed weakly via Nitsche's method [69].

In this work, we will extend the LSM-XFEM framework prosed by Villanueva and Maute [10] to allow for the enforcement of the Kn-slip boundary condition. We will show that when the physical scaling and fluid properties would results in a finite Kn number, the slip boundary condition should be accounted for during the optimization process; additionally, we will show the influence, in terms of design and performance, of this boundary condition when compared to the traditional no-slip condition.

3.1.1 General problem description

Before introducing the slip boundary condition in detail, we first show the supporting framework for this work, including the governing equations, stabilization, and the ghost-penalty formulation.

Fig. 3.2 shows the general setup for the fluid problems considered in this work. The fluid and solid domains are denoted as Ω^f and Ω^s, respectively. The example shown has a disconnected

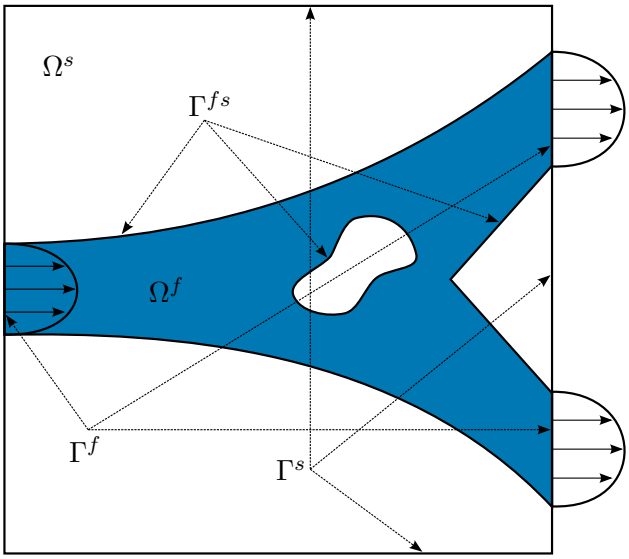

Figure 3.2: General problem and boundary setup.

solid subdomain; it is also possible to have disconnected fluid subdomains, as shown in [10]. The external fluid and solid boundaries are denoted as Γ^f and Γ^s, respectively. Finally, the internal fluid-solid interface is denoted as Γ^{fs}.

3.2 Governing Equations

In this study, we model the flow with the incompressible Navier-Stokes (NS) equations. Energy transport is descried by coupling an advection-diffusion equation to our flow model. The governing equations in the fluid and solid phases are summarized subsequently.

3.2.1 Weak form of NS Equations

This work adopts the same weak form of the Navier-Stokes (NS) equations as Villanueva and Maute [10]. The residual of the weak form is decomposed into surface and volume contributions:

$$r_{\boldsymbol{u},p} = r^{\Omega}_{\boldsymbol{u},p} + r^{\hat{\Omega}}_{\boldsymbol{u},p} + r^{D}_{\boldsymbol{u},p} + r^{fs}_{\boldsymbol{u},p} + r^{N}_{\boldsymbol{u},p} + r^{GP}_{\boldsymbol{u},p}, \tag{3.2}$$

where $r^{\Omega}_{\boldsymbol{u},p}$ and $r^{\hat{\Omega}}_{\boldsymbol{u},p}$ are the non-stabilized and stabilized volumetric residual contributions, respectively. The terms $r^{D}_{\boldsymbol{u},p}$ and $r^{fs}_{\boldsymbol{u},p}$ enforce Dirichlet boundary conditions on the external surfaces

and on the fluid-solid (or fluid-void) interface, respectively; while the term $r^N_{\boldsymbol{u},p}$ enforces Neumann boundary conditions on the external boundary. Finally, $r^{GP}_{\boldsymbol{u},p}$ represents the ghost-penalty formulation.

The stabilization term is discussed in Section 3.4. The ghost-penalty stabilization terms is described in Section 3.5. Finally, the boundary condition enforcement terms, as well as the proposed velocity slip model, are discussed in Section 3.6.

The non-stabilized volume contribution takes the form:

$$r^{\Omega}_{\boldsymbol{u},p} = \int_{\Omega^f} \left(v_i^f \rho^f \left(\frac{\partial u_i^f}{\partial t} + u_i^f \frac{\partial u_i^f}{\partial x_j} \right) + \epsilon_{ij}(\boldsymbol{v}^f) \sigma_{ij}(\boldsymbol{u}^f, p^f) \right) \mathrm{d}\Omega + \int_{\Omega^f} \left(q^f \frac{\partial u_i^f}{\partial x_i} \right) \mathrm{d}\Omega. \tag{3.3}$$

The first integral describes the momentum equations with test functions v_i^f; the second integral describes the incompressibility condition with test functions q_i^f. The fluid velocities are given by u_i^f, p^f is the pressure, ρ^f is the fluid density, μ^f is the dynamic viscosity, ϵ_{ij} is the strain rate tensor given by:

$$\epsilon_{ij}(\boldsymbol{u}^f) = \frac{1}{2} \left(\frac{\partial u_i^f}{\partial x_j} + \frac{\partial u_j^f}{\partial x_i} \right), \tag{3.4}$$

and σ_{ij} is the Cauchy stress tensor for Newtonian fluids:

$$\sigma_{ij}(\boldsymbol{u}^f, p^f) = -p^f \delta_{ij} + 2\mu^f \epsilon_{ij}^f(\boldsymbol{u}^f). \tag{3.5}$$

The residual contribution for Dirichlet boundary conditions presented in [10] only accepts no-slip boundary conditions; in this work, we generalize the formulation to also allow for the proposed slip model. This is discussed in detail in Section 3.6. Neumann boundary conditions are defined as:

$$\sigma_{ij}(\boldsymbol{u}^f, p^f) n_j^f = \hat{t}_i^f \quad \forall \boldsymbol{x} \in \Gamma_N^f, \tag{3.6}$$

and the residual contribution from external Neumann boundary conditions is defined as:

$$r^N_{\boldsymbol{u},p} = \int_{\Gamma_N^f} v_i^f \hat{t}_i^f \mathrm{d}\Gamma. \tag{3.7}$$

3.2.2 Advection-Diffusion

Similar to the treatment for the NS, we follow the work of Villanueva and Maute [10] and denote the weak form of the advection-diffusion model as $r_{\boldsymbol{u},T}$ and decompose it into volumetric

and surface components:

$$r_{\boldsymbol{u},T} = r^{\Omega}_{\boldsymbol{u},T} + r^{\hat{\Omega}}_{\boldsymbol{u},T} + r^{D}_{\boldsymbol{u},T} + r^{D,fs}_{\boldsymbol{u},T} + r^{N}_{\boldsymbol{u},T} + r^{N,fs}_{\boldsymbol{u},T} + r^{GP}_{\boldsymbol{u},T}, \tag{3.8}$$

where $r^{\Omega}_{\boldsymbol{u},T}$ and $r^{\hat{\Omega}}_{\boldsymbol{u},T}$ are the non-stabilized and stabilized volumetric residual contributions, respectively; $r^{D}_{\boldsymbol{u},T}$ and $r^{D,fs}_{\boldsymbol{u},T}$ are the residuals of the weak enforcement of Dirichlet boundary conditions, on external boundaries and on the fluid-solid interface, respectively; similarly, $r^{N}_{\boldsymbol{u},T}$ and $r^{N,fs}_{\boldsymbol{u},T}$ are the residuals corresponding to Neumann boundary conditions; and $r^{G}P_{\boldsymbol{u},T}$ models the ghost-penalty formulation. The boundary conditions terms are discussed presently. The volumetric stabilization term and the ghost-penalty formulation are presented in Sections 3.4 and 3.5, respectively.

The non-stabilized volumetric residual contribution is defined as:

$$r^{\Omega}_{\boldsymbol{u},T} = \sum_{m\in\{f,s\}} \int_{\Omega^m} \left(d^m \rho^m c_p^m \left(\frac{\partial T^m}{\partial t} + u_i^m \frac{\partial T^m}{\partial x_i} \right) + \frac{\partial d^m}{\partial x_i} \left(J_i(T^m) \right) - d^m \hat{q}^m_{\Omega} \right) \mathrm{d}\Omega, \tag{3.9}$$

where d^m is a temperature test function, ρ^m and c_p^m represent the density and specific heat capacity, respectively, T^m is the temperature field, u_i^m is the velocities vector field, $\hat{q}^m_{\Omega}$ is a volumetric heat source, and $J_i(T^m)$ is the diffusive heat flux defined as:

$$J_i(T^m) = k^m \delta_{ij} \frac{\partial T^m}{\partial x_j}, \tag{3.10}$$

where k^m is the isotropic thermal conductivity. The summation in (3.9) indicates that we model energy and species transport in both the fluid and solid phases; however, because the solid phase is stationary, (3.9) reduces to a linear diffusion model in the solid region.

Dirichlet and Neumann boundary conditions boundary conditions are imposed on the fluid-solid interface, Γ^{fs}, and on the external boundaries, Γ^m, as:

$$T^m = \hat{T}^m \qquad \forall \boldsymbol{x} \in \Gamma^m_D \tag{3.11}$$

$$T^m = \hat{T}^{fs} \qquad \forall \boldsymbol{x} \in \Gamma^{fs}_D \tag{3.12}$$

$$J_i(T^m) n_i^m = \hat{q}^m_{\Gamma} \qquad \forall \boldsymbol{x} \in \Gamma^m_N \tag{3.13}$$

$$J_i(T^m) n_i^{fs} = \hat{q}^{fs}_{\Gamma} \qquad \forall \boldsymbol{x} \in \Gamma^{fs}_N, \tag{3.14}$$

where n_i^{fs} is the normal vector on the fluid-solid interface pointing towards the solid phase, $\hat{T}^m$ and $\hat{T}^{fs}$ are prescribed temperature values, and $\hat{q}_\Gamma^m$ and $\hat{q}_\Gamma^{fs}$ are prescribed heat flux values.

As presented in [10], the weak enforcement of Dirichlet boundary conditions is modeled using Nitsche's method [70]. The residual contribution of the Dirichlet conditions at the fluid-solid interface follows the formulation of [71] and is defined as:

$$r_{\boldsymbol{u},T}^{D,fs} = \int_{\Gamma^{fs}} \Big([\![d]\!] \{J_i(T^f, T^s)\} n_i^{fs} + \{J_i(d^f, d^s)\} n_i^{fs} [\![T]\!] + \gamma_{N,T} [\![d]\!] [\![T]\!] \Big) \, \mathrm{d}\Gamma, \tag{3.15}$$

where the jump operators are defined as:

$$[\![\zeta]\!] = \zeta^f - \zeta^s, \tag{3.16}$$

$$\{J_i(\zeta^f, \zeta^s)\} = \gamma_J^f J_i(\zeta^f) + \gamma_J^s J_i(\zeta^s), \tag{3.17}$$

where γ_J^m is a weighting factor defined as:

$$\gamma_J^m = \frac{(\int_{\Omega^m} \mathrm{d}\Omega)/k^m}{(\int_{\Omega^f} \mathrm{d}\Omega)/k^f + (\int_{\Omega^s} \mathrm{d}\Omega)/k^s}, \tag{3.18}$$

and $\gamma_{N,T}$ is a penalty term defined as:

$$\gamma N, T = \frac{2\alpha_{N,T} \int_{\Gamma^{fs}} \mathrm{d}\Gamma}{(\int_{\Omega^f} \mathrm{d}\Omega)/k^f + (\int_{\Omega^s} \mathrm{d}\Omega)/k^s}, \tag{3.19}$$

with a problem-dependent constant $\alpha_{N,T}$. The first, second, and third terms in (3.15) represent the standard consistency term, the adjoint consistency term, and the penalty term of the Nitsche formulation, respectively [10].

The residual contribution of Dirichlet boundary conditions is defined as:

$$r_{\boldsymbol{u},T}^{D} = \sum_{m \in \{f,s\}} \int_{\Gamma_D^m} \Big(-d^m J_i(T^m) n_i^m + J_i(d^m) n_i^m T^m + \alpha_{N,T} h^{-1} d^m (T^m - \hat{T}^m) \Big) \, \mathrm{d}\Gamma. \tag{3.20}$$

Finally, the contributions from Neumann boundary conditions at the interface and external boundaries defined as:

$$r_{\boldsymbol{u},T}^{N,fs} = \int_{\Gamma_N^{fs}} d^f \hat{q}_\Gamma^{fs} \mathrm{d}\Gamma \tag{3.21}$$

and

$$r_{\boldsymbol{u},T}^{N} = \sum_{m \in \{f,s\}} \int_{\Gamma_N^m} d^m \hat{q}_\Gamma^m \mathrm{d}\Gamma, \tag{3.22}$$

respectively.

3.2.3 Hamilton-Jacobi Equation

The Kn-slip boundary condition, introduced in Section 3.6, requires knowing the gradient of the normal and tangential vectors at an interface. The normal vector at the fluid-solid interface (and, by extension, the tangential vector) is defined as the gradient of the level set fluid (LSF):

$$\hat{\boldsymbol{n}} = \frac{\nabla\phi}{|\nabla\phi|}. \tag{3.23}$$

Thus, the gradient of the normal vector requires second-order derivatives of the LSF, which are impossible to compute with bilinear elements. One option is to ignore the terms that require these gradients, thought there would be no ground to defend it. A second option is to provide analytical expressions for these terms along with the LSF. This option is attractive but is impossible to reproduce in a topology optimization framework, since the LSF is not known analytically; this option is used in Section 3.10 to show that these terms are indeed necessary for an accurate flow prediction. A third option is to introduce the normal vector as nodal degrees-of-freedom and enforce its definition in terms of the LSF weakly:

$$r_{\hat{\boldsymbol{n}}} = \int_\Omega \delta\hat{\boldsymbol{n}} \cdot \left(\hat{\boldsymbol{n}}\,|\nabla\phi| - \nabla\phi\right) \mathrm{d}\Omega. \tag{3.24}$$

Introducing the normal vector components as nodal degrees-of-freedom increases the number of degrees-of-freedom per node from 3 to 5. Because of this increase in problem size, it is important to understand if or when the $\boldsymbol{J}_{\{n,t\}}$ terms can be neglected.

3.3 Nondimensionalization

In this section, we briefly propose an alternative nondimensionalization scheme to the classical scheme involving a characteristic velocity.

3.3.1 Nondimensionalization of the NS equations

The strong form of the incompressible NS equations takes the form:

$$\rho\frac{\partial\boldsymbol{u}}{\partial t} + \rho\left(\boldsymbol{u}\cdot\boldsymbol{\nabla}\right)\boldsymbol{u} = -\boldsymbol{\nabla}p + \mu\nabla^2\boldsymbol{u}. \tag{3.25}$$

The classical nondimensionalization of the NS equations uses a reference velocity, which is typically the average or maximum prescribed velocity at an inlet, which is in turn enforced as a Dirichlet boundary condition. The nondimensional time, Cartesian coordinates, velocities, and pressure are thus given by:

$$\bar{t} = \frac{t}{L/U_0}, \quad \bar{\boldsymbol{x}} = \frac{\boldsymbol{x}}{L}, \quad \bar{\boldsymbol{u}} = \frac{\boldsymbol{u}}{U_0}, \quad \bar{p} = \frac{p}{\rho U_0^2}, \tag{3.26}$$

where L and U_0 are the reference length and velocity. Substituting 3.26 into 3.25 gives:

$$\frac{\partial \bar{\boldsymbol{u}}}{\partial \bar{t}} + \left(\bar{\boldsymbol{u}} \cdot \bar{\boldsymbol{\nabla}}\right) \bar{\boldsymbol{u}} = -\bar{\boldsymbol{\nabla}} \bar{p} + \frac{1}{Re} \bar{\nabla}^2 \bar{\boldsymbol{u}}, \tag{3.27}$$

which has the same form as 3.25, except that $\bar{\rho} = 1$ and $\bar{\mu} = 1/Re$, where Re is the Reynolds number defined as $Re = \frac{\rho U_0 L}{\mu}$.

In this work, we seek to nondimensionalize the NS equations without a reference velocity, since some problems considered here are pressure-driven, i.e. the inlet has a known pressure instead of a known velocity distribution. To this end, the nondimensionalized time, Cartesian coordinates, velocities, and pressure are given by:

$$\bar{t} = \frac{t}{\rho L^2/\mu}, \quad \bar{\boldsymbol{x}} = \frac{\boldsymbol{x}}{L}, \quad \bar{\boldsymbol{u}} = \frac{\boldsymbol{u}}{\mu/(\rho L)}, \quad \bar{p} = \frac{p}{\mu^2/(\rho L^2)}. \tag{3.28}$$

Substituting (3.28) into (3.25) gives:

$$\frac{\partial \bar{\boldsymbol{u}}}{\partial \bar{t}} + \left(\bar{\boldsymbol{u}} \cdot \bar{\boldsymbol{\nabla}}\right) \bar{\boldsymbol{u}} = -\bar{\boldsymbol{\nabla}} \bar{p} + \bar{\nabla}^2 \bar{\boldsymbol{u}}, \tag{3.29}$$

which has the same form as 3.25, except that $\bar{\rho} = \bar{\mu} = 1$. This second nondimensionalization scheme is equivalent to the first if the reference velocity is calculated from the fluid properties as $U_0 = \frac{\mu}{\rho L}$. Subsequently, we compare both schemes in problems with and without a known reference velocity.

3.3.1.1 Validation: flow between parallel plates

In this section, we will validate the proposed nondimensionalization scheme against the classical scheme by consider the flow through parallel plate and the flow past a cylinder, similar to the problem considered in Chapter 2. The problem setup for the flow between parallel plates in shows

in Fig. 3.3; all dimensions and fluid properties are given in self-consistent units. In this example, the channel height is set to $h = 10^{-4}$, the channel length is set to $L = 10^{-4}$, the inlet is given a Dirichlet pressure boundary condition, $p_{in} = 10$, and the outlet is given a traction-free boundary condition, equivalent to $p_{out} = 0$. Naturally, this problem has an analytical solution:

$$u(y) = \frac{p_{in}}{L}\frac{h^2}{8\mu}\left(1 - 4\left(\frac{y}{h}\right)^2\right) = u_{max}\left(1 - 4\left(\frac{y}{h}\right)^2\right), \tag{3.30}$$

where $u_{max} = \frac{p_{in}}{L}\frac{h^2}{8\mu}$ is the maximum velocity at the center of the flow. This allows us to define a mean velocity:

$$u_{avg} = \frac{1}{h}\int_{-h/2}^{h/2} u(y)\mathrm{d}y = \frac{2}{3}u_{max}, \tag{3.31}$$

and in turn the Reynolds number as $Re = \frac{\rho u_{avg} h}{\mu}$. Considering standard air as the choice of fluid, $\rho = 1.205$ and $\mu = 1.511 \times 10^{-5}$, the mean velocity is $u_{avg} = 5.5151$ and the Reynolds number is $Re \approx 44$.

We consider simulations using (i) a dimensional mesh and unscaled fluid properties, (ii) the proposed nondimensionalization scheme, (iii) the classical nondimensionalization scheme with an accurate reference solution and (iv) the classical nondimensionalization scheme with an arbitrary reference solution. We discretize the domain with a 100×100 square mesh. While the solution method is further discussed in Section 3.9, here we note that the numerical time step is chosen as $\Delta t = 10^{24}$, such that it is not affected by the nondimensionalization schemes.

Fig. 3.4 shows the resulting symmetric velocity profile and a close-up view near the center of the flow. Note the excellent agreement among the numerical solutions with the analytical solution. The largest relative error between any two solutions is $< 0.001\%$. Table 3.1 shows the resulting Reynolds number calculations in this study. The density and viscosity refer to the values used in the solution, the channel height refers to the total height of the mesh. The scaling velocity is the scaling term used to re-dimensionalize the flow solution, when applicable. The maximum and average velocities refer to the maximum and average scaled, i.e. nondimensional, velocities obtained from the flow solution. Finally, the Reynolds number refers to the calculation performed with the nondi-

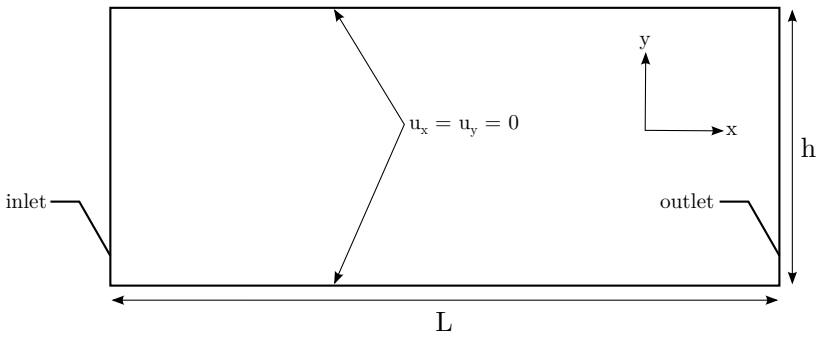

Figure 3.3: Problem setup for the flow through parallel plates.

mensionalized solution. Note that the physical solution and the proposed nondimensionalization scheme best approximate the analytical Reynolds number.

3.3.1.2 Validation: flow past a cylinder

The previous example makes use of an available analytical solution to define a reference velocity in the classical nondimensionalization scheme. We now consider a problem without such an available solution. We consider a similar problem setup as in the previous section, but with a cylinder inclusion of radius $h/8$ located at $(h, 0)$, shown in Fig. 3.5. To accommodate the inclusion, the channel has length $L = 3h$. The inlet and outlet have the same boundary conditions as in the previous section, $p_{in} = 10$ and $p_{out} = 0$.

We again consider simulations using (i) a physical mesh and unscaled fluid values, (ii) the proposed nondimensionalization scheme, and the classical nondimensionalization scheme with (iii) a reference velocity and (iv) an arbitrarily chosen reference velocity. The reference velocity used in case (iii) is first obtained from the average inlet velocity in case (i). Fig. 3.6 and 3.7 show the velocity distribution through the inlet and through the minimum cross-section, i.e. above the cylinder. Note the good agreement of all nondimensionalization schemes with the physical simulation. The close-up views reveal that the proposed scheme deviates slightly, but the relative difference is $< 0.06\%$, which is well-tolerable; note especially the vertical scale of the close-up views.

Table 3.2 summarizes this study. The maximum velocity is measured as the maximum nu-

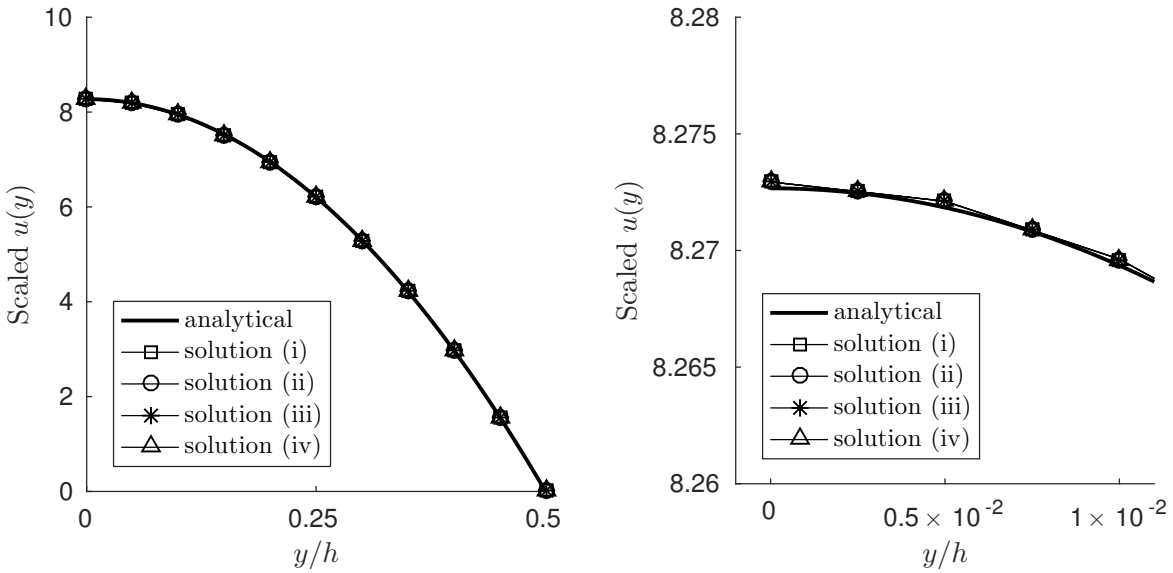

(a) Symmetric portion

(b) Close-up view

Figure 3.4: Velocity profiles for nondimensionalization study on the flow between parallel plates.

	Analytical Solution	Solution (i): Unscaled simulation	Solution (ii): Proposed scheme	Solution (iii): Classical scheme	Solution (iv): Classical scheme with arbitrary U_0
Density	$\rho = 1.205$	$\rho = 1.205$	$\rho = 1$	$\rho = 1$	$\rho = 1$
Viscosity	$\mu = 1.511(10^{-5})$	$\mu = 1.511 \times 10^{-5}$	$\mu = 1$	$\mu = 2.274 \times 10^{-2}$	$\mu = 5.016 \times 10^{-2}$
Channel Height	$h = 10^{-4}$	$h = 10^{-4}$	$h = 1$	$h = 1$	$h = 1$
Reference velocity	-	-	-	$U_0 = 5.5151$	$U_0 = 2.5$
Scaling velocity	-	-	$u_s = 0.12539$	$u_s = 5.5151$	$u_s = 2.5$
Maximum velocity	$u_{max} = 8.2727$	$u_{max} = 8.2750$	$u_{max} = 65.9000$	$u_{max} = 1.5000$	$u_{max} = 3.3100$
Average velocity	$u_{avg} = 5.5151$	$u_{avg} = 5.5151$	$u_{avg} = 43.9824$	$u_{avg} = 1.0000$	$u_{avg} = 2.2061$
Reynolds number	$Re = 43.9822$	$Re = 43.9824$	$Re = 43.9824$	$Re = 43.9826$	$Re = 43.9825$

Table 3.1: Resulting Reynolds number calculation for the flow between parallel plates.

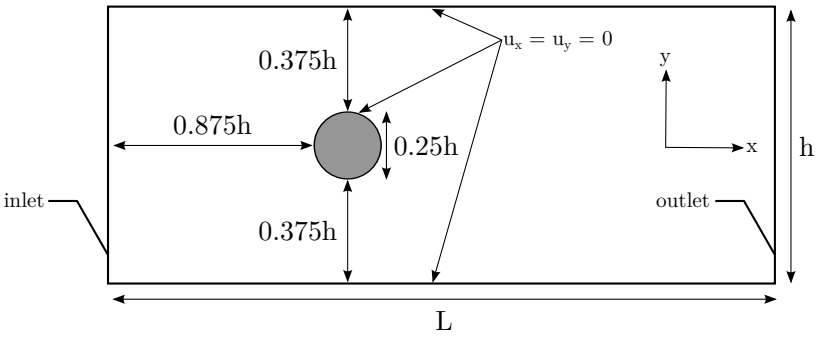

Figure 3.5: Problem setup for the flow past a cylinder.

merical velocity in the entire fluid domain, while the average velocity refers to the average velocity only at the inlet. These are additionally rescaled with the scaling velocity. Finally, note the general agreement between all three nondimensionalization schemes. We recognize that the proposed nondimensionalization scheme deviates slightly from the two classical approaches. However, we note that the proposed scheme is ultimately no different than the classical scheme with an arbitrary reference velocity, as a meaningful reference velocity is not known *a priori* in pressure driven flows without an analytical solution. Further, it is important to recognize that, as the design changes in a topology optimization framework, any inlet velocity distribution and its corresponding average velocity will continuously change. As such, we will make use of the proposed nondimensionalization scheme in the remainder of this Chapter.

3.3.2 Nondimensionalization of the advection-diffusion model

Consider the strong form of the advection-diffusion equation:

$$\rho^m c_p^m \left(\frac{\partial T^m}{\partial t} + (\boldsymbol{u}^m \cdot \boldsymbol{\nabla}) T^m \right) = k^m \Delta T^m, \tag{3.32}$$

where Δ is the Laplace operator. Because the advection-diffusion equation is solved for both the fluid and solid phases, it becomes important to explicitly state that the fluid properties are used to nondimensionalize the advection-diffusion equation. Consider the same nondimensionalized variables as with the NS equations,

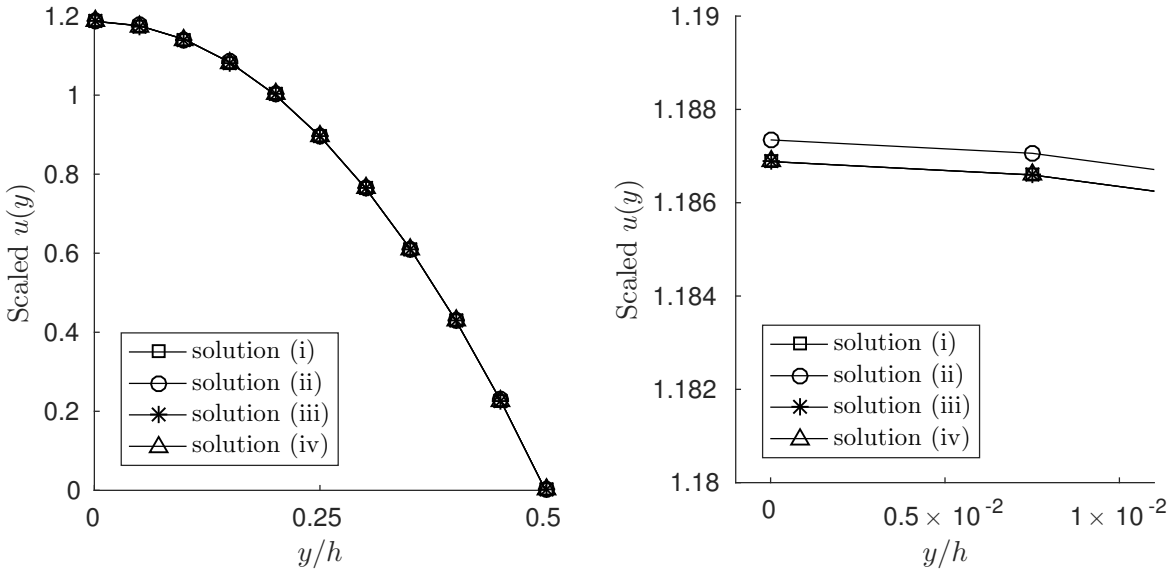

(a) Symmetric portion (b) Close-up view

Figure 3.6: Velocity profile through the inlet.

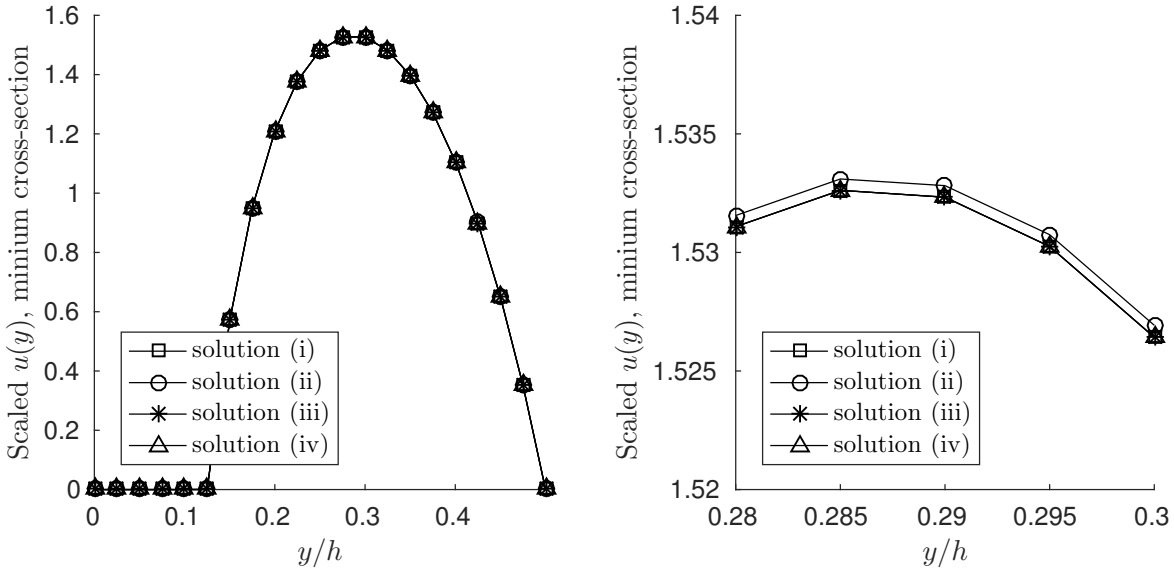

(a) Symmetric portion (b) Close-up view

Figure 3.7: Velocity profile through the minimum cross-section, $x = h$.

	Solution (i): Unscaled simulation	Solution (ii): Proposed scheme	Solution (iii): Classical scheme	Solution (iv): Classical scheme with arbitrary U_0
Density	$\rho = 1.205$	$\rho = 1$	$\rho = 1$	$\rho = 1$
Viscosity	$\mu = 1.511 \times 10^{-5}$	$\mu = 1$	$\mu = 1.5779 \times 10^{-2}$	$\mu = 5.0158 \times 10^{-2}$
Channel Height	$h = 10^{-4}$	$h = 1$	$h = 1$	$h = 1$
Reference velocity	-	-	$U_0 = 0.7947$	$U_0 = 2.5$
Scaling velocity	-	$u_s = 0.12539$	$u_s = 0.79547$	$u_s = 2.5$
Maximum velocity (in Ω^f)	$u_{max} = 1.5340$	$u_{max} = 12.2400$	$u_{max} = 1.929$	$u_{max} = 0.6135$
Scaled maximum velocity (in Ω^f)	-	$u_s \times u_{max} = 1.5348$	$u_s \times u_{max} = 1.5330$	$u_s \times u_{max} = 1.5338$
Average velocity (inlet)	$u_{avg} = 0.7947$	$u_{avg} = 6.3410$	$u_{avg} = 1.0000$	$u_{avg} = 0.3179$
Rescaled average velocity (inlet)	-	$u_s \times u_{avg} = 0.7951$	$u_s \times u_{avg} = 0.7947$	$u_s \times u_{avg} = 0.7947$
Reynolds number	$Re = 6.3374$	$Re = 6.3410$	$Re = 6.3374$	$Re = 6.3374$

Table 3.2: Resulting Reynolds number calculation for the flow past a cylinder.

$$\bar{\boldsymbol{x}} = \frac{\boldsymbol{x}}{L},\ \bar{t} = \frac{\mu^f}{\rho^f L^2} t,\ \bar{\boldsymbol{u}}^m = \frac{\rho^f L}{\mu^f} \boldsymbol{u}^m,$$

along with

$$\bar{T}^m = \frac{T^m}{T_0}, \tag{3.33}$$

where T_0 is a reference temperature. Substituting these into 3.32 gives:

$$\rho^m c_p^m \frac{T_0 \mu^f}{\rho^f L^2} \left(\frac{\partial \bar{T}^m}{\partial \bar{t}} + (\bar{\boldsymbol{u}}^m \cdot \bar{\boldsymbol{\nabla}}) \bar{T}^m \right) = \frac{k^m T_0}{L^2} \bar{\Delta} \bar{T}^m.$$

Eliminating the common factor of T_0/L^2 and then diving both sides by $\mu^f c_p^f$ gives the final nondimensional form:

$$\frac{\rho^m}{\rho^f} \frac{c_p^m}{c_p^f} \left(\frac{\partial \bar{T}^m}{\partial \bar{t}} + (\bar{\boldsymbol{u}}^m \cdot \bar{\boldsymbol{\nabla}}) \bar{T}^m \right) = \frac{k^m}{\mu^f c_p^f} \bar{\Delta} \bar{T}^m. \tag{3.34}$$

Note that, in the fluid, the density and specific heat capacity terms vanish to 1 but not so in the solid phase. Note also that the temperature field can just as easily be nondimensionalized as:

$$\bar{T}^m = \frac{T^m - T_L}{T_U - T_L}, \tag{3.35}$$

in problems with a lower, T_L, and upper, T_U, reference temperatures.

3.4 Subgrid Stabilization

The convective terms in the incompressible NS equations may cause spurious node-to-node oscillations in the velocities field. Furthermore, equal-order approximations used for v_i^f and q^f may cause oscillations in the pressure field. To prevent these oscillations, this work augments the NS equations with Streamline Upwind Petrov-Galerkin (SUPG) and the Pressure Stabilized Petrov-Galerkin (PSPG) stabilization formulations introduced by Tezduyar [72]:

$$\begin{aligned} r_{\boldsymbol{u},p}^{\hat{\Omega}} = \sum_{\Omega_e \in \Omega} \int_{\Omega_e \cap \Omega^f} \Bigg(\Bigg(\tau_{SUPG} \left(u_i^f \frac{\partial v_i^f}{\partial x_j} \right) + \tau_{PSPG} \left(\frac{1}{\rho_f} \frac{\partial q^f}{\partial x_i} \right) \Bigg) \cdot \\ \left(\rho^f \left(\frac{\partial u_i^f}{\partial t} + u_i^f \frac{v_i^f}{\partial x_j} \right) \frac{\partial p^f}{\partial x_j} \delta_{ij} - 2\mu^f \frac{\partial}{\partial x_j} \left(\epsilon_{ij}(\boldsymbol{u}^f) \right) \right) \Bigg) \mathrm{d}\Omega, \end{aligned} \tag{3.36}$$

where Ω_e denotes the set of all elements in the domain Ω, and the stabilization terms τ_{SUPG} and τ_{PSPG} are defined in [72].

The stabilized volumetric contribution in (3.8) uses the SUPG method and is defined as:

$$r_{\boldsymbol{u},T}^{\hat{\Omega}} = \sum_{\Omega_e \in \Omega} \int_{\Omega_e \cap \Omega^f} \left(\tau_{SUPG,T} \cdot \left(\frac{1}{\rho^f c_p^f} u_i^f \frac{\partial d^f}{\partial x_i} \right) \cdot \left(\rho^f c_p^f \left(\frac{\partial T^f}{\partial t} + u_i^f \frac{\partial T^f}{\partial x_i} \right) - \frac{\partial}{\partial x_i} \left(J_i(T^f) \right) \right) \right) \mathrm{d}\Omega, \tag{3.37}$$

where the stabilization term $\tau_{SUPG,T}$ is defined in [73].

3.5 Ghost-Penalty Stabilization

As the optimization process changes the geometry of the design, the interface may move close to a mesh node; if this occurs, certain degrees-of-freedom interpolate into very small subdomains. This in turn produces an ill-conditioning of the system, which results in an increase in the condition number of the linearized system and may slow down or prevent the convergence of the nonlinear program. Face-oriented ghost-penalty stabilization terms are used in the vicinity of the fluid-solid interface to guarantee stability, as well as improve the condition number, cf. [67]. The ghost-penalty term in (3.2) is defined as:

$$r_{\boldsymbol{u},p}^{GP} = r_{\boldsymbol{u},p}^{GP,\mu} + r_{\boldsymbol{u},p}^{GP,p} + r_{\boldsymbol{u},p}^{GP,\boldsymbol{u}}, \tag{3.38}$$

where $r_{\boldsymbol{u},p}^{GP,\mu}$, $r_{\boldsymbol{u},p}^{GP,p}$, $r_{\boldsymbol{u},p}^{GP,\boldsymbol{u}}$ are the viscous, pressure, and convective ghost-penalty formulations, respectively.

The viscous face-oriented ghost-penalty formulation as proposed in [74] is used to overcome stability issues related to the weak enforcement of boundary conditions via Nitsche's method and is defined as:

$$r_{\boldsymbol{u},p}^{GP,\mu} = \sum_{F \in \Xi^f} \int_F \left(\gamma_{GP,\mu} \left[\!\!\left[\frac{\partial v_i^f}{\partial x_j} \right]\!\!\right] n_j^f \left[\!\!\left[\frac{\partial u_i^f}{\partial x_k} \right]\!\!\right] n_k^f \right) \mathrm{d}\Gamma, \tag{3.39}$$

where $\gamma_{GP,\mu}$ is a penalty parameter defined as:

$$\gamma_{GP,\mu} = \alpha_{GP,\mu} \mu^f h, \tag{3.40}$$

and $\alpha_{GP,\mu}$ is a chosen scaling factor. The jump operator is defined as:

$$[\![\zeta]\!] = \zeta|_{\Omega_e^1} - \zeta|_{\Omega_e^2}, \tag{3.41}$$

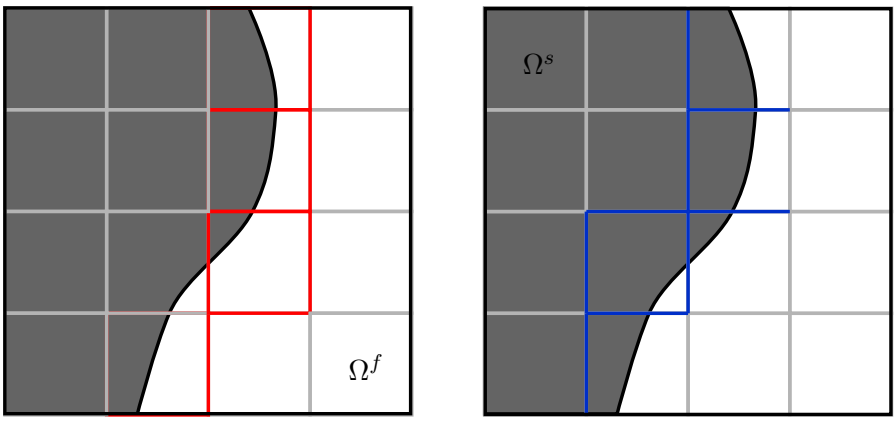

(a) Facets Ξ^f in domain Ω^f. (b) Facets Ξ^s in domain Ω^s.

Figure 3.8: Integration facet domains for the face-oriented ghost-penalty method.

and is evaluated at the edge or face between two adjacent elements, Ω_e^1 and Ω_e^2. Because the integration domain is the entire edge or face, this formulation is able to mitigate the issue of small ratio of volumes on elements bisected by the interface. The set Ξ^f belonging to the domain Ω_f contains all facets F in the immediate vicinity of the fluid-solid interface, for which at least one of the two adjacent elements is intersected by the interface; for example, see Fig. 3.8.

The pressure ghost-penalty stabilization term is applied to reduce pressure instabilities due to a violated inf-sup condition for equal-order approximations used for the velocity and pressure degrees-of-freedom and defined as:

$$r_{\boldsymbol{u},p}^{GP,p} = \sum_{F \in \Xi^f} \int_F \left(\gamma_{GP,p} \left[\!\!\left[\frac{\partial q_i^f}{\partial x_j} \right]\!\!\right] n_j^f \left[\!\!\left[\frac{\partial p_i^f}{\partial x_k} \right]\!\!\right] n_k^f \right) \mathrm{d}\Gamma, \tag{3.42}$$

where $\gamma_{GP,p}$ is a penalty parameter defined as:

$$\gamma_{GP,p} = \alpha_{GP,p} \left(\frac{\mu^f}{h} + \frac{\rho ||\boldsymbol{u}^f||_\infty}{6} \right)^{-1} h^2, \tag{3.43}$$

and $\alpha_{GP,p}$ is a chosen constant scaling parameter [68].

Schott and Wall [75] further proposed a convective ghost-penalty formulation to sufficiently control the convective derivative in the incompressible NS equations for high Reynolds number

flows. This formulation is defined as:

$$r_{\boldsymbol{u},p}^{GP,\boldsymbol{u}} = \sum_{F\in\Xi^f} \int_F \left(\gamma_{GP,\boldsymbol{u}} \left[\!\left[\frac{\partial v_i^f}{\partial x_j} \right]\!\right] n_j^f \left[\!\left[\frac{\partial p_i^f}{\partial x_k} \right]\!\right] n_k^f \right) \mathrm{d}\Gamma, \tag{3.44}$$

where $\gamma_{GP,\boldsymbol{u}}$ is a penalty parameter defined as:

$$\gamma_{GP,\boldsymbol{u}} = \alpha_{GP,\boldsymbol{u}} \rho^f ||u_i^f n_i^f|| h^2, \tag{3.45}$$

and $\alpha_{GP,\boldsymbol{u}}$ is a chosen constant scaling parameter.

To stabilize the temperature field (3.9) in thermal trasport problems, we adopt the formulation in [76]:

$$r_{\boldsymbol{u},T}^{GP} = \sum_{m\in\{f,s\}} \sum_{F\in\Xi^m} \int_F \left(\gamma_{GP,T} \left[\!\left[\frac{\partial d^m}{\partial x_i} \right]\!\right] n_i^f \left[\!\left[J_j(T^m) \right]\!\right] n_j^f \right), \mathrm{d}\Gamma \tag{3.46}$$

where $\gamma_{GP,T}$ is a penalty term defined as:

$$\gamma_{GP,T} = \alpha_{GP,T} h, \tag{3.47}$$

and $\alpha_{GP,T}$ is a scaling term.

This work adopts the values for $\alpha_{GP,\boldsymbol{u}}$ and $\alpha_{GP,T}$ from [10]. The values for $\alpha_{GP,\mu}$ and $\alpha_{GP,p}$ are set on a per-problem basis and their influence is studied in Section 3.13.2.

3.6 Boundary Conditions for NSF

Fluid boundary conditions can be categorized as applying in the orthogonal (normal) or tangential directions. In the normal direction, the most common boundary condition is the no-penetration condition:

$$u_n - u_n^w = 0, \tag{3.48}$$

where u_n and u_n^w are the fluid and wall normal velocities, respectively.

The tangential direction offers a variety of boundary conditions. The most common of these is the traditional no-slip (or equally, *stick*) condition:

$$u_t - u_t^w = 0, \tag{3.49}$$

where u_t and u_t^w are the fluid and wall tangential velocities, respectively. However, this is only appropriate for very small Knudsen number flows [2]. Schaaf and Chambre [2] originally suggested this cut-off to be $Kn < 10^{-2}$, but Gad-el-Hak [3] suggested this be moved to $Kn < 10^{-3}$, due to the breakdown of the thermodynamic equilibrium assumption. For larger Kn numbers in the Slip Flow regime, there exists a variety of slip models for the tangential velocity. The wall-function method described the tangential velocity as a function of distance from the wall up to $O(\lambda)$, i.e. within the so-called Knudsen layer. However, the wall-function method is phenomenological, thus dependent on curve-fitting to experimental data, and has been primarily studied on planar surfaces [41]. Another option is to use higher-order continuum models, including the Burnett, BGK-Burnett, and super-Burnett models, inside the Knudsen layer. However, the goal in this work is to extend the regime of validity of the NS equations. The reader is referred to Zhang et al. [46] for a review of slip models.

To this end, this work adopts the second-order model proposed by Beskok and Karniadakis [77], which is based on Maxwell's proposal of the fundamental description of gas-surface interaction [78]:

$$u_t - u_t^w - \frac{2-\sigma_u}{\sigma_u}\frac{Kn}{1-bKn}\left(\frac{\partial u_t}{\partial n}\right) = 0. \tag{3.50}$$

For stationary walls, $u_t^w = 0$. The derivative term is the rate of change of the tangential velocity in the normal direction, i.e. a shear rate. σ_u is an accommodation coefficient, which typically depends on the fluids [77]. Further, there is no general agreement on the appropriate values for σ_u [46]. For simplicity, this work will use $\sigma_u = 1$. For fully developed flows, $b = -1$ [77]. This value is acceptable for Knudsen values less than 10^{-1}.

More recently, Colin [79] and Leontidis et al. [42] studied the effect of curved surfaces and recognized the important of a $\frac{\partial u_n}{\partial t}$ term. The boundary condition in that work takes the form:

$$u_t - u_t^w = \alpha\frac{2-\sigma_u}{\sigma_u}\lambda\left(\frac{\partial u_t}{\partial n} + \frac{\partial u_n}{\partial t}\right), \tag{3.51}$$

where u_n is the velocity in the normal direction, t is the tangential direction, and α is an additional correction factor, which may be used to calibrate the boundary condition for various gase. Méolans

[80] uses $\alpha\frac{2-\sigma_v}{\sigma_v} = 1.494$ for helium and $\alpha\frac{2-\sigma_v}{\sigma_v} = 1.262$ for nitrogen. In this work, we will use $\alpha = 1$, since our goal is to see the influence of the Kn on optimization results rather than model one specific fluid. The additional derivative term, $\frac{\partial u_n}{\partial t}$, can be omitted for straight-wall channels but plays a critical role along curved walls. This, however, is a first-order model, which Beskok and Karniadakis [77] improve to a second-order model, for planar surfaces. To this end, we extend the boundary condition proposed by Beskok and Karniadakis [77] to include the other derivative term, which gives:

$$u_t - u_t^w - \frac{Kn}{1+Kn}\left(\frac{\partial u_t}{\partial n} + \frac{\partial u_n}{\partial t}\right) = 0 \tag{3.52}$$

This work will refer to this boundary condition as the *Knudsen-slip* (or *Kn-slip*) condition.

Finally, the so-called "slip" boundary condition allows the tangential velocity in the fluid to be free:

$$\frac{\partial u_t}{\partial n} = 0. \tag{3.53}$$

This type of conditions appears in inviscid fluid-solid flows, liquid-gas interface flows or where symmetry in a flow is to be enforced. It is tempting to think of this slip condition as the end behavior (i.e. $Kn \to \infty$) of the first order Kn-slip model, just as the no-slip condition corresponds to the $Kn \to 0$ end behavior, but it is important to remember that such Kn-slip models are not valid for large Kn numbers. In this work, we will use this condition to enforce symmetry, where applicable. To avoid ambiguity, we will refer to this type of boundary condition as *free-slip*.

3.6.1 Generalization to 3D

While this work focuses on problems in 2D, we generalized our approach to the Kn-slip boundary condition to 3D and note that appropriate terms can be omitted for problems in 2D. The Kn-slip boundary condition (3.1) applies on a 2D plane, where there is only one tangential direction. In 3D, there is instead a tangent plane with infinite choices for basis vectors. One tangential vector, $\hat{\boldsymbol{t}}$, can be chosen such that:

$$\hat{\boldsymbol{t}} \cdot \hat{\boldsymbol{n}} = 0. \tag{3.54}$$

The other, $\hat{\boldsymbol{s}}$, is then calculated by:

$$\hat{\boldsymbol{t}} = \hat{\boldsymbol{n}} \times \hat{\boldsymbol{t}}. \tag{3.55}$$

Next, we write (3.1) in each of these directions,

$$\begin{aligned} R_t &= u_t - u_t^w - \frac{Kn}{1+Kn}\left(\frac{\partial u_t}{\partial n} + \frac{\partial u_n}{\partial t}\right), \\ R_s &= u_s - u_s^w - \frac{Kn}{1+Kn}\left(\frac{\partial u_s}{\partial n} + \frac{\partial u_n}{\partial s}\right), \end{aligned} \tag{3.56}$$

and apply each contribution in its respective direction:

$$\begin{aligned} \boldsymbol{R}_{Kn} &= R_t\hat{\boldsymbol{t}} + R_s\hat{\boldsymbol{s}} \\ &= \left(u_t - u_t^w - \frac{Kn}{1+Kn}\left(\frac{\partial u_t}{\partial n} + \frac{\partial u_n}{\partial t}\right)\right)\hat{\boldsymbol{t}} + \left(u_s - u_s^w - \frac{Kn}{1+Kn}\left(\frac{\partial u_s}{\partial n} + \frac{\partial u_n}{\partial s}\right)\right)\hat{\boldsymbol{s}}. \\ &= u_t\hat{\boldsymbol{t}} + u_s\hat{\boldsymbol{s}} - u_t^w\hat{\boldsymbol{t}} - u_s^w\hat{\boldsymbol{s}} - \frac{Kn}{1+Kn}\left(\frac{\partial u_t}{\partial n}\hat{\boldsymbol{t}} + \frac{\partial u_s}{\partial n}\hat{\boldsymbol{s}}\right) - \frac{Kn}{1+Kn}\left(\frac{\partial u_n}{\partial t}\hat{\boldsymbol{t}} + \frac{\partial u_n}{\partial s}\hat{\boldsymbol{s}}\right) \end{aligned} \tag{3.57}$$

We can then expand the derivative terms as:

$$\begin{aligned} \frac{\partial u_t}{\partial n} &= \frac{\partial(\boldsymbol{u}\cdot\hat{\boldsymbol{t}})}{\partial n} = \frac{\partial \boldsymbol{u}}{\partial n}\cdot\hat{\boldsymbol{t}} + \boldsymbol{u}\cdot\frac{\partial\hat{\boldsymbol{t}}}{\partial n} \\ &= (\boldsymbol{J}_u\hat{\boldsymbol{n}})\cdot\hat{\boldsymbol{t}} + \boldsymbol{u}\cdot(\boldsymbol{J}_t\hat{\boldsymbol{n}}) \\ &= \hat{\boldsymbol{t}}^T\boldsymbol{J}_u\hat{\boldsymbol{n}} + (\boldsymbol{J}_t\hat{\boldsymbol{n}})^T\boldsymbol{u} \end{aligned} \quad , \tag{3.58}$$

$$\begin{aligned} \frac{\partial u_s}{\partial n} &= \frac{\partial(\boldsymbol{u}\cdot\hat{\boldsymbol{s}})}{\partial n} = \frac{\partial \boldsymbol{u}}{\partial n}\cdot\hat{\boldsymbol{s}} + \boldsymbol{u}\cdot\frac{\partial\hat{\boldsymbol{s}}}{\partial n} \\ &= (\boldsymbol{J}_u\hat{\boldsymbol{n}})\cdot\hat{\boldsymbol{s}} + \boldsymbol{u}\cdot(\boldsymbol{J}_s\hat{\boldsymbol{n}}) \\ &= \hat{\boldsymbol{s}}^T\boldsymbol{J}_u\hat{\boldsymbol{n}} + (\boldsymbol{J}_s\hat{\boldsymbol{n}})^T\boldsymbol{u} \end{aligned} \quad , \tag{3.59}$$

$$\begin{aligned} \frac{\partial u_n}{\partial t} &= \frac{\partial(\boldsymbol{u}\cdot\hat{\boldsymbol{n}})}{\partial t} = \frac{\partial \boldsymbol{u}}{\partial t}\cdot\hat{\boldsymbol{n}} + \boldsymbol{u}\cdot\frac{\partial\hat{\boldsymbol{n}}}{\partial t} \\ &= (\boldsymbol{J}_u\hat{\boldsymbol{t}})\cdot\hat{\boldsymbol{n}} + \boldsymbol{u}\cdot(\boldsymbol{J}_n\hat{\boldsymbol{t}}) \\ &= \hat{\boldsymbol{n}}^T\boldsymbol{J}_u\hat{\boldsymbol{t}} + (\boldsymbol{J}_n\hat{\boldsymbol{t}})^T\boldsymbol{u} \\ &= \hat{\boldsymbol{t}}^T\boldsymbol{J}_u^T\hat{\boldsymbol{n}} + (\boldsymbol{J}_n\hat{\boldsymbol{t}})^T\boldsymbol{u} \end{aligned} \quad , \tag{3.60}$$

and

$$\begin{aligned}\frac{\partial u_n}{\partial s} &= \frac{\partial(\boldsymbol{u}\cdot\hat{\boldsymbol{n}})}{\partial s} = \frac{\partial \boldsymbol{u}}{\partial s}\cdot\hat{\boldsymbol{n}} + \boldsymbol{u}\cdot\frac{\partial\hat{\boldsymbol{n}}}{\partial s} \\ &= (\boldsymbol{J}_u\hat{\boldsymbol{s}})\cdot\hat{\boldsymbol{n}} + \boldsymbol{u}\cdot(\boldsymbol{J}_n\hat{\boldsymbol{s}}) \\ &= \hat{\boldsymbol{n}}^T\boldsymbol{J}_u\hat{\boldsymbol{s}} + (\boldsymbol{J}_n\hat{\boldsymbol{s}})^T\boldsymbol{u} \\ &= \hat{\boldsymbol{s}}^T\boldsymbol{J}_u^T\hat{\boldsymbol{n}} + (\boldsymbol{J}_n\hat{\boldsymbol{s}})^T\boldsymbol{u}\end{aligned}, \tag{3.61}$$

where

$$(\boldsymbol{J}_u)_{ij} = \frac{\partial u_i}{\partial x_j},\ (\boldsymbol{J}_n)_{ij} = \frac{\partial n_i}{\partial x_j},\ (\boldsymbol{J}_s)_{ij} = \frac{\partial s_i}{\partial x_j},\ \text{and}\ (\boldsymbol{J}_t)_{ij} = \frac{\partial t_i}{\partial x_j} \tag{3.62}$$

are the derivatives of the velocities and the normal and tangent vectors with respect to the Cartesian coordinates. Substituting (3.58)-(3.61) into (3.57) gives:

$$\begin{aligned}\boldsymbol{R}_{Kn} = {} & (\boldsymbol{u}\cdot\hat{\boldsymbol{s}})\hat{\boldsymbol{s}} + (\boldsymbol{u}\cdot\hat{\boldsymbol{t}})\hat{\boldsymbol{t}} - (\boldsymbol{u}^w\cdot\hat{\boldsymbol{s}})\hat{\boldsymbol{s}} + (\boldsymbol{u}^w\cdot\hat{\boldsymbol{t}})\hat{\boldsymbol{t}} \\ & - \frac{Kn}{1+Kn}\left(\hat{\boldsymbol{s}}\hat{\boldsymbol{s}}^T\boldsymbol{J}_u\hat{\boldsymbol{n}} + \hat{\boldsymbol{t}}\hat{\boldsymbol{t}}^T\boldsymbol{J}_u\hat{\boldsymbol{n}} + \hat{\boldsymbol{s}}\hat{\boldsymbol{s}}^T\boldsymbol{J}_u^T\hat{\boldsymbol{n}} + \hat{\boldsymbol{t}}\hat{\boldsymbol{t}}^T\boldsymbol{J}_u^T\hat{\boldsymbol{n}}\right) \\ & - \frac{Kn}{1+Kn}\left(\hat{\boldsymbol{s}}(\boldsymbol{J}_s\hat{\boldsymbol{n}})^T\boldsymbol{u} + \hat{\boldsymbol{t}}(\boldsymbol{J}_t\hat{\boldsymbol{n}})^T\boldsymbol{u} + \hat{\boldsymbol{s}}(\boldsymbol{J}_n\hat{\boldsymbol{s}})^T\boldsymbol{u} + \hat{\boldsymbol{t}}(\boldsymbol{J}_n\hat{\boldsymbol{t}})^T\boldsymbol{u}\right)\end{aligned}. \tag{3.63}$$

As currently written, (3.63) requires a choice of $\hat{\boldsymbol{s}}$ and $\hat{\boldsymbol{t}}$. As stated previously, this choice is not necessary in a 2D problem, as there is only one tangential direction; however, nothing in (3.56) suggest that the Kn-slip boundary condition would depend on the orientation of the tangent plane. Consider that:

$$\boldsymbol{I} = \hat{\boldsymbol{i}}\hat{\boldsymbol{i}}^T + \hat{\boldsymbol{j}}\hat{\boldsymbol{j}}^T + \hat{\boldsymbol{k}}\hat{\boldsymbol{k}}^T, \tag{3.64}$$

where

$$\hat{\boldsymbol{i}} = \{1,0,0\}^T,\ \hat{\boldsymbol{j}} = \{0,1,0\}^T,\ \text{and}\ \hat{\boldsymbol{k}} = \{0,0,1\}^T. \tag{3.65}$$

Next, consider the arbitrary rotation matrices,

$$\boldsymbol{R}_x(\alpha) = \begin{pmatrix} 1 & 0 & 0 \\ 0 & \cos(\theta) & -\sin(\theta) \\ 0 & \sin(\theta) & \cos(\theta) \end{pmatrix}, \tag{3.66}$$

$$\boldsymbol{R}_y(\beta) = \begin{pmatrix} \cos(\beta) & 0 & \sin(\beta) \\ 0 & 1 & 0 \\ -\sin(\beta) & & \cos(\beta) \end{pmatrix}, \tag{3.67}$$

$$\boldsymbol{R}_z(\gamma) = \begin{pmatrix} \cos(\gamma) & -\sin(\gamma) & 0 \\ \sin(\gamma) & \cos(\gamma) & 0 \\ 0 & 0 & 1 \end{pmatrix}, \tag{3.68}$$

and

$$\boldsymbol{R} = \boldsymbol{R}_z(\gamma)\boldsymbol{R}_y(\beta)\boldsymbol{R}_x(\alpha). \tag{3.69}$$

Finally, consider the rotated coordinate system at any point in the fluid-solid interface,

$$\hat{\boldsymbol{t}} = \boldsymbol{R}\hat{\boldsymbol{i}},\ \hat{\boldsymbol{s}} = \boldsymbol{R}\hat{\boldsymbol{j}},\ \text{and}\ \hat{\boldsymbol{n}} = \boldsymbol{R}\hat{\boldsymbol{k}}. \tag{3.70}$$

Substituting (3.70) into (3.64), it can be shown that:

$$\boldsymbol{I} = \hat{\boldsymbol{n}}\hat{\boldsymbol{n}}^T + \hat{\boldsymbol{s}}\hat{\boldsymbol{s}}^T + \hat{\boldsymbol{t}}\hat{\boldsymbol{t}}^T, \tag{3.71}$$

regardless of the rotation angles, (α, β, γ), or the order of transformation, i.e. $\boldsymbol{R} = \boldsymbol{R}_x\boldsymbol{R}_y\boldsymbol{R}_z$ has the same results, such that:

$$\hat{\boldsymbol{s}}\hat{\boldsymbol{s}}^T + \hat{\boldsymbol{t}}\hat{\boldsymbol{t}}^T = \boldsymbol{I} - \hat{\boldsymbol{n}}\hat{\boldsymbol{n}}^T, \tag{3.72}$$

and thus (3.63) may be written as:

$$\begin{aligned} \boldsymbol{R}_{Kn} = &\left(\boldsymbol{I} - \hat{\boldsymbol{n}}\hat{\boldsymbol{n}}^T\right)\boldsymbol{u} - \left(\boldsymbol{I} - \hat{\boldsymbol{n}}\hat{\boldsymbol{n}}^T\right)\boldsymbol{u}^w \\ &- \frac{Kn}{1+Kn}\left(\boldsymbol{I} - \hat{\boldsymbol{n}}\hat{\boldsymbol{n}}^T\right)\left(\boldsymbol{J}_u + \boldsymbol{J}_u^T\right)\hat{\boldsymbol{n}} \\ &- \frac{Kn}{1+Kn}\left(\left(\boldsymbol{I} - \hat{\boldsymbol{n}}\hat{\boldsymbol{n}}^T\right)\boldsymbol{J}_n^T\boldsymbol{u} + \hat{\boldsymbol{s}}\hat{\boldsymbol{n}}^T\boldsymbol{J}_s^T\boldsymbol{u} + \hat{\boldsymbol{t}}\hat{\boldsymbol{n}}^T\boldsymbol{J}_t^T\boldsymbol{u}\right). \end{aligned} \tag{3.73}$$

Note that (3.72) nearly eliminates need to define the two tangent vectors, but the terms that involve the gradients of the tangent vectors, $\hat{\boldsymbol{s}}$ and $\hat{\boldsymbol{t}}$, cannot make use of this identity (3.72). The influence of these terms will be studied for problems with and without analytical solutions in Sections 3.10.5 and 3.12.1, respectively, and within an optimization problem in Section 4.2.

Note that $\hat{\boldsymbol{n}}$ in this section is defined as pointing into the fluid at a boundary. However, the normal vector derived from the level set function is defined as pointing outward from the fluid (i.e. opposite of what is used in this section). In (3.73), the first two terms are not affected by the direction of $\hat{\boldsymbol{n}}$, but the last two ultimately do; thus the sign on this term must be reversed to give:

$$\begin{aligned}\boldsymbol{R}_{Kn} = &\left(\boldsymbol{I} - \hat{\boldsymbol{n}}\hat{\boldsymbol{n}}^T\right)\boldsymbol{v} - \left(\boldsymbol{I} - \hat{\boldsymbol{n}}\hat{\boldsymbol{n}}^T\right)\boldsymbol{v}^w \\ &+ \frac{Kn}{1+Kn}\left(\boldsymbol{I} - \hat{\boldsymbol{n}}\hat{\boldsymbol{n}}^T\right)\left(\boldsymbol{J}_v + \boldsymbol{J}_v^T\right)\hat{\boldsymbol{n}} \\ &+ \frac{Kn}{1+Kn}\left(\left(\boldsymbol{I} - \hat{\boldsymbol{n}}\hat{\boldsymbol{n}}^T\right)\boldsymbol{J}_n^T\boldsymbol{v} + \hat{\boldsymbol{s}}\hat{\boldsymbol{n}}^T\boldsymbol{J}_s^T\boldsymbol{v} + \hat{\boldsymbol{t}}\hat{\boldsymbol{n}}^T\boldsymbol{J}_t^T\boldsymbol{v}\right).\end{aligned} \tag{3.74}$$

3.6.2 Implementation by Nitsche's Method

In this work, we adapt the boundary condition enforcement method described in Villanueva and Maute [10]. There, Nitsche's method is used to enforce Dirichlet boundary conditions as follows (presently, we drop the superscript fluid notation):

$$\begin{aligned}r^m_{\boldsymbol{u},p} = &\int_{\Gamma^m} \delta u_i \left(p\delta_{ij} - 2\mu\epsilon_{ij}(\boldsymbol{u})\right) n_j \delta\Gamma \\ &+ \int_{\Gamma^m} \left(\beta_p \delta p \delta_{ij} - \beta_\mu 2\mu\epsilon_{ij}(\delta\boldsymbol{u})\right) n_j \left(u_j - \hat{u}_j\right)\delta\Gamma \\ &+ \int_{\Gamma^m} \left(\lambda_{N,\boldsymbol{u}}\delta u_i \left(u_i - \hat{u}_i\right)\right)\delta\Gamma,\end{aligned}$$

where δu_i and δp are the trial functions for the velocities and pressure, respectively, $\lambda_{N,\boldsymbol{u}}$ is the Nitsche penalty parameter, and the terms β_p and β_μ determine whether a symmetric ($\beta_p = +1$,$\beta_\mu = +1$) or a skew-symmetric formulation ($\beta_p = -1$,$\beta_\mu = -1$) is used. $m \in \{D, fs\}$ denotes the enforcement of boundary conditions on the external boundaries or on the fluid-solid (or fluid-void) interface. The penalty term $\lambda_{N,\boldsymbol{u}}$ is taken from Schott et al. [68] and defined as:

$$\lambda_{N,\boldsymbol{u}} = \alpha_{N,\boldsymbol{u}}\left(\frac{\mu}{h} + \frac{\rho||\boldsymbol{u}||_\infty}{6}\right) \tag{3.75}$$

and its terms account for viscous-dominated and convection-dominated flows, respectively. The term $\alpha_{N,\boldsymbol{u}}$ is a problem-dependent parameter and the term $||\boldsymbol{u}^f||_\infty$ is the infinity norm evaluated at each integration point and differentiated at its maximum value. The influence of this term was previously studied by Villanueva and Maute [81].

This formulation, however, is written exclusively for fully no-slip boundary conditions; as written, it neither allows the free- and Kn-slip boundary conditions nor no-slip condition in particular directions (i.e. enforcing only the x-component velocities at a horizontal inlet). To this end, we seek to generalize the formulation.

First, we write the Cauchy stress tensor as $\sigma_{ij} = -p\delta_{ij} + 2\mu\epsilon_{ij}$ and the traction as $T_i = \sigma_{ij}n_j$. Similarly, we can write trial functions for the traction as $\delta T_i = \beta_p \delta p \delta_{ij} n_j - \beta_\mu 2\mu\epsilon_{ij}n_j$. This allows us to write the boundary condition as:

$$r_{\boldsymbol{u},p} = -\int \delta u_i T_i \delta\Gamma + \int \delta T_i (u_i - \hat{u}_i)\delta\Gamma + \int \lambda_{N,\boldsymbol{u}} \delta u_i (u_i - \hat{u}_i)\delta\Gamma,$$

or, in vector notation, as:

$$r_{\boldsymbol{u},p} = -\int \delta\boldsymbol{u}\cdot\boldsymbol{T}\delta\Gamma + \int \delta\boldsymbol{T}\cdot(\boldsymbol{u}-\hat{\boldsymbol{u}})\delta\Gamma + \int \lambda_{N,\boldsymbol{u}}\delta\boldsymbol{u}\cdot(\boldsymbol{u}-\hat{\boldsymbol{u}})\delta\Gamma. \tag{3.76}$$

Considering that $r_{\boldsymbol{u},p}$ is used to enforce a boundary at an interface, there exists normal and tangential directions and we may split each vector into components in each of those directions. Consider that $\boldsymbol{u} = \boldsymbol{u}_t + \boldsymbol{u}_n$ and $\boldsymbol{T} = \boldsymbol{T}_t + \boldsymbol{T}_n$, and similarly for $\delta\boldsymbol{u}$ and $\delta\boldsymbol{T}$, which gives:

$$\begin{aligned} r_{\boldsymbol{u},p} = &-\int (\delta\boldsymbol{u}_t + \delta\boldsymbol{u}_n)\cdot(\boldsymbol{T}_t + \boldsymbol{T}_n)\delta\Gamma \\ &+ \int (\delta\boldsymbol{T}_t + \delta\boldsymbol{T}_n)\cdot(\boldsymbol{u}_t - \hat{\boldsymbol{u}}_t + \boldsymbol{u}_n - \hat{\boldsymbol{u}}_n)\delta\Gamma \\ &+ \int \lambda_{N,\boldsymbol{u}}(\delta\boldsymbol{u}_t + \delta\boldsymbol{u}_n)\cdot(\boldsymbol{u}_t - \hat{\boldsymbol{u}}_t + \boldsymbol{u}_n - \hat{\boldsymbol{u}}_n)\delta\Gamma. \end{aligned} \tag{3.77}$$

Then, we expand the terms:

$$\begin{aligned} r_{\boldsymbol{u},p} = &-\int \delta\boldsymbol{u}_t\cdot\boldsymbol{T}_t\delta\Gamma - \int \delta\boldsymbol{u}_n\cdot\boldsymbol{T}_n\delta\Gamma \\ &+ \int \delta\boldsymbol{T}_t\cdot(\boldsymbol{u}_t - \hat{\boldsymbol{u}}_t)\delta\Gamma + \int \delta\boldsymbol{T}_n\cdot(\boldsymbol{u}_n - \hat{\boldsymbol{u}}_n)\delta\Gamma \\ &+ \int \lambda_{N,\boldsymbol{u}}\delta\boldsymbol{u}_t\cdot(\boldsymbol{u}_t - \hat{\boldsymbol{u}}_t)\delta\Gamma + \int \lambda_{N,\boldsymbol{u}}\delta\boldsymbol{u}_n\cdot(\boldsymbol{u}_n - \hat{\boldsymbol{u}}_n)\delta\Gamma. \end{aligned} \tag{3.78}$$

This separation is allowed since, by definition, the normal and tangential directions are orthogonal. At this point, different conditions may be applied in the normal and tangential directions; for

example, to enforce no-slip conditions (though the split is not necessary for this case),

$$\begin{aligned} \hat{\boldsymbol{u}}_n &= \mathbf{0} \\ \hat{\boldsymbol{u}}_t &= \mathbf{0}. \end{aligned} \tag{3.79}$$

For free-slip conditions,

$$\begin{aligned} \hat{\boldsymbol{u}}_n &= \mathbf{0} \\ \hat{\boldsymbol{u}}_t &= \boldsymbol{u}_t \\ \boldsymbol{T}_t &= \mathbf{0} \\ \delta\boldsymbol{T}_t &= \mathbf{0}. \end{aligned} \tag{3.80}$$

Note the additional conditions on the tangential traction: if the tangential velocity is to be free, then the tangential traction must be zero, i.e. recall that this condition is equivalent to $\delta u_t/\delta n = 0$ and $\delta u_t/\delta n$ is precisely the tangential traction. Finally, for the Kn-slip condition,

$$\begin{aligned} \hat{\boldsymbol{u}}_n &= \mathbf{0} \\ \boldsymbol{u}_t - \hat{\boldsymbol{u}}_t &= \boldsymbol{R}_{Kn}. \end{aligned} \tag{3.81}$$

Note that the normal-tangential splitting of (3.76) is only partially necessary. Thus, a partial splitting is suggested as follows:

$$r_{\boldsymbol{u},p} = -\int \delta\boldsymbol{u}\cdot(\boldsymbol{T}_t+\boldsymbol{T}_n)\delta\Gamma + \int (\delta\boldsymbol{T}_t+\delta\boldsymbol{T}_n)\cdot(\boldsymbol{u}-\hat{\boldsymbol{u}})\delta\Gamma \int \lambda_{N,\boldsymbol{u}}\delta\boldsymbol{u}\cdot(\boldsymbol{u}-\hat{\boldsymbol{u}})\delta\Gamma, \tag{3.82}$$

with

$$\boldsymbol{u}-\hat{\boldsymbol{u}} = \begin{cases} \boldsymbol{u} & , \text{ no-slip} \\ \boldsymbol{u}_n + \boldsymbol{R}_{Kn} & , \text{ Kn-slip} \\ \boldsymbol{u}_n & , \text{ free-slip} \end{cases}$$

and

$$\boldsymbol{T}_t = \delta\boldsymbol{T}_t = \mathbf{0}, \text{ for free-slip.}$$

3.6.3 Final Generalization

Disregarding the Kn-slip condition momentarily, (3.82) can be further generalized to enforce boundary conditions in any arbitrary direction, i.e. not just in the normal or tangential direction. To this end, consider (3.78), where the normal direction is replaced with an arbitrary direction, on which boundary conditions are desired, and the tangential direction remains tangent to this arbitrary direction, on which velocities are meant to be free:

$$r_{\boldsymbol{u},p} = -\int \delta\boldsymbol{u}\cdot(\boldsymbol{M}_{bc}\boldsymbol{T})\delta\Gamma + \int (\boldsymbol{M}_{bc}\delta\boldsymbol{T})\cdot(\boldsymbol{u}-\hat{\boldsymbol{u}})\delta\Gamma + \int \lambda_{N,\boldsymbol{u}}\delta\boldsymbol{u}\cdot(\boldsymbol{M}_{bc}(\boldsymbol{u}-\hat{\boldsymbol{u}}))\delta\Gamma, \tag{3.83}$$

where, for the no-slip conditions (or to enforce a no-slip condition in a particular Cartesian direction),

$$\boldsymbol{M}_{bc} = \begin{pmatrix} \delta_{x_1} & 0 & 0 \\ 0 & \delta_{x_2} & 0 \\ 0 & 0 & \delta_{x_3} \end{pmatrix}, \tag{3.84}$$

where $\delta_{x_i} = 1$ if a boundary condition should be enforce in the x_i-direction, or 0 otherwise. Notice that for the full no-slip boundary condition, $\boldsymbol{M}_{bc} = \boldsymbol{I}$. For the free-slip boundary condition,

$$\boldsymbol{M}_{bc} = \hat{\boldsymbol{n}}\hat{\boldsymbol{n}}^T. \tag{3.85}$$

In this way, (3.83) handles both the no-slip and free-slip boundary conditions. Finally, the Kn-slip condition acts as an extension to the free-slip boundary condition, since it uses the same $\boldsymbol{M}_{bc}$ in (3.83) but with additional (underlined) terms,

$$\begin{aligned} r^{Kn}_{\boldsymbol{u},p} = &-\int \delta\boldsymbol{u}\cdot(\boldsymbol{M}_{bc}\boldsymbol{T})\delta\Gamma \underline{- \int \delta\boldsymbol{u}\cdot((\boldsymbol{I}-\boldsymbol{M}_{bc})\boldsymbol{T})\delta\Gamma} \\ &+\int (\boldsymbol{M}_{bc}\delta\boldsymbol{T})\cdot(\boldsymbol{u}-\hat{\boldsymbol{u}})\delta\Gamma \underline{+ \int ((\boldsymbol{I}-\boldsymbol{M}_{bc})\delta\boldsymbol{T})\cdot\boldsymbol{R}_{Kn}\delta\Gamma} \\ &+\int \lambda_{N,\boldsymbol{u}}\delta\boldsymbol{u}\cdot(\boldsymbol{M}_{bc}(\boldsymbol{u}-\hat{\boldsymbol{u}}))\delta\Gamma \underline{+ \int \lambda_{N,\boldsymbol{u}}\delta\boldsymbol{u}\cdot\boldsymbol{R}_{Kn}\delta\Gamma}. \end{aligned} \tag{3.86}$$

Thus, the most general implementation can be written as:

$$\begin{aligned} r_{\boldsymbol{u},p} = &- \int \delta\boldsymbol{u} \cdot (\boldsymbol{M}_{bc} + \beta_{Kn}(\boldsymbol{I} - \boldsymbol{M}_{bc})\boldsymbol{T})\delta\Gamma \\ &+ \int (\boldsymbol{M}_{bc}\delta\boldsymbol{T}) \cdot (\boldsymbol{u} - \hat{\boldsymbol{u}}) + \beta_{Kn}((\boldsymbol{I} - \boldsymbol{M}_{bc})\delta\boldsymbol{T}) \cdot \boldsymbol{R}_{Kn}\delta\Gamma, \\ &+ \int \lambda_{N,\boldsymbol{u}}\delta\boldsymbol{u} \cdot (\boldsymbol{M}_{bc}(\boldsymbol{u} - \hat{\boldsymbol{u}}) + \beta_{Kn}\boldsymbol{R}_{Kn})\delta\Gamma \end{aligned} \tag{3.87}$$

where

$$\beta_{Kn} = \begin{cases} 1, \text{ for Kn-slip} \\ \\ 0, \text{ otherwise} \end{cases},$$

and $\boldsymbol{M}_{bc}$ is given by (3.84) for no-slip conditions or by (3.85) for free- and Kn-slip conditions.

3.7 Level Set Function

The Level Set Method (LSM) describes the geometry of a body immersed in a domain by the zero isosurfaces of a higher dimensional Level Set Function (LSF), $\phi(\boldsymbol{x})$. The LSF is defined such that:

$$\begin{aligned} \phi(\boldsymbol{x}) > 0, &\quad \forall\, \boldsymbol{x} \in \Omega^s \\ \phi(\boldsymbol{x}) < 0, &\quad \forall\, \boldsymbol{x} \in \Omega^f \\ \phi(\boldsymbol{x}) = 0, &\quad \forall\, \boldsymbol{x} \in \Gamma^{fs}, \end{aligned} \tag{3.88}$$

where Ω^s is the solid phase, Ω^f is the fluid phase, and Γ^{fs} is the fluid-solid interface. The external boundaries of the solid and fluid phases are represented as Γ^s and Γ^f, respectively.

Topology optimization allows the emergence of a large set of geometries by parameterizing the LSF with local shape functions defined on a finite element mesh. Each node of the design mesh is assigned one optimization variable, s_i, for $i = 1...N_n$, where N_n is the number of nodes. Then, the LSF value of the i-th node, ϕ_i, is defined as:

$$\phi_i(\boldsymbol{s}, \boldsymbol{x}) = \left(\sum_{j=1}^{N_n} w_{ij} \right)^{-1} \left(\sum_{j=1}^{N_n} w_{ij} s_j \right), \tag{3.89}$$

where

$$w_{ij} = \max\left(0, r_\phi - |\boldsymbol{x}_i - \boldsymbol{x}_j|\right), \tag{3.90}$$

and r_ϕ is the smoothing filter radius. Kreissl and Maute [82] and Makhija and Maute [32] have used this linear filter (3.89) to widen the zone of influence of each optimization variable and to improve the convergence rate.

To define inlet and outlet ports, the LSF value on nodes outside the design domain can be overwritten, e.g. for a point, $\boldsymbol{x}_i$, near a desired horizontal port, the nodal LSF value, $\phi_i(\boldsymbol{x}_i)$, is overwritten with:

$$\phi_i = \min\left(\max\left(\phi_{min}, r - \sqrt{(y_i - y_c)^2}\right), \phi_{max}\right) \tag{3.91}$$

where $\phi_{min} = -h/2$, $\phi_{max} = h/2$, h is the element width, and y_c and r are the center axis and radius of the port. Vertical ports are created similarly. This approach is similar to the approach taken by Villanueva and Maute [10].

3.7.1 XFEM Discretization

The governing equations in the fluid phase are discretized in space by the XFEM. This paper adopts the generalized enrichment strategy based on the Heaviside-step enrichment of Hansbo and Hansbo [83], which consistently interpolates the solution field in the presence of small features and does not suffer from artificial coupling arising from disconnected phases. This particular approach has been used by Kreissl and Maute [82] for incompressible Navier-Stokes problems, Lang et al. [63] for linear diffusion problems, Makhija and Maute [32] for advection-diffusion problems, and Makhija and Maute [84] and Villanueva and Maute [81] for linear elasticity problems.

The XFEM can be used to approximate a state variable in a single phase phase or in both phases. Here, we present the most general case, where the state variables are modeled in both phases. The approximation for a solution field u, e.g. the fluid velocities, within an element is denoted as $\tilde{u}$ and is discretized by the enrichment strategy:

$$u(\boldsymbol{x}) \approx \tilde{u}(\boldsymbol{x}) = \sum_{l=1}^{N_l}\left(H(-\phi(\boldsymbol{x}))\sum_{i=1}^{N_n} v_i(\boldsymbol{x})\delta_{lk}^{i,f}u_{i,l}^{f} + H(+\phi(\boldsymbol{x}))\sum_{i=1}^{N_n} v_i(\boldsymbol{x})\delta_{ln}^{i,s}u_{i,l}^{s}\right), \tag{3.92}$$

where l is the enrichment level, N_l is the maximum number of enrichment levels used for each phase, $v_i(\boldsymbol{x})$ are the nodal basis function, i.e. the shape functions, $u_{i,l}^{f}$ and $u_{i,l}^{s}$ are the degrees-of-

freedom of enrichment level l at node i in the fluid and solid phase, respectively, and H denotes the Heaviside function, which turns the interpolation for phase m on and off, and is defined as:

$$H(\zeta) = \begin{cases} 1, & \zeta < 0 \\ 0, & \zeta > 0. \end{cases} \tag{3.93}$$

The Kronecker delta, $\delta_{ab}^{i,m}$, selects the degrees-of-freedom for phase m. The indices k and n denote the active degree-of-freedom at node i in the fluid and solid phases, respectively. Ensuring the partition of unity is satisfied, only one degree-of-freedom per node is used to interpolate the solution at any given point. For problems where the solid phase is void, the respective degrees-of-freedom are set to zero and condensed out of the problem.

For each phase, multiple enrichment levels may be necessary to interpolate the state variables in multiple, physically disconnected regions of the same phase, cf. [85], [86], and [84]. In order to accurately integrate the weak form of the governing equations by Gaussian quadrature, intersected elements are decomposed into triangles in 2D or into tetrahedrons in 3D using Delaunay triangulation. The reader is referred to Makhija and Maute [84] for more details on the particular XFEM implementation used in this paper.

The Heaviside-step enrichment formulation (3.92) has a singularity for cases in which the fluid-solid interface lies exactly on a node, i.e. the level set value ϕ_i at node i equals 0. To avoid this issue, we adopt the perturbation approach outlined in [87] and [63]. If the magnitude of the level set value at a node is smaller than some critical value, ϕ_c, it is modified to a shifted value, ϕ_s. This perturbation results in the fluid-solid interface moving away from the node, solving the singularity issue. In this study, we adopt the values of $\phi_c = \phi_s = 10^{-6} \times h$, where h is the size of an element. This perturbation strategy was used by Sharma et al. [88], who shows that the influence of the perturbation is negligible.

3.8 Analytical Implementation of Unit Vector Gradients

In this section, we will describe how an analytical $\boldsymbol{J}_n$ is obtained for use in (3.73). Consider the definition of the normal vector in terms of the level set field,

$$\boldsymbol{n} = \frac{\boldsymbol{\nabla}\phi}{|\boldsymbol{\nabla}\phi|}, \tag{3.94}$$

or, in indicial notation,

$$n_i = \frac{\phi_{x_i}}{\sqrt{\phi_x^2 + \phi_y^2 + \phi_z^2}}, \tag{3.95}$$

where the subscript notation denotes differentiation, i.e. $\phi_{x_i} = \frac{\partial \phi}{\partial x_i}$. Thus $\boldsymbol{J}_n$ is written as:

$$(\boldsymbol{J}_n)_{ij} = \frac{\partial n_i}{\partial x_j} \tag{3.96}$$

$$= \frac{\phi_{x_i x_j}(\phi_x^2 + \phi_y^2 + \phi_z^2) - \phi_{x_i}(\phi_x \phi_{x x_j} + \phi_y \phi_{y x_j} + \phi_z \phi_{z x_j})}{(\phi_x^2 + \phi_y^2 + \phi_z^2)^{3/2}}, \tag{3.97}$$

where $\phi_{x_i x_j} = \frac{\partial^2 \phi}{\partial x_i \partial x_j}$. This requires second-order derivatives, which are not available with bilinear elements unless an analytical expression for $\phi(\boldsymbol{x})$ is known. For a non-analytical expression for $\boldsymbol{J}_n$, we use (3.96) and use the normal vector degrees-of-freedom, as discussed in Section 3.2.3. This is studied in Sections 3.10.5 and 3.12.

Further, in 2D, $\hat{\boldsymbol{t}} = \hat{\boldsymbol{n}} \times \hat{\boldsymbol{z}}$, thus $t_1 = n_2$ and $t_2 = -n_1$. Finally,

$$\boldsymbol{J}_t = \begin{pmatrix} \frac{\partial t_1}{\partial x} & \frac{\partial t_1}{\partial y} \\ \frac{\partial t_2}{\partial x} & \frac{\partial t_2}{\partial y} \end{pmatrix} = \begin{pmatrix} +\frac{\partial n_2}{\partial x} & +\frac{\partial n_2}{\partial y} \\ -\frac{\partial n_1}{\partial x} & -\frac{\partial n_1}{\partial y} \end{pmatrix}. \tag{3.98}$$

3.9 Numerical Examples

In the following, we study the characteristics of the proposed Kn-slip boundary condition for steady-state flow problems in 2D. We first validate the implementation of the Kn-slip boundary condition for planar geometries with analytical solution. In planar flows, the $\boldsymbol{J}_{\{n,t\}}$ terms vanish. Further, we study the influence of the ghost-penalty method proposed in [10] in comparison to the geometric preconditioner of [63]. We then validate the implementation of the $\boldsymbol{J}_{\{n,t\}}$ terms in a problem with non-planar geometry and an analytical solution. Further, we study the importance

of the $\boldsymbol{J}_{\{n,t\}}$ terms in a problem with variable curvature. We then discuss the spurious errors that appear in the solution process and study various strategies to mitigate these errors. Finally, we study the influence of the ghost-penalty method and its parameters for more complex geometries. Unless otherwise stated, geometric and material parameters are given in non-dimensional and self-consistent units.

In this work, the time integration is performed by a 1-step backward differentiation scheme. Most steady-state flow problems use a homotopy approach, i.e. a sufficiently small time step is initially chosen to achieve stability and it is then gradually increased until a steady-state solution is achieved. The problems considered in this paper where not found to need this approach; instead, the time step is initially large and the solution is advanced until a steady-state solution is reached.

The equilibrium at any time step (n) is satisfied by solving the nonlinear system $\boldsymbol{R}^{(n)}$ via Newton's Method, where:

$$\boldsymbol{R} = r_{\boldsymbol{u},p} + r_{\hat{\boldsymbol{n}}}, \tag{3.99}$$

or

$$\boldsymbol{R} = r_{\boldsymbol{u},p} + r_{\boldsymbol{u},T} + r_{\hat{\boldsymbol{n}}} \tag{3.100}$$

in examples involving energy transport. The linear problem is solved using the Generalized Minimal RESidual (GMRES) iterative method [89] with an Incomplete LU factorization with dual Threshold (ILUT) preconditioner [90].

3.9.1 Scope

The Knudsen number (1.1) is also given by the Reynolds and Mach numbers via: [91]

$$Kn = \frac{Ma}{Re}\sqrt{\frac{\gamma\pi}{2}}. \tag{3.101}$$

Because the incompressible NS equations, used in this paper, are valid only for $Ma < 0.3$, we will limit the maximum Kn number of interest to allow a larger Re number, which in turn allows for larger inertial effects in the fluid flow problems considered.

3.10 Analytical Solutions for Simple Geometries

In this section, we validate components of our implementation of the Kn-slip boundary condition in problems with an available analytical solution. Further, we study the influence of the ghost-penalty terms when compared to XFEM preconditioner of [63]. Finally, we study the influence of the $\boldsymbol{J}_{\{n,t\}}$ terms in an example with curved surfaces.

All examples considered here use the nondimensionalized NS equations (3.29). As such, the fluid density and viscosity are chosen as $\bar{\rho} = \bar{\mu} = 1$ and the geometry is nondimensionalized with a characteristic length. The inlet pressure boundary condition and the wall velocities in Section 3.10.5 are chosen in nondimensional form.

3.10.1 Planar Poiseuille flow

In this section, we again consider the flow between parallel plates. The problem setup is similar to the one in Fig. 3.3, except that the walls enforce Kn-slip boundary conditions instead of no-slip boundary conditions. The updated problem setup is shown in Fig. 3.9. Because the walls are planar, the $\boldsymbol{J}_{\{n,t\}}$ terms vanish and we can focus on validating the remaining portion of the Kn-slip implementation. The inlet is given a pressure boundary condition such that:

$$\bar{p}_{in} = \frac{\rho h^2}{\mu^2} p_{in} = 10. \tag{3.102}$$

For this problem, the NS equations admit the general solution:

$$u(y) = -\frac{B}{2} y^2 + C_1 y + C_2. \tag{3.103}$$

A symmetry condition at $y = 0$ gives $C_1 = 0$. The Kn-slip boundary condition at the top wall, (3.1), simplifies to:

$$u\Big|_{y=h/2} + \frac{Kn}{1+Kn} \frac{du}{dy}\Big|_{y=h/2} = 0. \tag{3.104}$$

This in turn gives the analytical solution:

$$u(y) = \frac{1}{2\mu} \frac{p_{in}}{L} \left(1 - 4\left(\frac{y}{h}\right)^2 + h\frac{Kn}{1+Kn}\right). \tag{3.105}$$

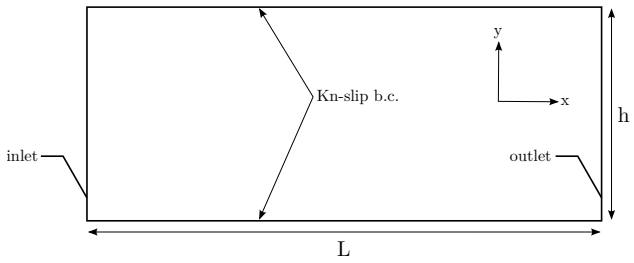

Figure 3.9: Problem description for the flow past a cylinder with Kn-slip boundary conditions.

Additionally, the mass flow rate through half the domain is given as:

$$\dot{m} = \int_0^{h/2} \rho u(y) dy = \frac{h^3}{24} \frac{\rho}{\mu} \frac{p_{in}}{L} \left(1 + \frac{6}{h} \frac{Kn}{1 + Kn} \right). \tag{3.106}$$

A square domain is chosen, i.e. $L = h$, and because we consider the nondimensional NS equations, $h = 1$. We consider the domain $\Omega = \{(x, y),\ 0 \leq x \leq 1,\ 0 \leq y \leq 0.6\}$, and discretize it with a uniform mesh with $N_e \times \frac{5}{3} N_e$ square elements. The fluid domain and interface are defined with the LSF:

$$\phi = |2y| - 1. \tag{3.107}$$

Fig. 3.10a show the x-component velocities through the line $x = 0.5$ with several levels of refinement for $Kn = 0.01$. Fig. 3.10b is a close-up view. Note the pronounced agreement between the obtained solutions and the analytical solution, particular for the coarser levels of refinement. This agreement is not perfect, as the XFEM does not perfectly discretize the channel [9]. Fig. 3.10c shows the convergence of the mass flow for the same levels of refinement; note, in particular, the scale of the vertical axes.

Finally, Fig. 3.10d shows the convergence of the L^2 error against the analytical solution. The rate is approximated with a linear curve-fit through the log-log data. Fig. 3.11 and 3.12 show the same information for $Kn = 0.02$ and 0.05, respectively. We observe a larger deviation from the analytical solution, for a given level of refinement, as the Kn number increases. Further, the L^2 convergence rate decreases as the Kn number increases, indicating a potential interaction between the ghost-penalization and the Kn numbers. Fig. 3.13 aggregates the velocity distribution and

L^2 error for the Kn numbers considered in this study. We will further study the effect of the ghost-penalty formulation in Sections 3.13.2, 3.13.3, and 3.14.

3.10.2 Planar Poiseuille flow using the XFEM preconditioner

In the previous section, we showed that the L^2 convergence rate decreased as the Kn increased. In this example, we consider same flow between parallel plates but use the XFEM preconditioner of [63]. Recall from Section 3.5, that the ghost-penalty method is an alternative to the XFEM preconditioner, which simply scales the linear system with the area of influence of each node. We repeat the procedure of the previous section, for the same levels of refinement and Kn numbers.

Fig. 3.14, 3.15, and 3.16 show the velocity distribution, mass flow rate, and L^2 error for $Kn = 0.01$, 0.02, and 0.05, respectively. Note that the agreement of the velocity distributions with their respectively analytical solutions remains favorable for coarse meshes, but that convergence comes from above rather than below. This suggests that the XFEM preconditioner tends to over-approximate velocities, while the ghost-penalty method has a diffusive effect. This is consistent in the convergence of the mass flow rate. Finally, note that the L^2 convergence rate is the same for all Kn numbers, though considerably lower than with ghost-penalization.

For a more direct comparison, we overlay the convergence of the L^2 errors using ghost-penalization and the XFEM preconditioner in Fig. 3.17. This study shows the superior convergence rates of the ghost-penalty methods, though its interaction with the Kn numbers remains unstudied.

3.10.3 Couette Flow: Flow Between Moving Plates Flow

Consider the same problem as in the previous section, except that the flow is driven by moving plates rather than a pressure gradient. The problem setup is shown in Fig. 3.18. The plates move in opposite horizontal directions with speeds $u^w = \pm U/2$, where U is set such that:

$$\frac{\rho h}{\mu} U = 5.0 \tag{3.108}$$

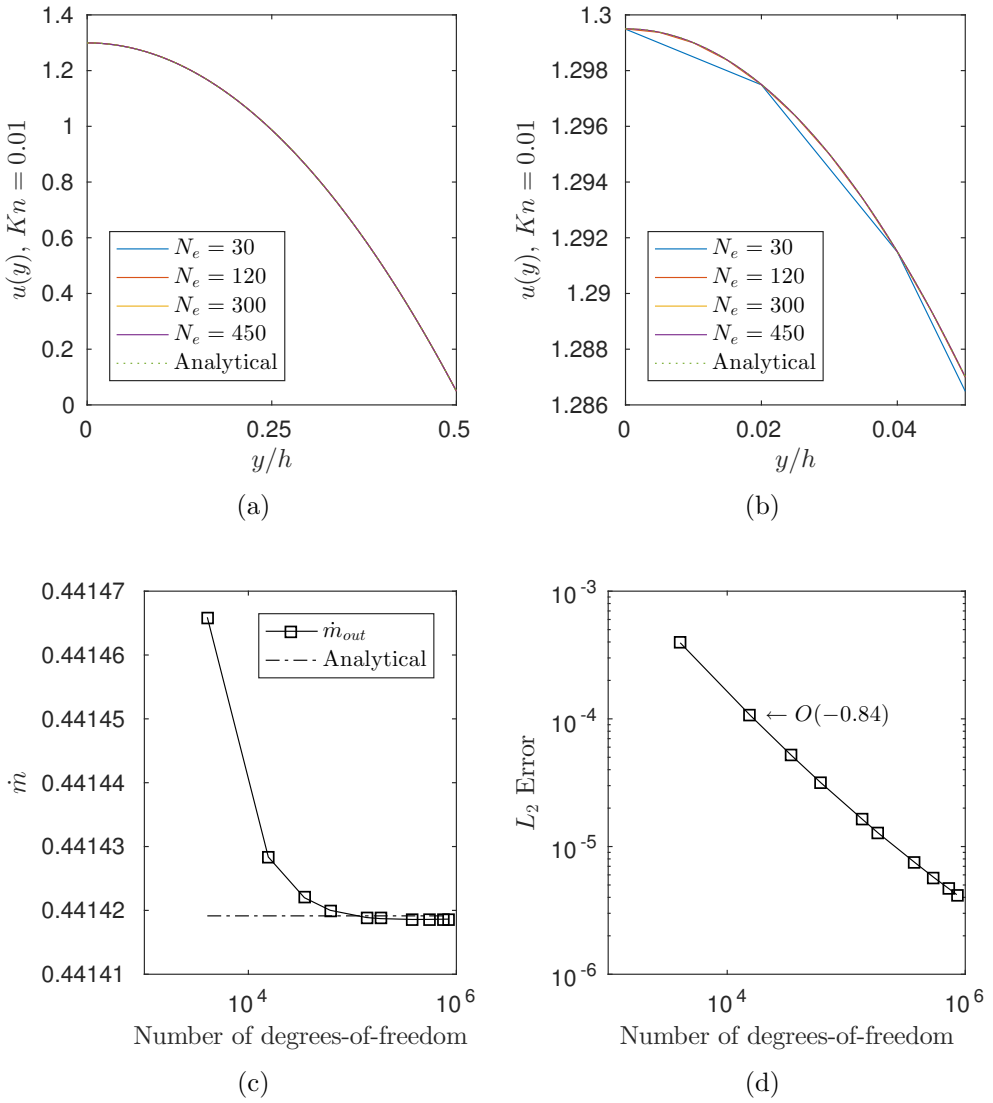

Figure 3.10: Velocity distribution (a) and close-up (b), mass flow rate (c), and L^2 error (d) for $Kn = 0.01$ and several levels of refinement.

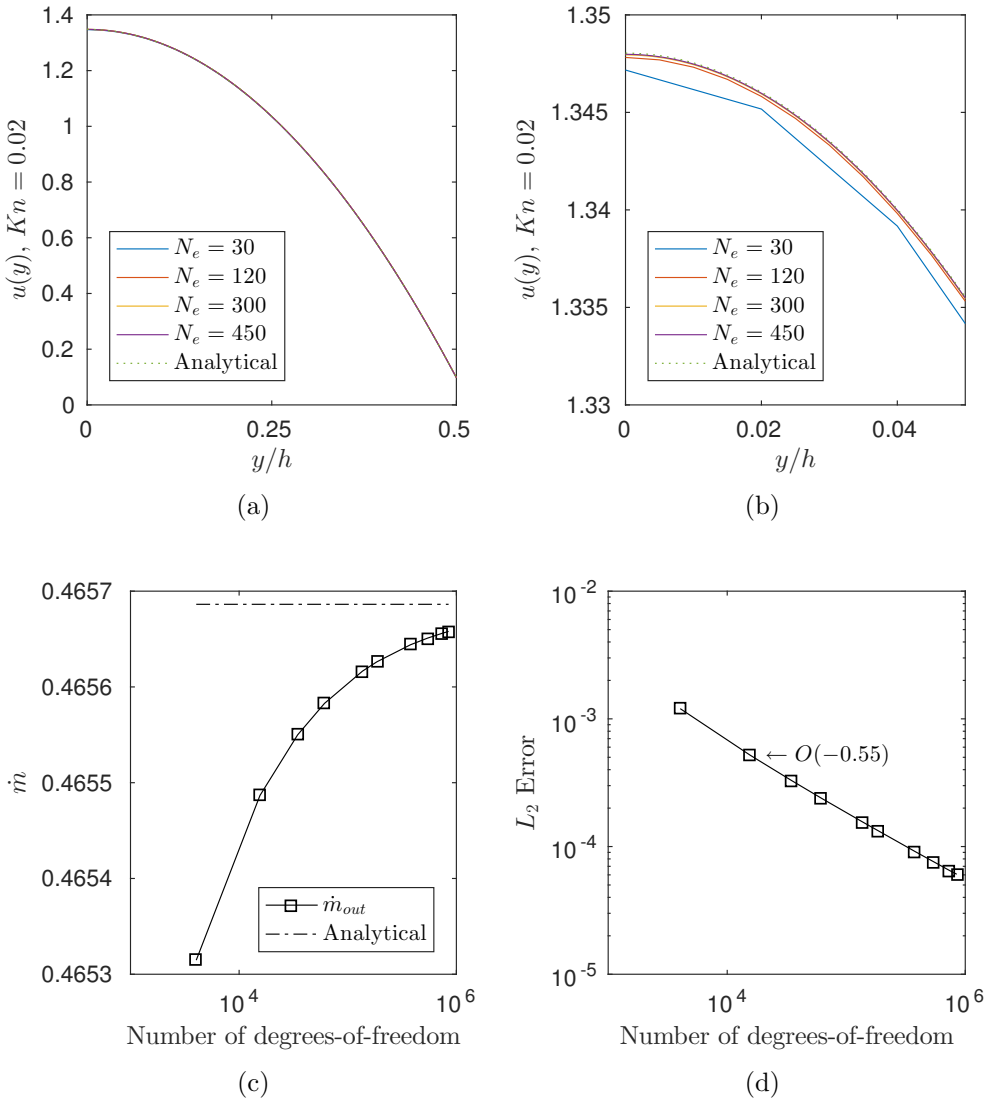

Figure 3.11: Velocity distribution (a) and close-up (b), mass flow rate (c), and L^2 error (d) for $Kn = 0.02$ and several levels of refinement.

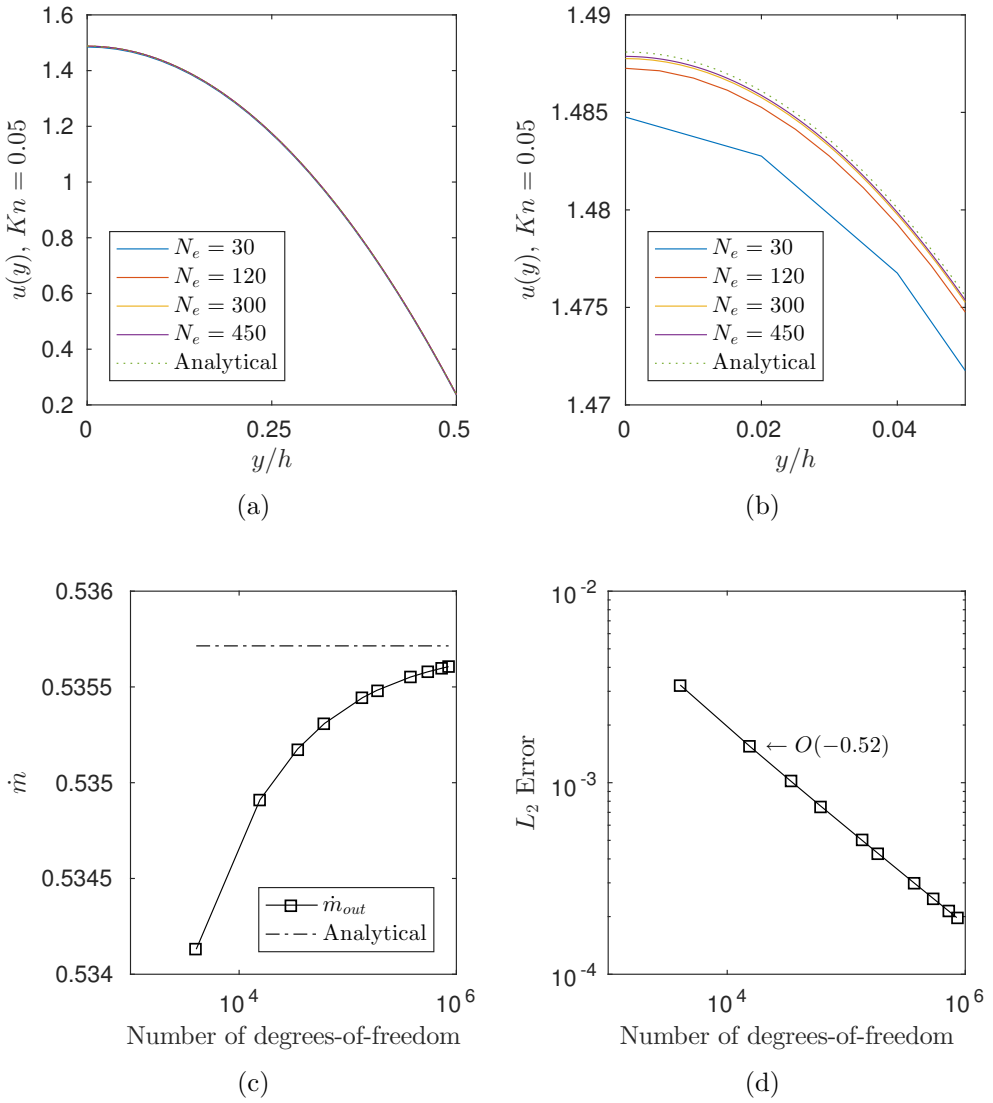

Figure 3.12: Velocity distribution (a) and close-up (b), mass flow rate (c), and L^2 error (d) for $Kn = 0.05$ and several levels of refinement.

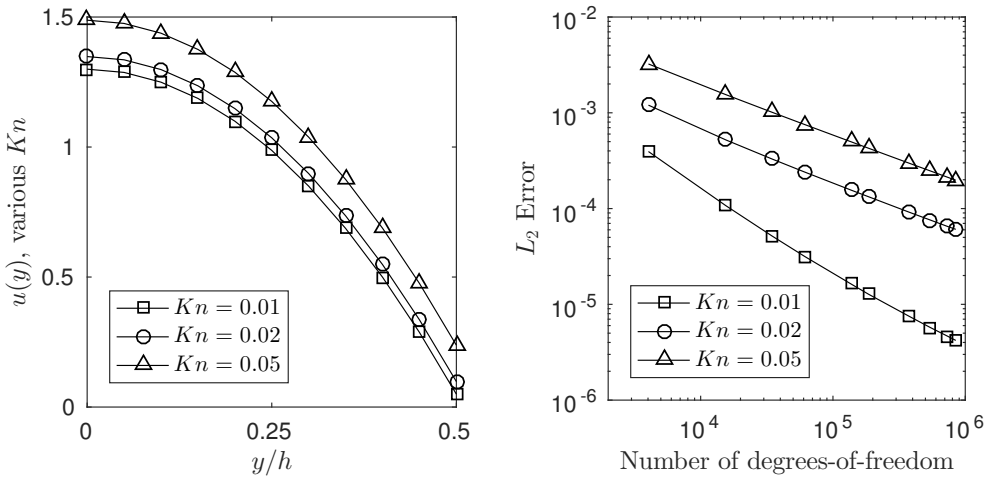

(a) (b)

Figure 3.13: Velocity distribution (a) and L^2 error (b) for several Kn numbers and several levels of refinement.

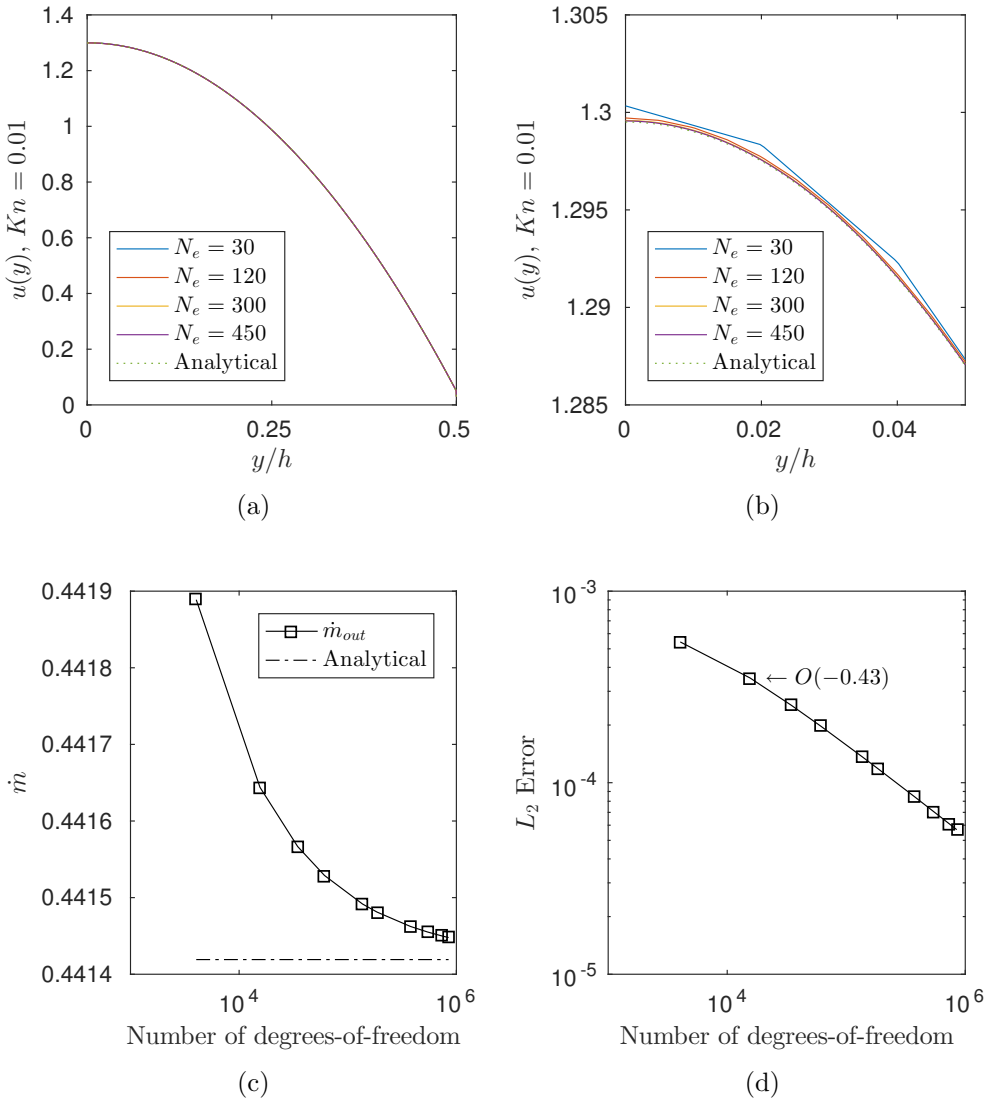

Figure 3.14: Velocity distribution (a) and close-up (b), mass flow rate (c), and L^2 error (d) for $Kn = 0.01$ and several levels of refinement using the XFEM preconditioner.

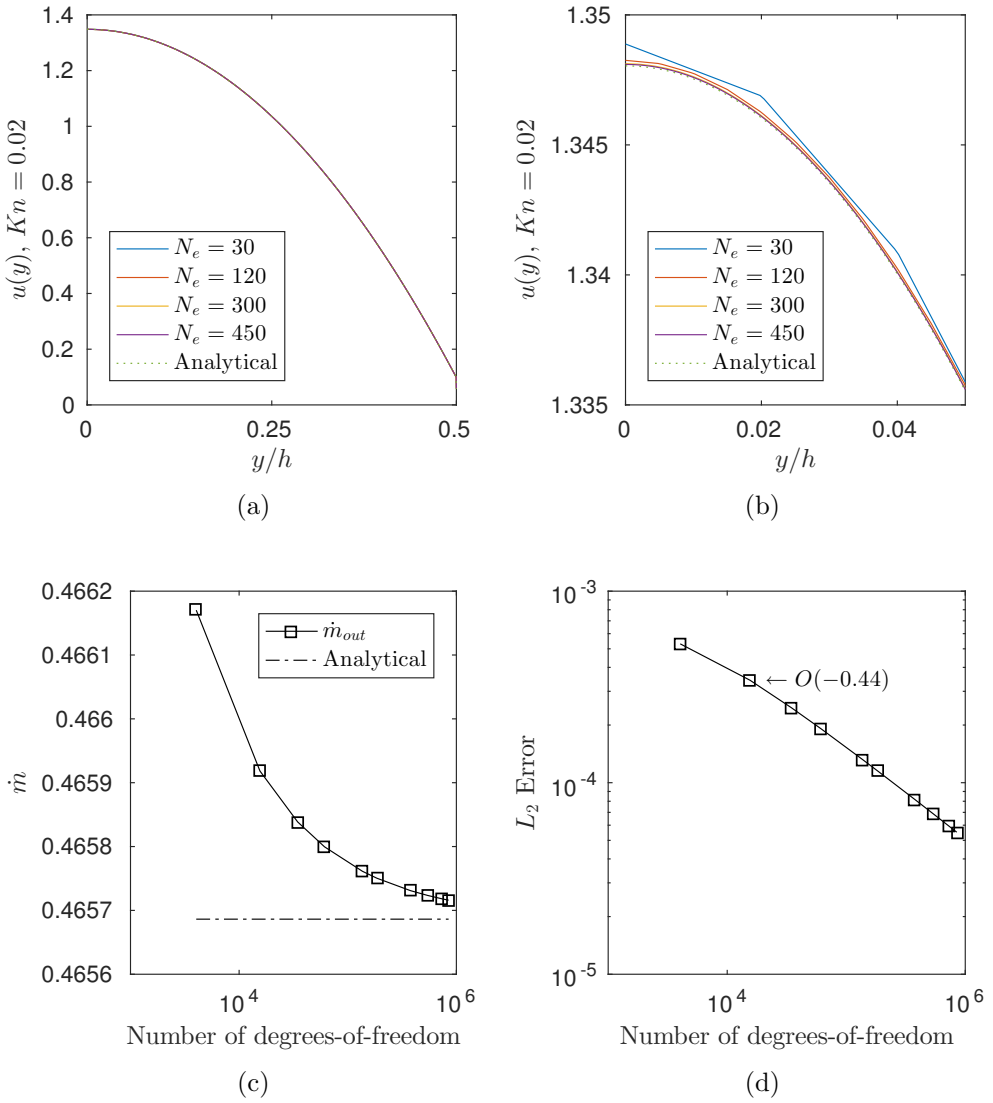

Figure 3.15: Velocity distribution (a) and close-up (b), mass flow rate (c), and L^2 error (d) for $Kn = 0.02$ and several levels of refinement using the XFEM preconditioner.

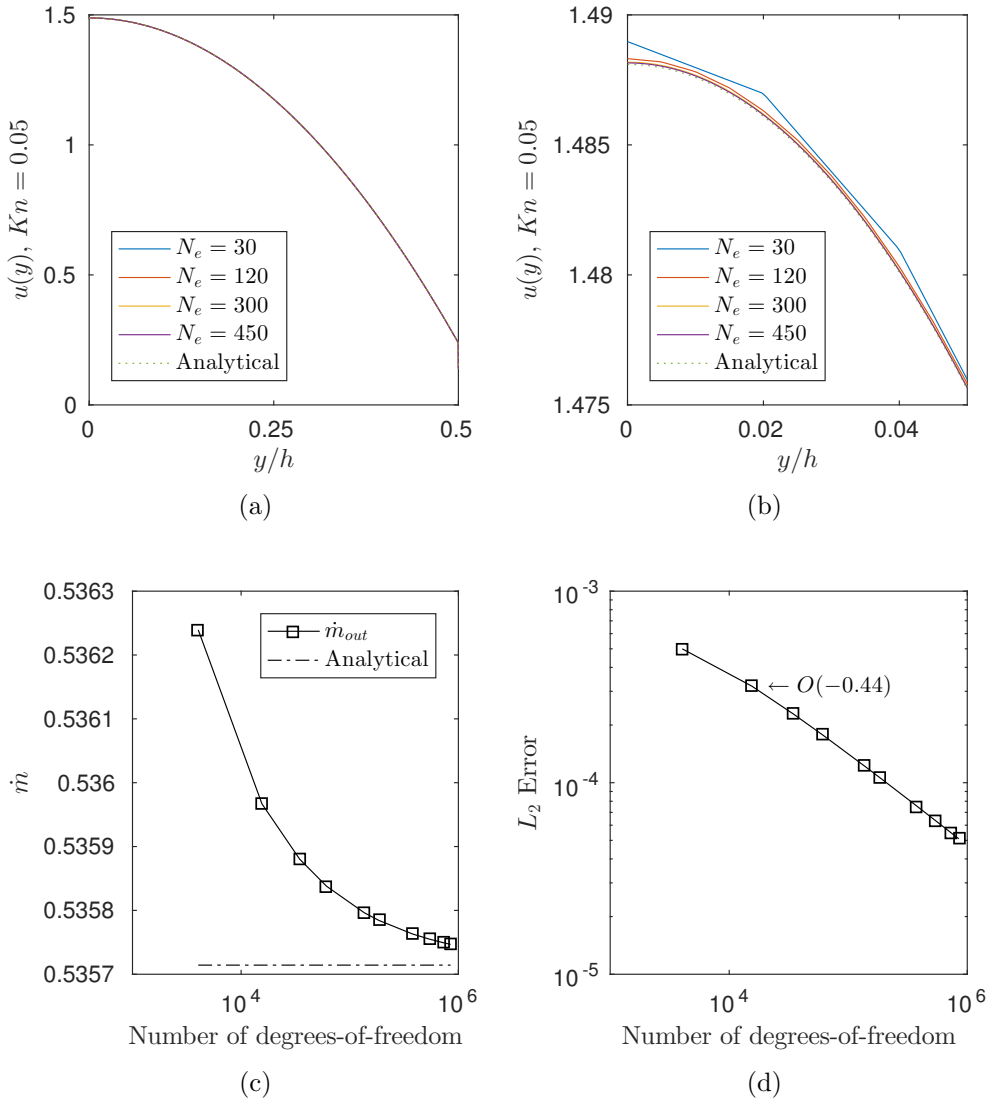

Figure 3.16: Velocity distribution (a) and close-up (b), mass flow rate (c), and L^2 error (d) for $Kn = 0.05$ and several levels of refinement using the XFEM preconditioner.

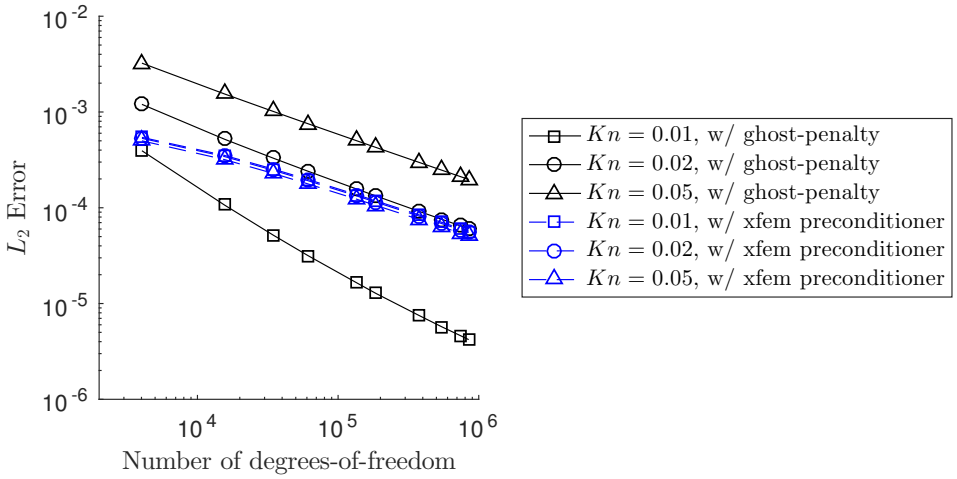

Figure 3.17: Convergence of L^2 error using ghost-penalization and the XFEM preconditioner for various Kn numbers and several levels of refinement.

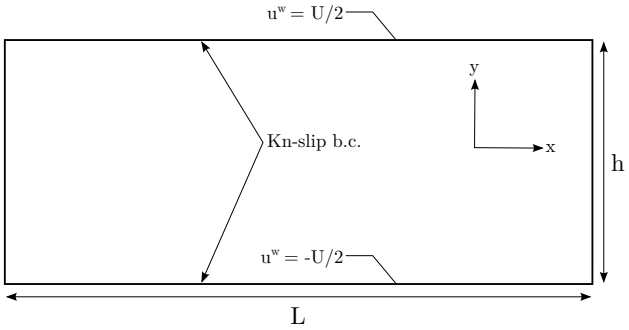

Figure 3.18: Problem description for the flow between moving plates with Kn-slip boundary conditions.

For this problem, the NS equations admit a general solution:

$$u(y) = C_1 y + C_2 \tag{3.109}$$

A symmetry condition at $y = 0$ gives $C_2 = 0$. The Kn-slip boundary condition at the top wall, (3.1), simplifies to:

$$u - u^w + C\frac{du}{dy} = 0, \tag{3.110}$$

which gives the final solution:

$$u(y) = U\frac{1 + Kn}{1 + 3Kn}y \tag{3.111}$$

Additionally, the mass flow rate through the half-domain is found as:

$$\dot{m} = \int_0^{h/2} u(y)dy = \frac{Uh^2}{8}\frac{1 + Kn}{h + (h + 2)Kn} \tag{3.112}$$

Naturally, the net mass flow rate between the plates is $\dot{m}_{net} = 0$.

We discretize the problem with the same domain and LSF as in the previous section and consider the same levels of refinement. In addition to finding the convergence behavior for this problem, we will additionally investigate the effect of ghost-penalization against the use of the XFEM preconditioner, as with the previous problem.

Fig. 3.19a shows the x-component nondimensional velocity distribution for $Kn = 0.01$. Fig. 3.19b shows a close-up. We observe good agreement with the analytical solution, except for the coarsest level of refinement. Fig. 3.19c shows the convergence of the mass flow with the same levels

of refinement; note the same. Fig. 3.19d shows the convergence of L^2 error, where the analytical solution is used as a reference solution. The shown convergence rate is approximate from a linear curve-fit through the log-log data. Fig. 3.20 and 3.21 show the same information for $Kn = 0.02$ and 0.05, respectively. The L^2 convergence rate is nearly identical for all Kn numbers, in direct contrast with the pressure-driven flow problem.

We summarize these results in Fig. 3.22, which shows the velocity distribution and L^2 error for several Kn numbers. As the Kn numbers increases, the fluid slips further from the wall velocity. We further observe nearly identical L^2 errors for all Kn numbers.

3.10.4 Couette flow using the XFEM preconditioner

We again consider using the XFEM preconditioner instead of ghost-penalization, as with the pressure-driven problem. Fig. 3.23, 3.24, 3.25 show the x-component nondimensional velocity between the moving plates and the convergence of the mass flow rate and L^2 error against the analytical solution using the XFEM preconditioner, for $Kn = 0.01$, 0.02, and 0.05, respectively. We observe that the use of the XFEM preconditioner does not change the convergence rate of the L^2 error. Because these results are nearly identical to those using ghost-penalization, we do not aggregate the results for all Kn numbers considered nor overlay them with the results using ghost-penalization.

3.10.5 Radial Couette Flow: Flow Between Rotating Cylinders

Having validated the implementation of the Kn-slip boundary condition and studied its effect with ghost-penalization and the XFEM preconditioner, we now seek to validate the implementation of the $\boldsymbol{J}_{\{n,t\}}$ terms. To this end, we consider the flow between concentric rotating cylinders. The inner and outer cylinders have radii, r_1 and r_2, and rotate with angular velocities, ω_1 and ω_2, respectively. The problem setup is shown in Fig. 3.26.

This problem is extensively discussed in the manuscript found in Appendix C. Here, we will summarize the relevant observations as follow: (i) the Kn-slip boundary conditions becomes

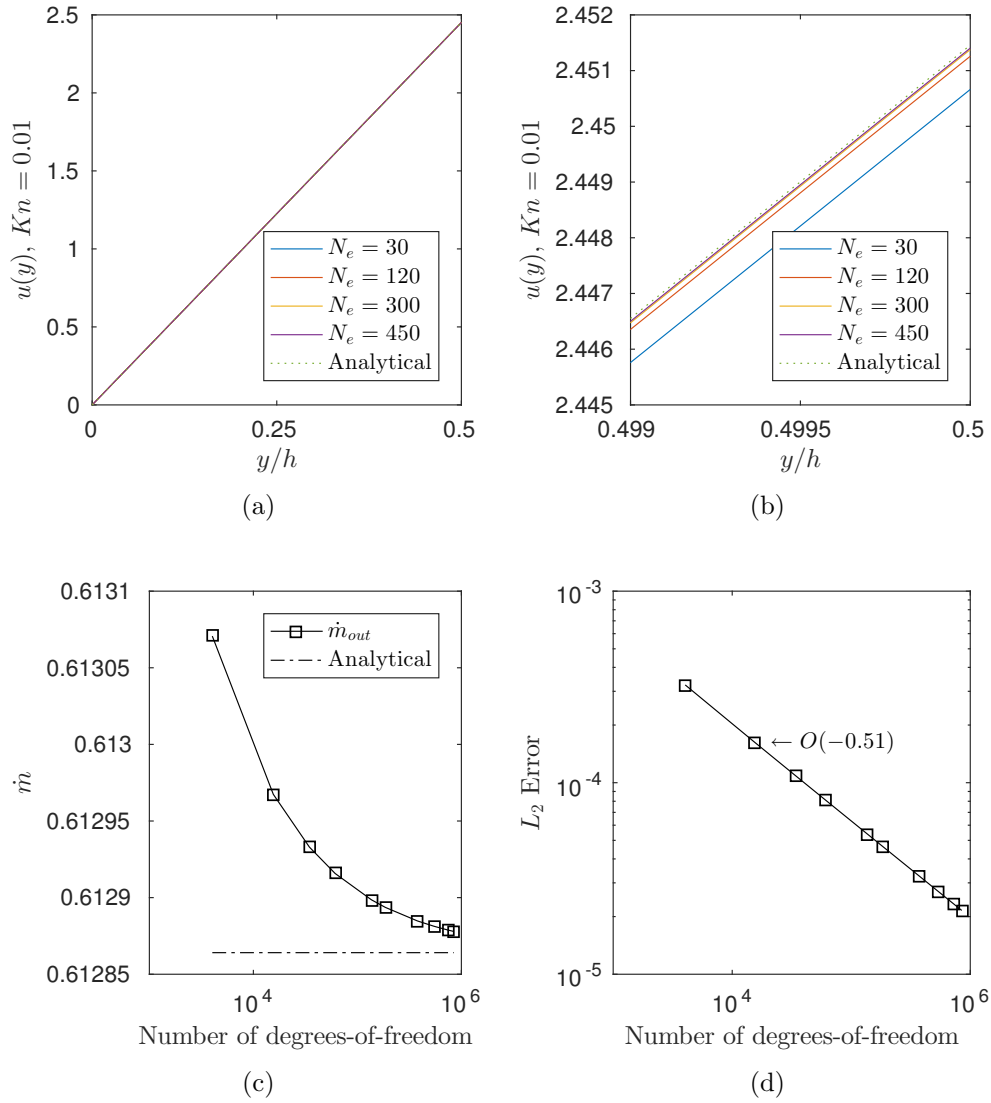

Figure 3.19: Velocity distribution (a) and close-up (b), mass flow rate (c), and L^2 error (d) for $Kn = 0.01$ and several levels of refinement.

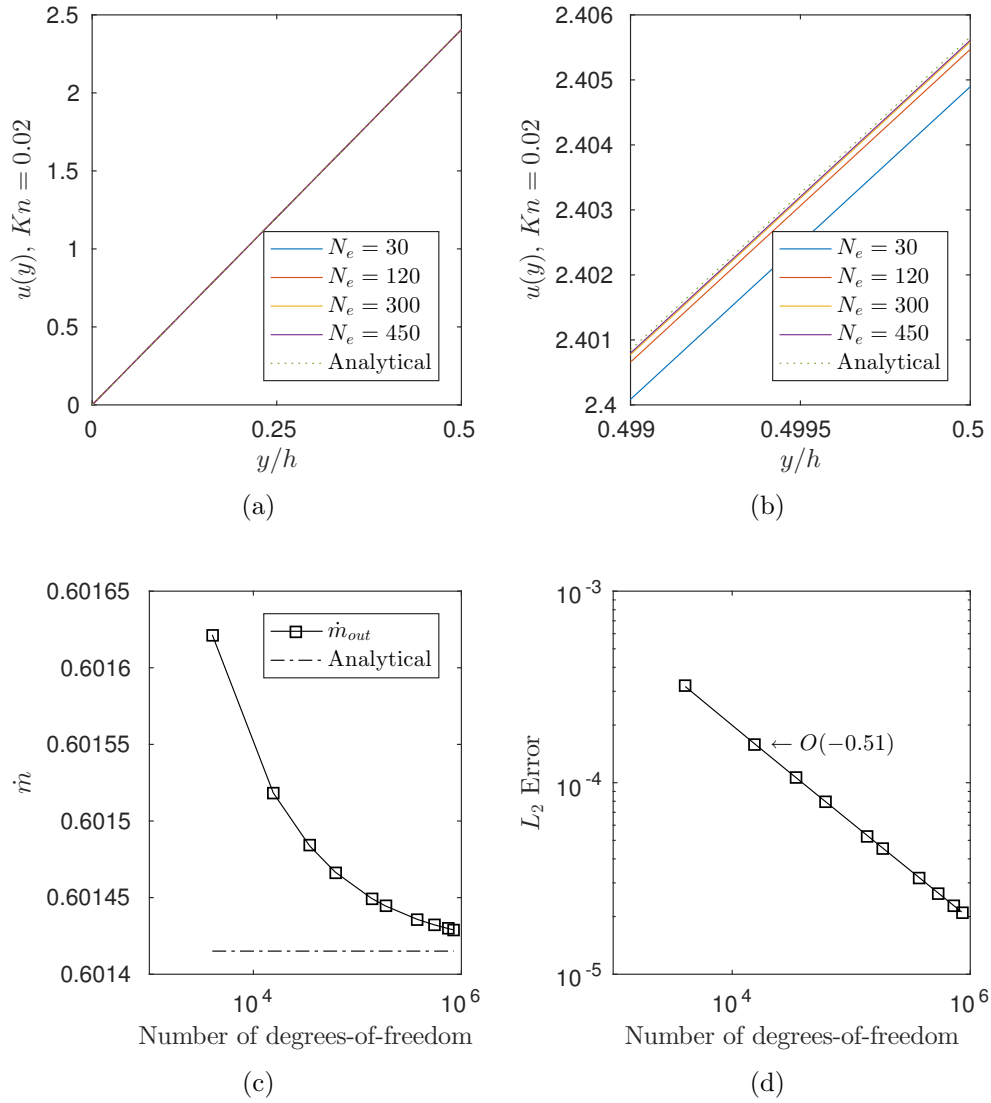

Figure 3.20: Velocity distribution (a) and close-up (b), mass flow rate (c), and L^2 error (d) for $Kn = 0.02$ and several levels of refinement.

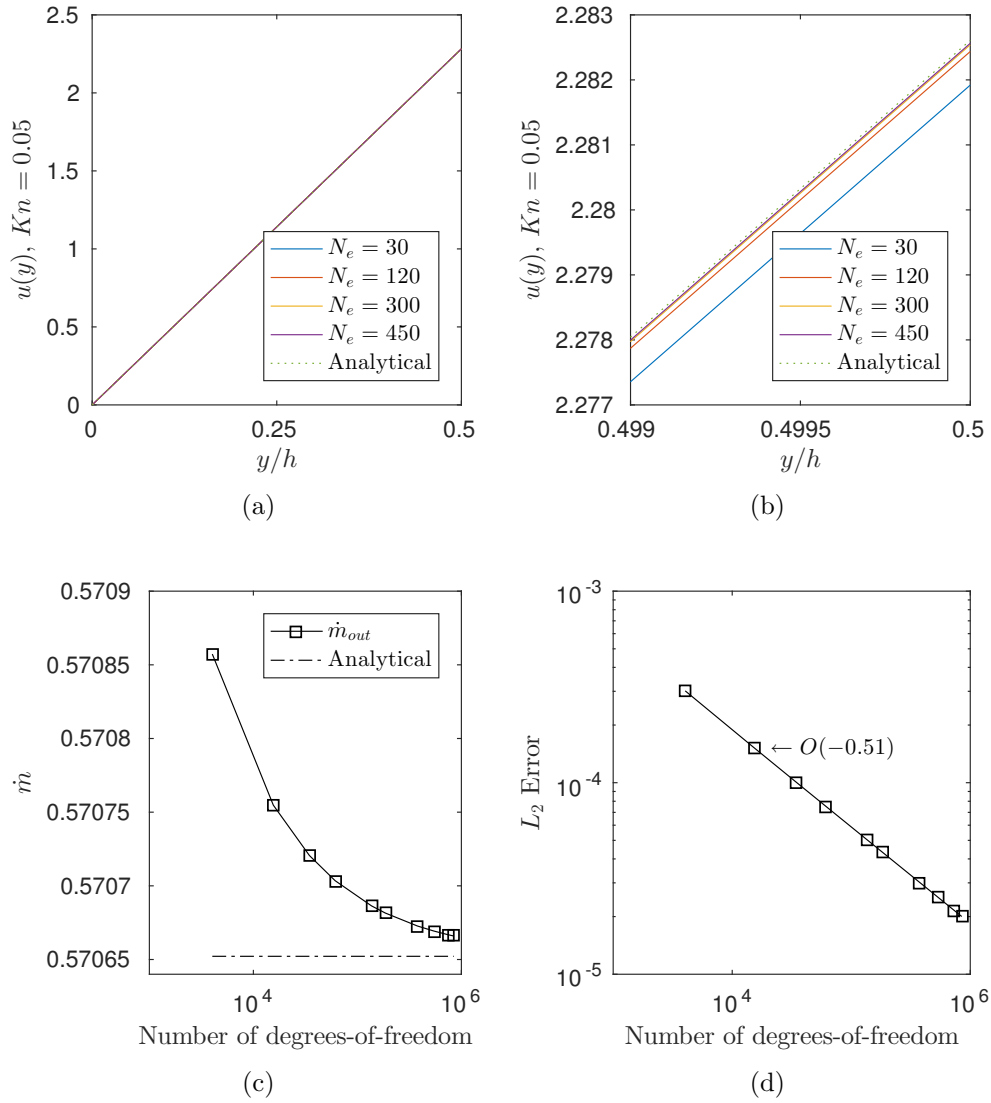

Figure 3.21: Velocity distribution (a) and close-up (b), mass flow rate (c), and L^2 error (d) for $Kn = 0.05$ and several levels of refinement.

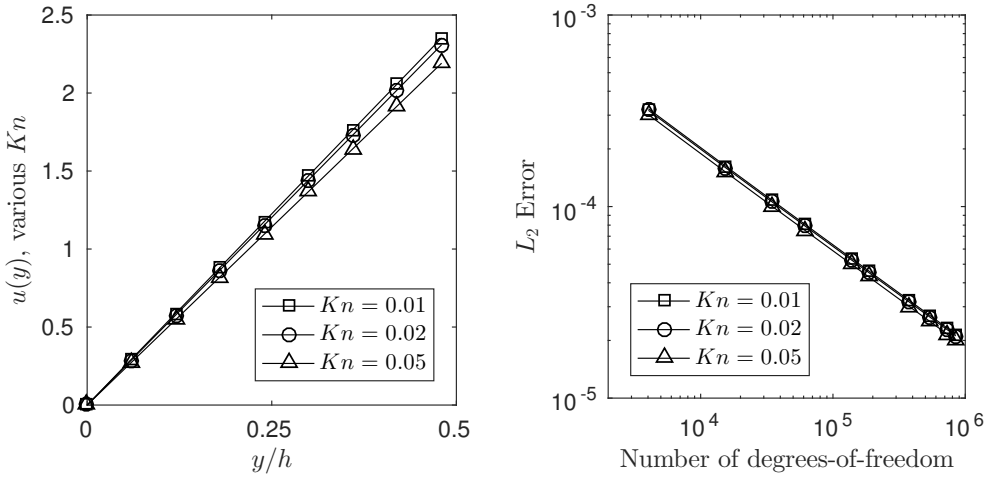

Figure 3.22: Velocity distribution (a) and L^2 error (b) for several Kn numbers and several levels of refinement.

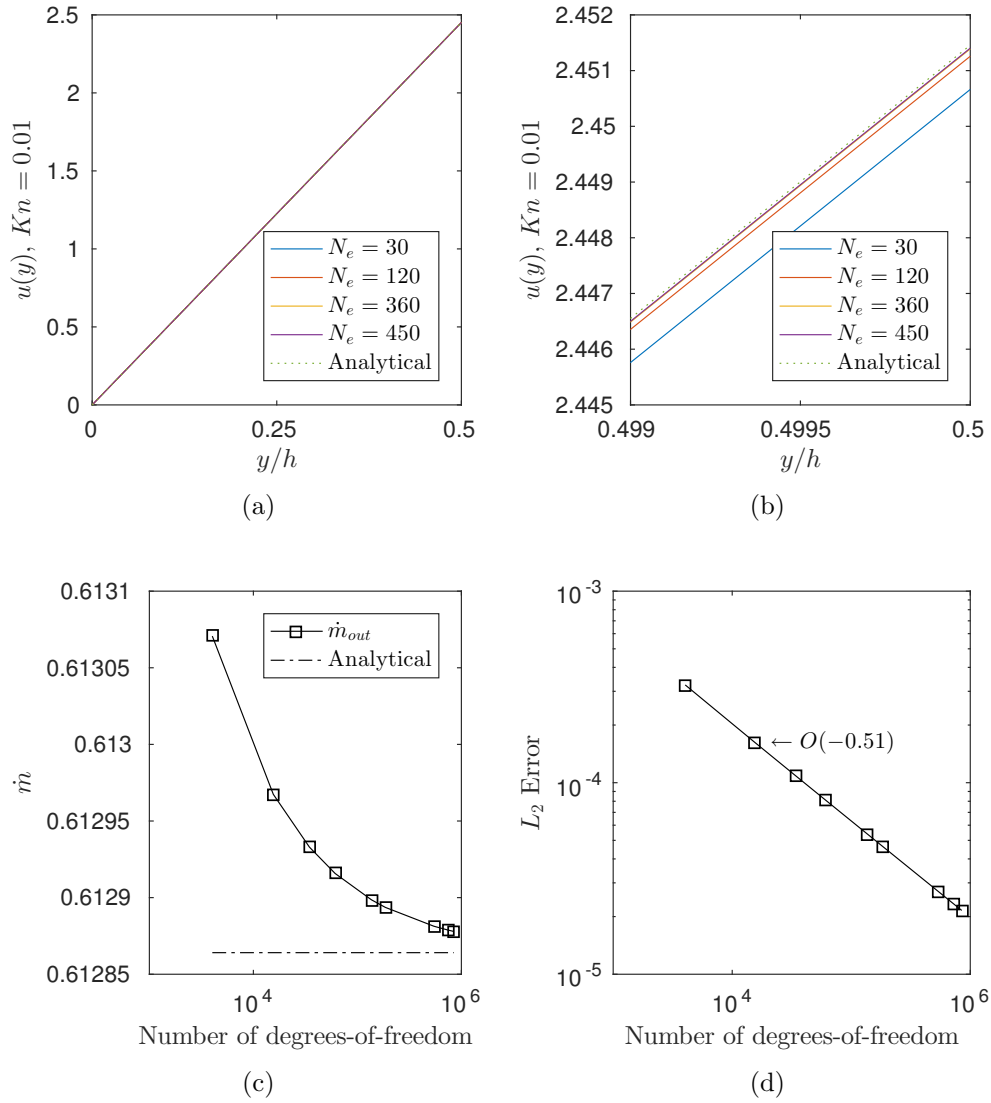

Figure 3.23: Velocity distribution (a) and close-up (b), mass flow rate (c), and L^2 error (d) for $Kn = 0.01$ using the XFEM preconditioner and several levels of refinement.

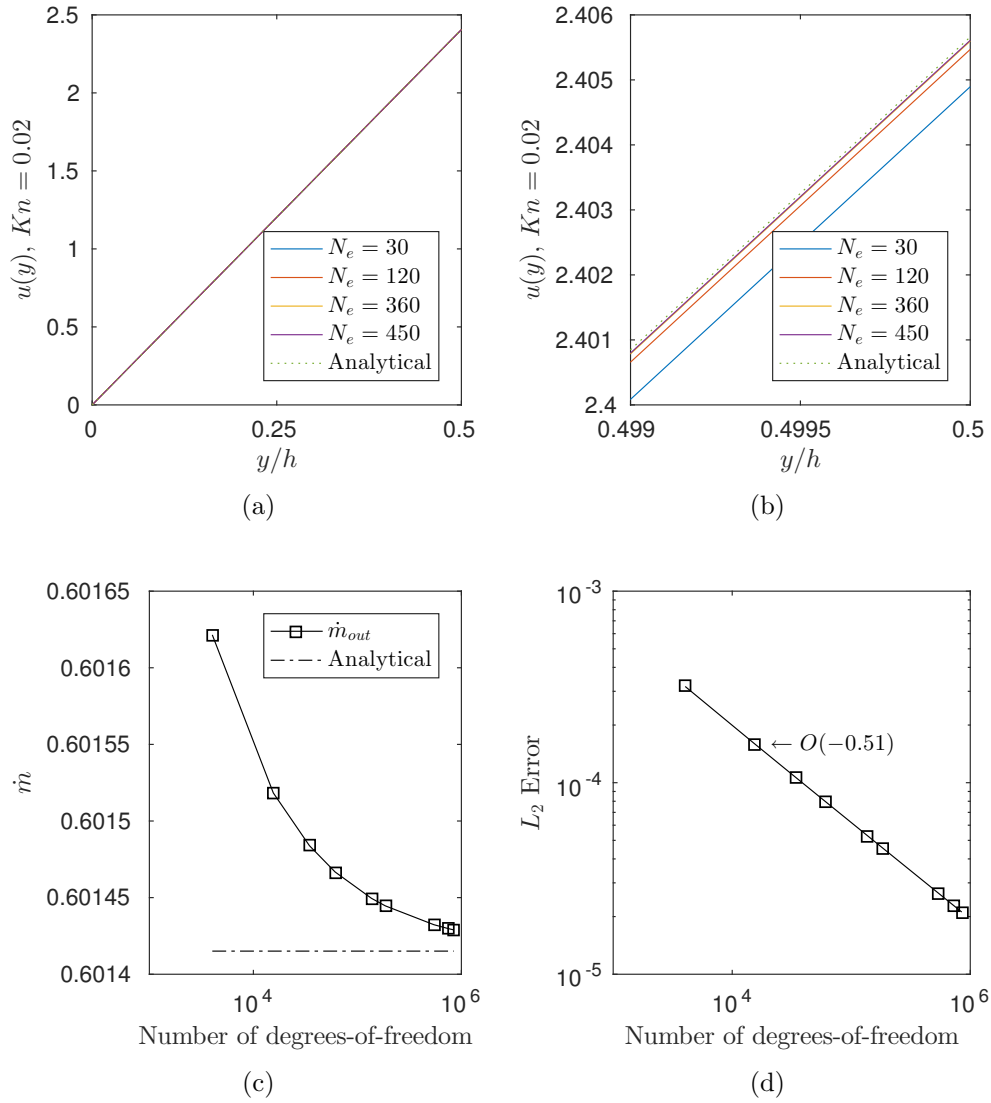

Figure 3.24: Velocity distribution (a) and close-up (b), mass flow rate (c), and L^2 error (d) for $Kn = 0.02$ using the XFEM preconditioner and several levels of refinement.

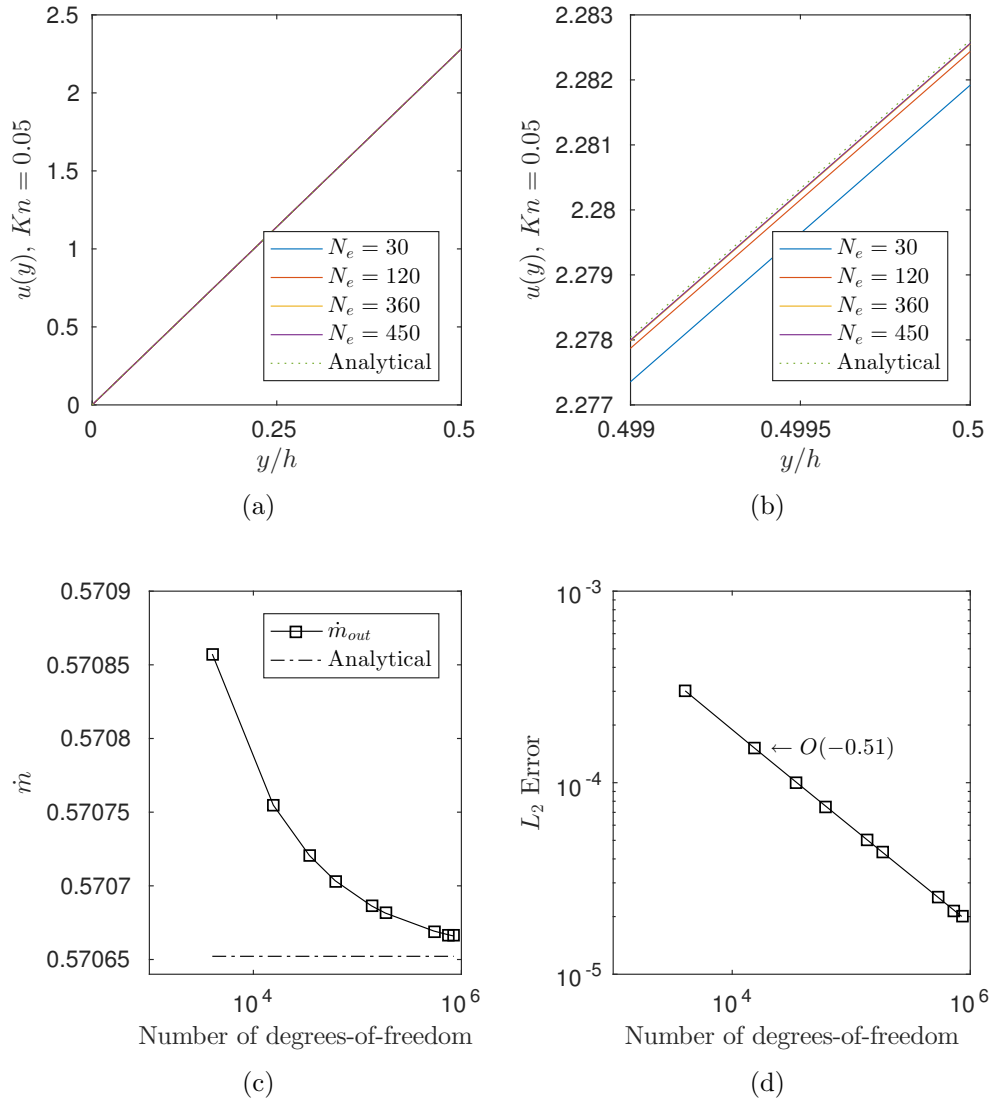

Figure 3.25: Velocity distribution (a) and close-up (b), mass flow rate (c), and L^2 error (d) for $Kn = 0.05$ using the XFEM preconditioner and several levels of refinement.

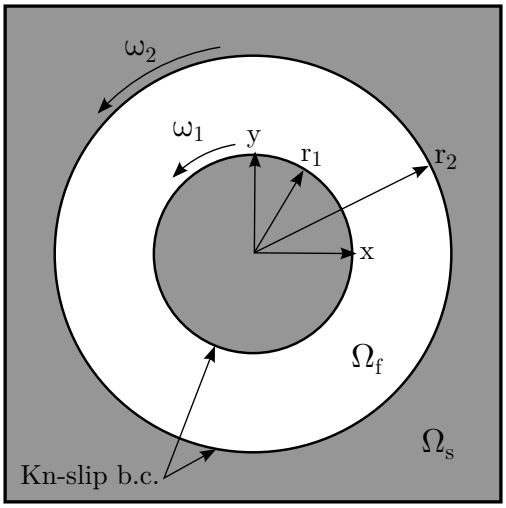

Figure 3.26: Problem description for the flow between concentric rotating cylinders with Kn-slip boundary conditions.

important around $Kn = 10^{-3}$, (ii) the $\boldsymbol{J}_{\{n,t\}}$ terms are necessary to fully recover the analytical solution, but (iii) the error in omitting these terms is smaller for small Kn numbers, and (iv) our inclusion of the weak enforcement of the normal vector definition (3.24) is validated against the available analytical solution.

3.10.6 Concluding Remarks

In this study, we considered two planar 2D problems, along with a non-planar problem, with analytical solutions. Our implementation of the Kn-slip boundary condition, including the $\boldsymbol{J}_{\{n,t\}}$ terms, is thus validated. In the plate-driven problem, we observe the similar convergence behavior of the ghost-penalty method to the use of the XFEM preconditioner. Our study of the pressure-driven problem, however, suggests that that the ghost-penalty method behaves differently in pressure-driven flows. The convergence rate of the L^2 error improves when using the ghost-penalty method, particularly for $Kn = 0.01$. However, the improved convergence rate lessens as the Kn number increases. Further, ghost-penalization appears to have a diffusive effect, causing slightly larger L^2 errors for coarser meshes. We further discuss the ghost-penalty method in Sections 3.13.2, 3.13.3, and 3.14.

3.11 Choice of normal vector definition

In this section, we will study the flow past a single cylinder and discuss two options for computing the normal vector at an integration point. The normal vector at an intersected element can be determined in two ways: using the geometry of the intersection or using the level set function. In the former, the intersection facet is treated as a plane (in 2D, a line) and its perpendicular outward-facing normal vector is found; this normal vector is thus constant through the interface but discontinuous between adjacent elements. This discontinuity may lead to the accidental omission of jump terms in the surface integral. In the latter, the normal vector is calculated from the level set field, (3.94), using the nodal LSF values; this normal vector is thus not guaranteed to be perpendicular to the interface, which may lead to inaccurate enforcement of the no-penetration

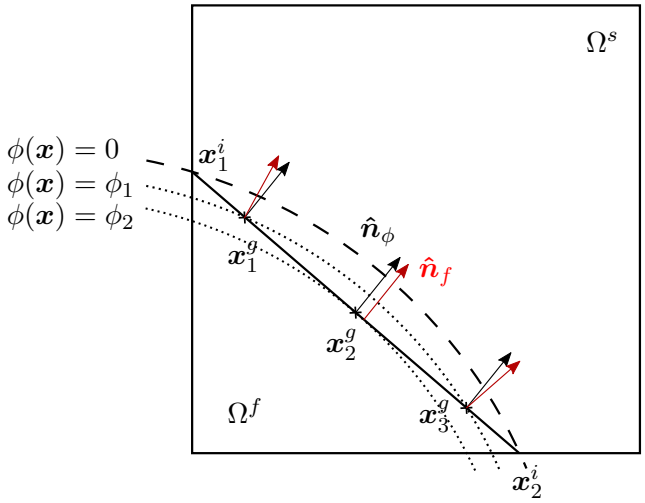

Figure 3.27: Example element with various normal vector definitions.

boundary condition.

We illustrate this choice for the normal vector in Fig. 3.27, shows an example of an intersected element. The points where the zero isosurface of the LSF intersects the edges of the elements are denoted $\boldsymbol{x}_1^i$ and $\boldsymbol{x}_2^i$. The solid straight line connecting these intersection points denotes the approximation of the fluid-solid interface by the XFEM that separate the fluid and solid domains, Ω^f and Ω^s, respectively. This line approximate the zero isosurface of the LSF, $\phi(\boldsymbol{x})$, denoted with a dashed line. The integration points are denoted as $\boldsymbol{x}_1^g$, $\boldsymbol{x}_2^g$, and $\boldsymbol{x}_3^g$. Dotted lines denote respective isosurfaces of the LSF at the integration points; in this example, two integration points share an isosurface but, in general, each integration point has its own isosurface. Finally, we denote the two options for the normal vector discussed in this section: $\hat{\boldsymbol{n}}_f$ denotes the normal which is constant through this element and always perpendicular to the fluid-solid interface, while $\hat{\boldsymbol{n}}_\phi$ denotes the normal vector computed via (3.94). In this example, $\hat{\boldsymbol{n}}_f$ and $\hat{\boldsymbol{n}}\phi$ are the same at $\boldsymbol{x}_2^g$, so $\hat{\boldsymbol{n}}_f$ is purposely displaced. We expect that the disadvantage of each option will vanish with mesh refinement, since both choices approach the true normal vector of the approximated shape.

In this example, the problem setup is similar to the one in Fig. 3.5, except that the cylinder is placed in the center, i.e. vertically as well as horizontally, of the channel and its radius is one

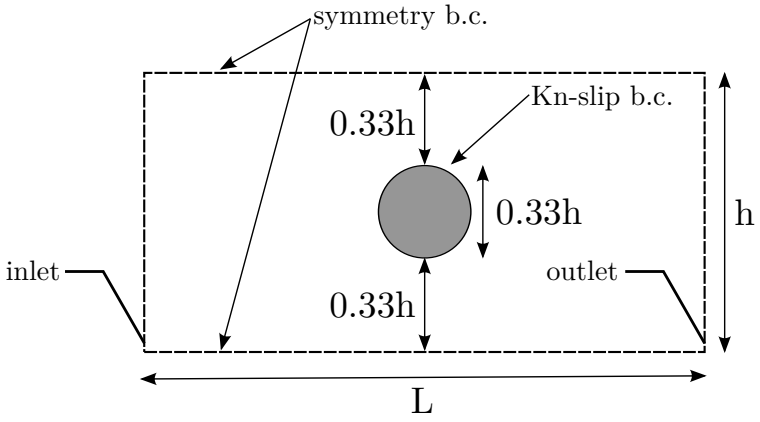

Figure 3.28: Problem description for the slow flow past a cylinder with Kn-slip boundary conditions.

quarter of the channel height. Thus, the LSF becomes:

$$\phi = r - \sqrt{\left(\frac{x_1 - h}{a}\right)^2 + \left(\frac{x_2 - k}{b}\right)^2}, \tag{3.113}$$

with $(h, k) = (0, 0)$, $r = 0.25$, and $a = b = 1$. Additionally, the channel walls are replaced with symmetry boundary conditions, such that we model a vertical array of cylinders. The updated problem setup is shown in Fig. 3.28. We model only the symmetric portion and discretize the domain, $\Omega^d = \{-3r \leq x \leq 3r, 0 \leq y \leq 3r\}$, with a uniform mesh with $N_{elem} \times 2N_{elem}$ square elements. The cylinder and channel walls enforce the Kn-slip boundary condition. The inlet is given an Dirichlet boundary condition, such that:

$$\bar{p}_{in} = \frac{\rho h^2}{\mu^2} p_{in} = 10 \tag{3.114}$$

and the outlet is given a zero-traction boundary condition, equivalent to $p_{out} = 0$. Finally, because there exists an analytical expression for the LSF, we will use analytical expressions for the $\boldsymbol{J}_{\{n,t\}}$ in this example. The Kn number will be set as in previous examples, $Kn = 0.01$, 0.02, and 0.05.

Fig. 3.29 shows the velocity distribution over the fluid domain with $Kn = 0.05$ using $\hat{\boldsymbol{n}}_f$ and the finest level of refinement, $N_e = 180$. Note especially the non-zero velocities at the top of the cylinder, indicative of the Kn-slip boundary condition. For clarity, we will not show similar velocity distributions for other Kn or choices of the normal vector calculation. Instead, we will sample the velocity distribution at the $y = 0.25$ line. Note that this line is tangent to the top of the cylinder.

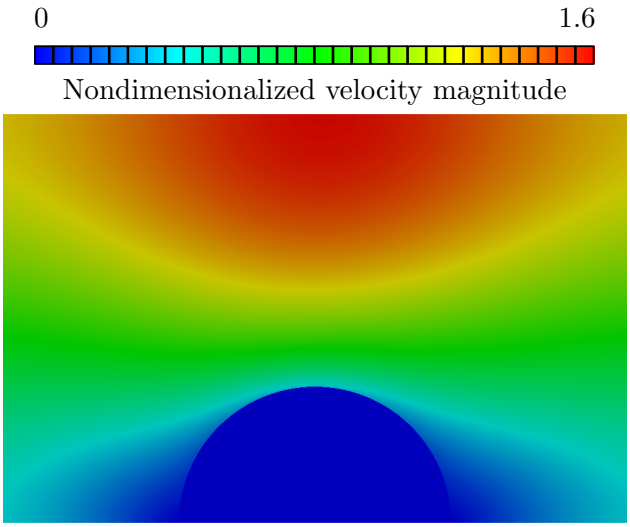

Figure 3.29: Example solution of the flow past a cylinder with $Kn = 0.05$ using $\hat{\boldsymbol{n}}_f$ and $N_e = 341$.

Fig. 3.30, 3.31, 3.32 show the x-component velocity through the sample line for $Kn = 0.01$, 0.02, 0.05, respectively. Note the non-zero velocity at $x = 0$ due to the Kn-slip boundary condition, i.e. if the no-slip boundary conditions had been used, $u(x = 0, y = 0.25) = 0$. We observe that the results using $\hat{\boldsymbol{n}}_f$ agree well with those using $\hat{\boldsymbol{n}}_\phi$, even for coarse meshes; further, we note that the disagreement increases slightly with Kn. Finally, Fig. 3.33 shows the difference in solution relative to the solution using the finest level of refinement and $\hat{\boldsymbol{n}}_\phi$ for several levels of refinement. We observe the unsmooth behavior of the differences, thought they remain small for nearly all levels of refinement and Kn numbers. Because these relative difference remain small and appear to at least remain bound, we suggest that the use of $\hat{\boldsymbol{n}}_f$ is interchangeable with the use of $\hat{\boldsymbol{n}}_\phi$. Unless otherwise noted, we will continue to use $\hat{\boldsymbol{n}}_\phi$ in the remaining sections of this work.

3.12 Flows without an analytical solution

In Section 3.10.5, we showed the importance of the $\boldsymbol{J}_{\{n,t\}}$ terms in the Kn-slip boundary condition. Though necessary to fully recover an analytical solution, their omission resulted in a small error for small Kn numbers. The $\boldsymbol{J}_{\{n,t\}}$ terms relate to the curvature of the fluid-solid interface; as the interface flattens, these terms vanish. In fact, for planar surfaces, the $\boldsymbol{J}_{\{n,t\}}$ terms

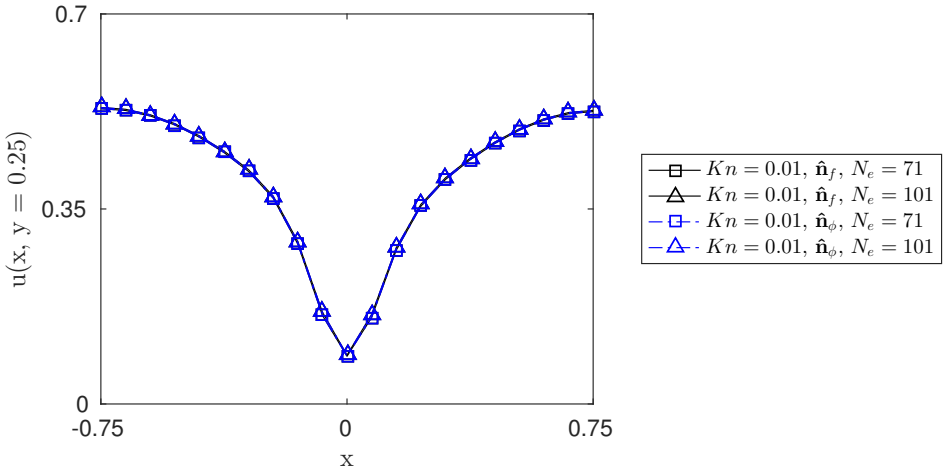

(a)

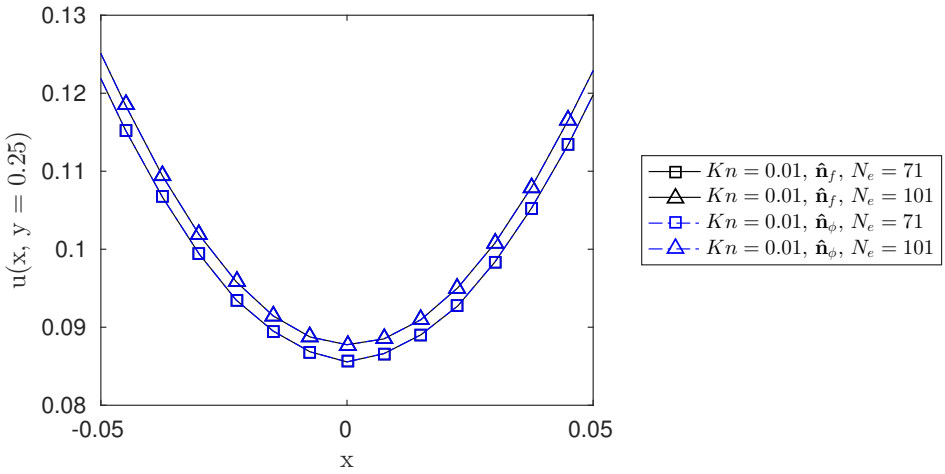

(b)

Figure 3.30: Velocity distribution (a) and close-up (b) for $Kn = 0.01$ and select levels of refinement.

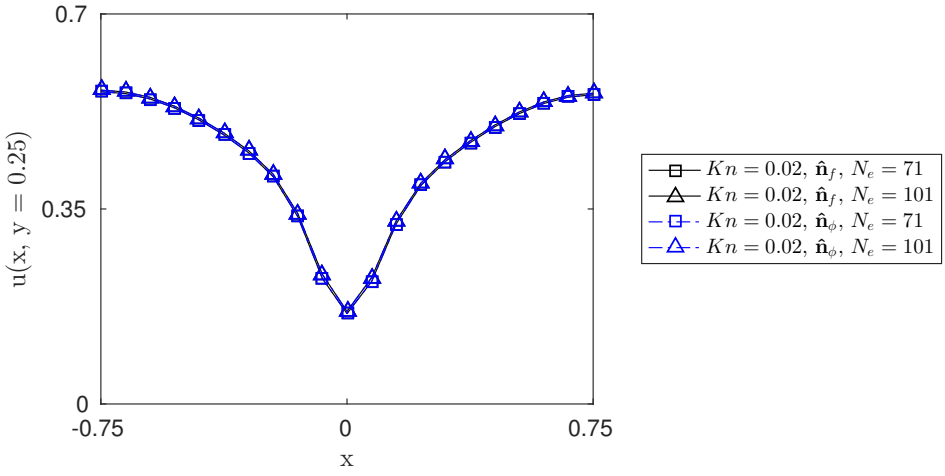

(a)

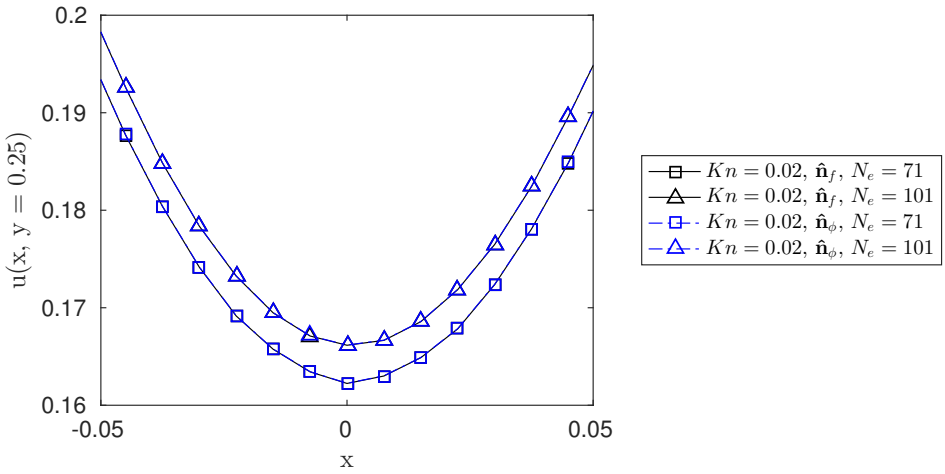

(b)

Figure 3.31: Velocity distribution (a) and close-up (b) for $Kn = 0.02$ and select levels of refinement.

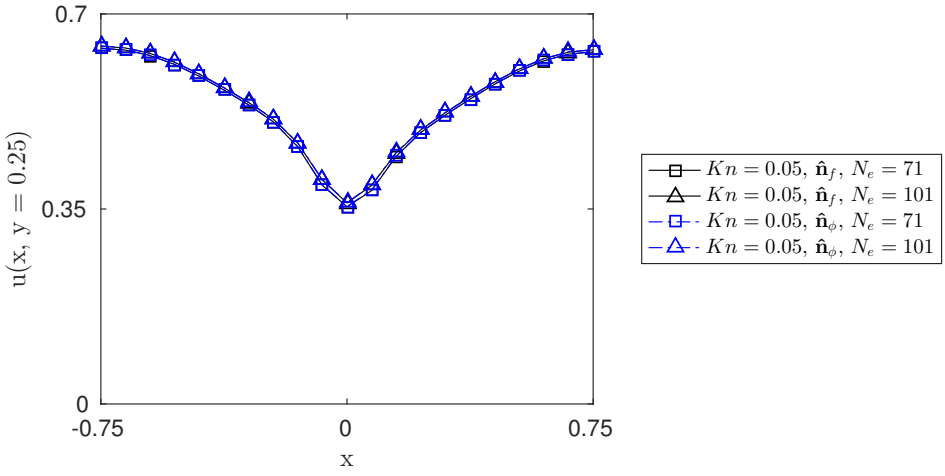

(a)

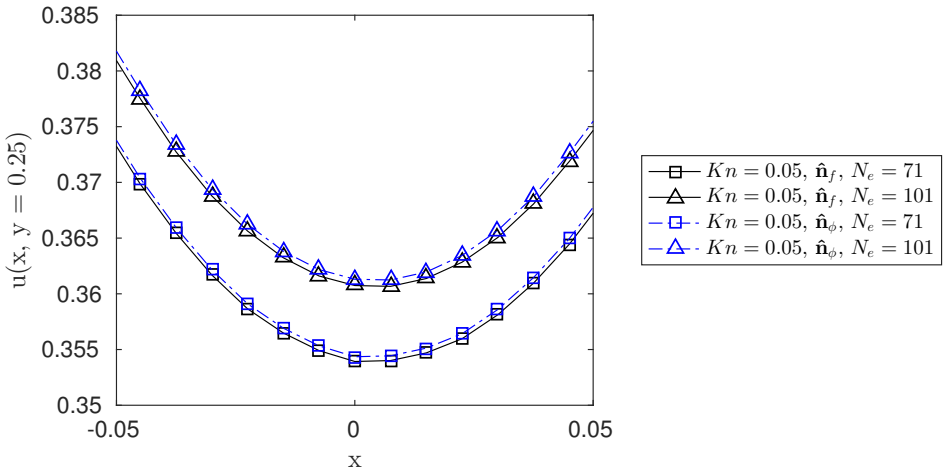

(b)

Figure 3.32: Velocity distribution (a) and close-up (b) for $Kn = 0.05$ and select levels of refinement.

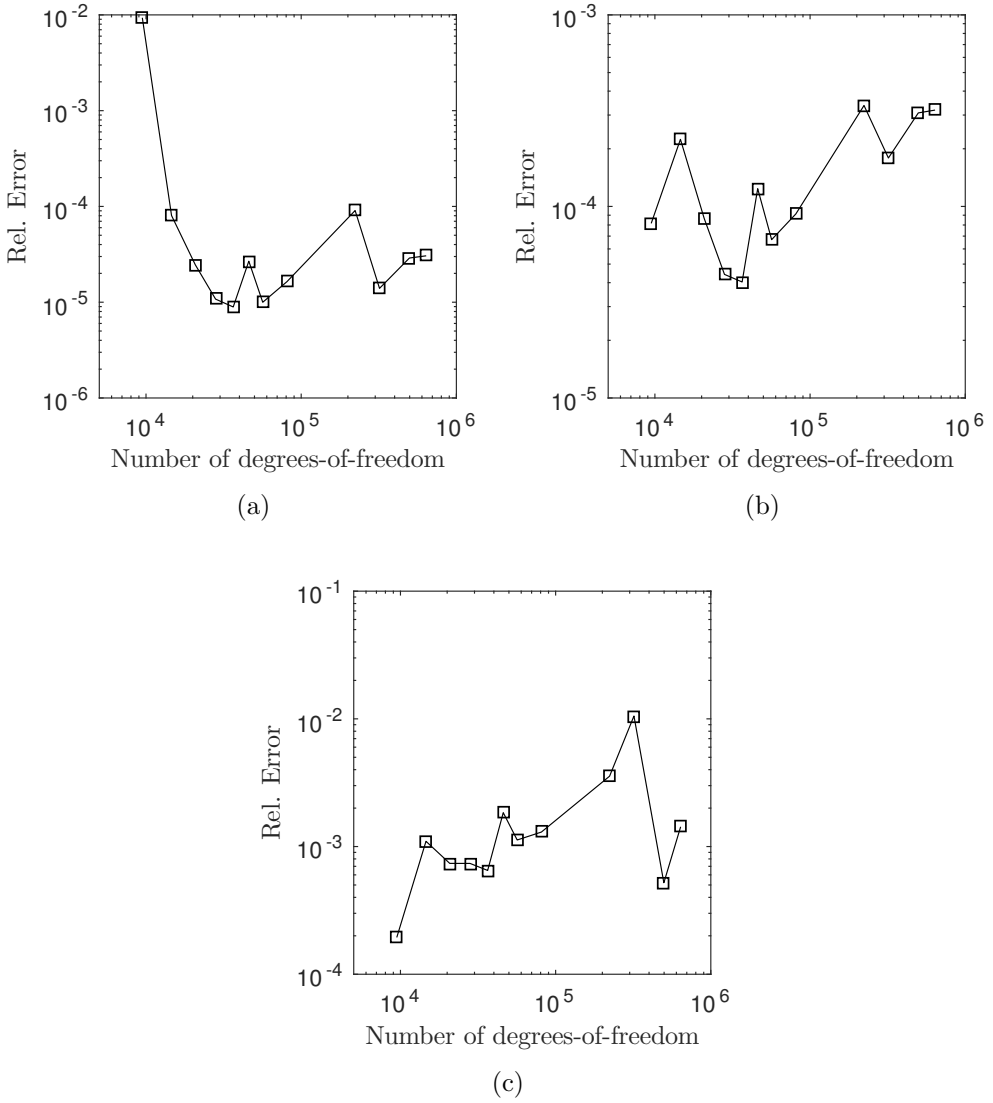

Figure 3.33: Relative difference in solution for (a) $Kn = 0.01$, (b) $Kn = 0.02$, and (c) $Kn = 0.05$. The reference solution is that using the finest level of refinement and $\hat{\boldsymbol{n}}_\phi$ for each Kn number.

vanish entirely. In this section, we will revisit the flow past a cylinder from Section 3.11 and study the effect of omitting the $\boldsymbol{J}_{\{n,t\}}$ terms on the flow solution.

Because Section 3.10.5 shows that the $\boldsymbol{J}_{\{n,t\}}$ terms found its weak form is equivalent to using analytical expressions, we will only use the later in this section. Thus, we consider solution (i) after omitting the $\boldsymbol{J}_{\{n,t\}}$ terms, and (ii) with analytical expressions for the $\boldsymbol{J}_{\{n,t\}}$ terms using (3.97).

Fig. 3.34a shows the x-component velocity sampled through the $y = 0.25$ tangent line for a coarse and the finest level of refinement; Fig. 3.34b is a close-up view. Note the disagreement in the velocity when the $\boldsymbol{J}_{\{n,t\}}$ are omitted for both levels of refinement. Fig. 3.34c shows the convergence of the mass flow with the level of refinement. The difference between the converged mass flow rates exemplifies the error in omitting the $\boldsymbol{J}_{\{n,t\}}$ terms. Finally, Fig. 3.34d show convergence of the L^2 error in the velocities, where the results with the finest level of refinement is used as the reference solution. We observe that omitting the $\boldsymbol{J}_{\{n,t\}}$ terms does not affect the L^2 error convergence rate, even if the flow converges to a different solution, e.g. Fig. 3.34c.

Fig. 3.35 and 3.36 represent similar results for $Kn = 0.02$ and 0.05, respectively. We observe that the disagreement between the results with and without th $\boldsymbol{J}_{\{n,t\}}$ terms widens as the Kn number increases. We recognize that Fig. 3.36c suggests that further refinement is necessary for $Kn = 0.05$ and will address this in Section 3.12.1.

Finally, we consider the relative error (3.115) due to omitting the $\boldsymbol{J}_{\{n,t\}}$ terms. The relative error is computed as the difference in the velocity results with and without the $\boldsymbol{J}_{\{n,t\}}$ terms at each level of refinement, relative to the results with the $\boldsymbol{J}_{\{n,t\}}$ terms and the finest level of refinement. We expect that this error will convergence for finer levels of refinement. Fig. 3.37 shows the relative error for $Kn = 0.01$, 0.02, and 0.05. We observe that, for the levels of refinement considered in this section, the relative error does not converge. However, we note that Fig. 3.37a suggests that convergence from below is possible. To study this further, we consider the same analysis with body-fitted meshes in the next section.

$$\text{Rel. Error} = \frac{\int \left(u_{w/o\ \boldsymbol{J}_{\{n,t\}},\ N_i} - u_{w/\ \boldsymbol{J}_{\{n,t\}},\ N_i} \right)^2}{\int \left(u_{w/\ \boldsymbol{J}_{\{n,t\}},\ N_{finest}} \right)^2} \tag{3.115}$$

3.12.1 Effect of the $\boldsymbol{J}_{\{n,t\}}$ terms using body-fitted meshes

In Section 3.12, we showed that the relative error due to omitting the $\boldsymbol{J}_{\{n,t\}}$ terms appears to increase for finer levels for refinement but suggested that this error should converge to a value dependent on the Kn number. To study this further, we consider the use of conforming meshes that do not require the LSM-XFEM. We consider two kinds of body-fitted meshes: unstructured or boundary-layer meshes. Examples of these two types of meshes are shown in Fig. 3.38.

Unstructured meshes are built such that the circumference of the cylinder and top wall are discretized with N_e elements; the inlet and outlet walls are discretized with $N_e/2$ elements, respectively. Finally, the two remaining faces, i.e. along the bottom axis of symmetry in front of and behind the cylinder, are discretized with $N_e/2$ elements each. These intervals tend to create square elements far away from the cylinder and slender elements near the cylinder. The transition between these two regions have elements of similar sizes, but some small elements are inevitable.

For the boundary-layered mesh, we first build a structured mesh around the cylinder and then fill the remaining domain with unstructured elements. The structured region is built in the following manner: the circumference of the cylinder is discretized with N_b layers of N_e elements. The width of the innermost elements is thus:

$$W = \frac{\pi r}{N_e}. \tag{3.116}$$

The thickness of each layer, b_i for $i = 1, 2, ..., N_b$, is such that the first layer has thickness $b_0 = f_1 W$ and $b_{i+1} = f_2 b_i$. The remaining unstructured region of this mesh is then built such that the top wall and the inlet and outlet have N_e and $N_e/2$ elements, respectively. The faces on the bottom line of symmetry in front and behind the cylinder are discretized with N_c elements, where:

$$N_c = \max\left(\frac{N_e}{2}, \frac{N_e}{4} + N_b \right). \tag{3.117}$$

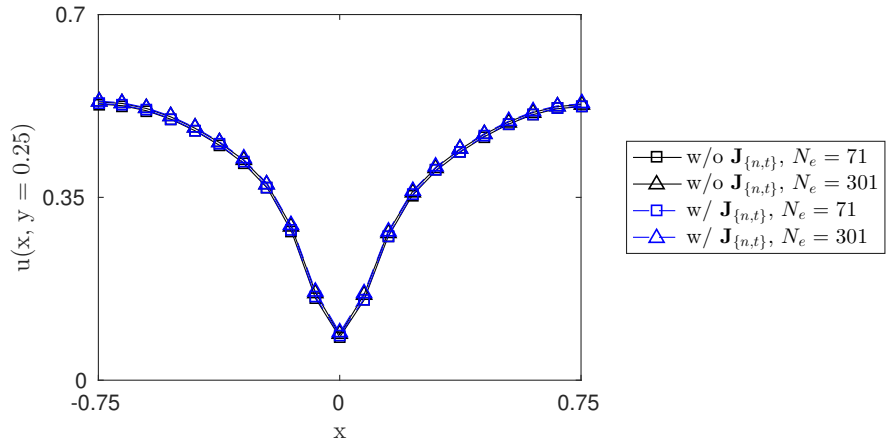

(a)

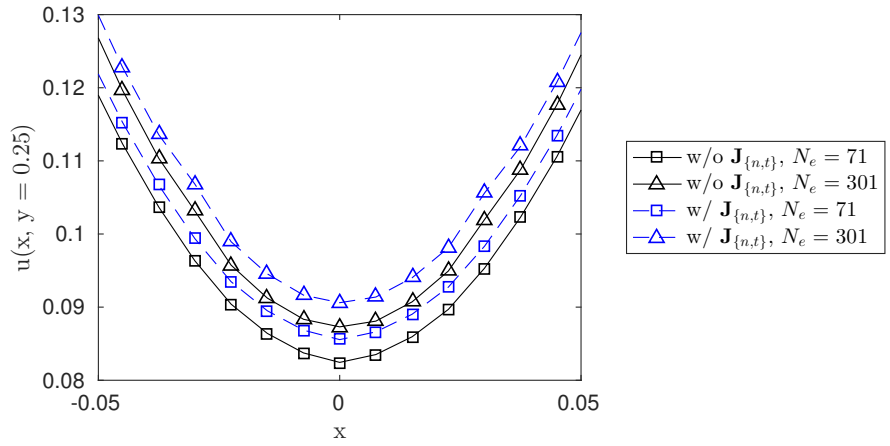

(b)

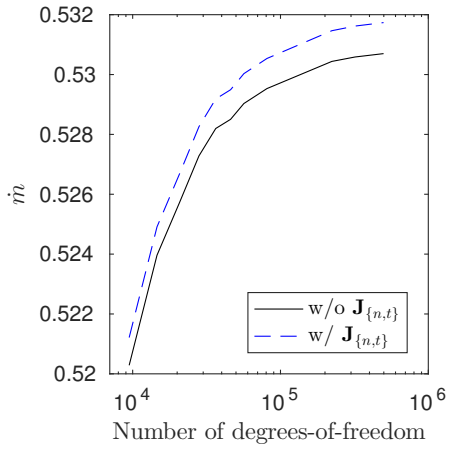

(c)

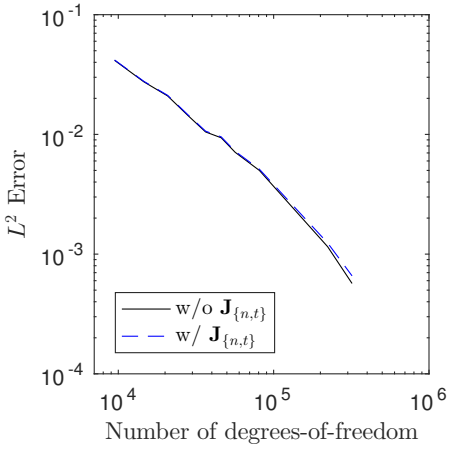

(d)

Figure 3.34: Velocity distribution (a) and close-up (b), mass flow rate (c), and L^2 error (d) for $Kn = 0.01$ with and without analytical expressions for the $\boldsymbol{J}_{\{n,t\}}$ terms.

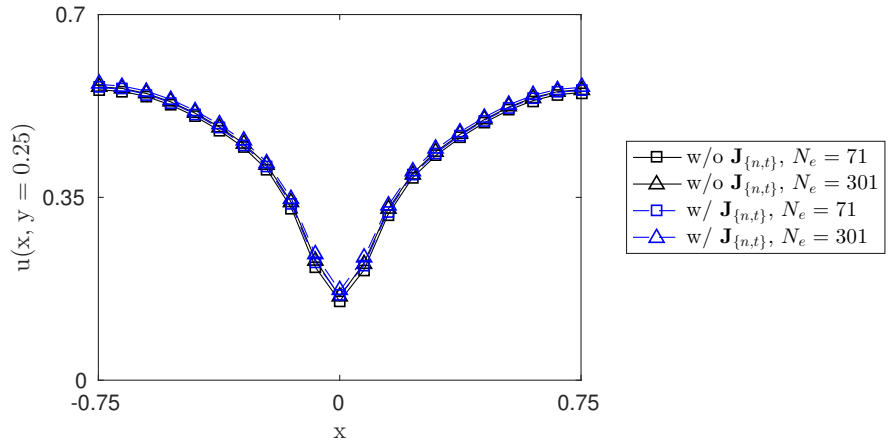

(a)

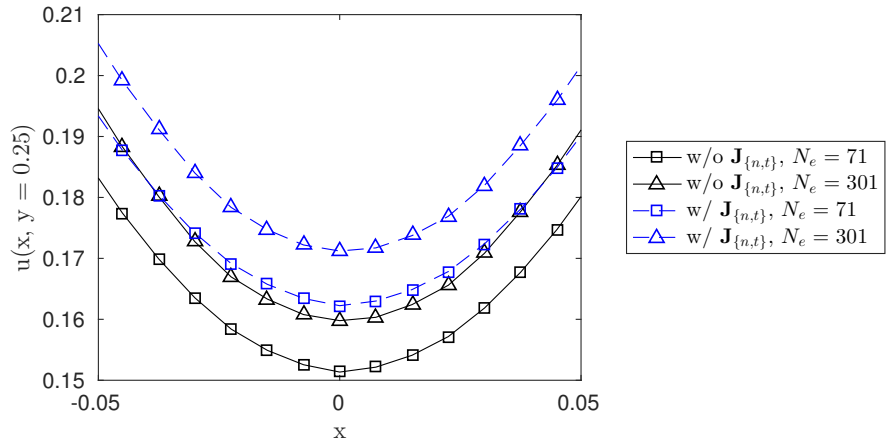

(b)

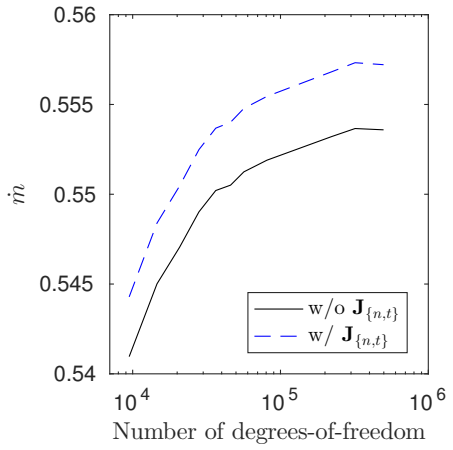

(c)

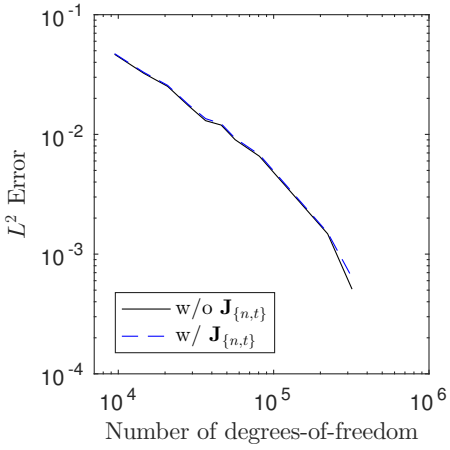

(d)

Figure 3.35: Velocity distribution (a) and close-up (b), mass flow rate (c), and L^2 error (d) for $Kn = 0.02$ with and without analytical expressions for the $\boldsymbol{J}_{\{n,t\}}$ terms.

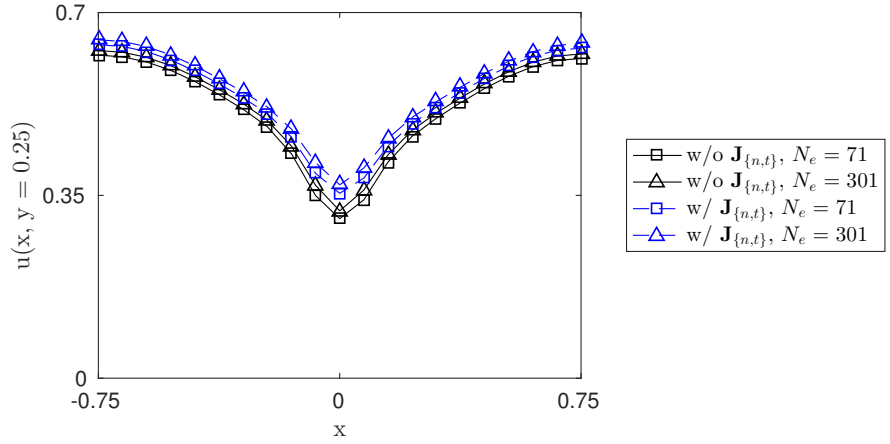

(a)

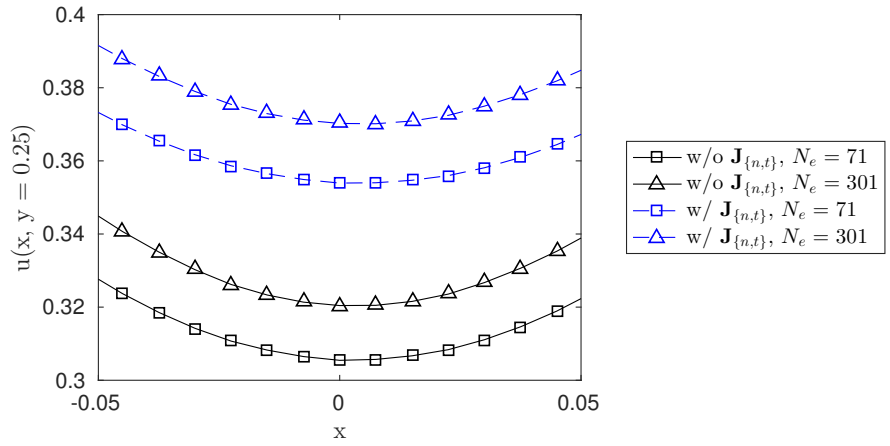

(b)

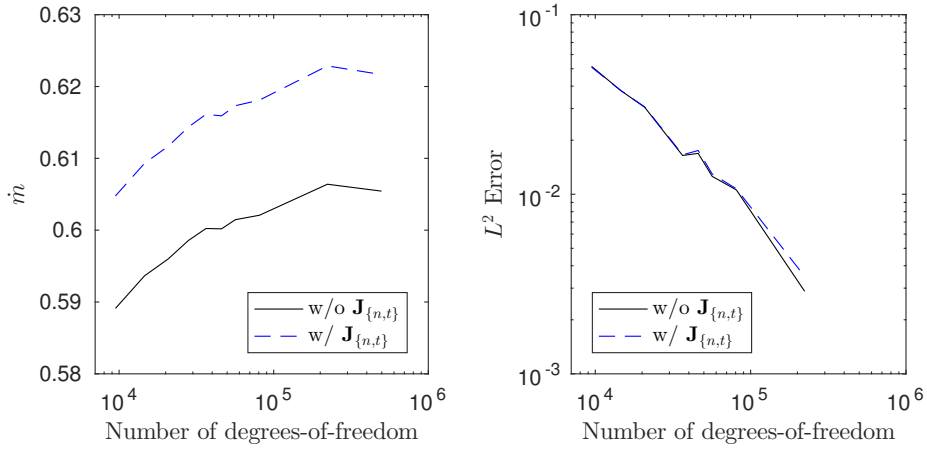

(c) (d)

Figure 3.36: Velocity distribution (a) and close-up (b), mass flow rate (c), and L^2 error (d) for $Kn = 0.05$ with and without analytical expressions for the $\boldsymbol{J}_{\{n,t\}}$ terms.

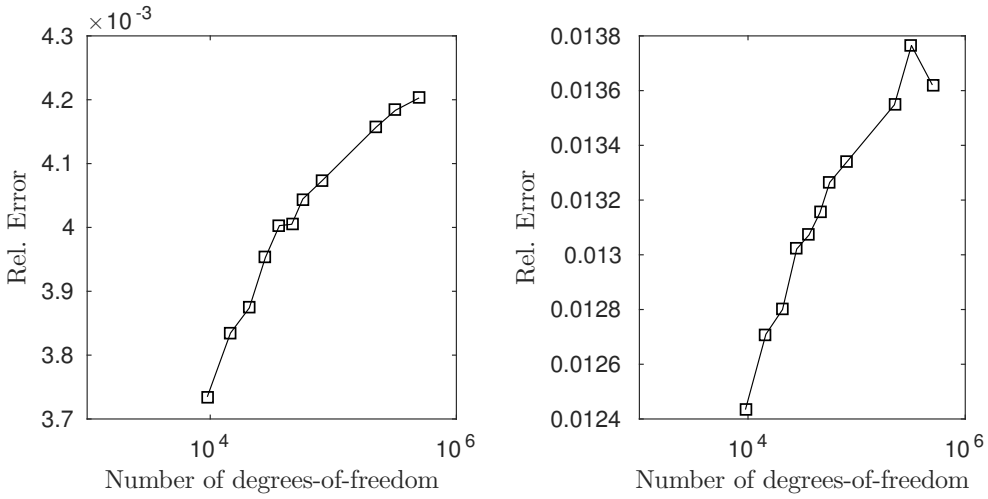

(a) $Kn = 0.01$ (b) $Kn = 0.02$

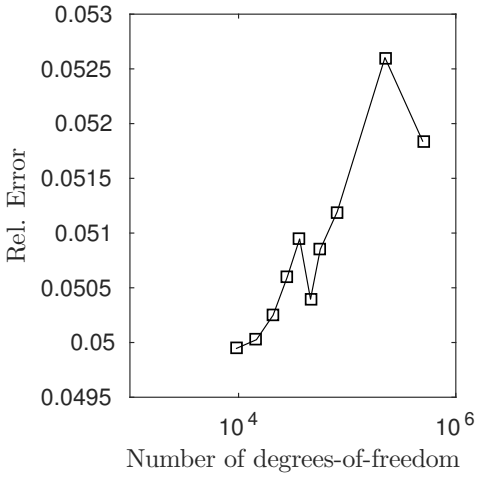

(c) $Kn = 0.05$

Figure 3.37: Relative error in the velocity distribution due to omitting the $\boldsymbol{J}_{\{n,t\}}$ terms for several levels of refinement.

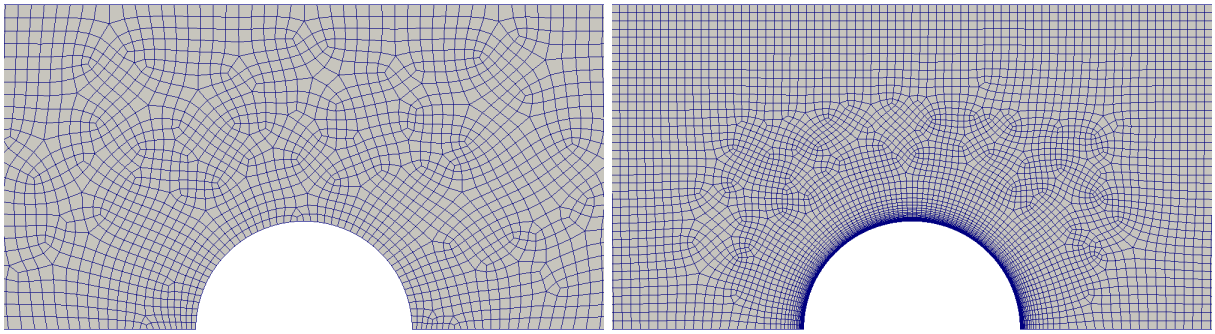

(a) Unstructured (b) Boundary-layer

Figure 3.38: Example of unstructured (a) and boundary-layer (b) meshes.

Note that N_b of the N_c elements are part of the boundary-layered structure. For all boundary-layer meshes used in this section, $f_1 = 0.01$, $f_2 = 1.2$ and N_b is such the last layer of boundary-layer elements has the same approximate thickness as an element along the top wall.

$$\begin{aligned} \frac{6r}{N_e} &= W f_1 f_2^{N_b} \\ \frac{6r}{N_e} &= \frac{\pi r}{N_e} f_1 f_2^{N_b} \end{aligned} \tag{3.118}$$

Approximating $\pi \approx 3$ gives:

$$2 = f_1 f_2^{N_b} \tag{3.119}$$

and thus:

$$N_b = \frac{\log(2) - \log(f_1)}{\log(f_2)} \approx 29. \tag{3.120}$$

We consider the same flow past a cylinder as in the previous section with the body-fitted meshes described previously for several levels of refinement. We update the convergence figures from the last section with the results using body-fitted meshes; for brevity, we do not update figures showing velocity distributions as they would not reveal important information. Fig. 3.39 shows the convergence of the mass flow rate for same Kn numbers considered previously. Results using the XFEM are repeated from before. We note that the unstructured body-fitted (BF) converge from below, just as with the XFEM, and that the boundary-layer (BL) converges from above. Both show a similar gap, confirming the error in omitting the $\boldsymbol{J}_{\{n,t\}}$ terms.

Further, Fig. 3.40 shows the L^2 error for several levels of refinement using the two types of body-fitted meshes. Again, the results using the XFEM are repeated from before. We note that both body-fitted meshes lead to smaller L^2 errors, approximately one order-of-magnitude less. Using unstructured meshes, however, leads to a smaller convergence rate. The convergence rates for the XFEM and boundary-layer meshes are approximately the same.

Finally, Fig. 3.41 shows the relative error in the velocity due to omitting the $\boldsymbol{J}_{\{n,t\}}$ terms using body-fitted meshes. We repeat the results using the XFEM for comparison. While the results in Fig. 3.37 initially suggested that this error grew unbounded with mesh refinement, the results

with body-fitted confirm our own suggestion: the error in omitting the $\boldsymbol{J}_{\{n,t\}}$ terms converges and this converged value depends on the Kn number.

Fig. 3.42 shows the maximum relative error due to omitting the $\boldsymbol{J}_{\{n,t\}}$ terms using the XFEM for each Kn number. As the Kn increases, this relative error increases; the approximate order is 1.56, using a linear curve-fit through the log-log data. While we recognize that this error is small, $< 1\%$, for $Kn = 0.01$, we note that it grows quickly as Kn increases. We show the influence of omitting these terms in a topology optimization framework in Section 5.4.3 in the manuscript found in Appendix C.

3.12.2 Flow past an elliptical cylinder

Thus far, we have considered the Kn-slip boundary condition around a circular cylinder, where the curvature of the fluid-solid interface is constant. In this section, we consider the flow past an elliptical cylinder, where the major axis aligns with the flow direction. In this case, the interface is more planar near the faster-moving fluid, compared to the circular cylinder. The elliptical cylinder has larger curvature at the head and tail, but the fluid moves more slowly in this region. Thus, we expect that omitting the $\boldsymbol{J}_{\{n,t\}}$ terms results in a smaller error. An ellipse is formed by setting $a = 2$ in (3.113). All other problem parameters are left the same.

In this section, we will limit ourselves to using the XFEM, as a comparison to body-fitted meshes would not reveal new information. Fig. 3.43 shows the nondimensional velocity in the fluid domain for $Kn = 0.05$. Because the ellipse is less obtrusive than the circular cylinder, the flow is faster and appears to approach the flow between parallel plates, cf. Fig. 3.29. Fig. 3.44 shows the velocity through the tangent line, which exemplifies the less obtrusive nature of the elliptical cylinder.

Finally, we compute the relative error in the velocity distribution due to omitting the $\boldsymbol{J}_{\{n,t\}}$ terms. Fig. 3.45 shows the relative error against the Kn number for the elliptical cylinder; the results for the cylinder are repeated from the previous study. We observe that the error grows at the same rate with respect to the Kn number, which suggests that the error *rate* is only dependent

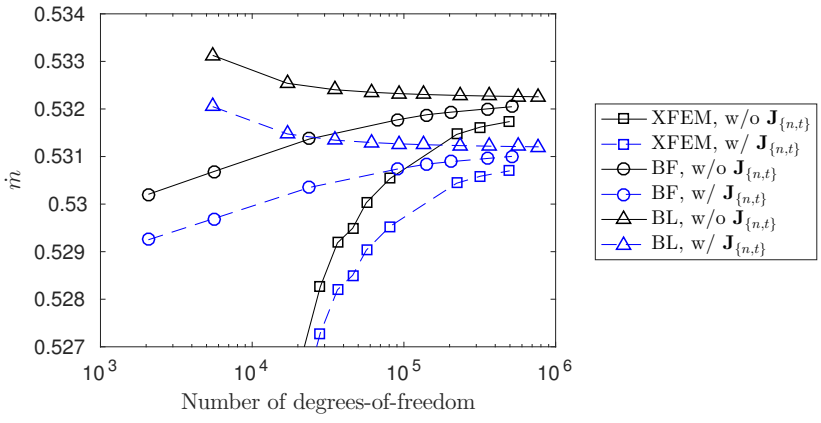

(a) $Kn = 0.01$

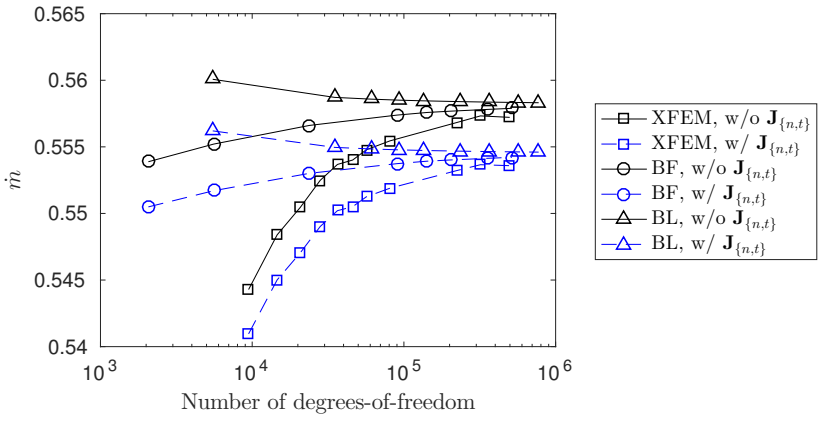

(b) $Kn = 0.02$

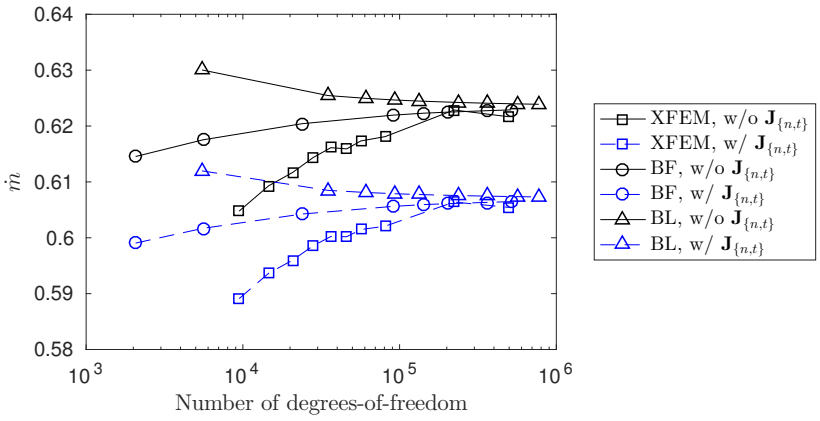

(c) $Kn = 0.05$

Figure 3.39: Convergence of mass flow rate using the XFEM and body-fitted meshes for various Kn numbers and several levels of refinement.

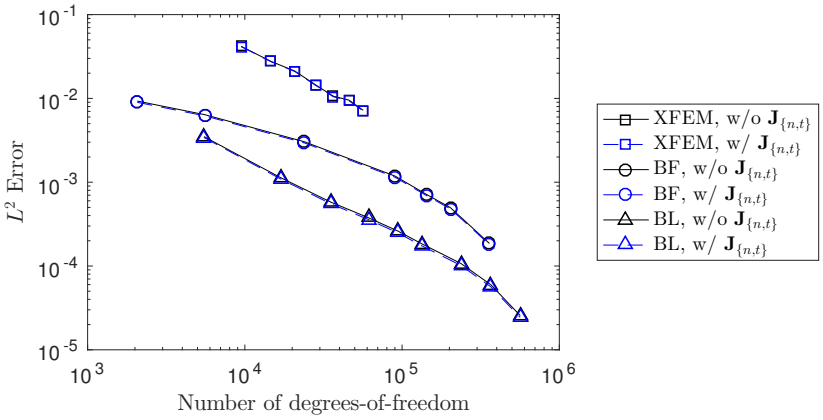

(a) $Kn = 0.01$

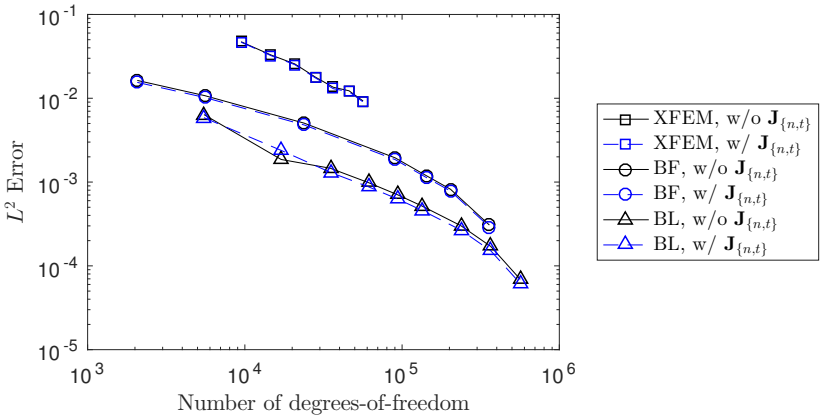

(b) $Kn = 0.02$

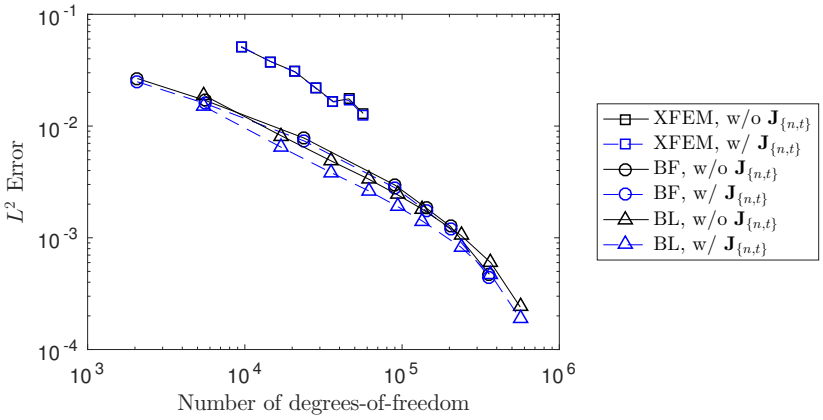

(c) $Kn = 0.05$

Figure 3.40: Convergence of L^2 error using the XFEM and body-fitted meshes for various Kn numbers and several levels of refinement.

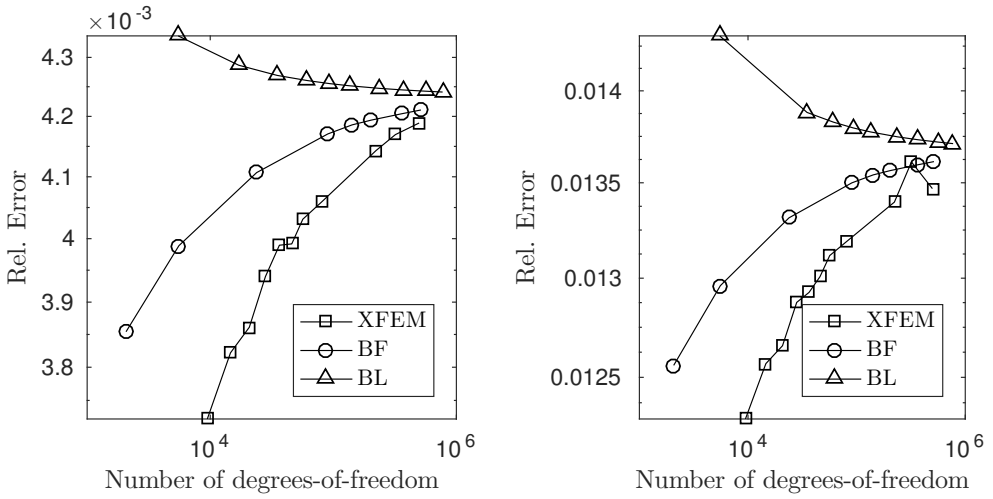

(a) $Kn = 0.01$ (b) $Kn = 0.02$

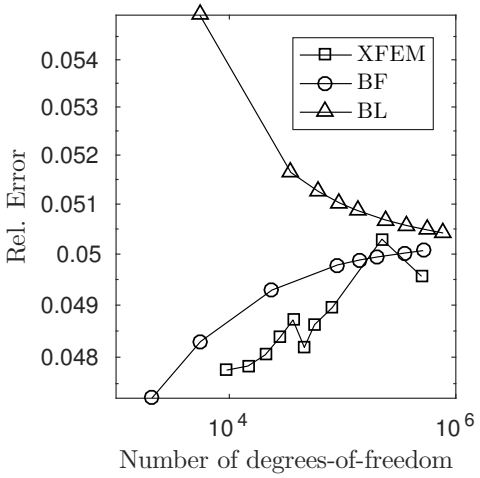

(c) $Kn = 0.05$

Figure 3.41: Relative error due to omitting the $\boldsymbol{J}_{\{n,t\}}$ terms using the XFEM and body-fitted meshes for various Kn numbers and several levels of refinement.

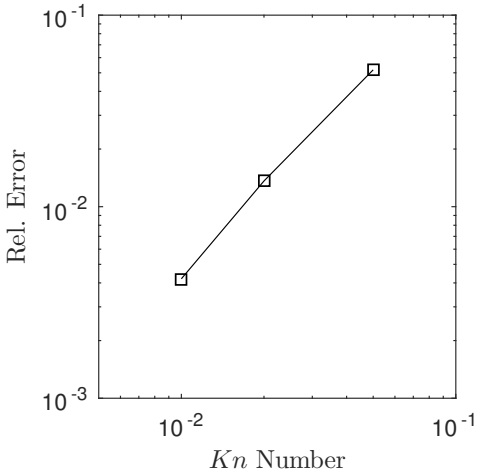

Figure 3.42: Relative error due to omitting the $\boldsymbol{J}_{\{n,t\}}$ terms for several Kn numbers using the XFEM.

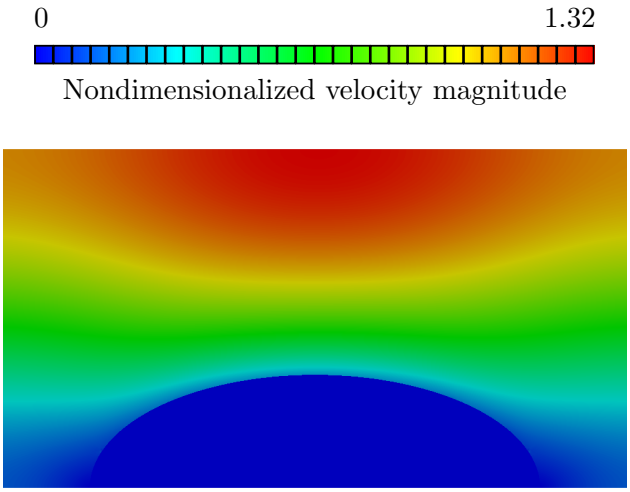

Figure 3.43: Example solution of the flow past an ellipse including the $\boldsymbol{J}_{\{n,t\}}$ terms, for $Kn = 0.05$.

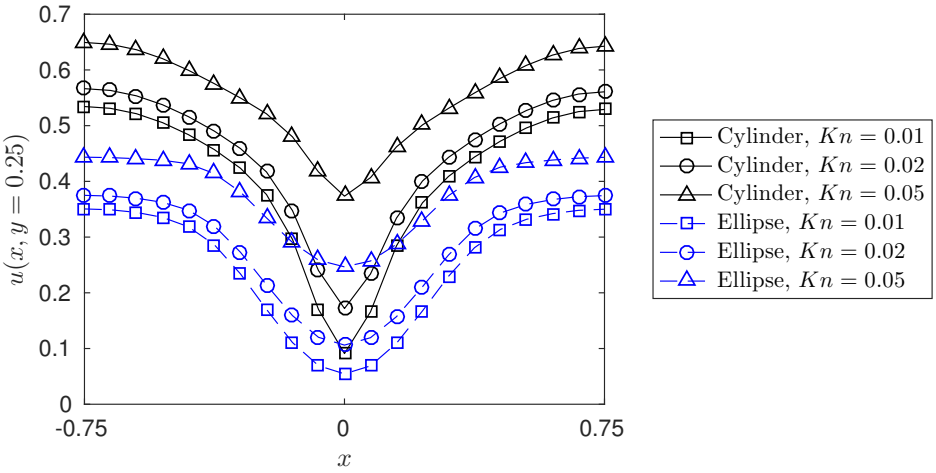

Figure 3.44: Velocity distribution through tangent line for two shapes, including the $\boldsymbol{J}_{\{n,t\}}$ terms, and several Kn numbers.

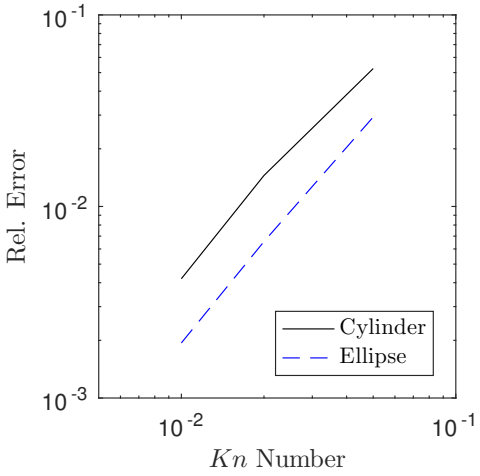

Figure 3.45: Relative error due to omitting the $\boldsymbol{J}_{\{n,t\}}$ terms for two shapes and several Kn numbers using the XFEM.

on the Kn number. Further, we note that the ratio in the relative error in the flow past a circle to the relative error in the flow past an ellipse is $2:1$. Considering the the curvature of the circular cylinder is always $\kappa = \frac{1}{r}$ and the curvature for the ellipse at the point of intersection is $\kappa = \frac{1}{4r}$, see Appendix B, this suggests that the relative error due to omitting the $\boldsymbol{J}_{\{n,t\}}$ terms grows with $\kappa^{1/2}$.

We summarize our findings as follows: in situations where the interface curvature is small and/or small Kn numbers, the $\boldsymbol{J}_{\{n,t\}}$ terms may be ignore in the Kn-slip boundary condition. This not only reduces the amount calculations at the interface, but also eliminates the need to augment the nodal degrees-of-freedom with additional degrees-of-freedom for the normal vector. For larger Kn numbers or problems with high curvature, this error cannot be as easily ignored. As mentioned previously, we show the influence of omitting the $\boldsymbol{J}_{\{n,t\}}$ terms in a topology optimization framework in Section 5.4.3 in the manuscript found in Appendix C.

3.13 Intersected elements with small ratio of areas

In this section, we explore some spurious errors caused by the emergence of intersected elements with small ratio of areas. We expect that these kinds of intersection patterns will appear as the fluid-solid interface is moved closer to a node during topology optimization and wish to study

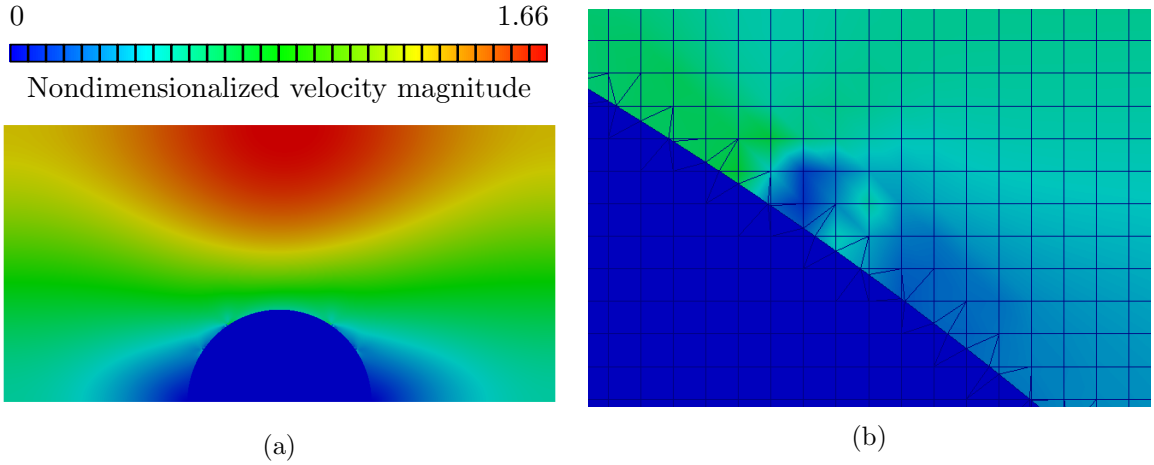

Figure 3.46: Errors in the velocity distribution at four locations along the fluid-surface interface (a) and a close-up view of the region near the top-right error (b).

their impact on the flow solution. These kinds of intersected elements tend to lead to errors in the velocity solution; here, we consider several strategies to mitigate these errors.

3.13.1 Local refinement

Consider again the flow past a circle, introduced in Section 3.11, with $Kn = 0.10$ and the finest mesh available. At lower Kn values, this particular mesh does not result in any errors along the fluid-solid interface. However, as shown in Fig. 3.46, when $Kn = 0.10$, discrepancies in the velocity field lead to four small areas along the interface where the flow behaves erroneously.

Focusing only on the top-right error, we identify the intersected element, shown in Fig. 3.47, that is potentially culpable for this error. The red lines identify the edges intersected by the fluid-solid interface, which is highlighted with a dotted line. Note the particularly small triangular subdomain; the approximate ratio of its area to the area of the square element is 1.3×10^{-3}. We subdivide the four elements shown in Fig. 3.47, i.e. the intersected element, the two elements adjacent to its intersected edges, and the element mutually adjacent to them.

The result of this local refinement is shown in Fig. 3.48. The error disappears and the flow becomes smooth, as expected. The other three errors, where refinement was not performed, remain.

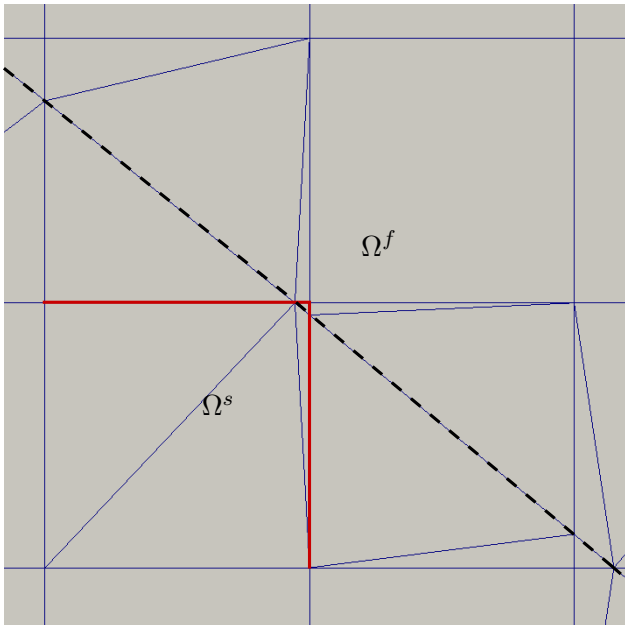

Figure 3.47: Edges surrounding a small region. Dotted line highlight the fluid-solid interface.

It is important to note that intersected elements with small area ratios appear at other location along the fluid-solid interface, yet they do not always results in the errors shown here. As stated previously, this kind of intersected elements did not results in errors for lower Kn numbers either.

This suggests that intersected elements with small ratio of areas do not always cause discrepancies in the velocity solutions; however, when these errors do appear, they do so near these type of elements. Refinement helps, as shown in this example, but as we will discuss in Section 3.13.3, there is no guarantee. Further, with the goal of topology optimization, local refinement proves an inconsistent strategy, as the fluid-solid interface will change locations after each design update. A more helpful solution, as we will discuss in Section 3.13.2, are carefully balanced ghost-penalty parameters.

3.13.2 Balancing problem parameters

In this Section, we will investigate the influence of various parameters on the errors described in Section 3.13.1. We again consider the finest level of refinement, $N_e = 341$, and $Kn = 0.10$. As a starting point, we set the ghost-penalty parameters as $\alpha_{GP,p} = \alpha_{GP,\boldsymbol{u}} = 0.5$ and $\alpha_{GP,\mu} = 5$. Additionally, in the Nitsche formulation, both β_μ and β_p are set to -1, i.e. the skew-symmetric variant is used, and $\alpha_{N,\boldsymbol{u}} = 100$. Fig. 3.49 shows the velocity distribution in the fluid domain with these settings. We again observe four locations along the fluid-solid interface with discrepancies in the velocity solution. The top-right error is caused by the element identified in Fig. 3.47.

Figure 3.50 shows the velocity distribution after switching to the symmetric variant of the viscous adjoint in the Nitsche formulation, i.e. setting $\beta_\mu = 1$. This switch does help with the two bottom errors, but does not mitigate the top two errors. While using this variant does not solve all errors, it does reduce them, as stated suggested by Vilanueva and Maute [10]. The remaining results in this Section use the symmetric variant.

Recall that Fig. 3.47 shows the intersected element with a small ratio of areas that is responsible for the errors along the fluid-solid interface. We focus our attention on the intersected edges highlighted in red and overwrite the ghost-penalty parameter $\alpha_{GP,\mu}$ on *these* edges only. Fig.

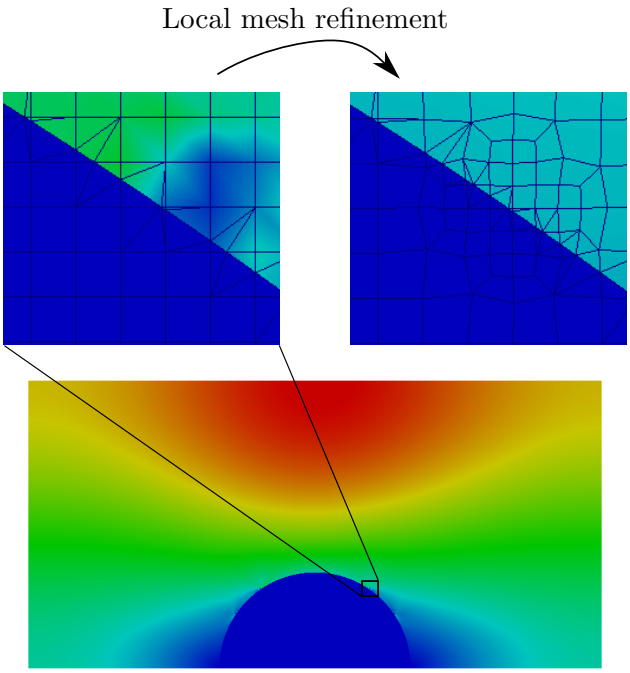

Figure 3.48: Effect of local mesh refinement on the spurious error.

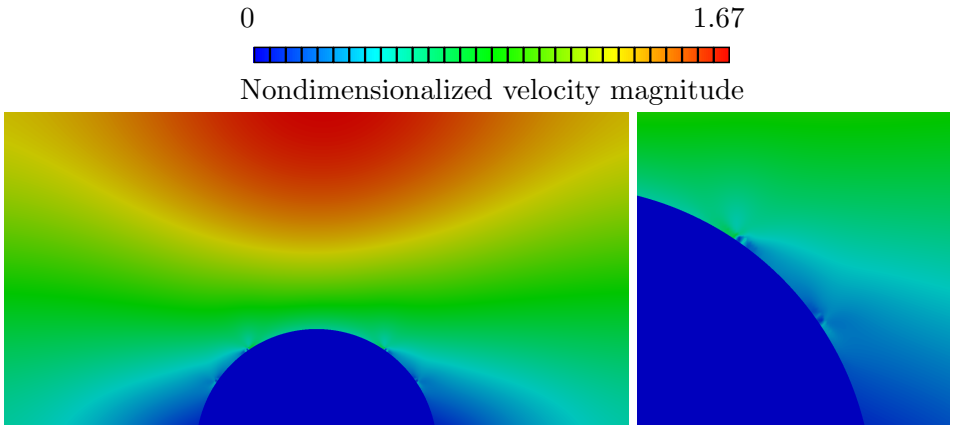

(a) Full fluid domain (b) Close-up

Figure 3.49: Resulting errors in the velocity distribution using base ghost-penalty and Nitsche parameters.

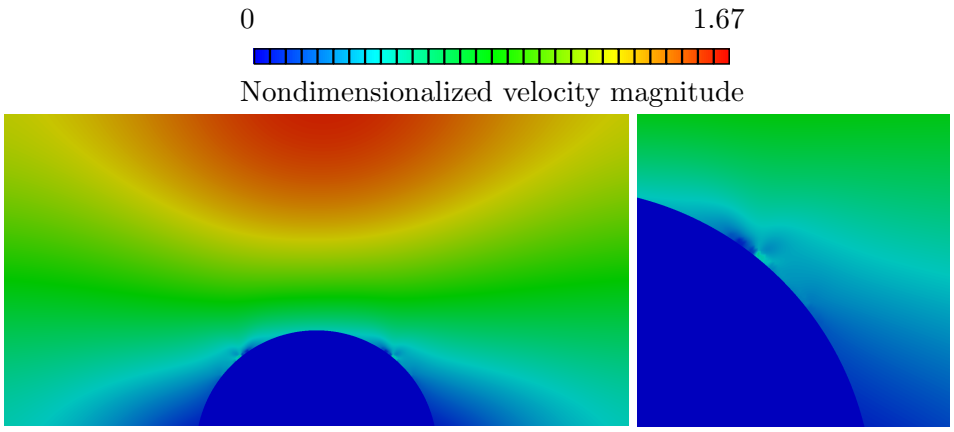

(a) Full fluid domain (b) Close-up

Figure 3.50: Resulting errors in the velocity distribution after switching the Nitsche viscous term to its symmetric variant, $\beta_\mu = 1$.

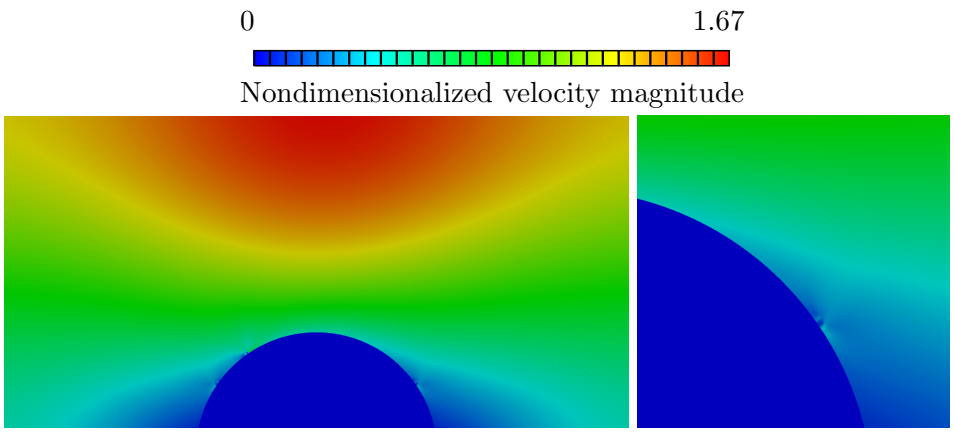

(a) Full fluid domain (b) Close-up

Figure 3.51: Resulting errors in the velocity distribution after decreasing $\alpha_{GP,\mu}$ to 0.5 locally.

3.51 and 3.52 show the resulting velocity distribution after decreasing $\alpha_{GP,\mu}$ to 0.5, and increasing it to 50, respectively. These changes address only the top-right error; that the other errors are still present is not relevant in our current discussion. Both local changes to the ghost-penalty parameter resolve the error caused by the ill-intersected element. This strategy could be employed for the remaining errors; however, this strategy is ultimately not sustainable because (i) the presence of errors cannot be known *a priori* and (ii) intersected elements with small ratio of areas do not always cause these errors. Instead, we consider changing the ghost-penalty parameters for all elements.

We again consider $\alpha_{GP,\mu}$, but change the parameter for *all* elements. Fig. 3.53 shows the resulting velocity distribution after decreasing $\alpha_{GP,\mu}$ by one order of magnitude, i.e. $\alpha_{GP,\mu} = 0.5$. Similarly, Figure 3.54 shows the resulting velocity distribution after increasing it by one order of magnitude, i.e. $\alpha_{GP,\mu} = 50$. Reducing this parameter mitigates the top errors, but creates new ones, though smaller, at different locations along the interface; in contrast, increasing the parameter eliminates the errors without introducing new ones and is thus more helpful.

We return $\alpha_{GP,\mu}$ to its original setting, $\alpha_{GP,\mu} = 5$, and now focus on the pressure parameter, $\alpha_{GP,p}$. Figures 3.55, 3.56, and 3.57 shows the resulting velocity distributions after setting $\alpha_{GP,p} = 0.05$, i.e. decreasing it by one order of magnitude, $\alpha_{GP,p} = 5$, i.e. increasing it by one order of magnitude, and $\alpha_{GP,p} = 50$, i.e. increasing it by two orders of magnitude, respectively. Decreasing

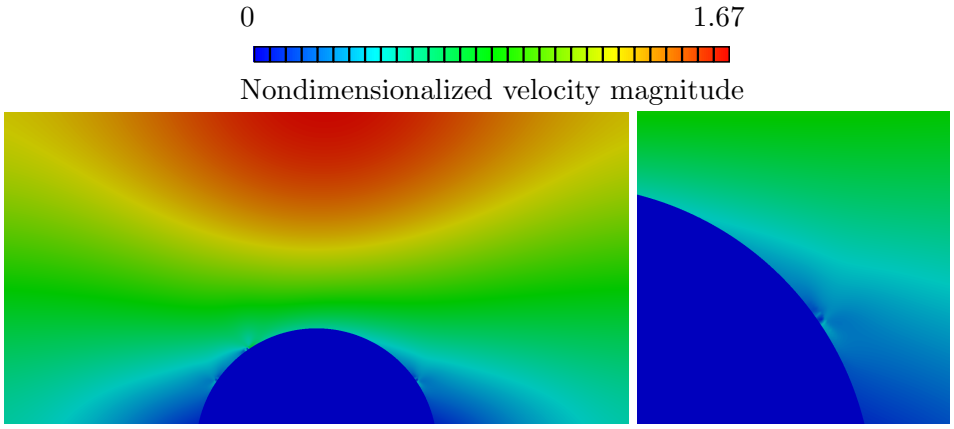

(a) Full fluid domain (b) Close-up

Figure 3.52: Resulting errors in the velocity distribution after increasing $\alpha_{GP,\mu}$ to 50 locally.

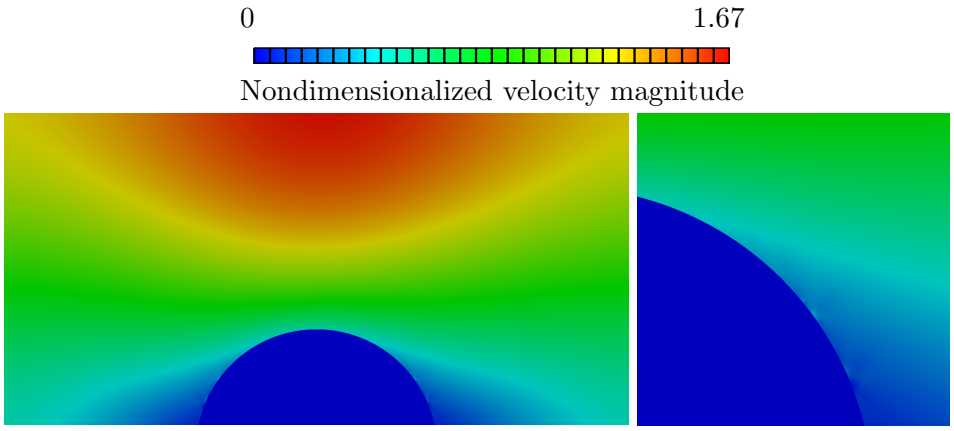

(a) Full fluid domain (b) Close-up

Figure 3.53: Resulting errors in the velocity distribution after decreasing $\alpha_{GP,\mu}$ to 0.5.

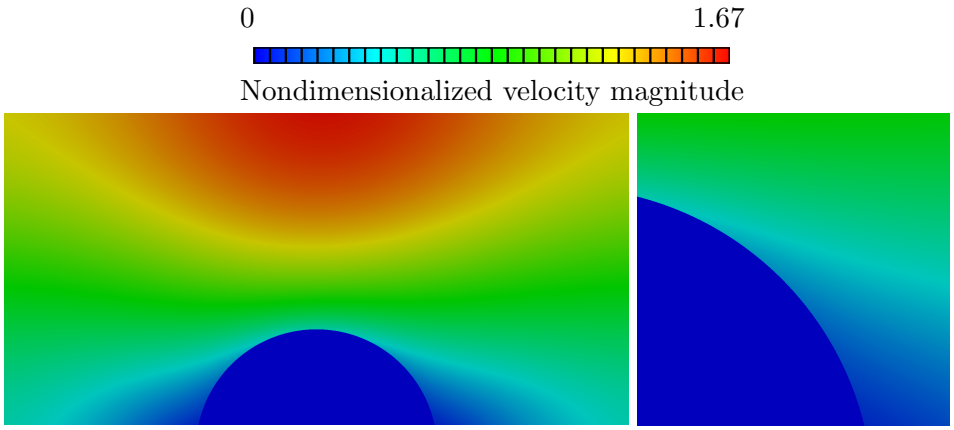

(a) Full fluid domain (b) Close-up

Figure 3.54: Resulting errors in the velocity distribution after increasing $\alpha_{GP,\mu}$ to 50.

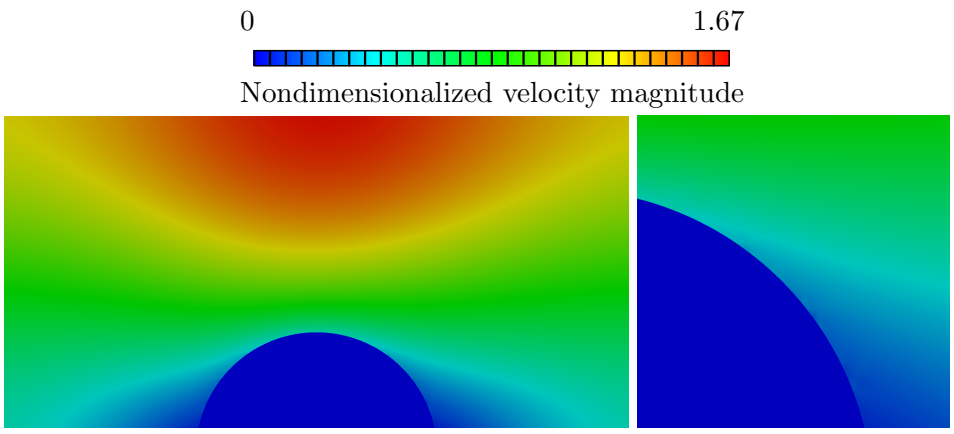

(a) Full fluid domain (b) Close-up

Figure 3.55: Resulting errors in the velocity distribution after decreasing $\alpha_{GP,p}$ to 0.05.

the parameter helps reduce the remaining errors in Fig. 3.50 but it leaves smaller errors lower on the fluid-solid interface. In contrast, increasing the parameter improves the solution without introducing new errors, though there is no need to increase it by two orders of magnitude.

Intersected elements with small ratio of areas sometimes lead to errors in the velocity solution at the fluid-solid interface. While local mesh refinement or a local modification to the ghost-penalty parameters mitigate these errors, these strategies are not scalable to a topology optimization framework. Instead, changing the ghost-penalty parameters globally is a more appropriate solution. We observe that the errors are reduced when the ghost-penalty parameters are decreased and fully eliminated when the parameters are increased. This suggests that the ghost-penalty parameters do not exhibit monotonic behavior, i.e. deceasing them does not make errors worse. Thus, the best ghost-penalty parameters for a given problem are found in local extrema rather than absolute extrema.

3.13.3 Strategies for the wavy ellipse

Thus far, we have considered strategies to mitigate the errors in the velocity solution caused by intersected elements with small ratio of areas and have shown that local mesh refinement and modification of ghost-penalty parameters mitigate these errors successfully but are potentially not

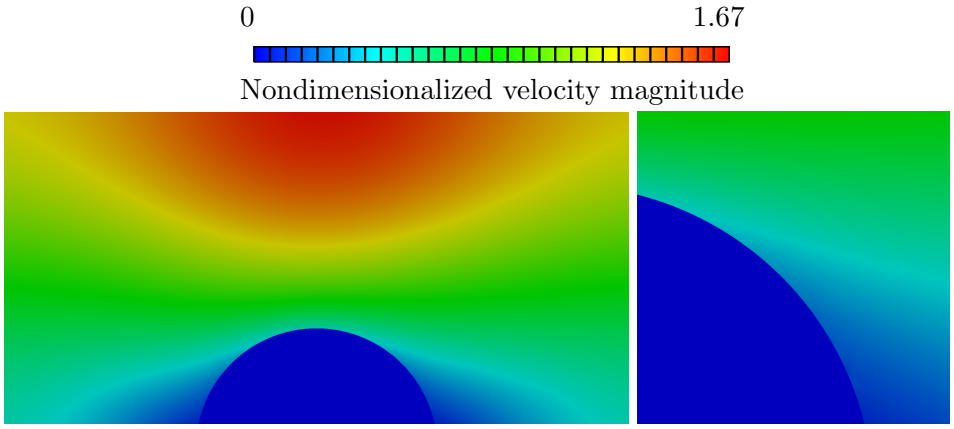

(a) Full fluid domain (b) Close-up

Figure 3.56: Resulting errors in the velocity distribution after increasing $\alpha_{GP,p}$ to 5.

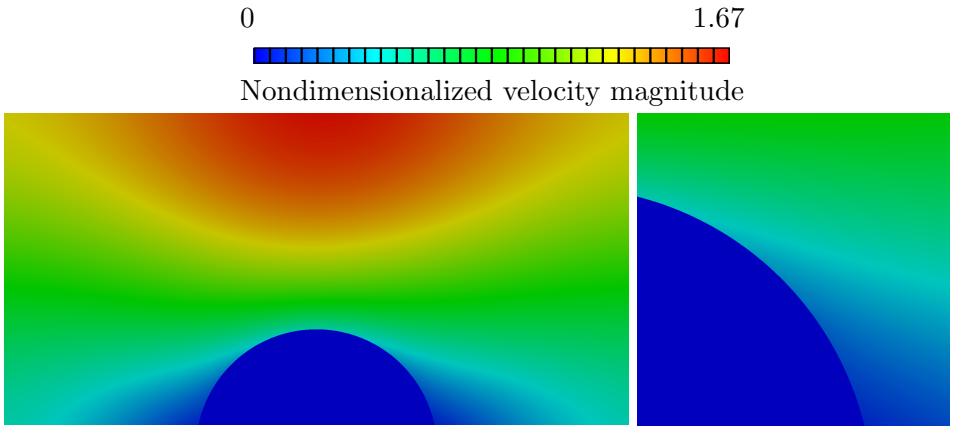

(a) Full fluid domain (b) Close-up

Figure 3.57: Resulting errors in the velocity distribution after increasing $\alpha_{GP,p}$ to 50.

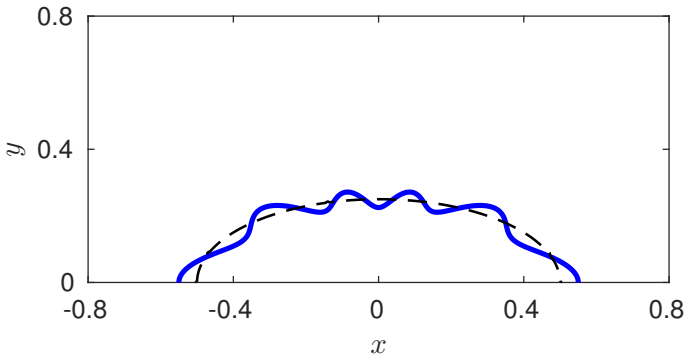

Figure 3.58: Example wavy ellipse with $f_r = 0.1$ and $\omega = 10$. Dotted line represents the regular ellipse.

appropriate solutions in the context of topology optimization. Changing the ghost-penalty parameters for all elements also mitigate the errors but this behavior is not monotonic.

In this Section, we consider the flow past a more complex shape: an ellipse with a wavy interface. We realize this shape by generalizing the LSF for an ellipse as:

$$\phi = r(1 + f_r \cos(\omega\theta)) - \sqrt{\left(\frac{x-h}{a}\right)^2 + \left(\frac{y-k}{b}\right)^2}, \tag{3.121}$$

where $\tan\theta = y/x$, and f_r and ω control the oscillations along the ellipse wall. Figure 3.58 show the wavy elliptical body with $f_r = 0.1$ and $\omega = 10$. We repeat the remaining LSF parameters used previously, $(h, k) = (0, 0)$, $a = 2$, $b = 1$, and $r = 0.25$. The problem setup and boundary conditions are otherwise identical to the ones shown in Fig. 3.28. The $\boldsymbol{J}_{\{n,t\}}$ are included in the Kn-slip boundary condition and are computed analytically from (3.121).

As a starting point, we use a mesh with $N_e = 221$ elements along the vertical direction. Because we have shown that the ideal ghost-penalty parameters are problem-dependent, we first set $\alpha_{GP,p} = \alpha_{GP,\boldsymbol{u}} = 0.5$, the sweep over various values for $\alpha_{GP,\mu} = \{0.05,\ 0.5,\ 5,\ 50,\ 500\}$ and show the results in Fig. 3.59. We observe some errors along the fluid-solid interface, which lead to spurious recirculation regions, best exemplified by Fig. 3.59b. As the ghost-penalty parameter continues to increase, the flow solution becomes smoother; at the largest value, the spurious errors return, e.g. note the disturbance in the streamlines after the third bump from the left. This confirmed the non-monotonic behavior of the ghost-penalty method.

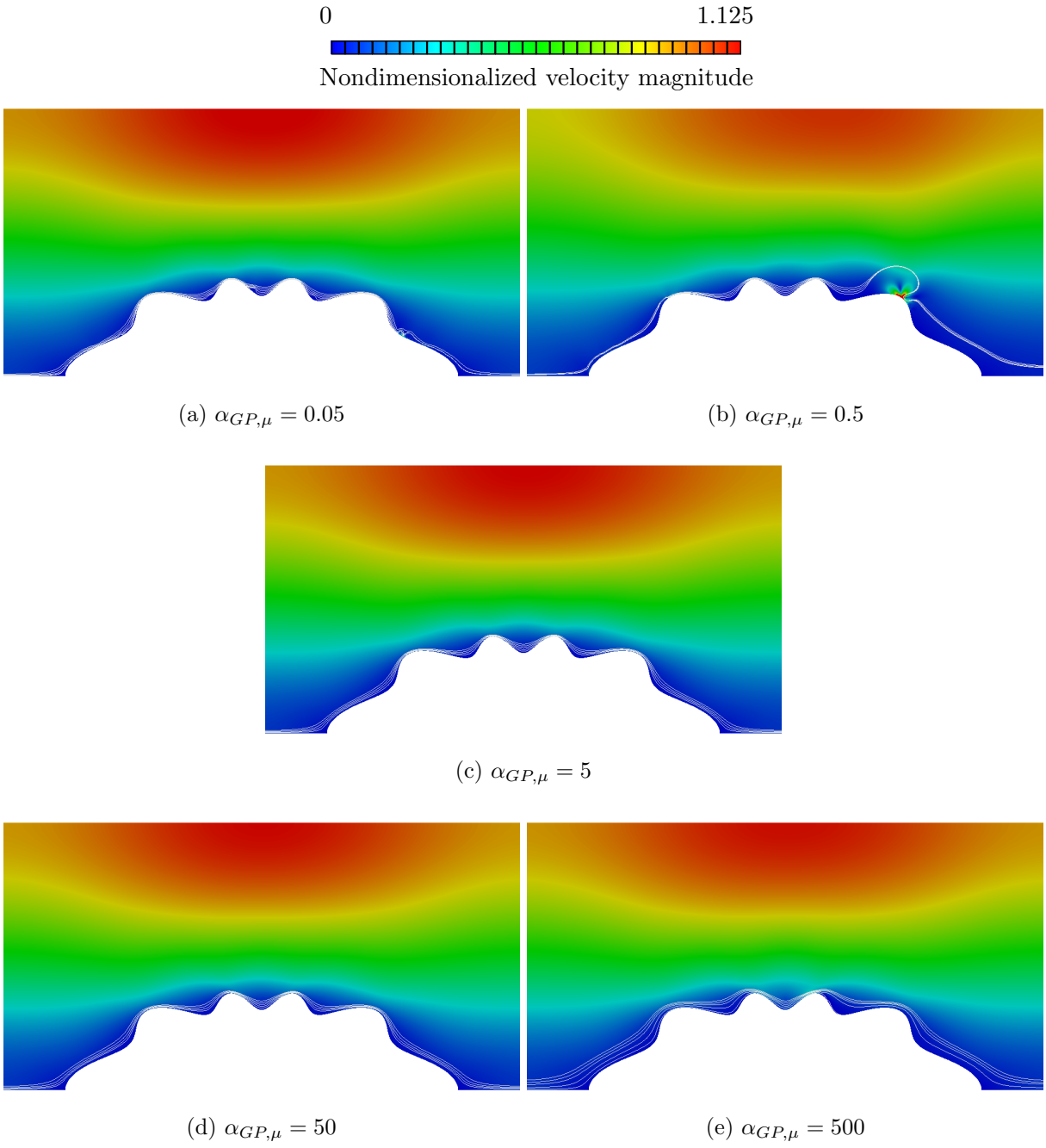

(a) $\alpha_{GP,\mu} = 0.05$

(b) $\alpha_{GP,\mu} = 0.5$

(c) $\alpha_{GP,\mu} = 5$

(d) $\alpha_{GP,\mu} = 50$

(e) $\alpha_{GP,\mu} = 500$

Figure 3.59: Resulting velocity distribution for increasing values of $\alpha_{GP,\mu}$ with $N_e = 221$. Spurious recirculation regions appear in (a), (b), and (c).

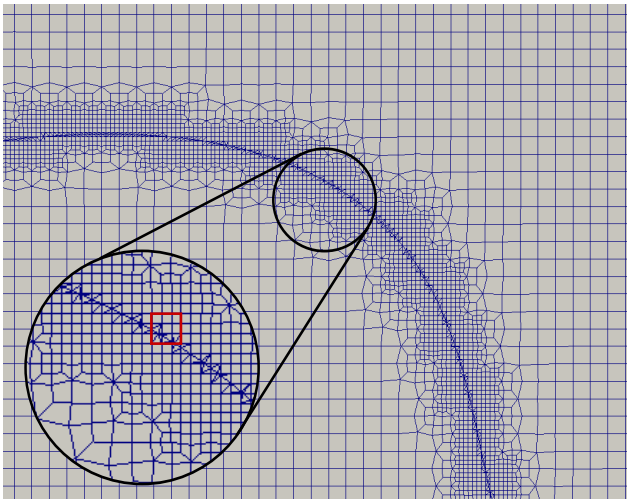

Figure 3.60: Partial refinement along the fluid-solid interface. Red highlight is an example of an element prior to refinement.

We reconsider this sweep over parameter values with two new meshes. The first undergoes partial refinement along the fluid-solid interface. Elements intersected by the zero isosurface of the LSF and their adjacent neighbors are subdivided into 9 smaller elements, as shown in Fig. 3.60. The red highlight represents an element prior to this refinement. Elements further away from the interface are also subdivided to transition smoothly into the original undivided elements. The second mesh is a simply global refinement to $N_e = 341$.

Fig. 3.61 shows the resulting velocity distributions as we sweep over the same values for $\alpha_{GP,\mu}$ with the partially refined mesh. Note the same type of errors and spurious recirculation regions appear as before but at different values of the parameter, e.g. Fig. 3.59d has no errors but Fig. 3.61d does. The results with $\alpha_{GP,\mu} = 500$ are smooth, which suggests that the "sweet" spots for the ghost-penalty parameter have simply shifted. Finally, Fig. 3.62 shows the resulting velocity distributions when the sweep over parameter values is performed on the $N_e = 341$ mesh. Again, the parameter values that do not lead to spurious recirculation regions have changed.

This study suggests that the ghost-penalty method does not solve all of the ill-conditioning caused by intersected elements with small ratio of areas. Further, the ghost-penalty parameter do not exhibit monotonic behavior; however, when errors are detected, increasing the ghost-penalty

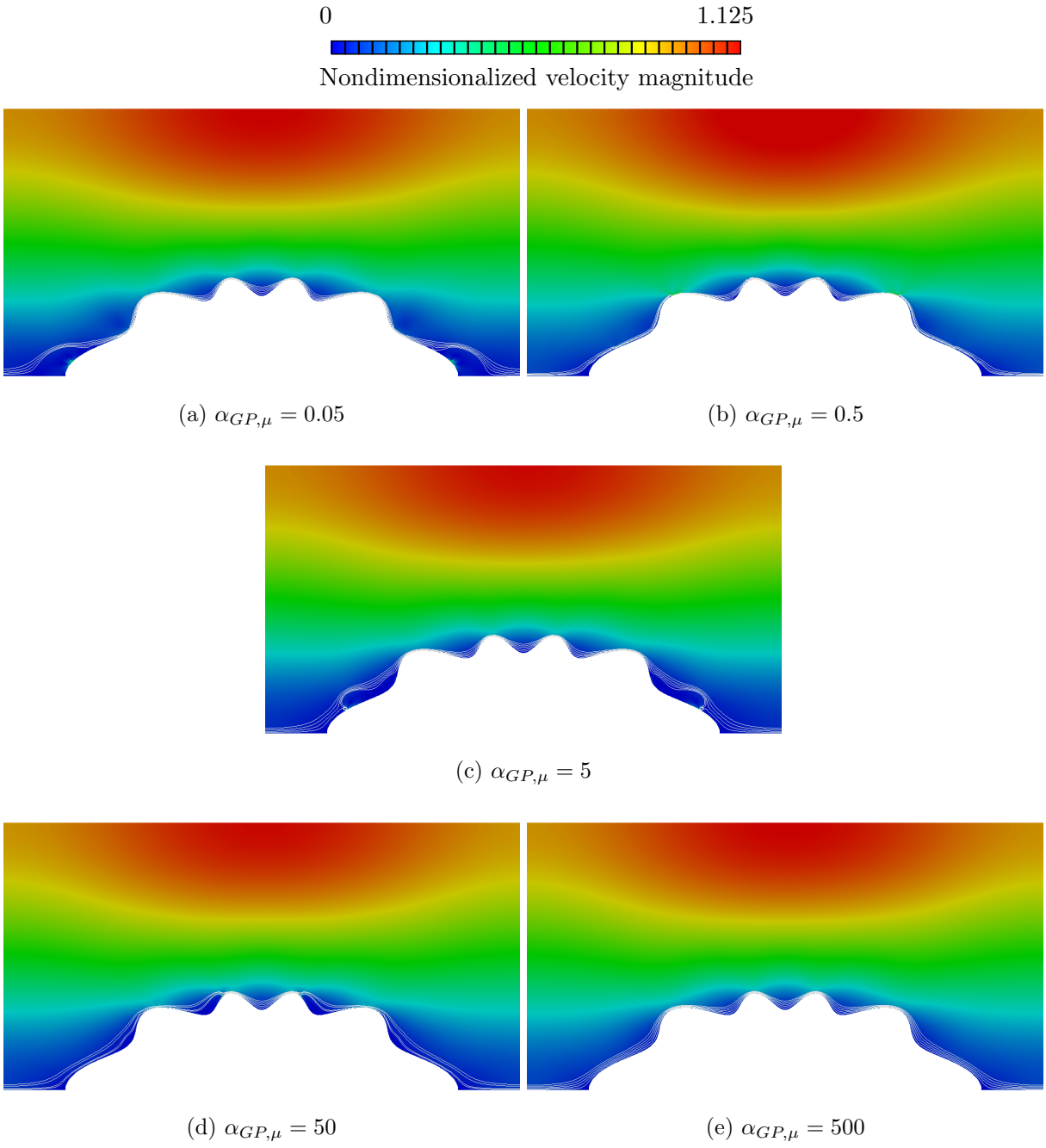

(a) $\alpha_{GP,\mu} = 0.05$

(b) $\alpha_{GP,\mu} = 0.5$

(c) $\alpha_{GP,\mu} = 5$

(d) $\alpha_{GP,\mu} = 50$

(e) $\alpha_{GP,\mu} = 500$

Figure 3.61: Resulting velocity distribution for increasing values of $\alpha_{GP,\mu}$ with the partially refined $N_e = 221$ mesh. Spurious recirculation regions appear in (a), (c), and (d).

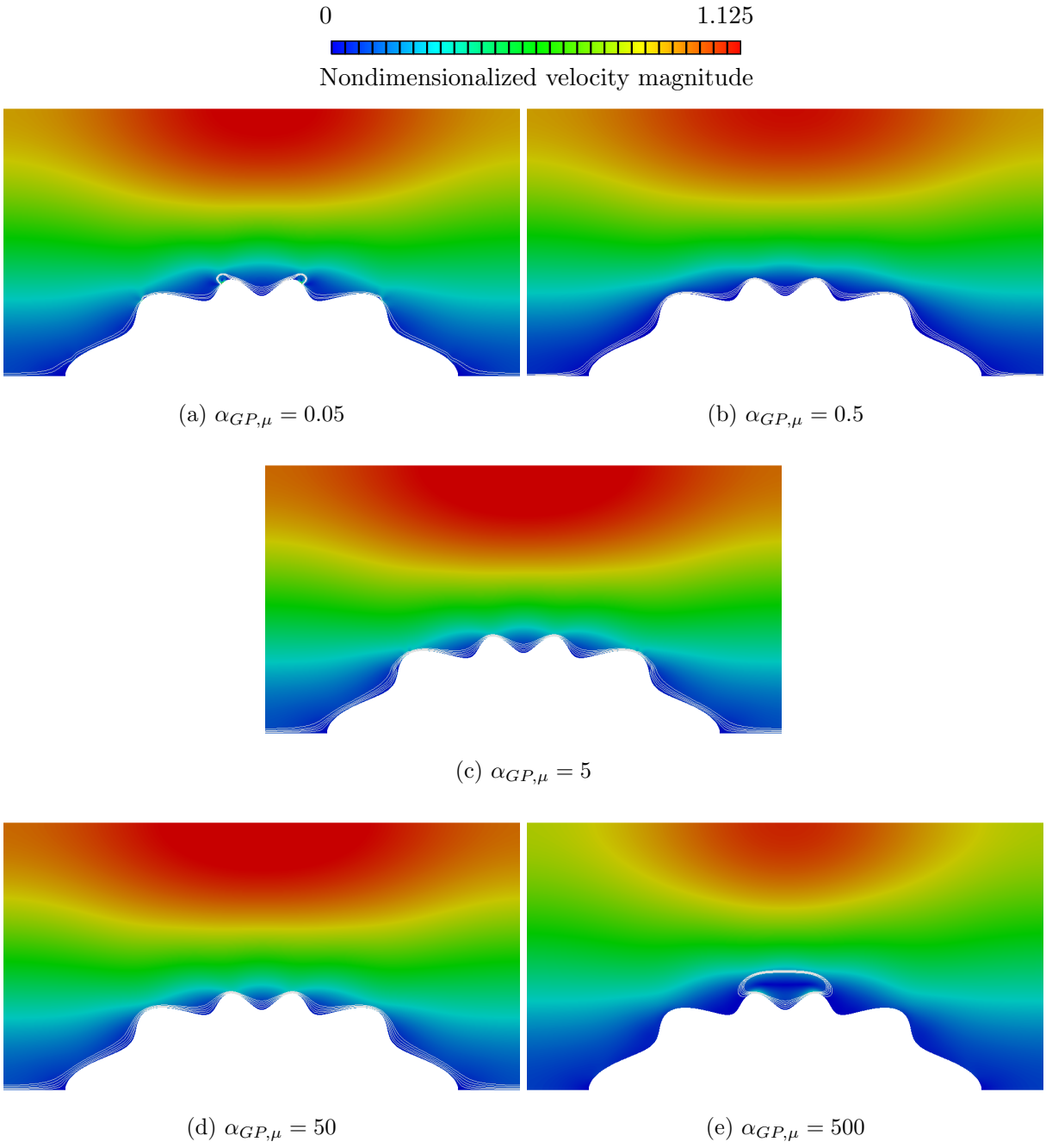

(a) $\alpha_{GP,\mu} = 0.05$

(b) $\alpha_{GP,\mu} = 0.5$

(c) $\alpha_{GP,\mu} = 5$

(d) $\alpha_{GP,\mu} = 50$

(e) $\alpha_{GP,\mu} = 500$

Figure 3.62: Resulting velocity distribution for increasing values of $\alpha_{GP,\mu}$ with $N_e = 341$. Spurious recirculation regions appear in (a), (c), and (e).

parameters generally help mitigate errors along the fluid-solid interface. Because these errors do seem to appear in a regular pattern in term of mesh size of Kn number, more careful and direct study is necessary in the future.

3.14 Flow through porous medium

As a final consideration, we will study the effect of the ghost-penalty method on the convergence rate. In this Section, we will consider the flow past several circular inclusions, which simulate the flow through a porous medium. This geometry is achieved with the LSF:

$$\phi(x, y) = \min_i \phi_i, \tag{3.122}$$

where

$$\phi_i(x, y) = r - \sqrt{(x - x_{c,i})^2 + (y - y_{c,i})^2}, \tag{3.123}$$

and $(x_{c,i}, y_{c,i})$ is the center of the i^{th} inclusion.

Consider the porous medium shown in Fig. 3.63. The porosity is symmetric about the bottom boundary and periodic vertically. The main parameter is the horizontal distance between the inclusions, L; all other dimensions are derived from it. The inlet is prescribed an inlet pressure, P_{in}, and the outlet, an outlet pressure, $p_{out} = 0$. The nondimensional inlet pressure boundary condition is set as:

$$\frac{\rho h^2}{\mu^2} p_{in} = 100. \tag{3.124}$$

The fluid-solid interface enforces the Kn-slip boundary condition. The problem is discretized with square elements elements, such that the mesh is N_e-by-$6N_e$, where N_e is the number of elements along the inlet and outlet.

We use a uniform mesh with $N_e = 91$ and set the ghost-penalty parameters as $\alpha_{GP,\mu} = \alpha_{GP,p} = 0.5$, the Nitsche parameter as $\alpha_{N,\boldsymbol{u}} = 1$, and consider various Kn numbers, $Kn = \{0,\ 0.01,\ 0.02,\ 0.03,\ 0.04,\ 0.05\}$. Note that setting $Kn = 0$ is equivalent to the no-slip boundary condition.

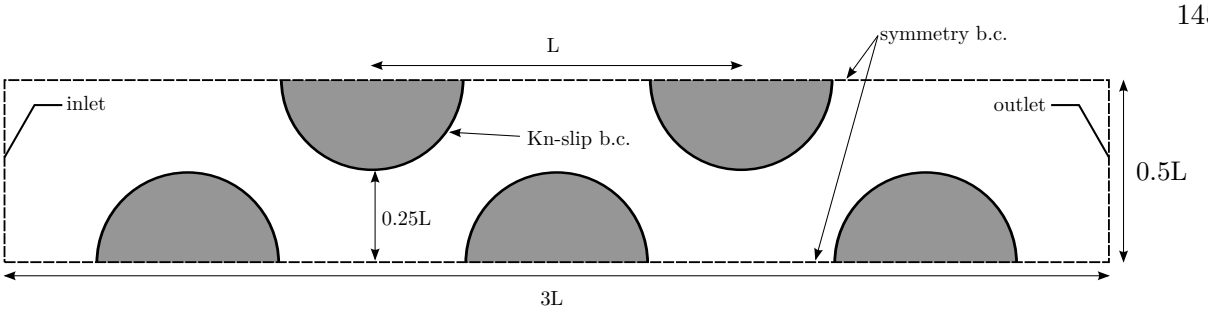

Figure 3.63: Porous Medium Description

Fig. 3.64 shows the nondimensional velocity magnitude in the fluid domain; the inclusions are removed for clarity. Similarly, Fig. 3.65 and 3.66 show the x- and y-component velocities. Note the increasing velocity at the fluid-solid interface and between inclusions. For a different perspective, Fig. 3.67 samples the velocities through the tangent line, $y = 0.25L$, which is tangent to each inclusion. This best shows the non-zero x-component velocity at the intersection points, i.e. the highest points of the bottom inclusions and the lowest points of the top inclusions. Naturally, $u_y = 0$ at these points because of the no-penetration boundary condition.

Now, we will focus on $Kn = 0.05$ and consider various Nitsche parameters, 10^0, 10^1, 10^2, 10^3, and 10^4. Fig. 3.68 and 3.69 show the x- and y-component velocity, respectively, sampled on the tangent line. We observe the oscillations appear when $\alpha_{N,\boldsymbol{u}} = 10^3$ and the divergent behavior when $\alpha_{N,\boldsymbol{u}} = 10^4$. Fig. 3.70a shows the L^2 error in the fluid velocity, where the reference solution is the solution with $\alpha_{N,\boldsymbol{u}} = 10^0$. Fig. 3.70b shows the relative mass loss through the channel, where:

$$\text{Rel. Mass Loss} = \frac{\dot{m}_{out} - \dot{m}_{in}}{\dot{m}_{in}}. \tag{3.125}$$

The relative mass loss is caused by the weak enforcement of the no-penetration boundary condition. This demonstrates the required balance in the Nitsche parameter: the Nitsche parameter should be chosen large enough to reduce the relative mass loss through the interface, but small enough so as to not introduce errors in the solution or a large L^2 error.

Secondly, we return the Nitsche parameter to $\alpha_{N,\boldsymbol{u}} = 1$ and consider various values for the viscous ghost-penalty parameter, 5×10^{-2}, 5×10^{-1}, $5 \times 10^{+0}$, $5 \times 10^{+1}$, and $5 \times 10^{+2}$. Fig. 3.71 and 3.72 show the x- and y-component velocities, respectively, through the $y = 0.25L$ tangent line.

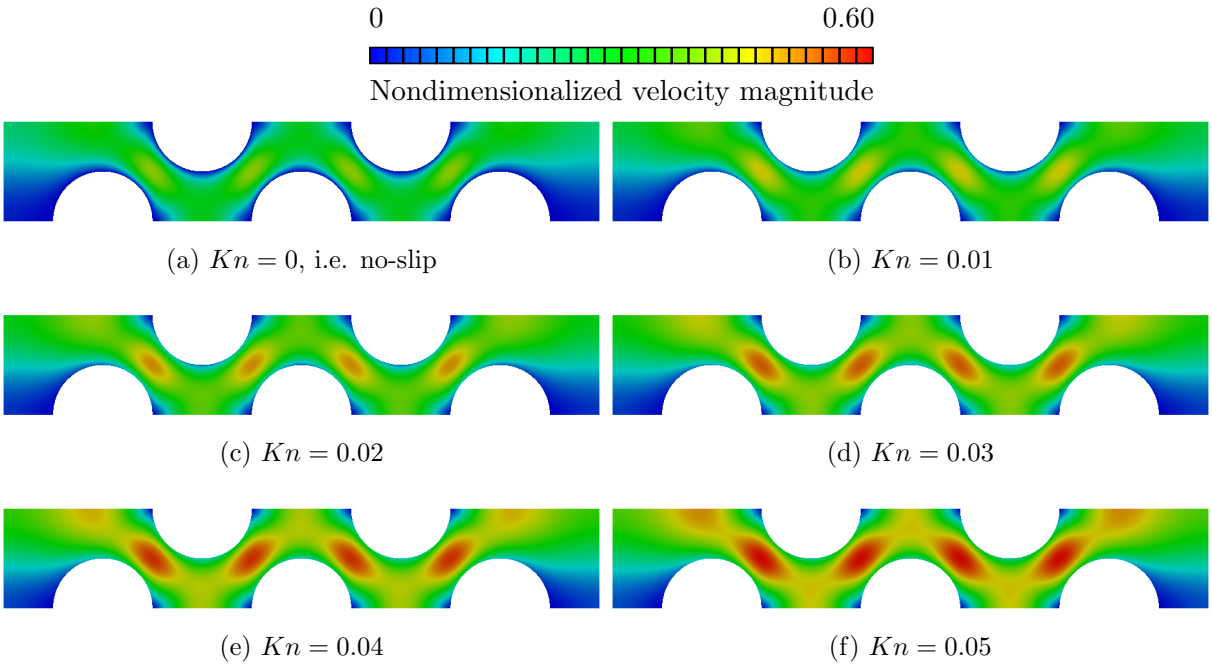

(a) $Kn = 0$, i.e. no-slip (b) $Kn = 0.01$

(c) $Kn = 0.02$ (d) $Kn = 0.03$

(e) $Kn = 0.04$ (f) $Kn = 0.05$

Figure 3.64: Velocity magnitude through the porous medium for various Kn numbers.

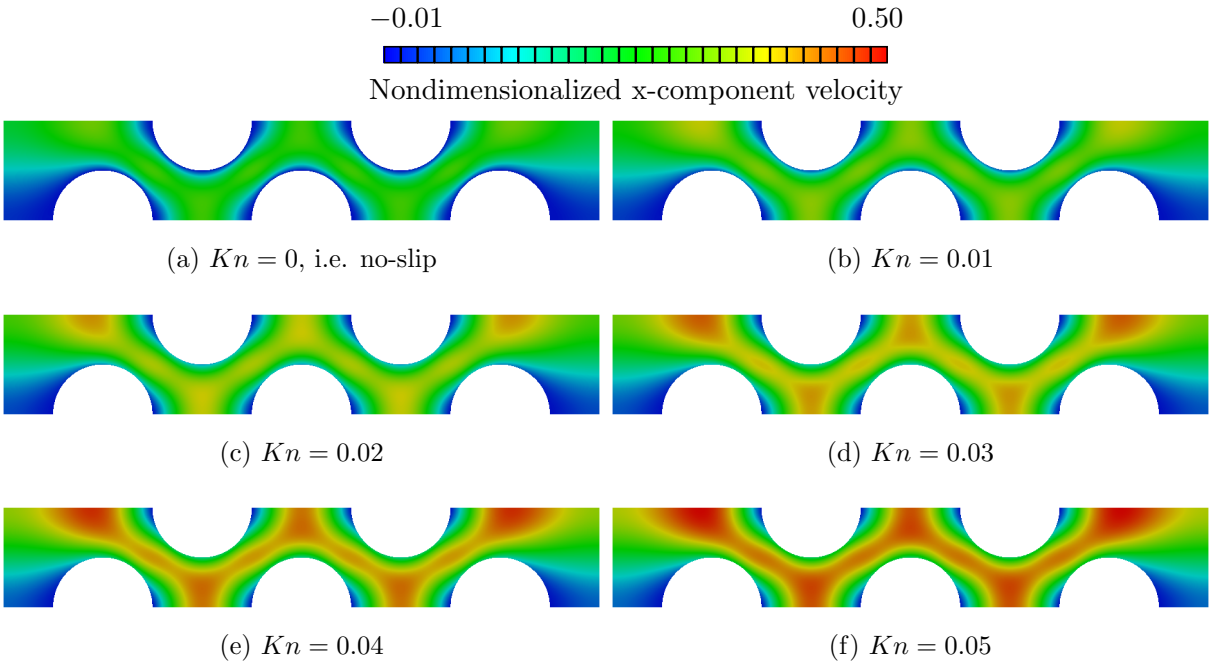

(a) $Kn = 0$, i.e. no-slip (b) $Kn = 0.01$

(c) $Kn = 0.02$ (d) $Kn = 0.03$

(e) $Kn = 0.04$ (f) $Kn = 0.05$

Figure 3.65: x-Component velocity through the porous medium for various Kn numbers.

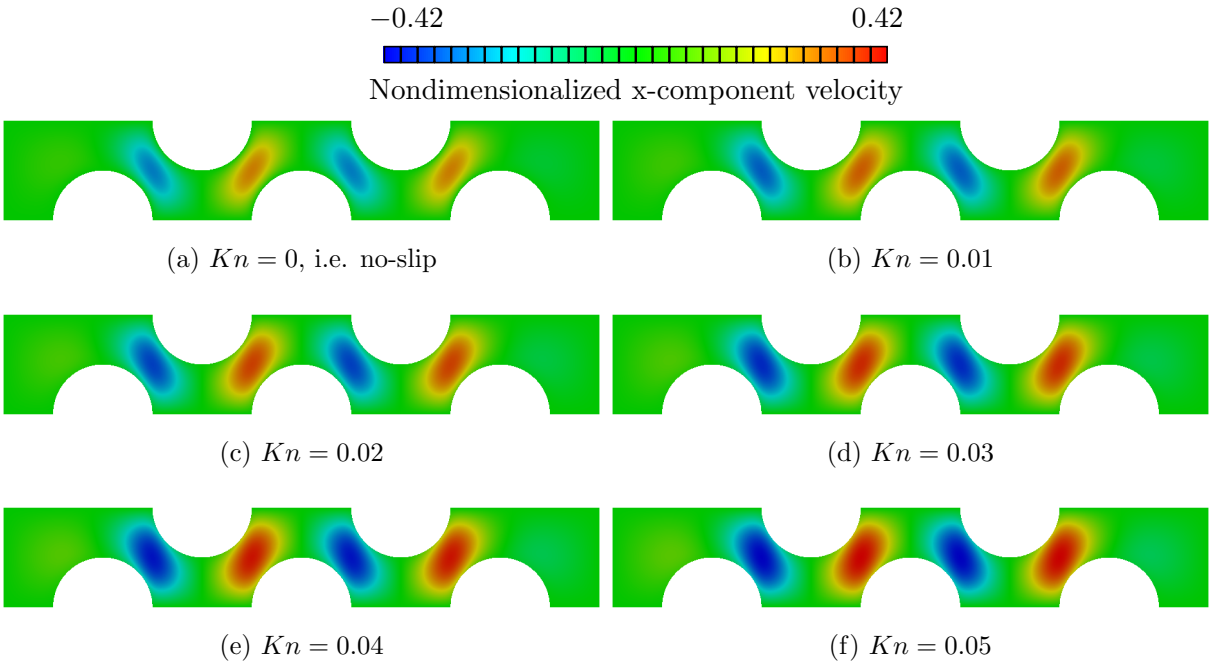

(a) $Kn = 0$, i.e. no-slip (b) $Kn = 0.01$

(c) $Kn = 0.02$ (d) $Kn = 0.03$

(e) $Kn = 0.04$ (f) $Kn = 0.05$

Figure 3.66: y-Component velocity through the porous medium for various Kn numbers.

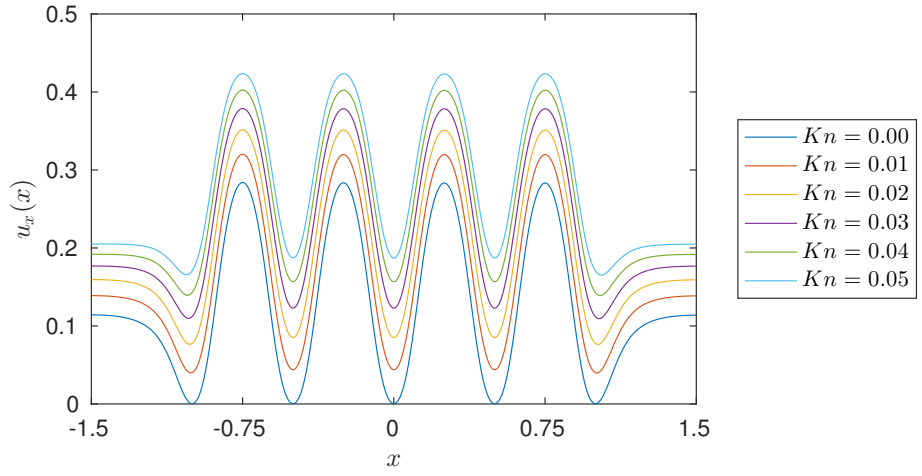

(a) $u_x(x, y = 0.25L)$

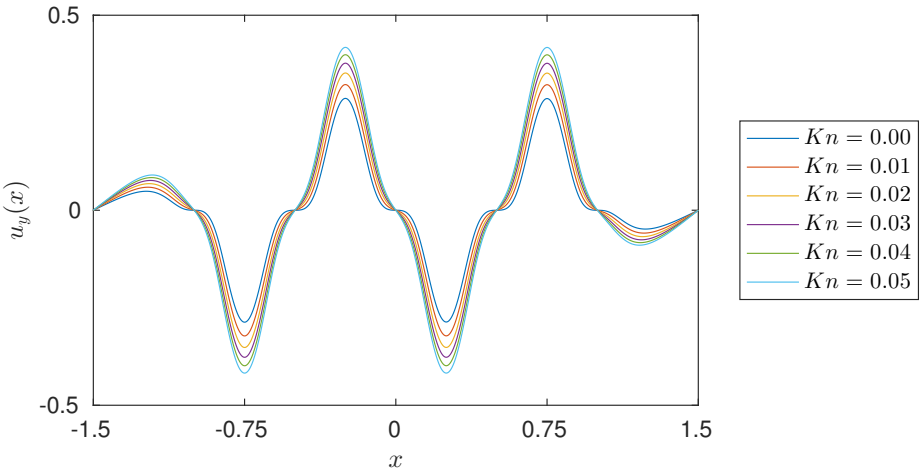

(b) $u_y(x, y = 0.25L)$

Figure 3.67: Velocity components through the $y = 0.25L$ tangent line for various Kn numbers.

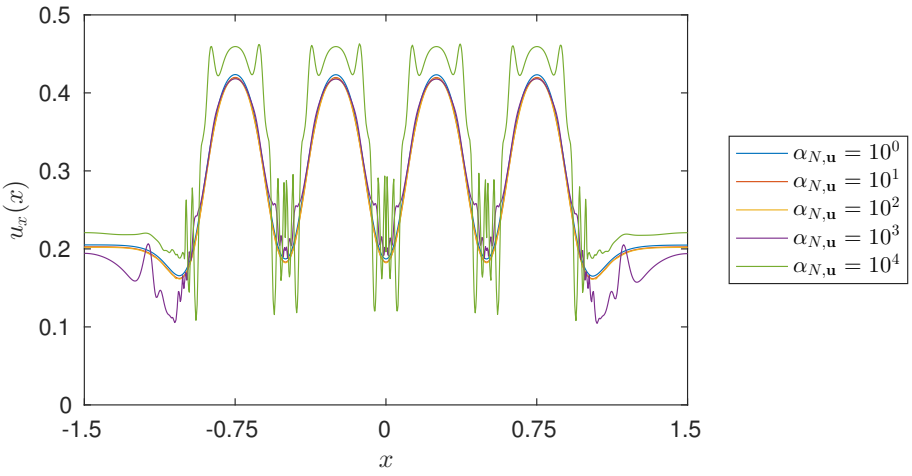

(a)

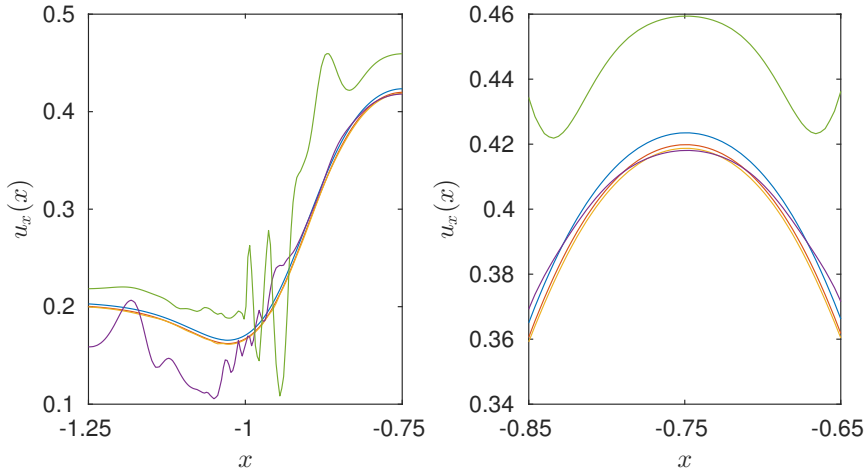

(b)

Figure 3.68: x-Component velocity through the $y = 0.25L$ tangent line for $Kn = 0.05$ and various values of $\alpha_{N,\boldsymbol{u}}$ (a) and select close-up views (b).

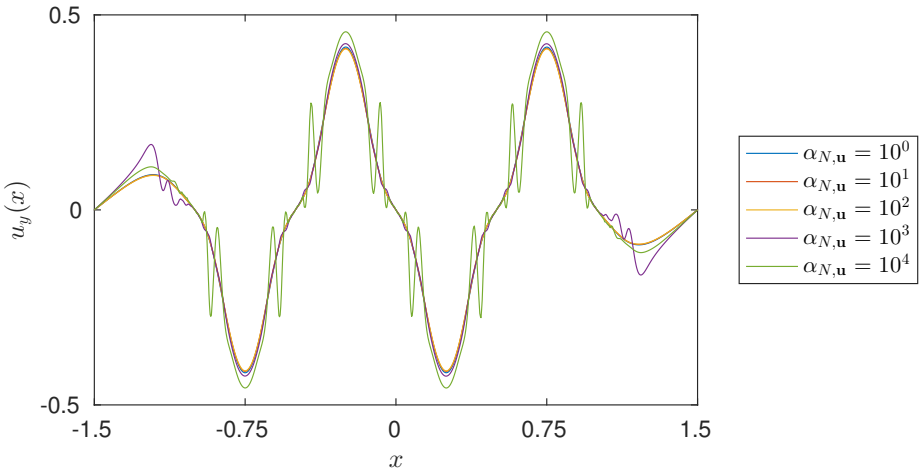

(a) $u_x(x, y = 0.25L)$

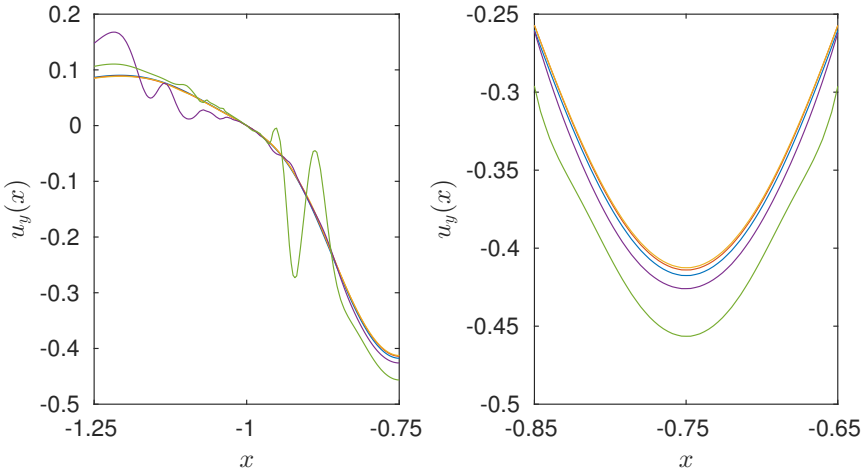

(b) $u_y(x, y = 0.25L)$

Figure 3.69: y-Component velocity through the $y = 0.25L$ tangent line for $Kn = 0.05$ and various values of $\alpha_{N,\boldsymbol{u}}$ (a) and select close-up views (b).

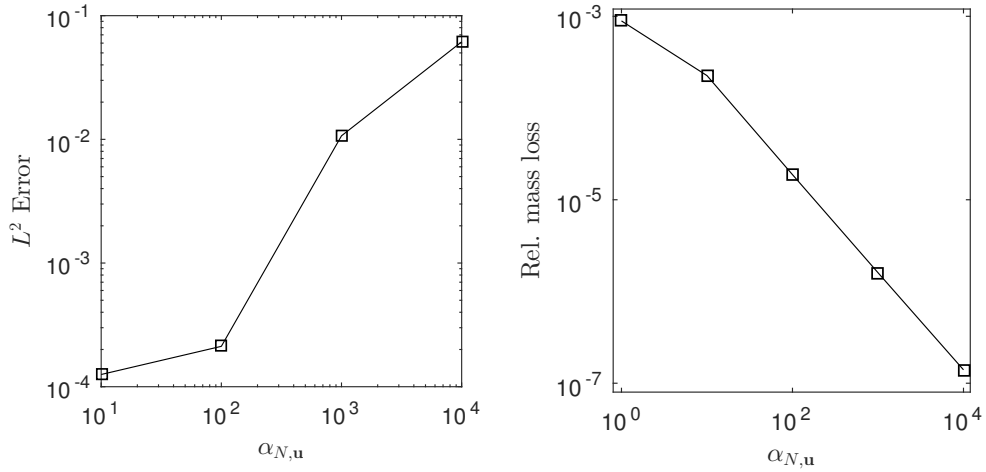

(a) L^2 Error

(b) Relative mass loss

Figure 3.70: L^2 error and relative mass loss in the velocity through the porous medium for $Kn = 0.05$ and various values of $\alpha_{N,\boldsymbol{u}}$.

In general, we cannot expect a solution to converge when the ghost-penalty parameter is zero. In this case, the results with $\alpha_{GP,\mu} = 0$ do converge; but the results with $\alpha_{GP,\mu} = 5 \times 10^{-2}$ display erroneous behavior. Otherwise, the velocity converge as the ghost-penalty parameter decreases. Fig. 3.73 shows the L^2 error, where reference solution is that with $\alpha_{GP,\mu} = 0$. This again illustrates the non-monotonic behavior of the ghost-penalty methods.

Finally, we sweep pressure ghost-penalty parameter, $\alpha_{GP,p}$, over the values 5×10^{-2}, 5×10^{-1}, $5 \times 10^{+0}$, $5 \times 10^{+1}$, and $5 \times 10^{+2}$. Fig. 3.74 and 3.75 show the x- and y-component velocities, respectively, and Fig. 3.76 shows the L^2 error in the velocity through the porous medium. Again, setting the parameter to 5×10^{-2} causes errors in the velocity; otherwise, the flow demonstrates smooth convergence as $\alpha_{GP,p}$ is decreased.

3.15 Conclusion

In Chapter 2, we studied the behavior of non-linear governing equations with the stabilization scheme used by Makhija and Maute [9]. The stabilization scheme was prohibitively diffusive on the non-linear equations and we expect that this behavior would continue for non-linear equations resulting from higher-order moment methods. Overcoming the diffusive effect of the stabilization scheme would require a level of mesh refinement not suitable for topology optimization. Instead of using higher-order moment methods to resolve flows in the Slip Regime, this Chapter introduced a slip boundary model to extend the applicability of the Navier-Stokes equations.

We extend the framework proposed by Villanueva and Maute [10] to accommodate the Kn-slip boundary condition. We then validate its implementation in problems with available analytical solutions and then show that the error in omitting the $\boldsymbol{J}_{\{n,t\}}$ terms from the Kn-slip boundary condition increases with the Kn number and the curvature of the fluid-solid interface. Finally, we study the behavior of the ghost-penalty method and find that increasing the ghost-penalty parameters mitigate spurious error in the velocity field; however, this behavior is non-monotonic. Thus, the ideal choice of ghost-penalty parameters is problem-dependent.

Having validated the implementation of the Kn-slip boundary condition and studied the

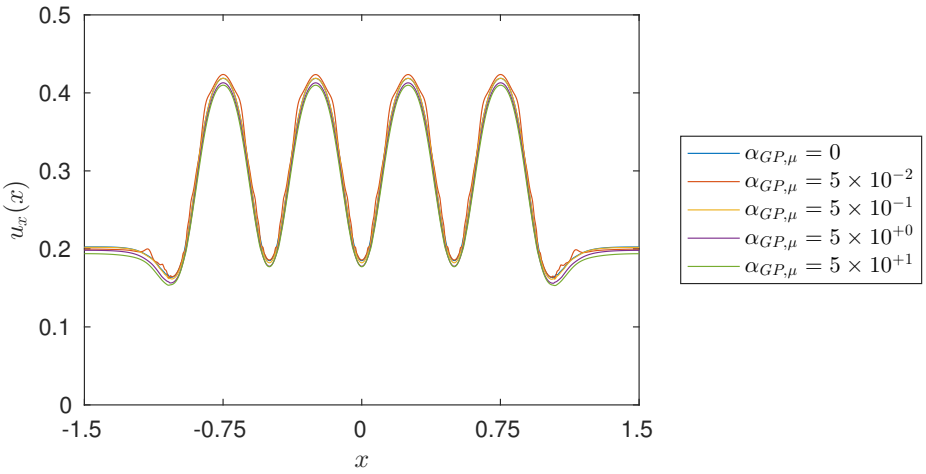

(a)

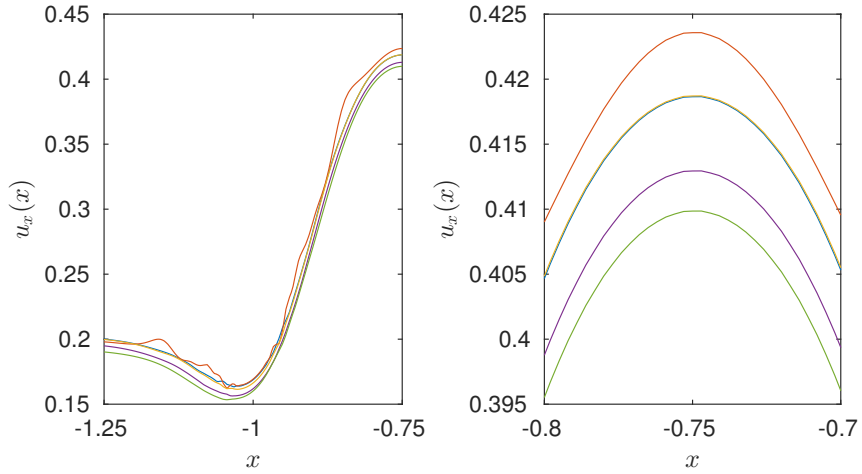

(b)

Figure 3.71: x-Component velocity through the $y = 0.25L$ tangent line for $Kn = 0.05$ and various values of $\alpha_{GP,\mu}$ (a) and select close-up views (b).

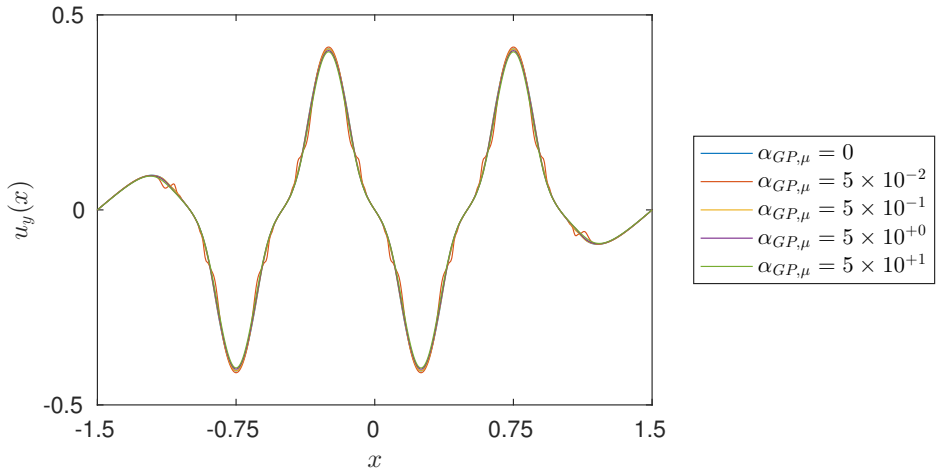

(a)

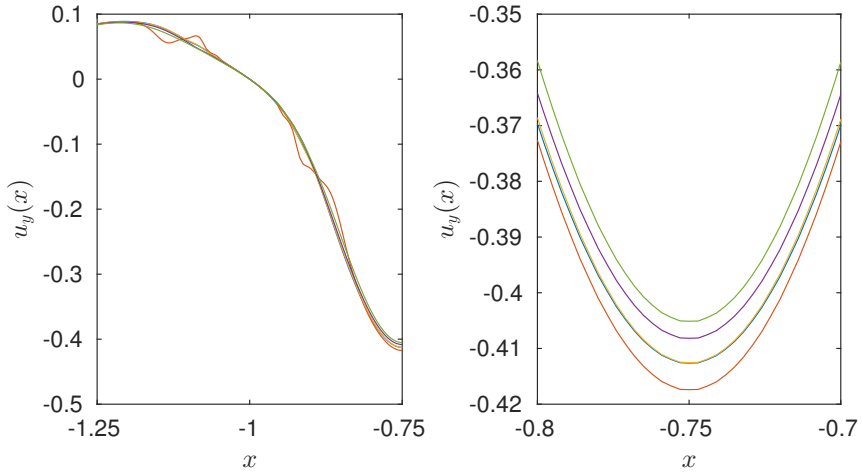

(b)

Figure 3.72: y-Component velocity through the $y = 0.25L$ tangent line for $Kn = 0.05$ and various values of $\alpha_{GP,\mu}$ (a) and select close-up views (b).

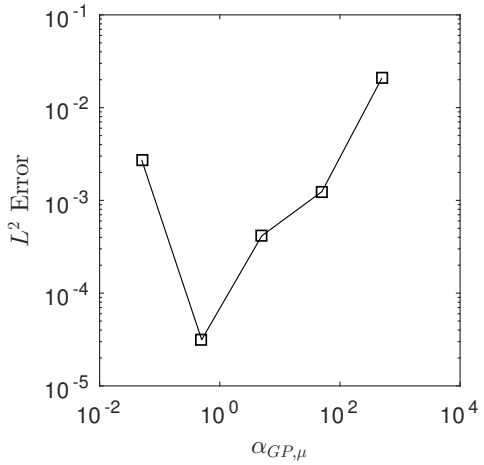

Figure 3.73: L^2 error in the velocity through the porous medium for $Kn = 0.05$ and various values of $\alpha_{GP,\mu}$.

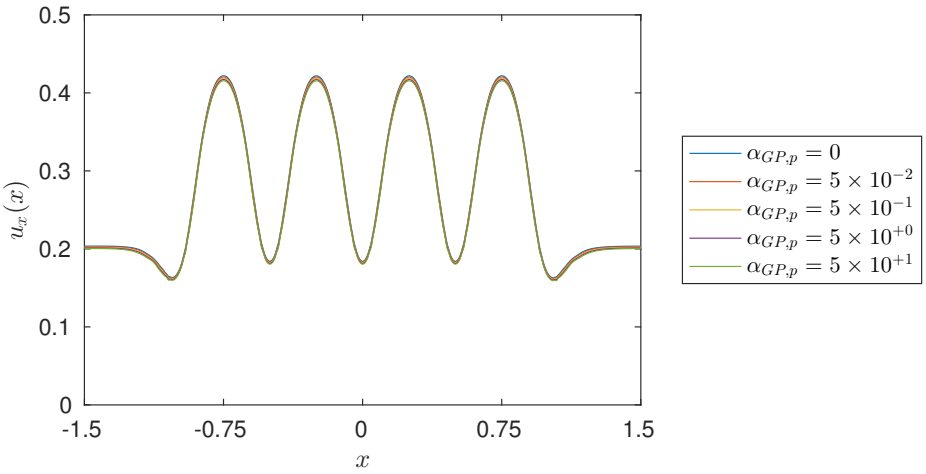

(a)

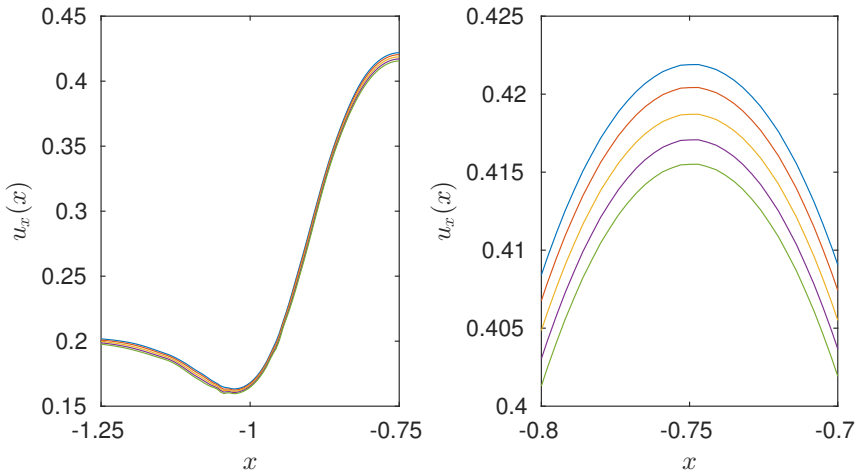

(b)

Figure 3.74: x-Component velocity through the $y = 0.25L$ tangent line for $Kn = 0.05$ and various values of $\alpha_{GP,p}$ (a) and select close-up views (b).

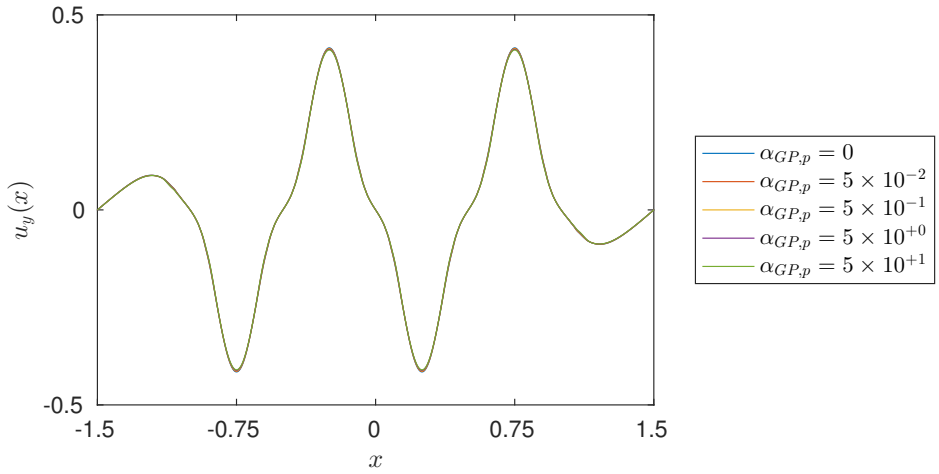

(a)

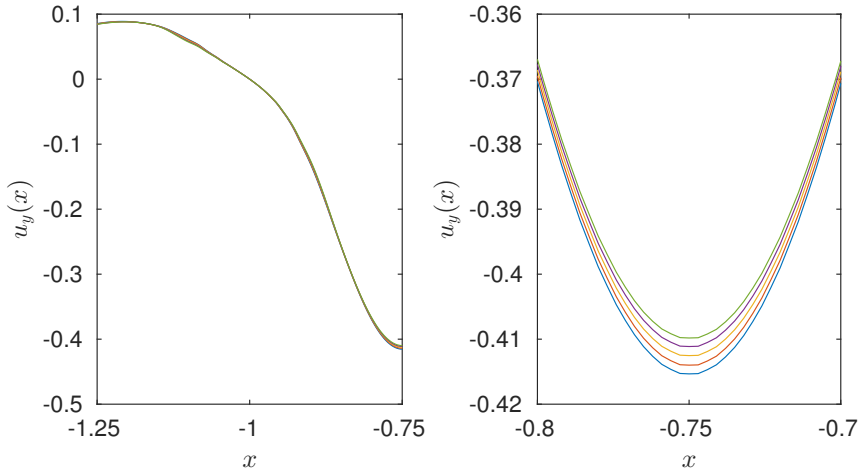

(b)

Figure 3.75: y-Component velocity through the $y = 0.25L$ tangent line for $Kn = 0.05$ and various values of $\alpha_{GP,p}$ (a) and select close-up views (b).

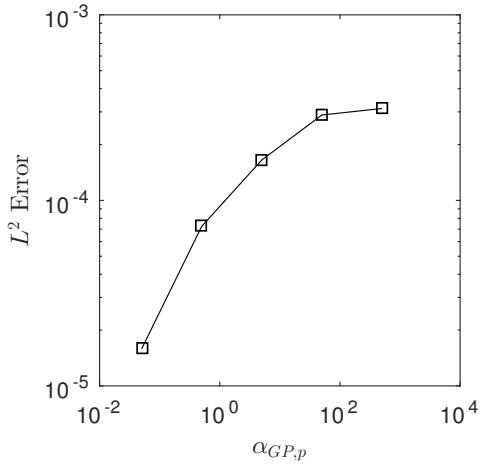

Figure 3.76: L^2 error in the velocity through the porous medium for $Kn = 0.05$ and various values of $\alpha_{GP,\mu}$.

influence of various parameters on the convergence of the flow solution and spurious errors, we are now ready investigate of the influence of the Kn number of the optimal design of various fluidic devices in the next Chapter.

Chapter 4

Topology optimization with the Kn-slip boundary condition

In this Chapter, we consider several topology optimization problems and show the effect of the Kn-slip boundary condition on the optimal designs. First, we present the optimization model; note that this is also shown in Section 2 of the manuscript found in Appendix C. Then, we consider the design of a splitting manifold. This work is found in in Section 5.4 of the manuscript in Appendix C, though a summary is provided here. Further, we consider the design of a Tesla valve in Section 5.5 of the manuscript in Appendix C and provide a summary here. Finally, we consider temperature-dependent problems in Sections 4.4 and 4.5.

4.1 Optimization model

The optimization problems considered in this work are formulated with respect to an objective and one or more constraints. The objective and constraints are defined in terms of design criteria, such as mass flow rate, pressure differences, fluid volume, etc. These design criteria can depend explicitly on the state and optimization variables, e.g. mass flow rate, or only on the optimization variables, e.g. fluid volume. The formulation for this type of optimization problem takes the form:

$$\begin{aligned} &\min_{\boldsymbol{s}} \mathcal{Z} = z(\boldsymbol{s}, \boldsymbol{u}(\boldsymbol{s})) \\ &\quad \text{s.t. } g_i(\boldsymbol{s}, \boldsymbol{u}) \leq 0, i = 1...N_g \\ &\boldsymbol{s} \in \boldsymbol{S} = \{\mathbb{R}^{N_s} | s_i^L \leq s_i \leq s_i^U, i = 1...N_s\} \\ &\boldsymbol{u} \in \boldsymbol{U} = \{\mathbb{R}^{N_{\boldsymbol{u}}} | R(\boldsymbol{s}, \boldsymbol{u}) = 0\}, \end{aligned} \tag{4.1}$$

	Value
Relative step size	0.01
Minimum asymptote adaptivity	0.5
Initial asymptote adaptivity	0.7
Maximum adaptivity	1.43
Constraint penalty	100

Table 4.1: GCMMA parameters for the topology optimization problems.

where $\boldsymbol{s}$ is the vector of optimization variables, of size N_s, and $\boldsymbol{u}$ is the vector of state variables, of size $N_{\boldsymbol{u}}$. $\mathcal{Z}$ is a function of the criteria to be optimized and includes a perimeter regularization term; for a discussion on the use of the perimeter as a regularization term, see Section 4.1.1. The function g_i is the i-th inequality constraint, and N_g is the number of constraints. The optimization variables s_i are bounded by lower and upper limits, s_i^L and s_i^U, respectively. The state variables satisfy the residual of the governing equations, $R(\boldsymbol{s}, \boldsymbol{u}) = 0$.

The optimization problem (4.1) uses a gradient-based algorithm, and the gradients of the objective and constraint functions with respect to the optimization variables, s_i, are computed via the adjoint method. In this paper, we adopt the discrete adjoint formulation for nonlinear fluid systems of Kreissl et al. [92] and Golmon et al. [93]. The problems are solved via the Globally Convergent Method of Moving Asymptotes (GCMMA) of Svanberg [94]. The GCMMA parameters are given in Table 4.1. The stopping criteria for the optimization are: (i) the change in the objective value relative to the previous value is less than 10^{-6}, and (ii) all constraints are satisfied.

4.1.1 Optimization Criteria

The objective and constraints described in Section 4.1 make use of geometric or state-dependent criteria. The two state-independent criteria are the perimeter of the fluid-solid interface and the volume of the fluid inside the design domain, defined as:

$$\mathcal{P} = \int_{\Gamma^{fs}} \mathrm{d}\Gamma \tag{4.2}$$

and

$$\mathcal{V}^{fd} = \int_{\Omega^f \cap \Omega^d} \mathrm{d}\Omega, \tag{4.3}$$

respectively. Minimizing the perimeter, either as a penalty in the objective function or as a constraint, discourages the appearance of small geometric features or oscillatory shapes during the optimization process. While a perimeter penalty does not explicitly control the local shape or feature size [81], it is effective in regularizing flow optimization problems [32, 59].

State-dependent criteria are defined over a part of the external fluid boundary, $\Gamma_i^f \in \Gamma^f$. The mass flow rate through a port is defined as:

$$\dot{m}_i = \int_{\Gamma_i^f} \rho^f \left(\boldsymbol{u}^f \cdot \hat{\boldsymbol{n}} \right) \mathrm{d}\Gamma, \tag{4.4}$$

and the total pressure on a port surface is defined as:

$$\mathcal{T}_i = \int_{\Gamma_i^f} \left(p^f + \frac{\rho^f |\boldsymbol{u}^f|^2}{2} \right) \mathrm{d}\Gamma. \tag{4.5}$$

In temperature-dependent problems, the thermal energy rate through a port is defined as:

$$\dot{e}_i = \int_{\Gamma_i^f} \rho^f c_p^f \left(\boldsymbol{u}^f \cdot \boldsymbol{n} \right) T^f d\Gamma. \tag{4.6}$$

4.2 Design of a splitting manifold

We consider the design of a splitting manifold in Section 5.4 of the manuscript in Appendix C. The problem setup and initial design is shown in Fig. 4.1. The objective is to maximize the mass flow rate through the manifold, which is equivalent to minimizing the total pressure difference given an inlet velocity distribution, subject to requiring specific mass flow rate ratios through the outlets. The objective is thus:

$$\mathcal{Z} = -\frac{\sum\limits_{i \in \{1a \ldots 2b\}} \dot{m}_{out,i}}{\sum\limits_{i \in \{1a \ldots 2b\}} \dot{m}^0_{out,i}} + w_{\mathcal{P}} \frac{\mathcal{P}}{\mathcal{P}^0}, \tag{4.7}$$

where the superscript "0" denotes the values of the initial design, the subscript i denotes the i-th outlet, and $w_{\mathcal{P}}$ is a constant scaling factor. Unless otherwise noted, $w_{\mathcal{P}} = 0.1$.

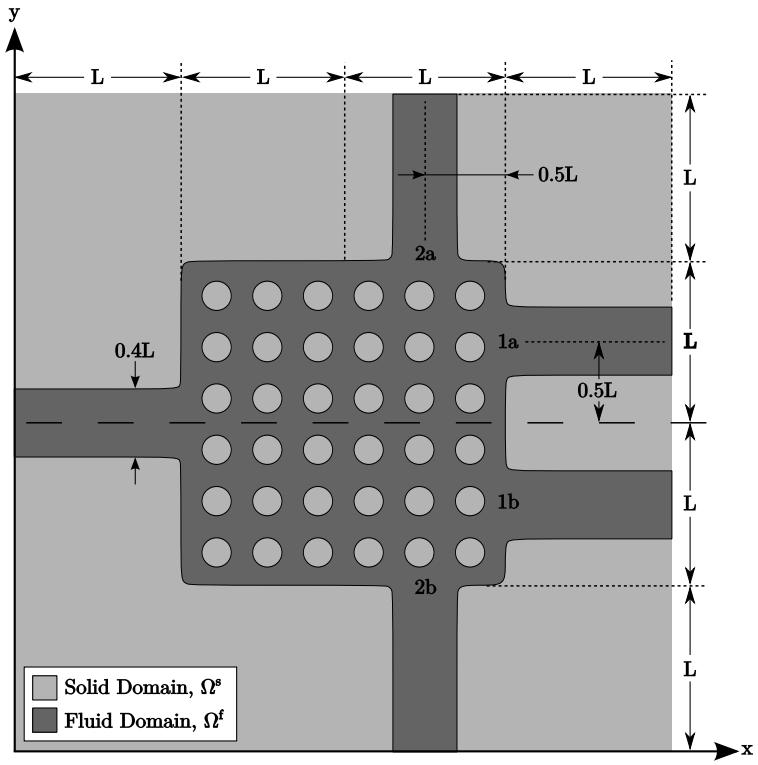

Figure 4.1: Problem setup for the splitting manifold problem.

The fluid volume inside the design domain is constrained to a fraction, $f_{\mathcal{V}}$, of the design domain to suppress trivial solutions and to promote the formation of distinct fluid channels:

$$g_1 = \frac{\mathcal{V}^{fd}}{f_{\mathcal{V}}\mathcal{V}^{d}} - 1. \tag{4.8}$$

Further, we wish to specify the ratio of the outlet mass flow rates. Given that the GCMMA algorithm does not allow equality constraints, we recourse to imposing inequality constraints with lower and upper limits on the mass flow rates. The lower and upper inequality constraint on the i-th outlet are given as:

$$g_{i+1} = \frac{(1-\tau)f_i\dot{m}_{in} - \dot{m}_{out,i}}{\dot{m}^0_{in}} \tag{4.9}$$

and

$$g_{i+5} = \frac{-(1+\tau)f_i\dot{m}_{in} + \dot{m}_{out,i}}{\dot{m}^0_{in}}, \tag{4.10}$$

respectively, where τ is a small tolerance value, f_i is the desired fraction of the total mass flow rate through outlet i, and $\sum f_i = 1$. Note that the tolerance on the outlet mass flows is such that each is allows to be within $\pm\tau f_i\dot{m}_{in}$ of the desired value. Unless otherwise stated, $\tau = 0.005$.

The results of this optimization study are shown in Section 5.4 of the manuscript in Appendix C, which discusses them in further detail. Presently, we summarize our findings as follows: (i) Including the Kn-slip boundary condition during the optimization process leads to slightly different optimal designs. Using a design obtained with the no-slip condition when the Kn number is finite leads to a sub-optimal performance in terms of the total mass flow rate and may result in violated flow rate ratio requirements. Our results suggest that when the Kn number is finite, the Kn-slip boundary condition should be included during the optimization process; however, the error due to ignoring it remains small for smaller Kn numbers. However, we expect that this error will become significant as the Kn number increases. These findings are further discussed in Section 5.4.1 in the manuscript in Appendix C. (ii) For $Kn > 10^{-3}$, designs obtained with the no-slip boundary condition begin to perform differently when analyzing with the Kn-slip boundary condition. This is is further described in Section 5.4.2 in the manuscript. (iii) Finally, we find that the $\boldsymbol{J}_{\{n,t\}}$ are similarly important in terms of design and performance. Our study suggests that omitting the

$\boldsymbol{J}_{\{n,t\}}$ terms from the Kn-slip condition results in similar errors as ignoring the Kn-slip boundary condition altogether. Thus, when the Kn is large enough that the Kn-slip boundary condition should not be ignored, the $\boldsymbol{J}_{\{n,t\}}$ terms should also be included.

4.3 Design of a Tesla valve

A Tesla valve allows fluid flow in one direction but restricts it when reversed. Experimentally, flow is achieved by enforcing a velocity distribution at the inlet, e.g. the inlet in the forward flow becomes the outlet in the reverse flow, or by enforcing a pressure difference between ports. In the case where a velocity distribution is used, the valve's property of allowing and restricting flow is captured in its diodicity, defined as:

$$Di = \frac{\Delta \mathcal{T}^{fwd}}{\Delta \mathcal{T}^{rev}} = \frac{\mathcal{T}^{fwd}_{\Gamma^f_1} - \mathcal{T}^{fwd}_{\Gamma^f_2}}{\mathcal{T}^{rev}_{\Gamma^f_2} - \mathcal{T}^{rev}_{\Gamma^f_1}}, \tag{4.11}$$

where $\mathcal{T}^{fwd}_{\Gamma^f_i}$ is the total pressure at port i with flow in the forward direction and similarly for $\mathcal{T}^{rev}_{\Gamma^f_i}$ in the reverse direction, and Γ^f_1 and Γ^f_2 are the external surfaces of the two ports. By this definition, $Di < 1$; smaller values of Di indicate valves that further restrict the reverse flow. Some works define the diodicity as the inverse of that defined here, e.g. [95].

For a shape optimization study of the traditional Tesla valve, shown in Fig. 4.2, the reader is referred to Gamboa et al. [96]. Alternatively, a Tesla valve can have axially aligned ports, which was studied for small Re by Deng et Re by Lin et al. [95]. Finally, it is also possible to consider valves with axially aligned but offset ports, as depicted in Fig. 4.5. The example in this paper is similar to the one previously studied by Pingen et al. [97].

4.3.1 Analysis of a Traditional Valve

The traditional Tesla value, shown in Fig 4.2, features a 45°-bend and a redirecting manifold. The radii of the redirecting manifold are given with respect to the reference length, $r = 0.2L$ and $R = 0.4L$. We consider this design for various Re using an unstructured body-fitted mesh, shown

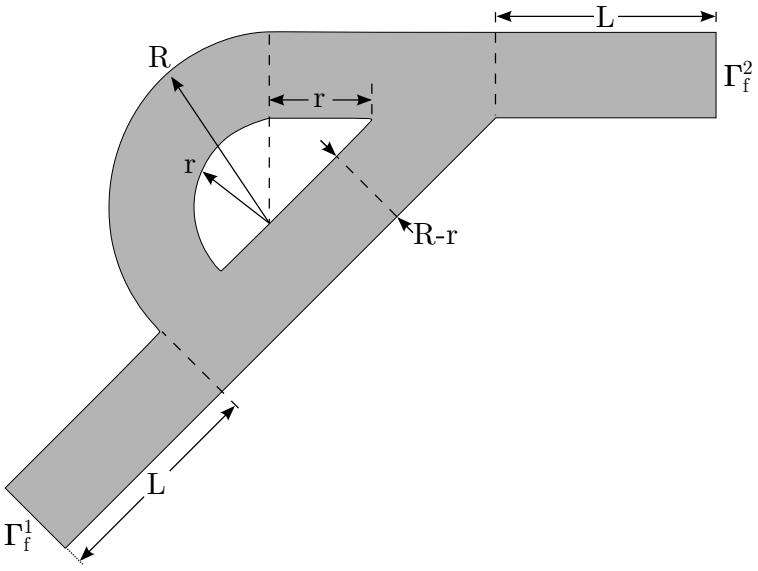

Figure 4.2: Traditional Tesla valve design.

in Fig. 4.3. The mesh is formed such that the ports, i.e. the width denoted $R - r$, are discretized with 31 elements.

Fig. 4.4 show the flow solution for the forward and reverse flows through the traditional Tesla value, for various Re numbers; these agree with those reported in [98]. For small Re numbers, there is no appreciable difference in the forward and reverse flow (aside from direction); however, for larger Re above 100, the manifold begins to truly prohibit the reverse flow. This is likewise shown in the manuscript in Appendix C; here, we append the results with $Re = 1$ and make the figure larger for an easier comparison.

The diodicity of this design is given in Table 4.2. For large Re numbers, the traditional Tesla valve offers considerably favorable diodicities. However, for smaller Re numbers in the range that would also have finite Kn numbers, see Section 3.9.1, the diodicity is very near unity: a new design is needed for low Re numbers.

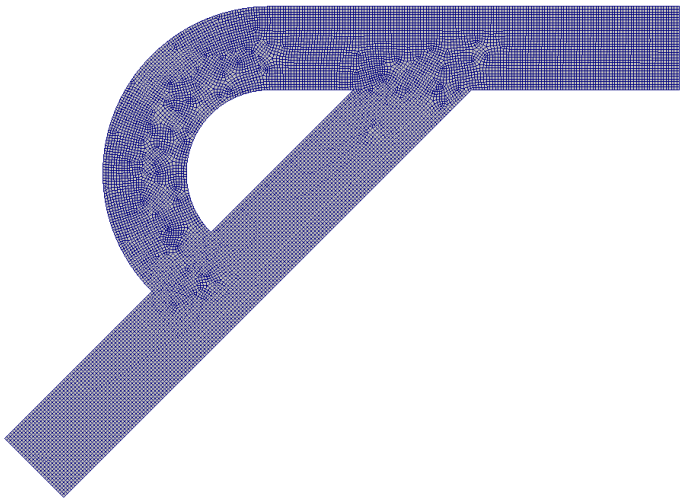

Figure 4.3: Body-fitted unstructured mesh for the traditional Tesla valve.

Re	Di
1	0.999994
10	0.999993
50	0.999831
100	0.996436
200	0.967686
500	0.816144

Table 4.2: Diodicity of the traditional Tesla valve for various Re numbers.

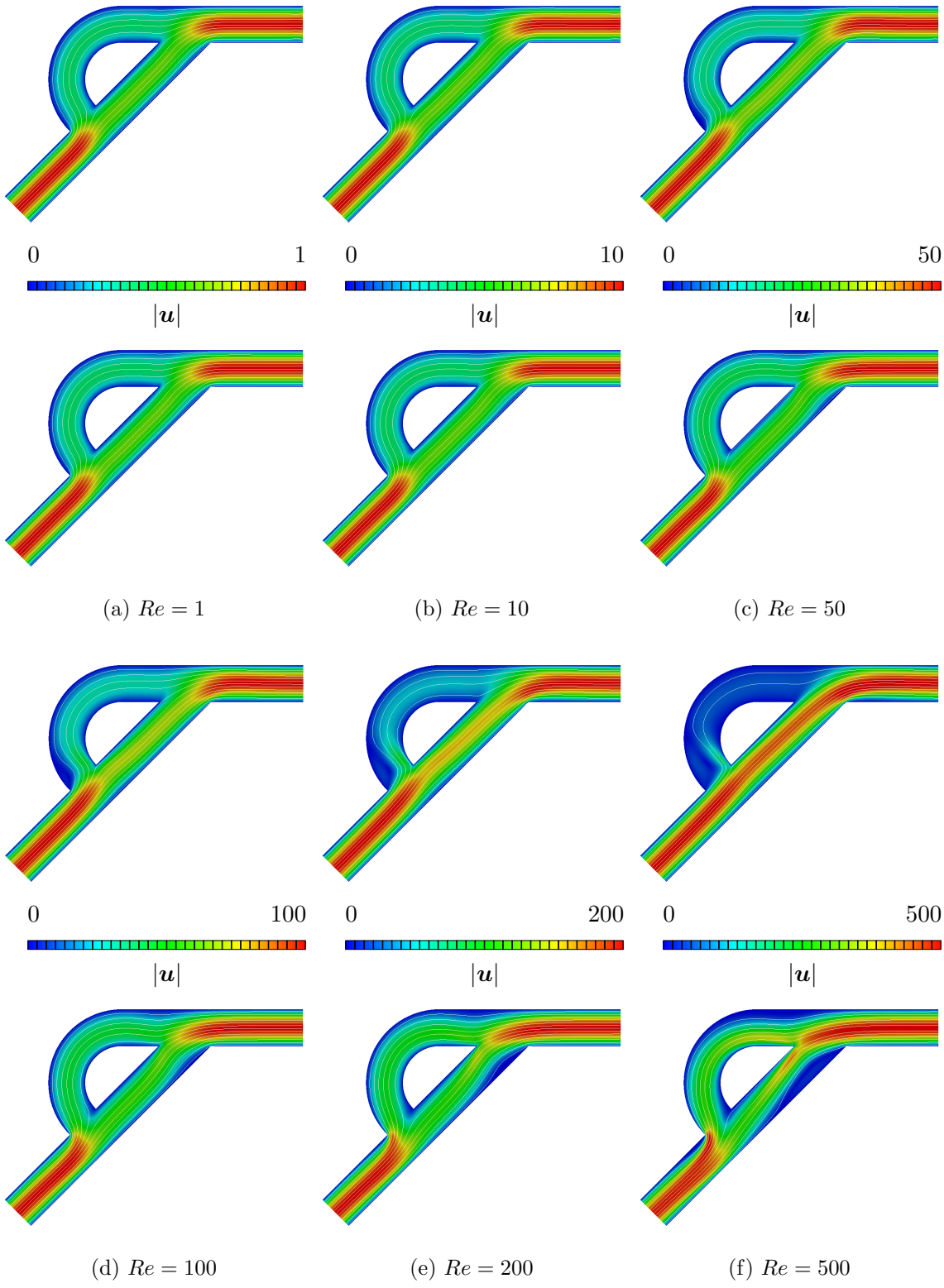

(a) $Re = 1$ (b) $Re = 10$ (c) $Re = 50$

(d) $Re = 100$ (e) $Re = 200$ (f) $Re = 500$

Figure 4.4: Velocity magnitude and streamlines in the forward (top) and reverse (bottom) flows through the traditional Tesla valve for various Re numbers.

4.3.2 Optimization

In this work, we formulate the optimization problem as in (4.1), where:

$$\mathcal{Z} = \frac{\Delta\mathcal{T}^{fwd}}{\Delta\mathcal{T}^{0}} + w_{\mathcal{P}}\frac{\mathcal{P}}{\mathcal{P}^{0}}, \tag{4.12}$$

where the superscript "0" denotes the values of the initial design and $w_{\mathcal{P}}$ is a constant scaling factor. A constraint on the diodicity is given by:

$$g_1 = \frac{\Delta\mathcal{T}^{fwd}}{\Delta\mathcal{T}^{rev}} - Di^*, \tag{4.13}$$

where Di^* is a chosen target diodicity. We seek to reproduce the diodicity at $Re = 200$ of the traditional Tesla valve but at $Re = 40$, where the incompressibility condition, (3.101), allows for $Kn = 0.01$; thus, the target diodicity is set to $Di^* = 0.97$. Finally, a volume constraint (4.8) may be included to discourage trivial solutions. While the optimization problem can alternatively be defined to minimize the valve's diodicity, e.g. [95], this paper follows the formulation found in [98], which performed a topology optimization using density methods for low Re number flows with no-slip boundary conditions. The problem setup is shown in Fig. 4.5.

In Section 5.5 of the manuscript in Appendix C, we perform a topology optimization for various volume constraint cases with the no-slip and Kn-slip with $Kn = 0.01$ boundary conditions. We summarize our observations as follows: (i) While this work is not meant to provide design guidelines, we observe that, when the Kn-slip boundary condition is enforced during the design process, the optimizer makes smaller recirculation regions and uses less pronounced constrictions in the valve. (ii) While differences in design and performance were small in the manifold problem, the differences in performance in this example are more pronounced. In most cases, there is a 23% drop in performance when a design is optimized with the no-slip boundary condition and subsequently analyzed with the Kn-slip boundary condition. This is analogous to designing a Tesla valve for an application where $Kn = 0.01$ but the Kn-slip boundary condition is ignored during the design optimization process. (iii) Our study suggests that if the geometry and fluid properties of the problem lead to a finite Kn number, the Kn-slip boundary should be enforced during the

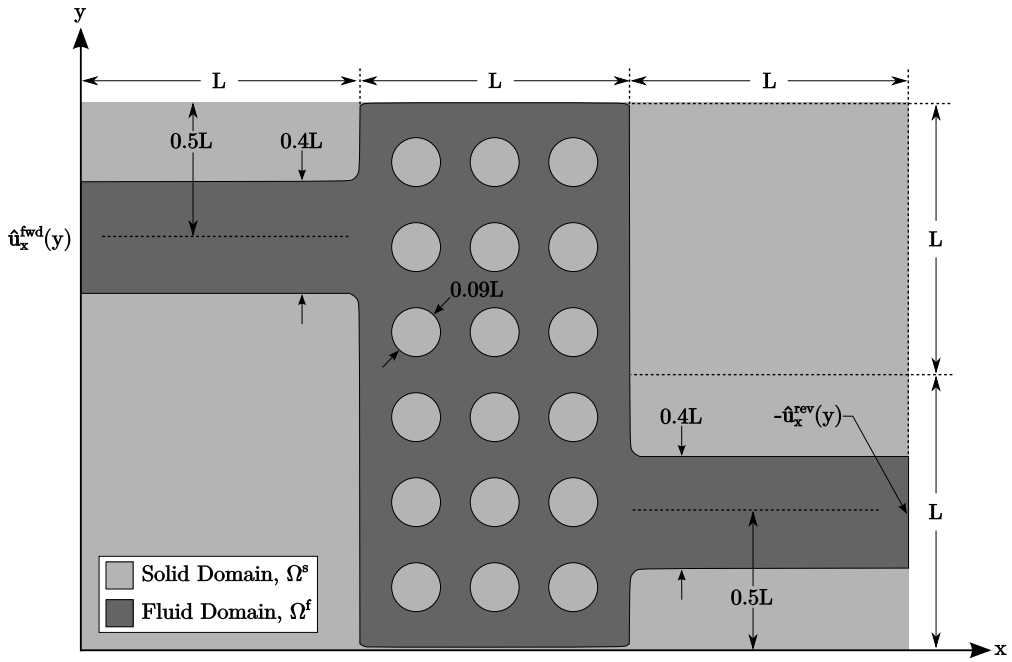

Figure 4.5: Problem setup for the Tesla valve problem.

optimization process.

4.4 Optimal number and layout of fins

In this Section, we consider the effects of the Kn-slip boundary condition on the design of an array of heated fins, whose goal is to heat incoming cool fluid. First, we motivate an optimization problem with an analysis of an array of elliptical fins, similar to the work of Laniewski-Wołłk [99]. We then consider a shape optimization example.

4.4.1 Analysis

We consider the flow past an array of heated fins, such that n_F fins are equally spaced over a unit section of height H. An example of this problem setup with $n_F = 3$ is shown in Fig. 4.6. The fins are elliptically shaped and have flow-wise width, w, and thickness, t. The channel length is set as $L = H$. Dashed lines denote symmetric boundary conditions and the fluid-solid interface enforces no-slip or Kn-slip with $Kn = 0.01$ boundary conditions. The outlet is given a traction-free boundary condition and the inlet is given a pressure Dirichlet boundary condition such that:

$$p_{in} = 1.5 \times 10^3. \tag{4.14}$$

The fluid properties are set as $\rho = 1.205$, $\mu = 1.511 \times 10^{-5}$, $c_p = 1.005 \times 10^3$, and $\kappa = 2.57 \times 10^{-2}$, and the channel height is set as $H = 5.356 \times 10^{-6}$. The fins are realized with the LSF:

$$\phi(x, y) = \max_i \phi_i(x, y), \tag{4.15}$$

where

$$\phi_i(x, y) = 1 - \sqrt{\left(\frac{2(x - x_{c,i})}{w}\right)^2 + \left(\frac{2(y - y_{c,i})}{t}\right)^2}. \tag{4.16}$$

The fins are vertically aligned; thus $x_{c,i} = 0$. The centers of the fins are such that $y_{c,i+1} - y_{c,i} = H/n_F$. Finally, the fins are uniformly heated to T_H and the incoming fluids enters the channel with temperature $T_{in} = T_L$. In this problem, $T_L = 300K$ and $T_H = 600K$.

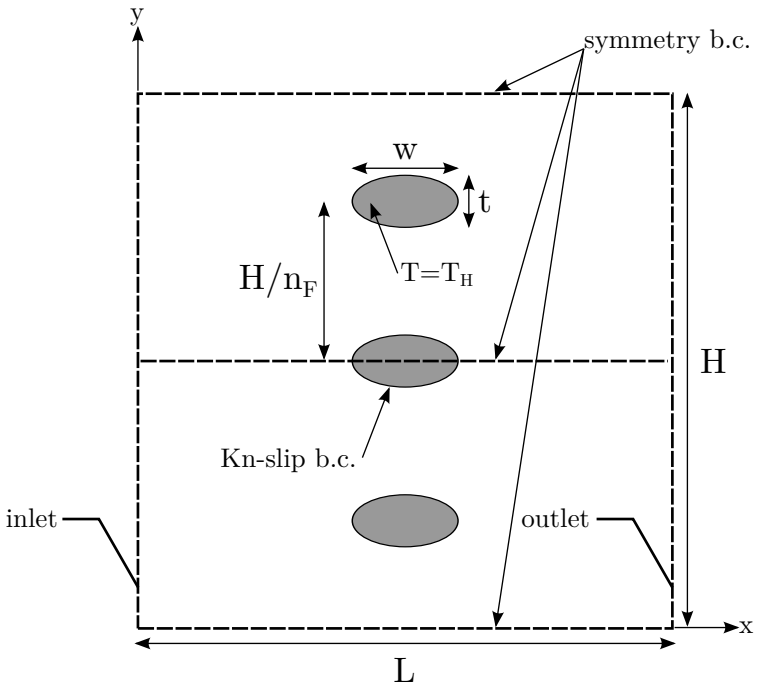

Figure 4.6: Problem setup for flow through heated fins. This example has $n_F = 3$.

We consider the flow past an array of 1, 2, 3, 4, and 5 fins with thickness $0.01H$, $0.03H$, and $0.05H$ with the no-slip and Kn-slip boundary conditions. Fig. 4.7 shows the mass flow rate and energy flow rate for various number and thickness of fins. As the number of fins or the fin thickness increases, the mass flow rate decreases as the flow is further obstructed. However, the energy flow rate increases initially due of the increasing heating surface area. We note that the optimal number of fins is 3 regardless of the type of boundary condition used. However, the optimal thickness is $0.01H$ when using the no-slip condition and $0.03H$ when using the Kn-slip condition. Because of the increased fluid momentum from the slip effect, the fins have a reduced opportunity to heat the fluid; thus, thicker fins are required to (i) impede the flow and (ii) increase the available heating surface area.

4.4.2 Optimization

We now consider this problem within the context of topology optimization. The goal is again to heat incoming fluid; thus, we formulate the optimization problem (4.1) as:

$$\mathcal{Z} = \frac{\dot{e}}{\dot{e}^0} + w_{\mathcal{P}} \frac{\mathcal{P}}{\mathcal{P}^0}, \tag{4.17}$$

where the superscript "0" denotes the values of the initial design and $w_{\mathcal{P}}$ is a constant scaling factor. The energy flow can be maximized by (i) increasing the temperature component in (4.6) or (ii) increasing the flow rate component. A volume constraint on the solid phase is enforced as:

$$g_1 = \frac{\mathcal{V}^s}{f_{\mathcal{V}} \mathcal{V}^d} - 1. \tag{4.18}$$

Here, we use $f_{\mathcal{V}} = 0.50$. The objective has conflicting contributions; on one hand, removing solid material will improve the mass flow rate but weakening the fins' ability to heat the fluid. These influences are not balanced, and the optimizer heavily favors material. To mitigate this, we enforce a minimum heating constraint in the form of:

$$\frac{\dot{e}}{c_p \dot{m}} > T^*, \tag{4.19}$$

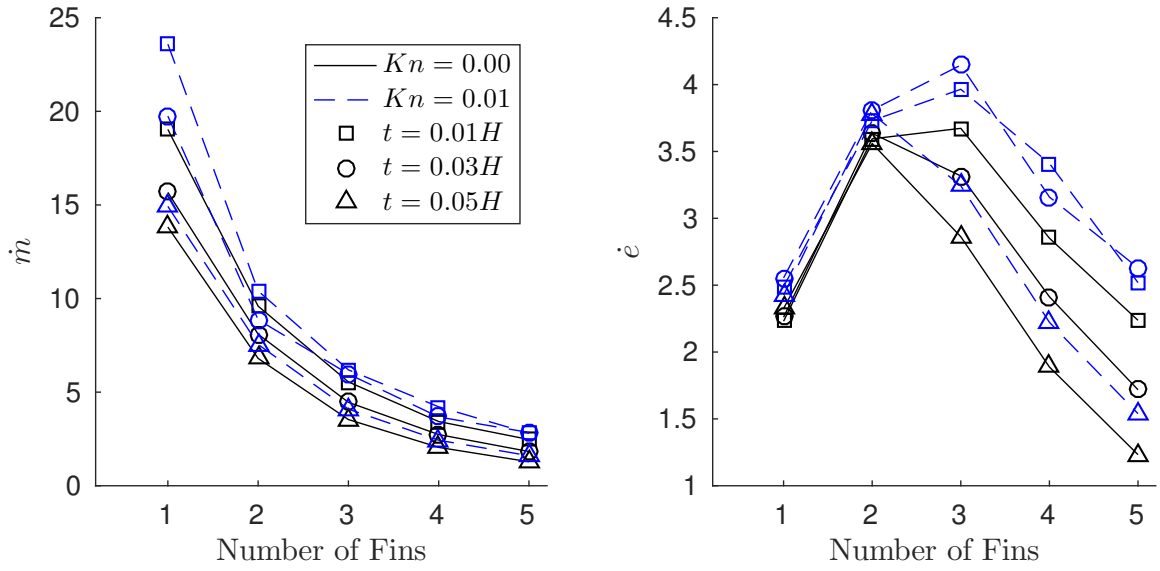

Figure 4.7: Mass (a) and energy flow rate (b) past a various number of fins with several thickness values.

which we write as:

$$g_2 = \frac{c_p T^* \dot{m} - \dot{e}}{\dot{m}^0}. \tag{4.20}$$

The problem setup is shown in Fig. 4.8. The design domain, $\Omega^d = \{-0.5L \leq x \leq 0.5L,\ -0.5H \leq y \leq 0.5H$, is the center region of the flow domain and is initialized with a 3×1 array of circular inclusions of radii $0.05H$. The center inclusion is forced to be solid, while the rest of the design domain is free to be solid or fluid. Dashed lines denote the planes of symmetry; the unit design is symmetry about the $y = 0$ line and then vertically periodic. As with the analysis problem, $L = H$. The remaining parameters are shown in Table 4.3; note that properties for the solid phase are not listed because the solid phase is heated uniformly to T_H.

Fig. 4.9 shows the converged designs (in white) and the surrounding velocity and temperature distributions in the fluid phase. Recall that the solid phase is heated uniformly. We observe that the optimizer makes no changes to the center inclusion when the no-slip boundary conditions are used; however, when the Kn-slip boundary condition is used, a more elliptical shape with larger surface area is favored. Further, the flanking fins show more pronounced differences: the no-slip design favors a slender aerodynamic fin shape, while the Kn-slip design requires thicker fins. Because of the velocity slip, there is less opportunity to heat the flow; thicker and blunter fins counter this effect.

We analyze the no-slip design with the Kn-slip boundary condition and compare its performance to the Kn-slip design. Table 4.4 summarizes this comparison. The no-slip design performs approximately 7% better than the Kn-slip design but suffers from a 4% violation in the minimum heating constraint. This violation is measured as:

$$\text{Violation} = \frac{\dot{m} c_p T^* - \dot{e}}{\dot{m} c_p T^*} \tag{4.21}$$

The increase in performance in the no-slip design is ultimately not surprising; however, this study suggests that such designs may not adequately heat incoming fluid if the Kn number is finite. This is similar to the results for the splitting manifold, where the biggest differences where in the mass flow rate requirement violations. We recognize that this study ignores the temperature jump

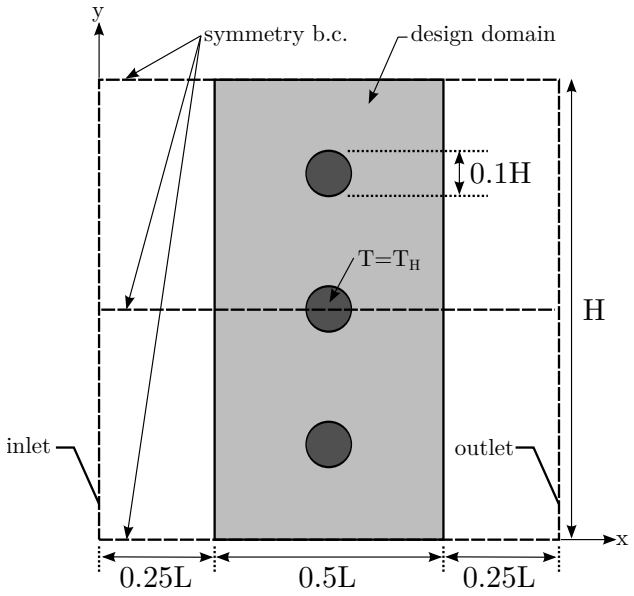

Figure 4.8: Problem setup for the heat fins optimization problem. Dashed line denotes the plane of symmetry.

	Value
Mesh size	80×160
Element size	$h = 0.0125H$
Characteristic length	$H = 5.356 \times 10^{-6}$
Fluid density	$\rho^f = 1.205$
Fluid viscosity	$\mu^f = 1.511 \times 10^{-5}$
Fluid heat capacity	$c_p^f = 1.005 \times 10^3$
Fluid conductivity	$\kappa^f = 2.57 \times 10^{-2}$
Inlet pressure	$p_{in} = 10^4$
Inlet temperature	$T_{in} = 300$
Heated fin temperature	$T_H = 375$
Perimeter scaling factor	$w_{\mathcal{P}} = 0.1$
Volume constraint factor	$f_{\mathcal{V}} = 0.5$
Nitsche velocity parameter	$\alpha_{N,\boldsymbol{u}} = 1$
Viscous ghost-penalty	$\alpha_{GP,\mu} = 5 \times 10^{+0}$
Pressure ghost-penalty	$\alpha_{GP,p} = 5 \times 10^{-1}$
Convective ghost-penalty	$\alpha_{GP,\boldsymbol{u}} = 5 \times 10^{-1}$
Relative Optimization Step	$\Delta s = 0.01$
Design variable bounds	$s_i^L = -0.0125H, s_i^U = +0.0125H$
Smoothing radius	$r_\phi = 2.4h$
Number of design variables	$6,427$

Table 4.3: Parameters for the heated fins optimization problem.

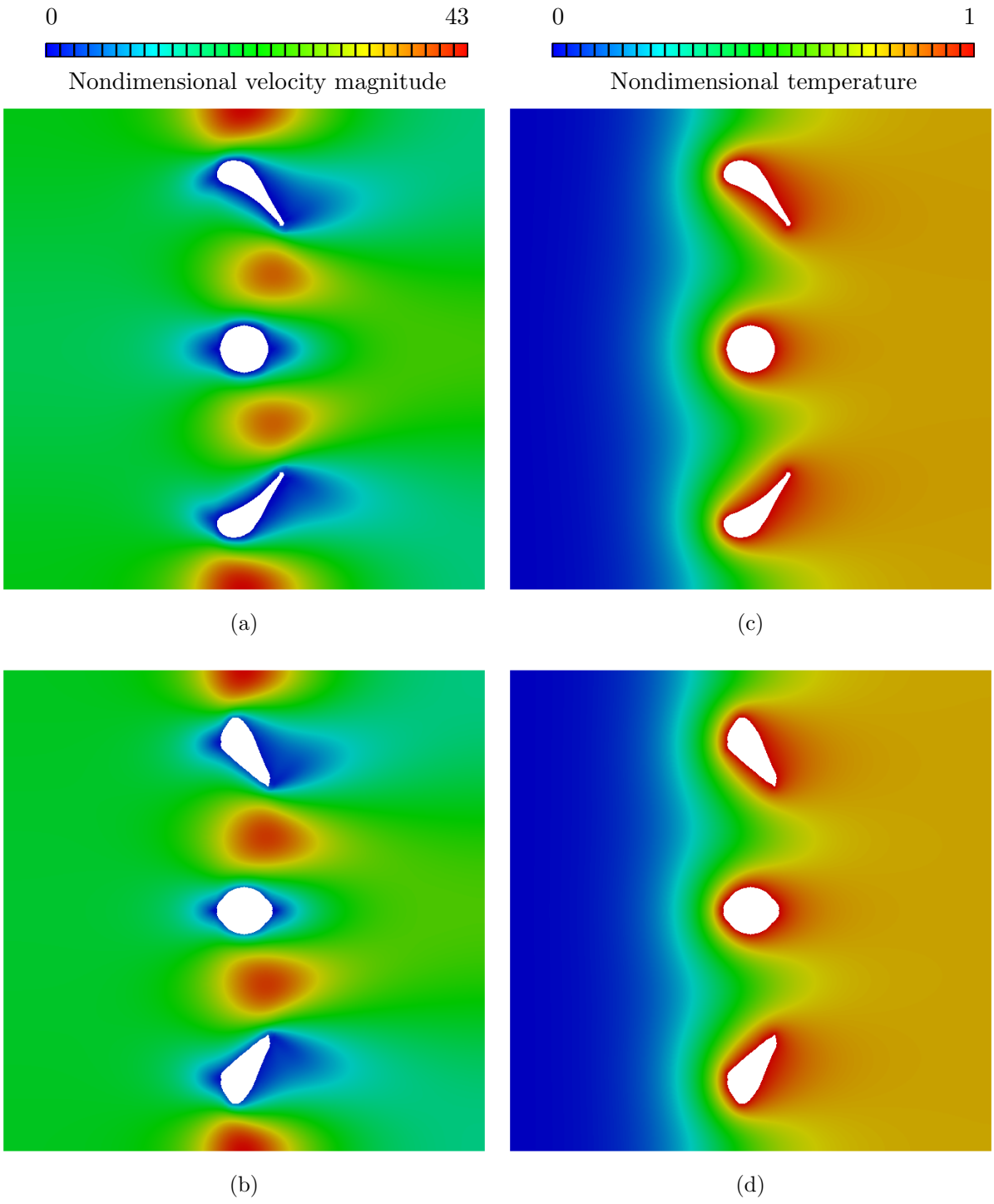

Figure 4.9: Velocity magnitude (a,b) and temperature (c,d) in fluid domain, using the no-slip (a,c) and Kn-slip (b,d) boundary conditions.

Design	$\mathcal{Z}$	$\dot{e}$	g_1
no-slip	-0.7214	12.4178	V (4%)
Kn-slip	$\mathbf{-0.6718}$	**11.5922**	**S**

Table 4.4: Analysis of both designs with the Kn-slip boundary condition. Minimum heating constraint can be satisfied (S) or violated (V) with a reported percentage.

condition analogous to the Kn-slip boundary condition but plan to include it in future work.

4.5 Design of a heat exchanger

As a final example, we consider the design of a heat exchanger, similar to that considered by Laniewski-Wołłk [99]. The goal of the exchanger is the same as the heated fins example examined in Section 4.4.2, namely, to heat incoming cool fluid while simultaneously maximizing the mass flow rate; this is achieved by the maximizing energy flow rate (4.6). In addition, we penalize the interface surface area to promote smooth designs. Thus, the optimization model (4.1) is formulated as:

$$\mathcal{Z} = \frac{\dot{e}}{\dot{e}^0} + w_{\mathcal{P}} \frac{\mathcal{P}}{\mathcal{P}^0}, \tag{4.22}$$

where the superscript "0" denotes the values of the initial design and $w_{\mathcal{P}}$ is a constant scaling factor. The energy flow can be maximized by (i) increasing the temperature component in (4.6) and (ii) increasing the flow rate component. A volume constraint on the solid phase is enforced as:

$$g_1 = \frac{\mathcal{V}^s}{f_{\mathcal{V}} \mathcal{V}^d} - 1. \tag{4.23}$$

Here, we use $f_{\mathcal{V}} = 0.25$. Table 4.5 shows the remaining problem parameters.

The problem setup is shown in Fig. 4.10. The domain consists of a $7D \times D \times D$ channel. The center of the channel is designated as the design domain, while the two sections ahead and behind the design domain are strictly forced to be in the fluid domain. The design domain is the $3D \times D \times D$ region in the middle of the channel and the center $D \times D$ plate on the bottom wall is heated to T_H. The four channel walls enforce either the no-slip or the Kn-slip boundary condition in the fluid problem and have adiabatic condition in the temperature problem. The fluid-solid

	Value
Mesh size	$150 \times 30 \times 15$
Element size	$h = 0.033D$
Characteristic length	$D = 1$
Fluid density	$\rho^f = 1$
Fluid viscosity	$\mu^f = 0.01$
Fluid heat capacity	$c_p^f = 1$
Fluid conductivity	$\kappa^f = 0.003$
Solid density	$\rho^s = 1$
Solid heat capacity	$c_p^s = 1$
Solid conductivity	$\kappa^s = 1$
Nondimensional inlet pressure	$p_{in} = 10^4$
Perimeter scaling factor	$w_{\mathcal{P}} = 0.1$
Volume constraint factor	$f_{\mathcal{V}} = 0.5$
Nitsche velocity parameter	$\alpha_{N,\boldsymbol{u}} = 1$
Viscous ghost-penalty	$\alpha_{GP,\mu} = 5 \times 10^{+0}$
Pressure ghost-penalty	$\alpha_{GP,p} = 5 \times 10^{-1}$
Convective ghost-penalty	$\alpha_{GP,\boldsymbol{u}} = 5 \times 10^{-1}$
Relative Optimization Step	$\Delta s = 0.01$
Design variable bounds	$s_i^L = -0.0333L, s_i^U = +0.0333L$
Smoothing radius	$r_\phi = 3.6h$
Number of design variables	$44,488$

Table 4.5: Parameters for the heat exchanger problem.

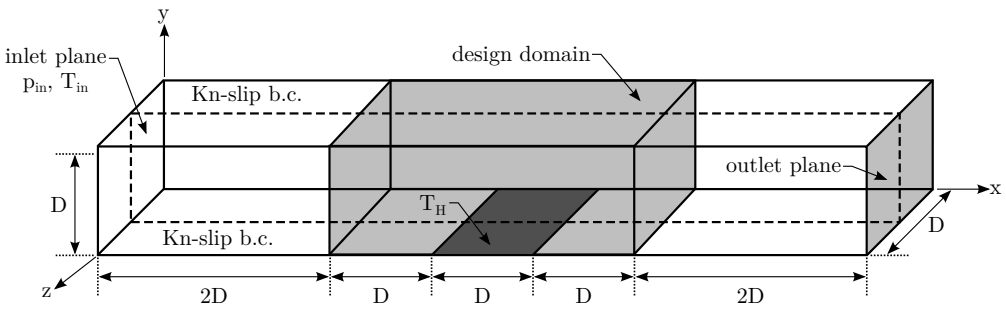

Figure 4.10: Problem setup for the heat exchanger problem. Dashed lines denote the plane of symmetry.

interface enforce the no-slip or Kn-slip boundary condition in the fluid problem and have Dirichlet boundary condition in the temperature problem. We recognize that this ignores the temperature slip effect, analogous to the Kn-slip boundary condition. This will be considered in future work. The inlet has pressure and temperature Dirichlet boundary conditions and the outlet has a traction-free boundary condition. We model only half of the domain and a symmetry boundary condition is enforced on the $z = D/2$ plane. The design is initialized with a lattice, shown in Fig. 4.11.

The convergence of the objective and volume constraint using the no-slip and Kn-slip boundary conditions is shown in Fig. 4.12. We recognize that the objective history suggests that more iterations are require; however, we reasonable expect that the designs will not undergo further significant changes.

Fig. 4.13 and 4.14 show the final designs after 500 iterations using the no-slip and Kn-slip boundary conditions, respectively.

Finally, Fig. 4.15 shows side-by-side comparisons of the two designs; the design obtained with the no-slip boundary condition are shown in gray, while the Kn-slip design is colored with the nondimensional temperature.

Table 4.6 shows the performance of both designs when analyzed with the Kn-slip boundary condition. The Kn-slip design is optimal though the difference in the objective value is very small; more importantly, the average heating is about 3% better when the Kn-slip is used. This suggests that if the heat exchanger will be used in an application where $Kn = 0.01$, using a design was was

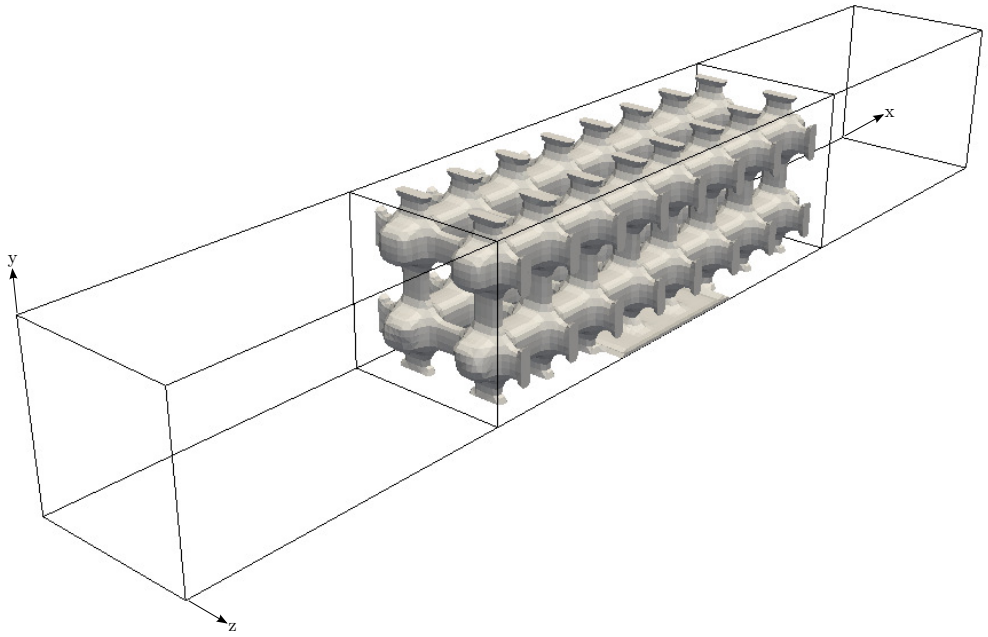

(a) Aerial view

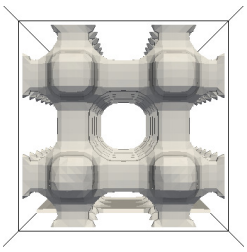

(b) Head-on view

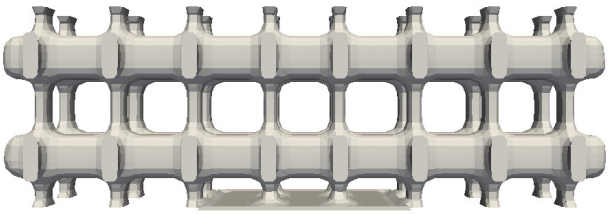

(c) Side view

Figure 4.11: Initial design for the heat exchanger problem. Dashed line denotes the plane of symmetry.

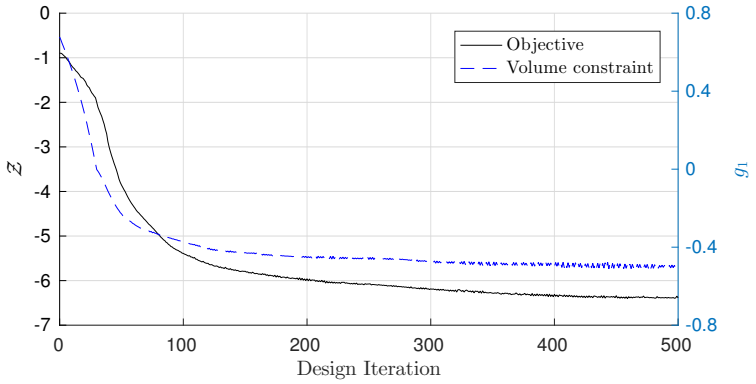

(a) no-slip boundary condition

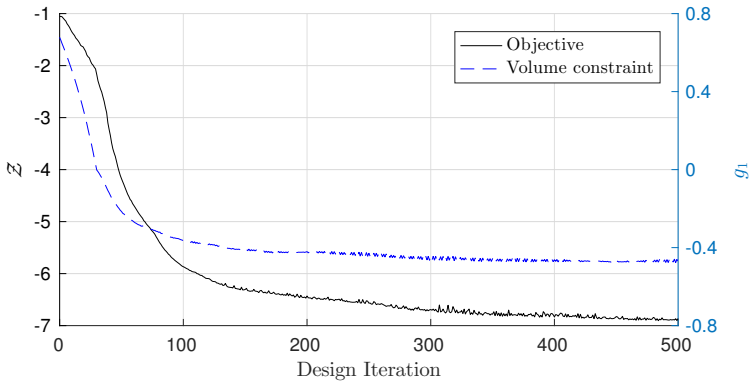

(b) Kn-slip boundary condition

Figure 4.12: Convergence of objective and volume constraint for the heat exchanger problem.

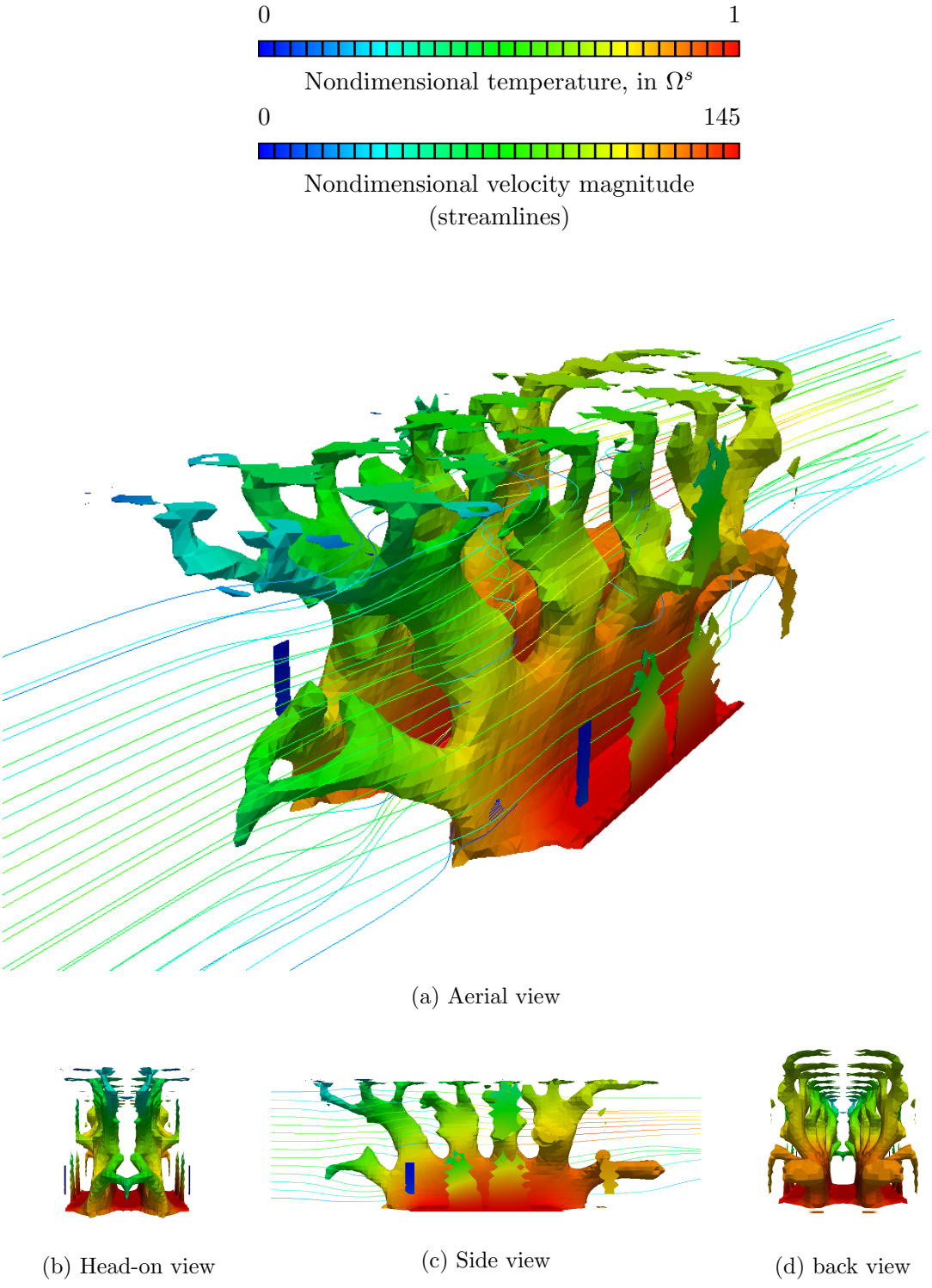

(a) Aerial view

(b) Head-on view

(c) Side view

(d) back view

Figure 4.13: Final design using the no-slip boundary condition.

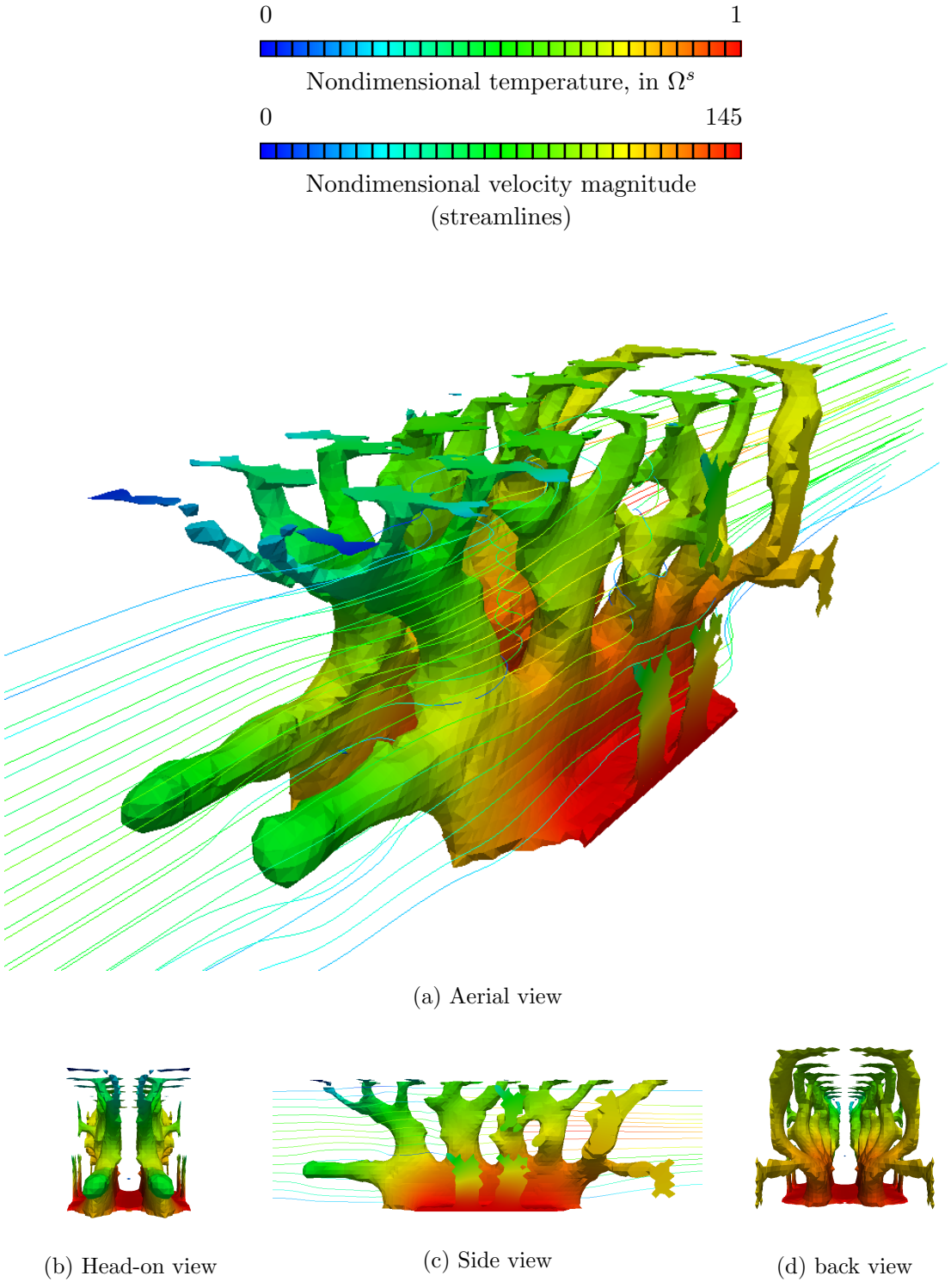

(a) Aerial view

(b) Head-on view

(c) Side view

(d) back view

Figure 4.14: Final design using the Kn-slip boundary condition.

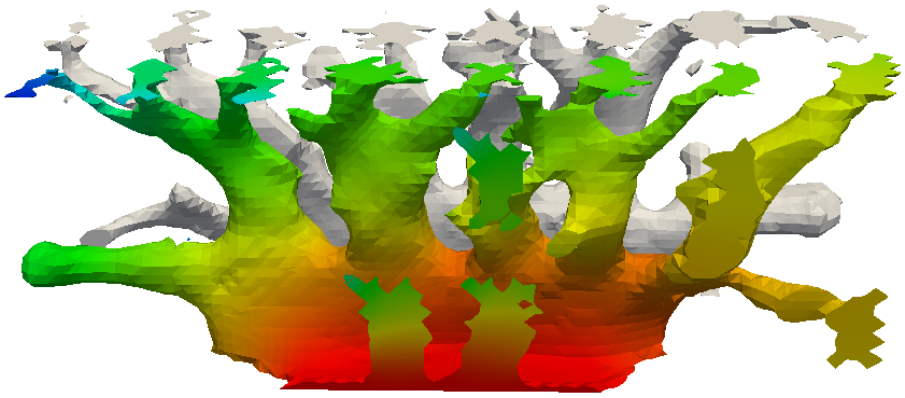

(a) Side view

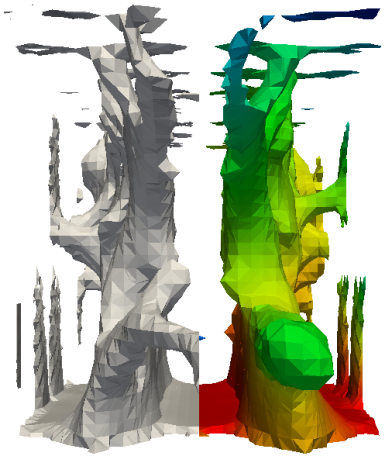

(b) Front view

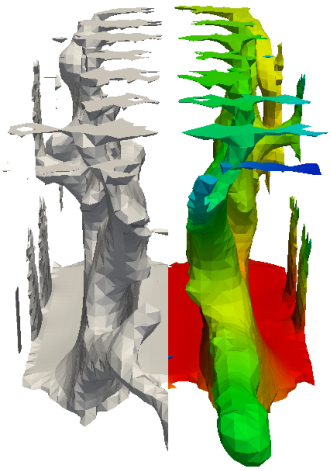

(c) Front view from above

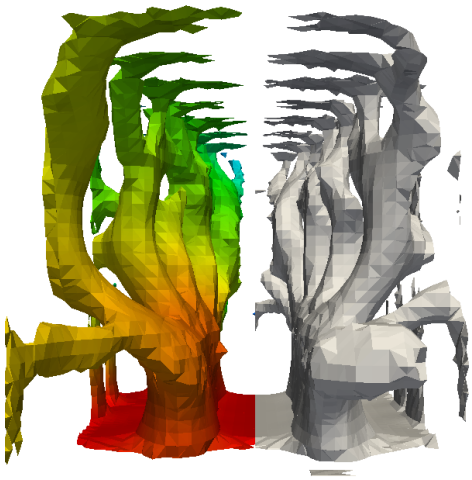

(d) Back view

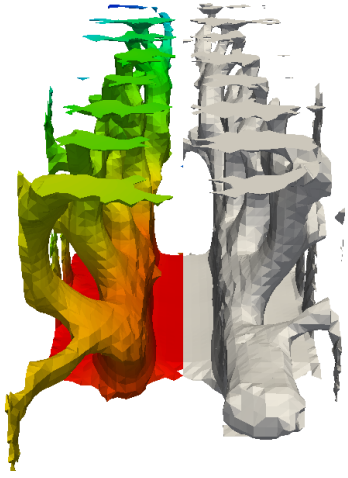

(e) Back view from above

Figure 4.15: Various views of the final designs: results using the no-slip boundary condition are shown in gray and those using the Kn-slip condition are colored.

Design	$\mathcal{Z}$	$\dot{e}$	$\dot{m}$	T_{avg}
no-slip	-6.9116	13.2206	22.3293	0.5921
Kn-slip	-6.9207	13.2371	21.7025	0.6099

Table 4.6: Analysis of both designs with the Kn-slip boundary condition.

obtained with the no-slip boundary condition, i.e. ignoring the Kn-slip effect, would result in a less-than-ideal heating.

4.6 Conclusions

Barber and Emerson [7] suggest that the boundaries between flow regimes depend on the fluidic device, i.e. the empirical $Kn = 10^-3$ cut-off between the continuum and slip regimes might only apply to certain devices. In this Chapter, we consider several design applications and study the influence of the Kn-slip boundary condition for moderate Kn numbers in the slip regime. We find that for the splitting manifold, heated fins, and heat exchanger, ignoring the Kn-slip design during the topology optimization process lead to only minor differences in design and performance. However, with the splitting manifold problem, we observe that the differences become more pronounced for larger Kn numbers. If the Kn-slip boundary condition does not lead to significant difference in design or performance, it may be sufficient to design the fluidic device with the no-slip condition. In this case, the expensive LSM-XFEM framework presented here may not be necessary and less expensive density method approach could be used.

In contrast, our study of the Tesla valve problem suggests that the difference in performance could be as large as 23% in some situations. In these situations, inclusion of the Kn-slip boundary condition during the optimization process is critical and an approach that allows for the precise location, orientation and curvature of the fluid-solid interface, such as the LSM-XFEM framework shown here, is appealing.

Future work should include the temperature jump condition, which is the temperature analogue to the Kn-slip boundary condition, for energy transport problems.

Bibliography

[1] Gui-Hua Tang, Yong-Hao Zhang, and David R Emerson. Lattice boltzmann models for nonequilibrium gas flows. Physical Review E, 77(4):046701, 2008.

[2] Samuel A Schaaf and Paul L Chambre. Flow of rarefied gases. Princeton University Press, Princenton, 1961.

[3] Mohamed Gad el Hak. The fluid mechanics of microdevices-the freeman scholar lecture. ASME Journal of Fluid Engineering, 121:5–33, 1999.

[4] G A Bird. The DSMC method. CreateSpace Independent Publishing Platform, 2013.

[5] Harold Grad. On the kinetic theory of rarefied gases. Communications on pure and applied mathematics, 2(4):331–407, 1949.

[6] Nishanth Dongari, Franz Durst, and Suman Chakraborty. Predicting microscale gas flows and rarefaction effects through extended navier–stokes–fourier equations from phoretic transport considerations. Microfluidics and nanofluidics, 9(4-5):831–846, 2010.

[7] Robert W Barber and David R Emerson. Challenges in modeling gas-phase flow in microchannels: from slip to transition. Heat Transfer Engineering, 27(4):3–12, 2006.

[8] Jonas Tölke, Manfred Krafczyk, Manuel Schulz, and Ernst Rank. Discretization of the boltzmann equation in velocity space using a galerkin approach. Computer physics communications, 129(1):91–99, 2000.

[9] David Makhija, Georg Pingen, and Kurt Maute. An immersed boundary method for fluids using the xfem and the hydrodynamic boltzmann transport equation. Computer Methods in Applied Mechanics and Engineering, 273:37–55, 2014.

[10] Carlos H Villanueva and Kurt Maute. Cutfem topology optimization of 3d laminar incompressible flow problems. Computer Methods in Applied Mechanics and Engineering, 320:444–473, 2017.

[11] J Y Yang and J C Huang. Rarefied flow computations using nonlinear model boltzmann equations. Journal of Computational Physics, 120(2):323–339, 1995.

[12] Dazhi Yu, Renwei Mei, Li-Shi Luo, and Wei Shyy. Viscous flow computations with the method of lattice boltzmann equation. Progress in Aerospace Sciences, 39(5):329–367, 2003.

[13] Dazhi Yu, Renwei Mei, and Wei Shyy. A multi-block lattice boltzmann method for viscous fluid flows. International journal for numerical methods in fluids, 39(2):99–120, 2002.

[14] Renwei Mei and Wei Shyy. On the finite difference-based lattice boltzmann method in curvilinear coordinates. Journal of Computational Physics, 143(2):426–448, 1998.

[15] Dhiraj V Patil and K N Lakshmisha. Finite volume tvd formulation of lattice boltzmann simulation on unstructured mesh. Journal of Computational Physics, 228(14):5262–5279, 2009.

[16] Taehun Lee and Ching-Long Lin. A characteristic galerkin method for discrete boltzmann equation. Journal of Computational Physics, 171(1):336–356, 2001.

[17] Yusong Li, Eugene J LeBoeuf, and P K Basu. Least-squares finite-element lattice boltzmann method. Physical Review E, 69(6):065701, 2004.

[18] Yusong Li, Eugene J LeBoeuf, and P K Basu. Least-squares finite-element scheme for the lattice boltzmann method on an unstructured mesh. Physical Review E, 72(4):046711, 2005.

[19] Alexander Düster, Leszek Demkowicz, and Ernst Rank. High-order finite elements applied to the discrete boltzmann equation. International journal for numerical methods in engineering, 67(8):1094–1121, 2006.

[20] Misun Min and Taehun Lee. A spectral-element discontinuous galerkin lattice boltzmann method for nearly incompressible flows. Journal of Computational Physics, 230(1):245–259, 2011.

[21] Xiaolin Zhong, Robert W MacCormack, and Dean R Chapman. Stabilization of the burnett equations and application to hypersonic flows. AIAA journal, 31(6):1036–1043, 1993.

[22] Shi Jin and Marshall Slemrod. Regularization of the burnett equations via relaxation. Journal of Statistical Physics, 103(5-6):1009–1033, 2001.

[23] Ramesh Balakrishnan. An approach to entropy consistency in second-order hydrodynamic equations. Journal of Fluid Mechanics, 503:201–245, 2004.

[24] Duncan A Lockerby, Jason M Reese, and Michael A Gallis. The usefulness of higher-order constitutive relations for describing the knudsen layer. Physics of Fluids (1994-present), 17(10):10060, 2005.

[25] Henning Struchtrup and Manuel Torrilhon. Regularization of grads 13 moment equations: derivation and linear analysis. Physics of Fluids, 15(9):2668–2680, 2003.

[26] Peyman Taheri, Manuel Torrilhon, and Henning Struchtrup. Couette and poiseuille microflows: analytical solutions for regularized 13-moment equations. Physics of Fluids (1994-present), 21(1):017102, 2009.

[27] Manuel Torrilhon. Slow gas microflow past a sphere: Analytical solution based on moment equations. Physics of Fluids (1994-present), 22(7):072001, 2010.

[28] Anirudh Rana, Manuel Torrilhon, and Henning Struchtrup. A robust numerical method for the r13 equations of rarefied gas dynamics: Application to lid driven cavity. Journal of Computational Physics, 236:169–186, 2013.

[29] Anirudh S Rana, Alireza Mohammadzadeh, and Henning Struchtrup. A numerical study of the heat transfer through a rarefied gas confined in a microcavity. Continuum Mechanics and Thermodynamics, 27(3):433–446, 2015.

[30] Igor Eduardovich Ivanov, Igor Anatol'evich Kryukov, and M Yu Timokhin. Application of moment equations to the mathematical simulation of gas microflows. Computational Mathematics and Mathematical Physics, 53(10):1534–1550, 2013.

[31] X J Gu, R W Barber, and D R Emerson. How far can 13 moments go in modeling microscale gas phenomena? Nanoscale and microscale thermophysical engineering, 11(1-2):85–97, 2007.

[32] David Makhija and Kurt Maute. Level set topology optimization of scalar transport problems. Structural and Multidisciplinary Optimization, 51(2):267–285, 2015.

[33] Prabhu Lal Bhatnagar, Eugene P Gross, and Max Krook. A model for collision processes in gases. i. small amplitude processes in charged and neutral one-component systems. Physical review, 94(3):511, 1954.

[34] C David Levermore. Moment closure hierarchies for kinetic theories. Journal of statistical Physics, 83(5-6):1021–1065, 1996.

[35] C David Levermore and William J Morokoff. The gaussian moment closure for gas dynamics. SIAM Journal on Applied Mathematics, 59(1):72–96, 1998.

[36] C K S Lam and C P T Groth. Numerical prediction of three-dimensional non-equilibrium gaseous flows using the gaussian moment closure. AIAA Paper, 3401, 2011.

[37] Christian Kuehn. Moment closure: A brief review. In Control of Self-Organizing Nonlinear Systems, pages 253–271. Springer, 2016.

[38] Alexander N Brooks and Thomas JR Hughes. Streamline upwind/petrov-galerkin formulations for convection dominated flows with particular emphasis on the incompressible navier-stokes equations. Computer methods in applied mechanics and engineering, 32(1):199–259, 1982.

[39] Michael Schäfer, Stefan Turek, Franz Durst, Egon Krause, and Rolf Rannacher. Benchmark computations of laminar flow around a cylinder. Springer, 1996.

[40] Bing-Yang Cao, Min Chen, and Zeng-Yuan Guo. Effect of surface roughness on gas flow in microchannels by molecular dynamics simulation. International Journal of Engineering Science, 44(13):927–937, 2006.

[41] Lynne O Hare, Duncan A Lockerby, Jason M Reese, and David R Emerson. Near-wall effects in rarefied gas micro-flows: some modern hydrodynamic approaches. International Journal of Heat and Fluid Flow, 28(1):37–43, 2007.

[42] Vlasios Leontidis, Jie Chen, Lucien Baldas, and Stéphane Colin. Numerical design of a knudsen pump with curved channels operating in the slip flow regime. Heat and Mass Transfer, 50(8):1065–1080, 2014.

[43] Matthew J. McNenly, Michael A. Gallis, and Iain D. Boyd. Empirical slip and viscosity model performance for microscale gas flow. International Journal for Numerical Methods in Fluids, 49(11):1169–1191, 2005.

[44] J Van Rij, T Ameel, and T Harman. An evaluation of secondary effects on microchannel frictional and convective heat transfer characteristics. International Journal of Heat and Mass Transfer, 52(11):2792–2801, 2009.

[45] J Van Rij, T Harman, and T Ameel. Slip flow fluid-structure-interaction. International Journal of Thermal Sciences, 58:9–19, 2012.

[46] Wen-Ming Zhang, Guang Meng, and Xueyong Wei. A review of slip models for gas microflows. Microfluidics and nanofluidics, 13(6):845–882, 2012.

[47] Martin P Bendsøe. Optimal shape design as a material distribution problem. Structural optimization, 1(4):193–202, 1989.

[48] M Zhou and G I N Rozvany. The coc algorithm, part ii: topological, geometrical and generalized shape optimization. Computer Methods in Applied Mechanics and Engineering, 89(1-3):309–336, 1991.

[49] Thomas Borrvall and Joakim Petersson. Topology optimization of fluids in stokes flow. International journal for numerical methods in fluids, 41(1):77–107, 2003.

[50] Allan Gersborg-Hansen, Ole Sigmund, and Robert B Haber. Topology optimization of channel flow problems. Structural and Multidisciplinary Optimization, 30(3):181–192, 2005.

[51] Fridolin Okkels, Laurits H Olesen, and Henrik Bruus. Applications of topology optimization in the design of micro-and nanofluidic systems. In Technical Proceedings of the 2005 NSTI Nanotechnology Conference and Trade Show, pages 575–578, 2005.

[52] Laurits Højgaard Olesen, Fridolin Okkels, and Henrik Bruus. A high-level programming-language implementation of topology optimization applied to steady-state navier-stokes flow. Int. J. Numer. Meth. Engng, 65:975–1001, 2006.

[53] Anton Evgrafov, Georg Pingen, and Kurt Maute. Topology optimization of fluid domains: kinetic theory approach. ZAMM-Journal of Applied Mathematics and Mechanics/Zeitschrift für Angewandte Mathematik und Mechanik, 88(2):129–141, 2008.

[54] Aycan Erentok and Ole Sigmund. Topology optimization of sub-wavelength antennas. IEEE transactions on antennas and propagation, 59(1):58–69, 2011.

[55] Shintaro Yamasaki, Tsuyoshi Nomura, Atsushi Kawamoto, Kazuo Sato, and Shinji Nishiwaki. A level set-based topology optimization method targeting metallic waveguide design problems. International Journal for Numerical Methods in Engineering, 87(9):844–868, 2011.

[56] James A Sethian and Andreas Wiegmann. Structural boundary design via level set and immersed interface methods. Journal of computational physics, 163(2):489–528, 2000.

[57] Michael Yu Wang, Xiaoming Wang, and Dongming Guo. A level set method for structural topology optimization. Computer methods in applied mechanics and engineering, 192(1):227–246, 2003.

[58] Grégoire Allaire, François Jouve, and Anca-Maria Toader. Structural optimization using sensitivity analysis and a level-set method. Journal of computational physics, 194(1):363–393, 2004.

[59] Nico P van Dijk, Kurt Maute, M Langelaar, and F Van Keulen. Level-set methods for structural topology optimization: a review. Structural and Multidisciplinary Optimization, 48(3):437–472, 2013.

[60] Arun L Gain and Glaucio H Paulino. A critical comparative assessment of differential equation-driven methods for structural topology optimization. Structural and Multidisciplinary Optimization, 48(4):685–710, 2013.

[61] Ivo Babuška and Jens M Melenk. The partition of unity method. International journal for numerical methods in engineering, 40(4):727–758, 1997.

[62] Ted Belytschko and Tom Black. Elastic crack growth in finite elements with minimal remeshing. International journal for numerical methods in engineering, 45(5):601–620, 1999.

[63] Christopher Lang, David Makhija, Alireza Doostan, and Kurt Maute. A simple and efficient preconditioning scheme for heaviside enriched xfem. Computational mechanics, 54(5):1357–1374, 2013.

[64] Henning Sauerland and Thomas-Peter FriesFries. The stable xfem for two-phase flows. Computers & Fluids, 87:41–49, 2013.

[65] Éric Béchet, Hans Minnebo, Nicolas Moës, and B Burgardt. Improved implementation and robustness study of the xfem for stress analysis around cracks. International Journal for Numerical Methods in Engineering, 64(8):1033–1056, 2005.

[66] Alexander Menk and Stéphane Bordas. A robust preconditioning technique for the extended finite element method. International Journal for Numerical Methods in Engineering, 85(13):1609–1632, 2011.

[67] Erick Burman, Miguel A Fernández, and Peter Hansbo. Continuous interior penalty finite element method for oseen's equations. SIAM journal on numerical analysis, 44(3):1248–1274, 2006.

[68] B Schott, U Rasthofer, V Gravermeier, and W Wall. A face-oriented stabilized nitsche-type extended variational multiscale method for incompressible two-phase flow. International journal for numerical methods in engineering, 104(7), 2014.

[69] Yuri Bazilevs and Thomas J R Hughes. Weak imposition of dirichlet boundary conditions in fluid mechanics. Computers & Fluids, 36(1):12–26, 2007.

[70] Joachim Nitsche. Über ein variationsprinzip zur lösung von dirichlet-problemen bei verwendung von teilräumen, die keinen randbedingungen unterworfen sind. In Abhandlungen aus dem mathematischen Seminar der Universität Hamburg, volume 36, pages 9–15. Springer, 1971.

[71] John Dolbow and Isaac Harari. An efficient finite element method for embedded interface problems. International journal for numerical methods in engineering, 78(2):229–252, 2009.

[72] Tayfun E Tezduyar, Sanjay Mittal, S E Ray, and R Shih. Incompressible flow computations with stabilized bilinear and linear equal-order-interpolation velocity-pressure elements. Computer Methods in Applied Mechanics and Engineering, 95(2):221–242, 1992.

[73] Leopoldo P Franca, Sergio L Frey, and Thomas J R Hughes. Stabilized finite element methods: I. application to the advective-diffusive model. Computer Methods in Applied Mechanics and Engineering, 95(2):253–276, 1992.

[74] Erick Burman and Peter Hansbo. Fictitious domain methods using cut elements: Iii. a stabilized nitsche method for stokes problems. ESAIM: Mathematical modeling and numerical analysis, 48(3):859–874, 2014.

[75] B Schott and W Wall. A new face-oriented stabilized xfem approach for 2d and 3d incompressible navier-stokes equations. Computer Methods in Applied mechanics and engineering, 276(1):233–265, 2014.

[76] Erik Burman and Peter Hansbo. Fictitious domain finite element methods using cut elements: Ii. a stabilized nitsche method. Applied Numerical Mathematics, 62(4):328–341, 2012.

[77] Ali Beskok and George Em Karniadakis. Report: A model for flows in channels, pipes, and ducts at micro and nano scales. Microscale Thermophysical Engineering, 3(1):43–77, 1999.

[78] J Clerk Maxwell. On stresses in rarefied gases arising from inequalities of temperature. Phil. Trans. R. Soc. Lond., 170:231–256, 1879.

[79] Stéphane Colin. Gas microflows in the slip flow regime: a critical review on convective heat transfer. Journal of Heat Transfer, 134(2):020908, 2012.

[80] J G Méolans and I A Graur. Continuum analytical modeling of thermal creep. European Journal of Mechanics - B/Fluids, 27(6):785–809, 2008.

[81] Carlos Hernan Villanueva and Kurt Maute. Density and level set-xfem schemes for topology optimization of 3-d structures. Computational Mechanics, 54(1):133–150, 2014.

[82] Sebastian Kreissl and Kurt Maute. Levelset based fluid topology optimization using the extended finite element method. Structural and Multidisciplinary Optimization, 46(3):311–326, 2012.

[83] Anita Hansbo and Peter Hansbo. A finite element method for the simulation of strong and weak discontinuities in solid mechanics. Computer Methods in Aplied Mechanics and Engineering, 193(33-35):3523–3540, 2004.

[84] David Makhija and Kurt Maute. Numerical instabilities in level set topology optimization with the extended finite element method. Structural and multidisciplinary optimization, 49(2):185–197, 2014.

[85] Kenjiro Terada, Mitsuteru Asai, and Michihiro Yamagishi. Finite cover method for linear and non-linear analyses of heterogeneous solids. International joournal for numerical methods in engineering, 58(9):1321–1646, 2003.

[86] T Q N Tran, H P Lee, and S P Lim. Modeling porous structures by penalty approach in the extended finite element method. Computer Methods in Biomechanics and Biomedical Engineering, 16(4):347–357, 2013.

[87] Young Joon Choi, Martien A Hulsen, and Han E H Meijer. Simulation of the flow of a viscoelastic fluid around a stationary cylinder using an extended finite element method. Computers & Fluids, 57:183–194, 2012.

[88] Ashesh Sharma, Carlos H Villanueva, and Kurt Maute. On shape sensitivities with heaviside-enriched xfem. Structural and Multidisciplinary Optimization, 55(2):385–408, 2017.

[89] Youcef Saad and Martin H schultz. Gmres: a generalized minimal residual algorithm for solving nonsymmetric linear systems. SIAM Jounral on scientific and statistical computing, 7(3):856–869, 1986.

[90] Youcef Saad. Ilut: A dual threshold incomplete lu factorization. Numerical Linear Algebra with Applications, 1(4):387–402, 1994.

[91] Stéphane Colin. Rarefaction and compressibility effects on steady and transient gas flows in microchannels. Microfluidics and Nanofluidics, 1(3):268–279, 2005.

[92] Sebastian Kreissl, Georg Pingen, and Kurt Maute. Topology optimization for unsteady flow. Topology optimization for unsteady flow, 87(13):1229–1253, 2011.

[93] Stephanie Golmon, Kurt Maute, and Martin L Dunn. Multiscale design optimization of lithium ion batteries using adjoint sensitivity analysis. International Journal for Numerical Methods in Engineering, 92(5):475–494, 2012.

[94] Krister Svanberg. A globally convergent version of mma without line search. In Proceedings of the first world congress of structural and multidisciplinary optimization, volume 28, pages 9–16. Goslar, Germany, 1995.

[95] Sen Lin, Longyu Zhao, James K Guest, Timothy P Weihs, and Zhenyu Lui. Topology optimization of fixed-geometry fluid diodes. Journal of Mechanical Design, 137(8):081402, 2015.

[96] Adrian R Gamboa, Christopher J Morris, and Fred K Forster. Improvements in fixed-valve micropump performance through shape optimization of valves. Journal of Fluids Engineering, 127(2):339–346, 2005.

[97] Georg Pingen, Anton Evgrafov, and Kurt Maute. A parallel schur complement solver for the solution of the adjoint steady-state lattice boltzmann equations: application to design optimization. International Journal of Computational Fluid Dynamics, 22(7):457–464, 2008.

[98] Yongbo Deng, Zhenyu Liu, Ping Zhang, Yihui Wu, and Jan G Korvink. Optimization of no-moving-part fluidic resistance microvalves with low reynolds number. In Proceedings IEEE international conference on Micro Electro MechanicalSystems (MEMS), pages 67–70, 2010.

[99] Ł. Laniewski-Wołłk and J. Rokicki. Adjoint lattice boltzmann for topology optimization on multi-gpu architecture. Computers & Mathematics with Applications, 71(3):833–848, 2016.

Appendix A

Summary of Moment Equations

A.1 Overview

All four systems of equations described in Section 2.2 can be written as:

$$\frac{\delta \mathbf{a}}{\delta t} + (\mathbf{A}(\mathbf{a}) \cdot \boldsymbol{\nabla})\, \mathbf{a} + \mathbf{C}\,(\mathbf{a}) = 0, \tag{A.1}$$

where $\mathbf{A}$ are the coefficient matrices:

$$\mathbf{A}(\mathbf{a}) = [A_x(\mathbf{a}), A_y(\mathbf{a})] \tag{A.2}$$

and $\mathbf{C}$ is the collision vector. Additionally, the GHF2 and LHF2 equations relate the physical moments to the expansion coefficients with:

$$\rho(\boldsymbol{x}, t) = \int f(\boldsymbol{x}, \boldsymbol{\xi}, t) \mathrm{d}\boldsymbol{\xi}, \tag{A.3}$$

$$\rho u_i(\boldsymbol{x}, t) = \int \xi_i f(\boldsymbol{x}, \boldsymbol{\xi}, t) d\boldsymbol{\xi}, \tag{A.4}$$

and

$$\sigma_{ij} = \int c_i c_j f(\boldsymbol{x}, \boldsymbol{\xi}, t) \mathrm{d}\boldsymbol{\xi}, \tag{A.5}$$

where $\boldsymbol{c}$ is the intrinsic velocity:

$$\boldsymbol{c}(\boldsymbol{\xi}, \boldsymbol{x}, t) = \boldsymbol{\xi} - \boldsymbol{u}(\boldsymbol{x}, t). \tag{A.6}$$

For the GHF2 and GMF2 equations, the particle distribution, f, is approximated with an *absolute* (or global) expansion:

$$f \approx \hat{f}_{glb} = \frac{1}{(2\pi RT)^{D/2}} \exp\left(-\frac{\boldsymbol{\xi}^2}{2RT}\right) \sum_{k=1}^{n_{D,N}} a_k(\boldsymbol{x}, t) \phi_k\,(\boldsymbol{\xi}), \tag{A.7}$$

whereas the LHF2 and LMF2 equations are derived with a *local* expansion:

$$f \approx \hat{f}_{loc} = \frac{1}{(2\pi RT)^{D/2}} \exp\left(-\frac{(\boldsymbol{\xi}-\boldsymbol{u})^2}{2RT}\right) \sum_{k=1}^{n_{D,N}} a_k(\boldsymbol{x},t)\phi_k\left(\boldsymbol{\xi}-\boldsymbol{u}\right) \tag{A.8}$$

A.1.1 GHF2 Equations

For the GHF2 equations, $\mathbf{a} = \begin{pmatrix} a_1 & a_2 & a_3 & a_4 & a_5 & a_6 \end{pmatrix}^T$, and the coefficient matrices and collision vector are given by:

$$A_x = \sqrt{RT}\begin{pmatrix} 0 & 1 & 0 & 0 & 0 & 0 \\ 1 & 0 & 0 & 0 & \sqrt{2} & 0 \\ 0 & 0 & 0 & 1 & 0 & 0 \\ 0 & 0 & 1 & 0 & 0 & 0 \\ 0 & \sqrt{2} & 0 & 0 & 0 & 0 \\ 0 & 0 & 0 & 0 & 0 & 0 \end{pmatrix}, \quad A_y = \sqrt{RT}\begin{pmatrix} 0 & 0 & 1 & 0 & 0 & 0 \\ 0 & 0 & 0 & 1 & 0 & 0 \\ 1 & 0 & 0 & 0 & 0 & \sqrt{2} \\ 0 & 1 & 0 & 0 & 0 & 0 \\ 0 & 0 & 0 & 0 & 0 & 0 \\ 0 & 0 & \sqrt{2} & 0 & 0 & 0 \end{pmatrix}, \tag{A.9}$$

and

$$\mathbf{C}(\mathbf{a}) = \frac{1}{\tau}\begin{pmatrix} 0 & 0 & 0 & a_4 - \frac{a_2 a_3}{a_1} & a_5 - \frac{a_2^2}{a_1\sqrt{2}} & a_6 - \frac{a_3^2}{a_1\sqrt{2}} \end{pmatrix}^T. \tag{A.10}$$

Finally, the physical moments are obtained with:

$$\begin{aligned} \rho &= a_1 \\ u_x &= \frac{a_2}{a_1}\sqrt{RT} \\ u_y &= \frac{a_3}{a_1}\sqrt{RT} \\ \sigma_{xy} &= -RT\left(a_4 - \frac{a_2 a_3}{a_1}\right) \\ \sigma_{xx} &= -RT\left(\sqrt{2}a_5 - \frac{a_2^2}{a_1}\right) \\ \sigma_{yy} &= -RT\left(\sqrt{2}a_6 - \frac{a_3^2}{a_1}\right). \end{aligned} \tag{A.11}$$

A.1.2 GMF2 Equations

For the GMF2 equations, $\mathbf{a} = \begin{pmatrix} \rho & u_x & u_y & \sigma_{xy} & \sigma_{xx} & \sigma_{yy} \end{pmatrix}^T$, and the coefficient matrices and collision vector are given by:

$$A_x = \begin{pmatrix} u_x & \rho & 0 & 0 & 0 & 0 \\ \frac{RT}{\rho} & u_x & 0 & 0 & -\frac{1}{\rho} & 0 \\ 0 & 0 & u_x & -\frac{1}{\rho} & 0 & 0 \\ u_x^2 u_y & 2\rho u_x u_y & \rho(u_x^2 - RT) & -u_x & -u_y & 0 \\ u_x^3 & \rho(3u_x^3 - 2RT) & 0 & 0 & -2u_x & 0 \\ u_x u_y^2 & \rho u_y^2 & 2\rho u_x u_y & -2u_y & 0 & 0 \end{pmatrix},$$

$$A_y = \begin{pmatrix} u_y & 0 & \rho & 0 & 0 & 0 \\ 0 & u_y & 0 & -\frac{1}{\rho} & 0 & 0 \\ \frac{RT}{\rho} & 0 & u_y & 0 & 0 & -\frac{1}{\rho} \\ u_x u_y^2 & \rho(u_y^2 - RT) & 2\rho u_x u_y & -u_y & 0 & -u_x \\ u_x^2 u_y & 2\rho u_x u_y & \rho u_x^2 & -2u_x & 0 & 0 \\ u_y^3 & 0 & \rho(3u_y^2 - 2RT) & 0 & 0 & -2u_y \end{pmatrix}, \tag{A.12}$$

and

$$\mathbf{C}(\mathbf{a}) = \frac{1}{\tau} \begin{pmatrix} 0 & 0 & 0 & \sigma_{xy} & \sigma_{xx} & \sigma_{yy} \end{pmatrix}^T. \tag{A.13}$$

A.1.3 LHF2 Equations

For the LHF2 Equations, $\mathbf{a} = \begin{pmatrix} a_1 & u_x & u_y & a_4 & a_5 & a_6 \end{pmatrix}^T$, and the coefficient matrices and collision vector are given by:

$$A_x = \begin{pmatrix} u_x & a_1 & 0 & 0 & 0 & 0 \\ \frac{RT}{a_1} & u_x & 0 & 0 & \frac{\sqrt{2}RT}{a_1} & 0 \\ 0 & 0 & u_x & \frac{RT}{a_1} & 0 & 0 \\ 0 & 2a_4 & a_1 + \sqrt{2}a5 & u_x & 0 & 0 \\ 0 & \sqrt{2}a_1 + 3a_5 & 0 & 0 & u_x & 0 \\ 0 & a_6 & \sqrt{2}a_4 & 0 & 0 & u_x \end{pmatrix},$$

$$A_y = \begin{pmatrix} u_y & 0 & a_1 & 0 & 0 & 0 \\ 0 & u_y & 0 & \frac{RT}{a_1} & 0 & 0 \\ \frac{RT}{a_1} & 0 & u_y & 0 & 0 & \frac{\sqrt{2}RT}{a_1} \\ 0 & a_1 + \sqrt{2}a_6 & 2a_4 & u_y & 0 & 0 \\ 0 & \sqrt{2}a_4 & a_5 & 0 & u_y & 0 \\ 0 & 0 & \sqrt{2}a_3a_6 & 0 & 0 & u_y \end{pmatrix}, \tag{A.14}$$

and

$$\mathbf{C}(\mathbf{a}) = \frac{1}{\tau}\begin{pmatrix} 0 & 0 & 0 & a_4 & a_5 & a_6 \end{pmatrix}^T. \tag{A.15}$$

When using the local expansion, (A.4) requires that $a_2 = a_3 = 0$; thus, u_x and u_y are added as degrees-of-freedom. The remaining physical moments are given by:

$$\begin{aligned} \rho &= a_1 \\ \sigma_{xy} &= -a_4 RT \\ \sigma_{xx} &= -\sqrt{2}a_5 RT \\ \sigma_{yy} &= -\sqrt{2}a_6 RT \end{aligned} \tag{A.16}$$

A.1.4 LMF2 Equations

For the LMF2 equations, $\mathbf{a} = \begin{pmatrix} \rho & u_x & u_y & \sigma_{xy} & \sigma_{xx} & \sigma_{yy} \end{pmatrix}^T$, and the coefficient matrices and collision vector are given by:

$$A_x = \begin{pmatrix} u_x & \rho & 0 & 0 & 0 & 0 \\ \frac{RT}{\rho} & u_x & 0 & 0 & -\frac{1}{\rho} & 0 \\ 0 & 0 & u_x & -\frac{1}{\rho} & 0 & 0 \\ 0 & 2\sigma_{xy} & \sigma_{xx} - \rho RT & u_x & 0 & 0 \\ 0 & 3\sigma_{xx} - 2\rho RT & 0 & 0 & u_x & 0 \\ 0 & \sigma_{yy} & 2\sigma_{xy} & 0 & 0 & u_x \end{pmatrix},$$

$$A_y = \begin{pmatrix} u_y & 0 & \rho & 0 & 0 & 0 \\ 0 & u_y & 0 & -\frac{1}{\rho} & 0 & 0 \\ \frac{RT}{\rho} & 0 & u_y & 0 & 0 & -\frac{1}{\rho} \\ 0 & \sigma_{yy} - \rho RT & 2\sigma_{xy} & u_y & 0 & 0 \\ 0 & 2\sigma xy & \sigma_{xx} & 0 & u_y & 0 \\ 0 & 0 & 3\sigma_{yy} - 2\rho RT & 0 & 0 & u_y \end{pmatrix} \tag{A.17}$$

and

$$\mathbf{C}(\mathbf{a}) = \frac{1}{\tau} \begin{pmatrix} 0 & 0 & 0 & \sigma_{xy} & \sigma_{xx} & \sigma_{yy} \end{pmatrix}^T. \tag{A.18}$$

Appendix B

Curvature of an ellipse

The curvature of a given path, $\boldsymbol{r}(t)$, is given as:

$$\kappa = \frac{|\boldsymbol{r}'(t) \times \boldsymbol{r}''(t)|}{|\boldsymbol{r}'(t)|^3}. \tag{B.1}$$

An elliptical cylinder is parametrized as:

$$\boldsymbol{r}(t) = (a\cos t)\hat{\boldsymbol{i}} + (b\sin t)\hat{\boldsymbol{j}}, \tag{B.2}$$

which gives a curvature of:

$$\begin{aligned} \kappa &= \frac{\left|\left((-a\sin t)\hat{\boldsymbol{i}} + (b\cos t)\hat{\boldsymbol{j}}\right) \times \left((-a\cos t)\hat{\boldsymbol{i}} + (-b\sin t)\hat{\boldsymbol{j}}\right)\right|}{\left|(-a\sin t)\hat{\boldsymbol{i}} + (b\cos t)\hat{\boldsymbol{j}}\right|^3} \\ \kappa &= \frac{ab}{\left(a^2\sin^2(t) + b^2\cos^2(t)\right)^{3/2}}. \end{aligned} \tag{B.3}$$

At the point of intersection with the horizontal tangent line, $t = \frac{\pi}{2}$, and for $a = 2r$ and $b = r$, the curvature is $\kappa = \frac{1}{4r}$.

Appendix C

Manuscript: Fluid topology optimization with a slip boundary model for finite Knudsen numbers

Fluid topology optimization with a slip boundary model for finite Knudsen numbers

Luis F Negrete, Kurt Maute*, Georg Pingen

Abstract

As fluidic devices become smaller in scale, non-equilibrium effects begin to manifest in the flow, starting with a non-zero fluid velocity at solid boundaries. This increase in momentum can have important implications in terms of design. To capture this effect, a slip boundary model is adopted into an existing Navier-Stokes model and is enforced with Nitsche's method. The ghost-penalty stabilization method encourages smooth velocity gradients at the fluid-solid boundary, which in term encourages a smooth fluid velocity. The slip boundary model is validated against numerical examples. The effect of the slip velocity is then studied with two topology optimization examples. We find that effect of the non-zero fluid velocity depends on the application of the fluidic device and is more pronounced in flows with larger Knudsen numbers.

1 Introduction

The study of optimal designs for fluid flows, through shape and topology optimization, for example, has gained widespread attention for Stokes and Navier-Stokes flow regimes in recent years. In these regimes, gas microflows in microfluidic devices have a broad range of applications, such as extracting biological samples, cooling integrated circuits and actively controlling aerodynamic flows [1, 2]. However, as fluidic devices become smaller in scale, e.g. in microelectromechanical systems, rarefaction effects begin to matter. Flows in the microscale behave different than those in the macroscale [3], beginning with effects near solid boundaries and extending into the fluid domain. While these effects have been readily studied for simple geometries [4–7] and, more recently, for fluid-structure-interaction problems with complex geometries [8], their impact on optimal designs has not been fully explored. In this paper, we will introduce a topology optimization framework for microfluidic flows and will show that the Knudsen-number-dependent slip boundary condition considerably affects the optimal designs of some fluid devices.

The Knudsen number is a nondimensional parameter that characterizes the rarefaction of a fluid and is defined as:

$$Kn = \frac{\lambda}{L_c}, \tag{1}$$

where λ is the mean-free path of the fluid, i.e. the average distance a fluid particle travels between collisions with other particles, and L_c is a global characteristic length, e.g. the height of the channel. Flows for which

*Corresponding autor: kurt.maute@colorado.edu

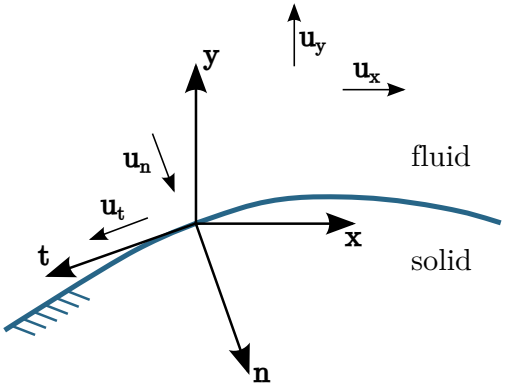

Figure 1: Cartesian and local coordinate system at the fluid-solid interface and velocity components.

$Kn < 10^{-3}$ are considered to be in the Hydrodynamic Regime, where the Navier-Stokes (NS) equations with traditional no-slip boundary conditions are valid [9–11]. However, in the Slip Flow Regime, where $10^{-3} < Kn < 10^{-1}$, the NS equations cannot be used with the traditional no-slip boundary condition. Instead, velocity and temperature slip effects begin to occur as the Kn number increases. Specifically, the tangential velocity and temperature of the fluid and the solid are no longer the same.

For flows in the Slip Flow Regime, there exists a variety of slip models for the tangential velocity at the fluid-solid interface. The wall-function method describes the tangential velocity as a function of the distance from the wall up to $O(\lambda)$, i.e. within the so-called Knudsen layer [4]. Another option is to use higher-order continuum models, including the Burnett, BGK-Burnett, and super-Burnett models, inside the Knudsen layer, e.g. [12–15]. The reader is referred to [11] for a review of slip models. The boundary condition used in this paper is introduced in Section 4.4 and is represented by:

$$u_t - u_t^w + \frac{2-\sigma}{\sigma}\frac{Kn}{1+Kn}\left(\frac{\partial u_t}{\partial n} + \frac{\partial u_n}{\partial t}\right) = 0, \tag{2}$$

where u_t and u_t^w are the fluid and wall tangential velocities, respectively, u_n is the fluid normal velocity, σ is an accommodation coefficient, and $\partial()/\partial n$ and $\partial()/\partial t$ denote derivatives in the normal and tangential directions, respectively. Figure 1 shows the local coordinate system at the fluid-solid interface. Throughout this paper, we will refer to this boundary condition as the Knudsen-slip (or simply, Kn-slip) boundary condition. To adequately model slip, the proposed boundary condition requires accurate near-wall velocity gradients, which will dictate the choice of our boundary representation for topology optimization as discussed in the following.

The majority of fluid topology optimization studies use density methods [16, 17]. Topology optimization in fluids was pioneered by [18], who adopted the concept of density methods to Stokes flows and modeled the presence of a wall in the fluid flow as a body force, i.e. a penalization approach. The work on Stokes models

has been extended to the NS equations by several authors, including [19], [20], [21], and [22]. The density method typically describes the interface between different material domains by either using intermediate densities, which lead to ambiguous boundaries, or by discrete material distributions, which lead to jagged boundaries. For problems that require an accurate geometrical description of the interface, density methods will result in an inaccurate enforcement of boundary conditions due to the aforementioned ambiguous or jagged boundaries [23, 24]. Such issues can be mitigated by mesh refinement; however, they do not provide the exact location and orientation of the boundary *a priori*. Thus, unlike the no-slip boundary condition, the Kn-slip boundary condition cannot be enforced with the same penalization approach as is used with density methods.

In response to the shortcomings of density methods, we utilize the Level Set Method (LSM) to represent the geometry. External or internal phase boundaries, where phase may refer to either the fluid or solid domain, are described implicitly by the zero level set isosurfaces of a Level Set Function (LSF), $\phi(\boldsymbol{x})$, where $\boldsymbol{x}$ is the position vector [25–27]. Smooth changes in the LSF lead to smooth changes in the geometry, e.g. the merging or separation of geometric features, making the LSM a good choice for topology optimization.

The LSF is typically discretized on a fixed background mesh and updated during the optimization process by solving the Hamilton-Jacobi equations. An alternative, used in this paper, is to define the parameters of the LSF as explicit functions of the optimization variables. The resulting optimization problem is solved by standard nonlinear programming (NLP) methods [28]. For a detailed discussion of the LSM, the reader is referred to [28] and [29].

Further, we utilize the eXtended Finite Element Method (XFEM) to describe the material distribution in the discretized fluid model. The XFEM is an immersed boundary technique that does not require a conforming mesh. The XFEM was built upon the concept of partition of unity developed by [30] and was originally used to model crack propagation [31]. Alternatives to the XFEM include an Ersatz' material approach, which suffers from the same problems as density methods, and adaptive re-meshing after each LSF update, which is computationally expensive. The XFEM decomposes an element cut by a zero isosurface of the LSF into several subdomains, such that each subdomain has a distinct phase, i.e. is exclusively fluid or solid. Thus, the LSM and XFEM provide the precise location and orientation of the fluid-solid interface.

The XFEM, however, results in an ill-conditioned system of equations, when an element cut by the zero isosurface of the LSF has a small ratio of volumes, e.g. when the interface moves very close a node. Such configurations are often unavoidable when using a fixed background mesh. Several approaches have been proposed to avoid this ill-conditioning issue, such as the geometric, Jacobi, and Cholesky decomposition preconditioners of [32], [33], and [34] and [35], respectively, and face-oriented ghost-penalty methods [36]. Face-oriented ghost-penalty methods have been studied in the context of fluid flow problems, where discon-

tinuities in the spatial gradients of the velocities and pressure are penalized across the common facets of intersected elements [37]. This presents a clear advantage over preconditioners, since smooth gradients are particularly important for the Kn-slip boundary condition. Smooth velocity gradients in (2) result in smooth tangential velocities at the interface. Boundary conditions on the interface are imposed weakly via Nitsche's method [38].

In this paper, we will extend the LSM-XFEM framework proposed by Villanueva and Maute [39] to allow for the enforcement of the Kn-slip boundary condition. We will show that, for some fluid devices, the effects of the slip boundary might not be negligible and may need to be accounted for in the optimization process; additionally, we will show the influence, in terms of design and performance, of this boundary condition when compared to the traditional no-slip condition.

The remainder of the paper is structured as follows: Section 2 describes the formulation of the optimization problem. Section 3 provides a detailed description of the geometry using the design variables and the LSM. In Section 4, we present the governing equations, the ghost-penalty formulation, the velocity slip boundary condition and its implementation using Nitsche's method, and the discretization using the XFEM. Numerical examples are discussed in Section 5. Finally, conclusions drawn from these studies are presented in Section 6.

2 Optimization

The optimization problems considered in this paper are formulated with respect to an objective and one or more constraints. The objective and constraints are defined in terms of design criteria, such as mass flow rate, pressure differences, fluid volume, etc. These design criteria can depend explicitly on the state and optimization variables, e.g. mass flow rate, or only on the optimization variables, e.g. fluid volume. The formulation for this class of optimization problem takes the form:

$$\begin{aligned} &\min_{\boldsymbol{s}} \mathcal{Z} = z(\boldsymbol{s}, \boldsymbol{u}(\boldsymbol{s})) \\ &\quad \text{s.t. } g_i(\boldsymbol{s}, \boldsymbol{u}) \leq 0, i = 1...N_g \\ &\boldsymbol{s} \in \boldsymbol{S} = \{\mathbb{R}^{N_s} | s_i^L \leq s_i \leq s_i^U, i = 1...N_s\} \\ &\boldsymbol{u} \in \boldsymbol{U} = \{\mathbb{R}^{N_{\boldsymbol{u}}} | R(\boldsymbol{s}, \boldsymbol{u}) = 0\}, \end{aligned} \tag{3}$$

where $\boldsymbol{s}$ is the vector of optimization variables, of size N_s, and $\boldsymbol{u}$ is the vector of state variables, of size $N_{\boldsymbol{u}}$. $\mathcal{Z}$ is a function of the criteria to be optimized. The function g_i is the i-th inequality constraint, and N_g is the number of constraints. The optimization variables s_i are bounded by lower and upper limits, s_i^L and s_i^U,

respectively. The state variables satisfy the residual of the governing equations, $R(\boldsymbol{s}, \boldsymbol{u}) = 0$.

3 Geometric Description

The LSM describes the geometry of a body immersed in a domain by the zero isosurfaces of a higher dimensional LSF, $\phi(\boldsymbol{x})$. The LSF is defined such that:

$$\begin{aligned} \phi(\boldsymbol{x}) &> 0, \quad \forall\, \boldsymbol{x} \in \Omega^s \\ \phi(\boldsymbol{x}) &< 0, \quad \forall\, \boldsymbol{x} \in \Omega^f \\ \phi(\boldsymbol{x}) &= 0, \quad \forall\, \boldsymbol{x} \in \Gamma^{fs}, \end{aligned} \tag{4}$$

where Ω^s is the solid phase, Ω^f is the fluid phase, and Γ^{fs} is the fluid-solid interface. The external boundaries of the solid and fluid phases are represented as Γ^s and Γ^f, respectively.

Topology optimization allows the emergence of a large set of geometries by having the LSF be parametrized by local shape functions defined on a finite element mesh. One optimization variable, s_i, for $i = 1...N_n$, is assigned to each node of the design mesh, where N_n is the number of nodes. Then, the LSF value of the i-th node, ϕ_i, is defined as:

$$\phi_i(\boldsymbol{s}, \boldsymbol{x}) = \left(\sum_{j=1}^{N_n} w_{ij} \right)^{-1} \left(\sum_{j=1}^{N_n} w_{ij} s_j \right), \tag{5}$$

where

$$w_{ij} = \max\left(0, r_\phi - |\boldsymbol{x}_i - \boldsymbol{x}_j|\right), \tag{6}$$

and r_ϕ is the smoothing filter radius. The linear filter in (5) was used previously in [40] and [41] to widen the zone of influence of each optimization variable and to improve the convergence rate.

To define horizontal cylindrical inlet and outlet ports in 2D, the LSF value on nodes with coordinates (x_i, y_i), outside the design domain is defined as:

$$\phi_i = \min\left(\max\left(\phi_{min}, r - \sqrt{(x_i - x_c)^2 \sin^2(\alpha) + (y_i - y_c)^2 \cos^2(\alpha)} \right), \phi_{max} \right), \tag{7}$$

where $\phi_{min} = -h/2$, $\phi_{max} = h/2$, h is the element width, (x_c, y_c) is a point on the cylinder axis, α is the angle between the axis and the global x-axis, and r is the radius of the port.

4 Governing Equations

This work adopts the isothermal, single species version of the weak form of the NS equations of Villanueva and Maute [39], where the weak form is decomposed into volume and surface contributions:

$$r_{\boldsymbol{u},p} = r^{\Omega}_{\boldsymbol{u},p} + r^{\hat{\Omega}}_{\boldsymbol{u},p} + r^{D}_{\boldsymbol{u},p} + r^{fs}_{\boldsymbol{u},p} + r^{GP}_{\boldsymbol{u},p}, \tag{8}$$

where $r^{\Omega}_{\boldsymbol{u},p}$ and $r^{\hat{\Omega}}_{\boldsymbol{u},p}$ are the volumetric residual contributions, non-stabilized and stabilized, respectively [39]. The term $r^{D}_{\boldsymbol{u},p}$ is used to enforce Dirichlet boundary conditions on the external surfaces, while the term $r^{fs}_{\boldsymbol{u},p}$ is used to enforce boundary conditions on the fluid-solid interface. The ghost-penalty term $r^{GP}_{\boldsymbol{u},p}$ depends on the face-oriented ghost-penalty formulation. The volumetric stabilization and ghost-penalty terms are discussed in Sections 4.2 and 4.3, respectively. Both boundary condition enforcement terms are discussed in Section 4.4.

4.1 Weak form of NS Equations

The non-stabilized volume contribution takes the form:

$$r^{\Omega}_{\boldsymbol{u},p} = \int_{\Omega^f} \left(v_i^f \rho^f \left(\frac{\partial u_i^f}{\partial t} + u_i^f \frac{\partial u_i^f}{\partial x_j} \right) + \epsilon_{ij}(\boldsymbol{v}^f) \sigma_{ij}(\boldsymbol{u}^f, p^f) \right) \mathrm{d}\Omega + \int_{\Omega^f} \left(q^f \frac{\partial u_i^f}{\partial x_i} \right) \mathrm{d}\Omega. \tag{9}$$

The first integral describes the momentum equations, with admissible test functions v_i^f; the second integral describes the incompressibility condition, with admissible test functions q_i^f. The fluid velocity is given by u_i^f, p^f is the pressure, ρ^f is the fluid density, μ^f is the dynamic viscosity, ϵ_{ij} is the strain rate tensor given by:

$$\epsilon_{ij}(\boldsymbol{u}^f) = \frac{1}{2} \left(\frac{\partial u_i^f}{\partial x_j} + \frac{\partial u_j^f}{\partial x_i} \right), \tag{10}$$

and σ_{ij} is the Cauchy stress tensor for Newtonian fluids:

$$\sigma_{ij}(\boldsymbol{u}^f, p^f) = -p^f \delta_{ij} + 2\mu^f \epsilon_{ij}^f(\boldsymbol{u}^f). \tag{11}$$

4.2 Subgrid Stabilization

The convective terms in the incompressible NS equations may cause spurious node-to-node oscillations in the velocities field. Furthermore, equal-order approximations used for v_i^f and q^f may cause pressure oscillations. To prevent these oscillations, this work augments the NS equations with Streamline Upwind Petrov-Galerkin

(SUPG) and the Pressure Stabilized Petrov-Galerkin (PSPG) stabilization formulations introduced in [42]:

$$r_{\boldsymbol{u},p}^{\hat{\Omega}} = \sum_{\Omega_e \in \Omega} \int_{\Omega_e \cap \Omega^f} \left(\left(\tau_{SUPG} \left(u_i^f \frac{\partial v_i^f}{\partial x_j} \right) + \tau_{PSPG} \left(\frac{1}{\rho_f} \frac{\partial q^f}{\partial x_i} \right) \right) \cdot \left(\rho^f \left(\frac{\partial u_i^f}{\partial t} + u_i^f \frac{v_i^f}{\partial x_j} \right) \frac{\partial p^f}{\partial x_j} \delta_{ij} - 2\mu^f \frac{\partial}{\partial x_j} \left(\epsilon_{ij}(\boldsymbol{u}^f) \right) \right) \right) \mathrm{d}\Omega, \tag{12}$$

where Ω_e denotes the set of all elements in the domain Ω, and the stabilization terms τ_{SUPG} and τ_{PSPG} are defined in [42].

4.3 Ghost-Penalty Stabilization

As the optimization process updates the design geometry, the fluid-solid interface may lead to intersection patterns where certain degrees-of-freedom interpolate into very small subdomains, i.e. as the interfaces approaches a node [39]. This results in an ill-conditioning of the linear sub-problem, which in turn results in an increased condition number of the linearized system and may slow down or prevent the convergence of the nonlinear program. To guarantee stability, as well as improve the condition number, face-oriented ghost-penalty stabilization terms are used to in the vicinity of the fluid-solid interface [39], c.f. [36]. The ghost-penalty terms for the residual contribution of the incompressible NS equations are defined as:

$$r_{\boldsymbol{u},p}^{GP} = r_{\boldsymbol{u},p}^{GP,\mu} + r_{\boldsymbol{u},p}^{GP,p}, \tag{13}$$

where $r_{\boldsymbol{u},p}^{GP,\mu}$ and $r_{\boldsymbol{u},p}^{GP,p}$ are the viscous and pressure ghost-penalty formulations, respectively.

The viscous face-oriented ghost-penalty formulation, as proposed by [43], is used to overcome stability issues related to the weak enforcement of boundary conditions via Nitsche's method, and is defined as:

$$r_{\boldsymbol{u},p}^{GP,\mu} = \sum_{F \in \Xi^f} \int_F \left(\gamma_{GP,\mu} \left[\!\!\left[\frac{\partial v_i^f}{\partial x_j} \right]\!\!\right] n_j^f \left[\!\!\left[\frac{\partial u_i^f}{\partial x_k} \right]\!\!\right] n_k^f \right) \mathrm{d}\Gamma, \tag{14}$$

where $\gamma_{GP,\mu}$ is a penalty parameter defined as:

$$\gamma_{GP,\mu} = \alpha_{GP,\mu} \mu^f h, \tag{15}$$

and $\alpha_{GP,\mu}$ is a chosen constant scaling factor. The jump operator is defined as:

$$[\![\zeta]\!] = \zeta|_{\Omega_e^1} - \zeta|_{\Omega_e^2}, \tag{16}$$

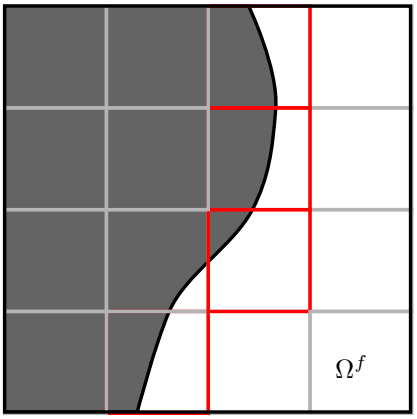

Figure 2: Facets Ξ^f in domain Ω^f.

and is evaluated at the facet between two adjacent elements, Ω_e^1 and Ω_e^2. This term overcomes the small-area issue on elements bisected by the interface because the domain of integration is the entire edge, regardless of the intersection pattern. The set Ξ^f belonging to the domain Ω_f contains all facets F for which at least one of the two adjacent elements is intersected by the fluid-solid interface; for example, see Figure 2.

We apply the pressure ghost-penalty stabilization term is to control pressure instabilities due to a violated inf-sup condition for equal-order approximations used for u_i^f and p^f [37, 44], defined as:

$$r_{\boldsymbol{u},p}^{GP,p} = \sum_{F \in \Xi^f} \int_F \left(\gamma_{GP,p} \left[\!\left[\frac{\partial q_i^f}{\partial x_j} \right]\!\right] n_j^f \left[\!\left[\frac{\partial p_i^f}{\partial x_k} \right]\!\right] n_k^f \right) \mathrm{d}\Gamma, \tag{17}$$

where $\gamma_{GP,p}$ is a penalty parameter defined as:

$$\gamma_{GP,p} = \alpha_{GP,p} \left(\frac{\mu^f}{h} + \frac{\rho ||\boldsymbol{u}^f||_\infty}{6} \right)^{-1} h^2, \tag{18}$$

and $\alpha_{GP,p}$ is a chosen constant scaling parameter.

As discussed by Villanueva and Maute [39], the literature has proposed additional ghost-penalty measures, e.g. to control instabilities arising from the incompressibility constraint. However, these additional formulations are not considered in our numerical examples because previous studies have not revealed any further improvement for the laminar flow situations analyzed here, see also [37].

4.4 Boundary Conditions

The Kn-slip boundary condition (2) extends the second-order model found in [45], which is based on Maxwell's proposal of the fundamental description of gas-surface interaction [46], to include the tangential gradients, i.e. $\partial u_n/\partial t$, for arbitrarily oriented interfaces found in [5].

Throughout the literature, the third term in (2) traditionally takes on a negative sign because the interface normal vector is defined as pointing towards the fluid domain. However, in this paper, the normal vector is defined as pointing outward from the fluid domain, see Figure 1; thus, the sign of the third term in (2) is positive. Note that the Kn-slip boundary convergences to the no-slip condition, as $Kn \to 0$. An empirical model for the accommodation coefficient, σ, has been proposed by McNenly [6] for simple flows; however, there is no general agreement on the appropriate value or form for the accommodation coefficient [11]. For simplicity, this paper will use $\sigma = 1$, as the goal of this paper is to study the general effect of the slip boundary condition on the optimal design without the desire to study a particular fluid.

The Kn-slip boundary condition governs the tangential velocity at the fluid-solid interface and requires gradients in the normal and tangential directions; as such, the exact location and orientation of the interface is required. We enforce the Kn-slip boundary condition (2) on the fluid-solid interface along the tangential direction via:

$$\boldsymbol{R}_{Kn} = \left(u_t - u_t^w + \frac{Kn}{1+Kn} \left(\frac{\partial u_t}{\partial n} + \frac{\partial u_n}{\partial t} \right) \right) \hat{\boldsymbol{t}}, \tag{19}$$

where $\hat{\boldsymbol{t}}$ is the unit tangential vector along the fluid-solid interface. Treating vectors as column matrices, we then expand the derivatives as:

$$\frac{\partial u_t}{\partial n} = \frac{\partial (\boldsymbol{u} \cdot \hat{\boldsymbol{t}})}{\partial n} = \frac{\partial \boldsymbol{u}}{\partial n} \cdot \hat{\boldsymbol{t}} + \boldsymbol{u} \cdot \frac{\partial \hat{\boldsymbol{t}}}{\partial n} = \hat{\boldsymbol{t}}^T \boldsymbol{J}_u \hat{\boldsymbol{n}} + (\boldsymbol{J}_t \hat{\boldsymbol{n}})^T \boldsymbol{u}, \tag{20}$$

where

$$(\boldsymbol{J}_u)_{ij} = \frac{\partial u_i}{\partial x_j}, \ (\boldsymbol{J}_n)_{ij} = \frac{\partial n_i}{\partial x_j}, \text{ and } (\boldsymbol{J}_t)_{ij} = \frac{\partial t_i}{\partial x_j}, \tag{21}$$

are the spatial derivatives of the velocities and normal and tangent vectors, and similarly for $\partial u_n / \partial t$,

Recognizing that, for any rotated local coordinate system,

$$\hat{\boldsymbol{t}}\hat{\boldsymbol{t}}^T = \boldsymbol{I} - \hat{\boldsymbol{n}}\hat{\boldsymbol{n}}^T, \tag{22}$$

we can write (19) as:

$$\begin{aligned} \boldsymbol{R}_{Kn} = & \left(\boldsymbol{I} - \hat{\boldsymbol{n}}\hat{\boldsymbol{n}}^T \right) \boldsymbol{u} - \left(\boldsymbol{I} - \hat{\boldsymbol{n}}\hat{\boldsymbol{n}}^T \right) \boldsymbol{u}^w \\ & + \frac{Kn}{1+Kn} \left(\boldsymbol{I} - \hat{\boldsymbol{n}}\hat{\boldsymbol{n}}^T \right) \left(\boldsymbol{J}_u + \boldsymbol{J}_u^T \right) \hat{\boldsymbol{n}} + \frac{Kn}{1+Kn} \left(\left(\boldsymbol{I} - \hat{\boldsymbol{n}}\hat{\boldsymbol{n}}^T \right) \boldsymbol{J}_n^T \boldsymbol{u} + \hat{\boldsymbol{t}}\hat{\boldsymbol{n}}^T \boldsymbol{J}_t^T \boldsymbol{u} \right). \end{aligned} \tag{23}$$

Note that (22) nearly eliminates the need to define the tangent vector, i.e. $\hat{\boldsymbol{t}}$ only appears in the last term, but the terms that involve its gradients cannot make use of the identity (22). In future sections of this

paper, we will collectively refer to the last two terms in (23) as the "$\boldsymbol{J}_{\{n,t\}}$ terms". These terms relate to the curvature of the interface and are included in the Kn-slip boundary condition found in [5]. Thus, besides the location and orientation of the fluid-solid interface, the Kn-slip boundary condition may also require knowledge of the interface curvature. These terms are studied in Section 5.2.

4.4.1 Implementation with Nitsche's method

In this paper, we adapt the boundary condition enforcement method described in [39]. There, Nitsche's method is used to enforce no-slip boundary conditions with:

$$\begin{aligned} r^m_{\boldsymbol{u},p} = &\int_{\Gamma^m} v_i^f \left(p^f \delta_{ij} - 2\mu^f \epsilon_{ij}(\boldsymbol{u}^f)\right) n_j^f \,\mathrm{d}\Gamma \\ &+ \int_{\Gamma^m} \left(\beta_p q^f \delta_{ij} - \beta_\mu 2\mu^f \epsilon_{ij}(\boldsymbol{v}^f)\right) n_j^f \left(u_i^f - \hat{u}_i^f\right) \mathrm{d}\Gamma \\ &+ \int_{\Gamma^m} \left(\lambda_{N,\boldsymbol{u}} v_i^f \left(u_i^f - \hat{u}_i^f\right)\right) \mathrm{d}\Gamma, \end{aligned} \tag{24}$$

where $\lambda_{N,\boldsymbol{u}}$ is the Nitche penalty parameter. The terms β_p and β_μ determine whether the second term uses a symmetric ($\beta_p = +1$, $\beta_\mu = +1$) or a skew-symmetric formulation ($\beta_p = -1$, $\beta_\mu = -1$). In this paper, we follow [39] and use the symmetric variant for the viscous term, i.e. $\beta_\mu = 1$, and the skew-symmetric variation for the pressure term, i.e. $\beta_p = -1$. The symmetric variant for the viscous term leads to smaller errors when compared to the skew-symmetric variant, as reported by [47]. The skew-symmetric variant for the pressure term is used because it consistently controls the mass conservation, $u_i^f n_i^f = 0$ [37, 48]. $m \in \{D, fs\}$ denotes the enforcement of boundary conditions on the external boundaries or on the fluid-solid interface. The penalty term $\lambda_{N,\boldsymbol{u}}$ is adopted from [37] and defined as:

$$\lambda_{N,\boldsymbol{u}} = \alpha_{N,\boldsymbol{u}} \left(\frac{\mu^f}{h} + \frac{\rho^f ||\boldsymbol{u}^f||_\infty}{6}\right), \tag{25}$$

and its terms account for viscous-dominated and convection-dominated flows, respectively. $\alpha_{N,\boldsymbol{u}}$ is problem-dependent and the term $||\boldsymbol{u}^f||_\infty$ is the infinity norm evaluated at each integration point and differentiated at its maximum value. The influence of this term is studied in [39].

This formulation, however, is written exclusively for the no-slip boundary condition. We generalize this by first considering a split of (24) into normal and tangential components. We enforce the no-penetration condition, i.e. $u_n = u_n^w$, along the normal direction, and the no-slip or the Kn-slip condition in the tangential direction. After reassembling the terms, we can write (24) as:

$$
\begin{aligned}
r^m_{\boldsymbol{u},p} = &\int_{\Gamma^m} v_i^f \left(p^f \delta_{ij} - 2\mu^f \epsilon_{ij}(\boldsymbol{u}^f)\right) n_j^f \mathrm{d}\Gamma \\
&+ \int_{\Gamma^m} \left(\beta_p q^f \delta_{ij} - \beta_\mu 2\mu^f \epsilon_{ij}(\boldsymbol{v}^f)\right) n_j^f \Upsilon_j \mathrm{d}\Gamma \\
&+ \int_{\Gamma^m} \left(\lambda_{N,\boldsymbol{u}} v_i^f \Upsilon_j\right) \mathrm{d}\Gamma,
\end{aligned} \tag{26}
$$

where

$$
\boldsymbol{\Upsilon} = \begin{cases} \boldsymbol{u} - \hat{\boldsymbol{u}} & , \text{ to enforce no-slip} \\ \boldsymbol{u}_n - \hat{\boldsymbol{u}}_n + \boldsymbol{R}_{Kn} & , \text{ to enforce Kn-slip.} \end{cases} \tag{27}
$$

4.5 Weak enforcement of the normal vector

The Kn-slip boundary condition, introduced in Section 4.4, requires knowing the gradient of the normal and tangential vectors at an interface. The normal vector at the fluid-solid interface (and, by extension, the tangential vector) is defined as the gradient of the LSF:

$$
\hat{\boldsymbol{n}} = \frac{\nabla \phi}{|\nabla \phi|}. \tag{28}
$$

Thus, the gradient of the normal vector requires second-order derivatives of the LSF, which are not available when using bilinear elements. One option is to use analytical expressions for the LSF, which allows analytically evaluating (28). This option is attractive but is in general not applicable in a topology optimization framework, since the LSF is not known analytically. An alternative option is to project the level set gradients onto a smoother approximation space which allows computing curvature information using low-order elements. The projection is defined by:

$$
r_{\hat{\boldsymbol{n}}} = \int_\Omega \delta \hat{\boldsymbol{n}} \cdot \left(\hat{\boldsymbol{n}} \, |\nabla \phi| - \nabla \phi\right) \mathrm{d}\Omega, \tag{29}
$$

where $\hat{\boldsymbol{n}}$ is the projected normal. Introducing the normal vector components as nodal degrees-of-freedom increases the number of degrees-of-freedom per node from 3 to 5. Because of this increase in problem size, it is important to understand if or when the $\boldsymbol{J}_{\{n,t\}}$ terms can be neglected.

4.6 XFEM Discretization

The governing equations in the fluid phase are discretized in space by the XFEM. This paper adopts the generalized enrichment strategy based on the Heaviside-step enrichment of [49], which interpolates consis-

tently the solution field in the presence of small features and does not suffer from artificial coupling arising from disconnected phases. This particular approach has been used for incompressible Navier-Stokes [40], linear diffusion, [32], advection-diffusion, [41], and linear elasticity problems [44, 50].

The XFEM is used to approximate a state variable in only a single phase or in both phases. Here, we present the most general case, where the state variables are modeled in both phases. The approximation for a solution field u, i.e. the fluid velocity components, within an element is denoted as $\tilde{u}$ and is discretized by the enrichment strategy:

$$u(\boldsymbol{x}) \approx \tilde{u}(\boldsymbol{x}) = \sum_{l=1}^{N_l} \left(H(-\phi(\boldsymbol{x})) \sum_{i=1}^{N_n} v_i(\boldsymbol{x}) \delta_{lk}^{i,f} u_{i,l}^{f} + H(+\phi(\boldsymbol{x})) \sum_{i=1}^{N_n} v_i(\boldsymbol{x}) \delta_{ln}^{i,s} u_{i,l}^{s} \right), \tag{30}$$

where l is the enrichment level, N_l is the maximum number of enrichment levels used for each phase, $v_i(\boldsymbol{x})$ are the nodal basis function, i.e. the shape functions, $u_{i,l}^{f}$ and $u_{i,l}^{s}$ are the degrees-of-freedom of enrichment level l at node i in the fluid and solid phase, respectively, and H denotes the Heaviside function, which turns the interpolation for phase m on and off, and is defined as:

$$H(\zeta) = \begin{cases} 1, \ \zeta < 0 \\ 0, \ \zeta > 0, \end{cases} \tag{31}$$

The Kronecker delta, $\delta_{ab}^{i,m}$, selects the degrees-of-freedom for phase m. The indices k and n denote the active degree-of-freedom at node i in the fluid and solid phases, respectively. At any given point, only one degree-of-freedom per node is used to interpolate the solution, ensuring the partition of unity is satisfied. For problems where the solid phase is void, the respective degrees-of-freedom are condensed out of the problem and set to zero.

For each phase, multiple enrichment levels, i.e. sets of shape functions, may be necessary to interpolate the state variables in multiple, physically disconnected regions of the same phase, cf. [51], [52], and [50]. In order to accurately integrate the weak form of the governing equations by Gaussian quadrature, intersected elements are decomposed into triangles. The reader is referred to [50] for more details on the particular XFEM implementation used in this paper.

The Heaviside-step enrichment formulation (30) has a singularity for cases in which the fluid-solid interface lies exactly on a node, i.e. the level set value ϕ_i at node i equals 0. To avoid this issue, we adopt the level set perturbation approach outlined in [53] and [32]. If the magnitude of the level set value at a node is smaller than some critical value, ϕ_c, it is modified to a shift value, ϕ_s. This perturbation results in the fluid-solid interface moving away from the node, solving the singularity issue. In this study, we adopt the values of

$\phi_c = \phi_s = 10^{-6} \times h$, where h is the size of an element. This perturbation strategy was used by [54], where it is shown that the influence of the perturbation is negligible.

5 Numerical Examples

In the following, we study the characteristics of the proposed Kn-slip boundary condition for steady-state flow problems in 2D. We first compare the accuracy against an analytical solution and investigate the need for the normal and tangential vector gradients in the Kn-slip boundary condition (2). We then study the effect of the Kn-slip against the no-slip boundary condition, as well as the effect of the $\boldsymbol{J}_{\{n,t\}}$ terms, on the design of a splitting manifold. Finally, we study the impact of the Kn-slip boundary condition on the design of a fixed-valve. Unless otherwise stated, geometric and material parameters are given in non-dimensional and self-consistent units.

In this study, the time integration is performed by a 1-step backward differentiation scheme. Most steady-state flow problems use a homotopy approach, i.e. a sufficiently small time step is initially chosen to achieve stability and it is then gradually increased until a steady-state solution is achieved. The problems considered in this paper where not found to need this approach; instead, a sufficiently large time step is chosen.

The equilibrium at any time step (n) is satisfied by solving the nonlinear system $\boldsymbol{R}^{(n)}$ via Newton's Method, where:

$$\boldsymbol{R} = r_{\boldsymbol{u},p} + r_{\hat{\boldsymbol{n}}}. \tag{32}$$

In each Newton step, the linear sub-problem is solved using the Generalized Minimal RESidual (GMRES) iterative method [55], with an Incomplete LU factorization with dual Threshold (ILUT) preconditioner [56].

The optimization problem (3) is solved by a gradient-based algorithm, and the gradients of the objective and constraint functions with respect to the optimization variables, s_i, are computed via the adjoint method. In this paper, we adopt the discrete adjoint formulation for nonlinear fluid systems of [57] and [58]. The problems are solved via the Globally Convergent Method of Moving Asymptotes (GCMMA) of [59]. The GCMMA parameters are given in Table I. The stopping criteria for the optimization are: (i) the change in the objective value relative to the previous value is less than 10^{-6} and (ii) all constraints are satisfied.

5.1 Scope

The Knudsen number (1) is also given by the Reynolds and Mach numbers [60] via:

$$Kn = \frac{Ma}{Re}\sqrt{\frac{\gamma\pi}{2}}. \tag{33}$$

	Value
Relative step size	0.01
Minimum asymptote adaptivity	0.5
Initial asymptote adaptivity	0.7
Maximum adaptivity	1.43
Constraint penalty	100

Table I: GCMMA parameters for the topology optimization problems.

In our experience, flows with larger inertial effects experience more significant design changes. Because the incompressible NS equations, used in this paper, are valid only for $Ma < 0.3$, we will limit the maximum Kn number of interest to allow a larger Re number, which in turn allows for larger inertial effects in the fluid flow problems considered.

5.2 Radial Couette Flow: Flow Between Rotating Cylinders

To understand the effect of the Kn-slip boundary condition and the importance of the $\boldsymbol{J}_{\{n,t\}}$ terms in (23), we consider the flow between rotating concentric cylinders with inner and outer radii, r_1 and r_2, and angular speeds, ω_1 and ω_2, respectively. In polar coordinates, the NS equations admit the general solution:

$$u_\theta(r) = Ar + \frac{B}{r}, \tag{34}$$

where A and B are determined from the boundary condition. With the no-slip boundary condition, i.e. $u_\theta|_{r=r_1} = r_1\omega_1$ and $u_\theta|_{r=r_2} = r_2\omega_2$, A and B take the well-known form:

$$A = \frac{r_2^2\omega_2 - r_1^2\omega_1}{r_2^2 - r_1^2}, \quad B = \frac{r_2^2 r_1^2\left(\omega_1 - \omega_2\right)}{r_2^2 - r_1^2} \tag{35}$$

For the Kn-slip boundary condition, A and B are the solution to the system of equations:

$$\begin{aligned} \left(r_1 - \frac{Kn}{1+Kn}\right)A + \left(\frac{1}{r_1} + \frac{1}{r_1^2}\frac{Kn}{1+Kn}\right)B &= r_1\omega_1, \\ \left(r_2 + \frac{Kn}{1+Kn}\right)A + \left(\frac{1}{r_2} - \frac{1}{r_2^2}\frac{Kn}{1+Kn}\right)B &= r_2\omega_2. \end{aligned} \tag{36}$$

Note that (35) is the solution to (36) for $Kn = 0$. In this example, we use $r_1 = 1$, $r_2 = 2$, $\omega_1 = -5$, and $\omega_2 = 5$; in the fluid, $\rho = 1$ and $\mu = 1$. The domain $\Omega = \{(x, y)| - 2.25 \leq x \leq 2.25, -2.25 \leq y \leq 2.25\}$ is discretized with a $(9/2)N_e \times (9/2)N_e$ uniform square mesh, such that the width of an element is $1/N_e$, for

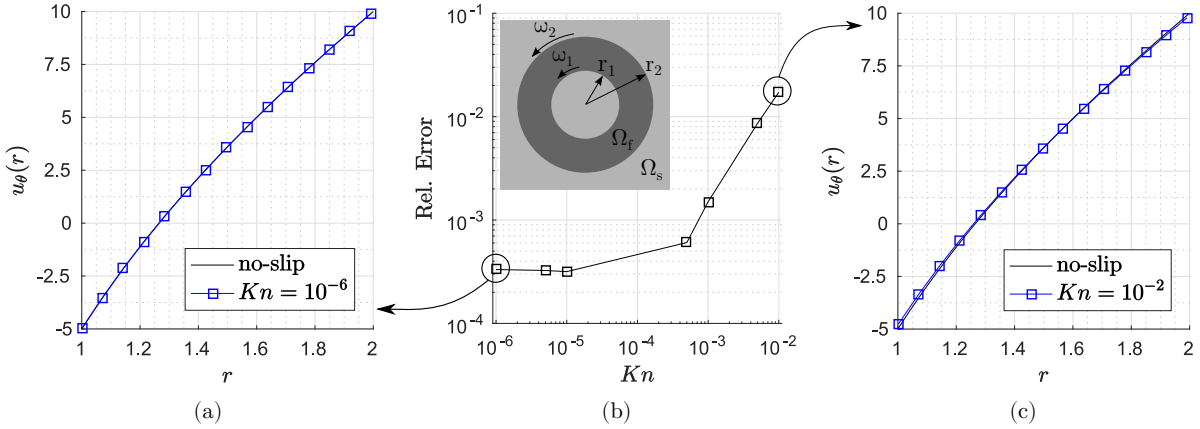

Figure 3: Numerical flow solutions against the no-slip analytical solution for $Kn = 10^{-6}$ (a) and $Kn = 10^{-2}$ (c), and relative error of flow solutions against the no-slip analytical solution (b).

values of N_e ranging from $N_e = 30$ to $N_e = 120$. The fluid domain is described with the LSF:

$$\phi(r) = \left| r - \frac{r_1 + r_2}{2} \right| - \frac{r_2 - r_1}{2}, \tag{37}$$

where $r = \sqrt{x^2 + y^2}$.

To find the critical Kn number at which the Kn-slip boundary condition becomes necessary, we simulate the flow between rotating cylinders with the Kn-slip boundary condition for Kn in the range of $10^{-6} - 10^{-2}$ and compare the results to the no-slip analytical solution. Figure 3a and Figure 3c show the velocity distributions of the simulated flows and the no-slip analytical solution for $Kn = 10^{-6}$ and $Kn = 10^{-2}$, respectively. The solution with $Kn = 10^{-6}$ overlaps the no-slip analytical solution, whereas the solution with $Kn = 10^{-2}$ begins to separate from the no-slip analytical solution near the rotating cylinders. Further, Figure 3b shows relative error of the flow solutions for various Kn numbers against the no-slip analytical solution, defined as:

$$\text{Rel. Error} = \frac{\int \left(u^{sol}_{\theta, Kn_i} - u^{analytical}_{\theta, no-sip} \right)^2 \mathrm{d}\Omega}{\int \left(u^{analytical}_{\theta, no-sip} \right)^2 \mathrm{d}\Omega}. \tag{38}$$

For $Kn < 10^{-3}$, it remains safe to use the no-slip boundary condition; however, the relative error begins to more rapidly increase near $Kn = 10^{-3}$. Thus, slip effects show an impact on the flow starting near $Kn = 10^{-3}$, as suggested by [10].

5.2.1 Effect of the normal and tangential vector gradients

Given that the Kn-slip boundary condition is important for $Kn > 10^{-3}$, we now seek to understand the importance of the $\boldsymbol{J}_{\{n,t\}}$ terms. As the LSF is defined analytically for this example, we can derive analytical expressions for $\boldsymbol{J}_{\{n,t\}}$:

$$\boldsymbol{J}_n = \operatorname{sgn}\left(r - \frac{r_1 + r_2}{2}\right)\begin{pmatrix} -\frac{y^2}{r^3} & +\frac{xy}{r^3} \\ +\frac{xy}{r^3} & -\frac{x^2}{r^3} \end{pmatrix}, \text{ and } \boldsymbol{J}_t = \operatorname{sgn}\left(r - \frac{r_1 + r_2}{2}\right)\begin{pmatrix} +\frac{xy}{r^3} & -\frac{x^2}{r^3} \\ +\frac{y^2}{r^3} & -\frac{xy}{r^3} \end{pmatrix}. \tag{39}$$

We analyze the flow with the Kn-slip boundary condition (a) without the $\boldsymbol{J}_{\{n,t\}}$ terms, (b) with the analytical expressions (39) for $\boldsymbol{J}_{\{n,t\}}$, and (c) computing $\boldsymbol{J}_{\{n,t\}}$ by (21) using the projected normal vectors (29), for $Kn = 0.01$, 0.02, and 0.05.

Figure 4a shows the Kn-slip analytical solutions (34), (36) for each Kn number, while Figures 4b and 4c additionally show the flow solutions with and without the $\boldsymbol{J}_{\{n,t\}}$ terms. The selected views show that the solutions obtained with the $\boldsymbol{J}_{\{n,t\}}$ terms, i.e. cases (b) and (c), agree with each other and with the analytical solution. The velocities obtained without the $\boldsymbol{J}_{\{n,t\}}$ terms diverge from the analytical solution for larger Kn numbers, especially for $Kn = 0.05$ in Figure 4c.

Figure 5 shows the relative error against the analytical solution, (34) and (36), for each case and Kn number. When the $\boldsymbol{J}_{\{n,t\}}$ terms are omitted, the relative error grows slowly but remains small for the smallest Kn value. For $Kn = 0.01$, the relative error after omitting the $\boldsymbol{J}_{\{n,t\}}$ terms approaches 1%; for $Kn = 0.05$, the relative error becomes more significant, at approximately 4%. These terms will be further studied in the context of topology optimization.

Further, when the $\boldsymbol{J}_{\{n,t\}}$ terms are included, the order of convergence with respect to the analytical solution is approximately linear for all Kn numbers. Both methods of including the $\boldsymbol{J}_{\{n,t\}}$ terms converge to the analytical solution, meaning that the projected normals are equivalent to the case where analytical expressions for the gradients are used.

Our implementation of the Kn-slip boundary condition is thus validated against an analytical solution. This study suggests that, for $Kn > 10^{-3}$, the Kn-slip boundary condition should be used over the no-slip condition and that the $\boldsymbol{J}_{\{n,t\}}$ terms should be included. Because analytical expressions for $\boldsymbol{J}_{\{n,t\}}$ are not available in the context of topology optimization, $\boldsymbol{J}_{\{n,t\}}$ can be computed from projected normals (29).

5.3 Design of a splitting manifold

In this example, we consider the design of a manifold with multiple outlets under steady-state flow conditions, where the objective is to maximize the mass flow rate through the manifold. The example is an extension of

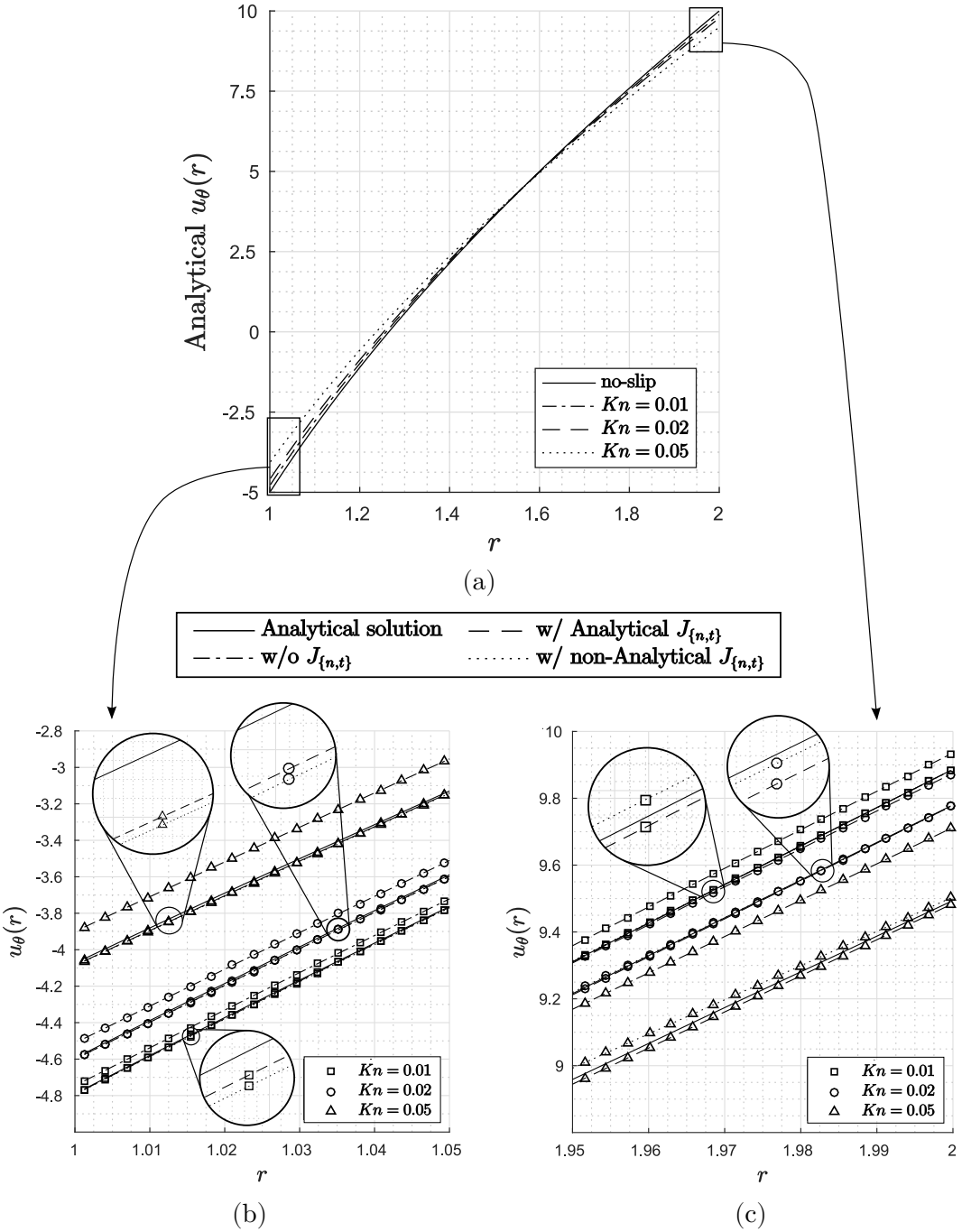

Figure 4: Velocity distributions of the analytical solution (a) and detailed views with and without the $\boldsymbol{J}_{\{n,t\}}$ terms (b and c).

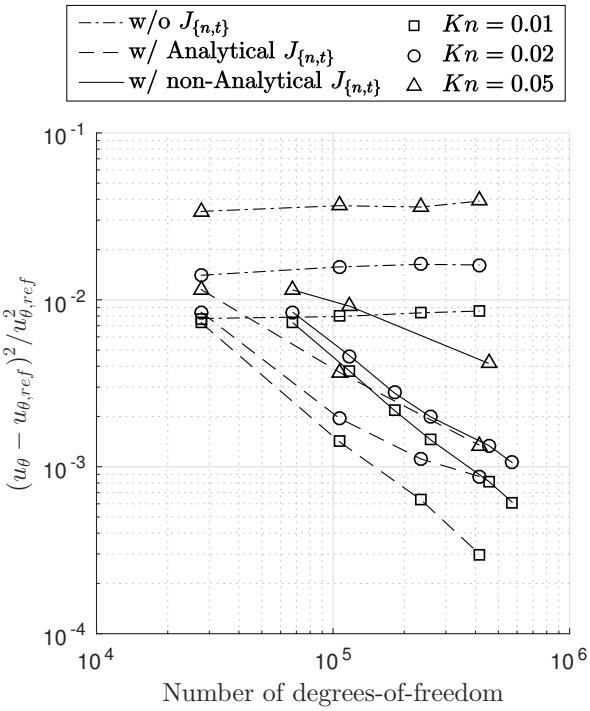

Figure 5: Relative error in the velocity distributions with and without the $\boldsymbol{J}_{\{n,t\}}$ terms with respect to the analytical solution using the Kn-slip boundary condition.

the bend problem found in [61] and is motivated by the following considerations: because the manifold must optimally split and redirect the flow, the increase in momentum due to the velocity slip that occurs at finite Kn numbers may require significant changes in the optimal design. Alternatively, if no significant changes are present, then the Kn-slip boundary condition could be safely ignored during the design optimization process and later considered in a *post-hoc* analysis.

The problem setup is shown in Figure 6. The design domain has one inlet (on the left) and four outlets (two on the right, and one on each of the other planes). Traction-free boundary conditions are enforced on all outlets and the inlet is given a prescribed pressure to drive the flow. We model only half of the domain, and a symmetry boundary condition is enforced on the $y = 2L$ plane.

In addition to maximizing the mass flow rate through the manifold, we minimize the perimeter of the fluid-solid interface. A perimeter penalty in the objective function was previously applied to species transport topology optimization by Makhija and Maute [41] to improve the smoothness of the final design and to regularize the optimization problem. Thus, the objective is defined as:

$$\mathcal{Z} = -\frac{\sum_{i\in\{1a\ldots 2b\}} \dot{m}_{out,i}}{\sum_{i\in\{1a\ldots 2b\}} \dot{m}^0_{out,i}} + w_{\mathcal{P}} \frac{\mathcal{P}}{\mathcal{P}^0}, \tag{40}$$

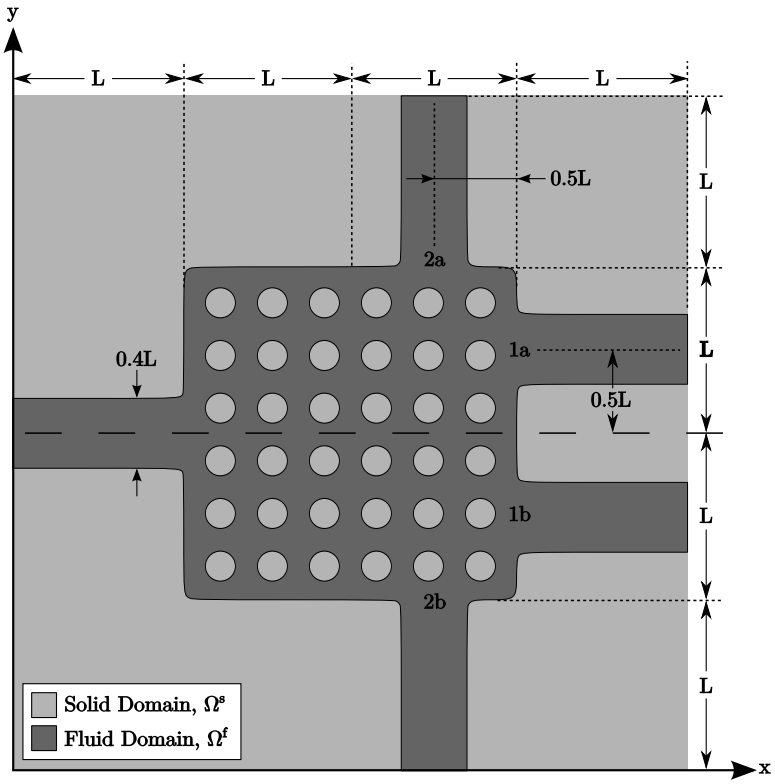

Figure 6: Problem setup and initial design for the splitting manifold problem. The dashed line denotes the symmetry plane.

Case	Description
(a)	no-slip boundary condition
(b)	Kn-slip boundary condition with $Kn = 0.01$
(c)	Kn-slip boundary condition with $Kn = 0.02$

Table II: Boundary condition cases for the splitting manifold problem.

where the superscript "0" denotes the values of the initial design, the subscript i denotes the i-th outlet, and $w_{\mathcal{P}}$ is a constant scaling factor. Unless otherwise noted, $w_{\mathcal{P}} = 0.1$. The mass flow rate through a port is defined as:

$$\dot{m}_i = \int_{\Gamma_i^f} \rho^f \left(\boldsymbol{u}^f \cdot \hat{\boldsymbol{n}}\right) \mathrm{d}\Gamma. \tag{41}$$

The perimeter is defined as:

$$\mathcal{P} = \int_{\Gamma^{fs}} \mathrm{d}\Gamma. \tag{42}$$

The fluid volume inside the design domain is constrained to a fraction, $f_{\mathcal{V}}$, of the design domain to suppress trivial solutions and to promote the formation of distinct fluid channels:

$$g_1 = \frac{\mathcal{V}^{fd}}{f_{\mathcal{V}} \mathcal{V}^d} - 1, \tag{43}$$

Configuration	Requirement
(i)	$f_{1a} = f_{1b} = 2/3,\ f_{2a} = f_{2b} = 1/3$
(ii)	$f_{1a} = f_{1b} = 1/2,\ f_{2a} = f_{2b} = 1/2$
(iii)	$f_{1a} = f_{1b} = 1/3,\ f_{2a} = f_{2b} = 2/3$

Table III: Outlet configurations for the splitting manifold problem.

	Value
Mesh size	62×93
Element size	$h = 0.03226L$
Characteristic length	$L = 1$
Fluid density	$\rho^f = 1.205$
Fluid viscosity	$\mu^f = 1.511 \times 10^{-5}$
Inlet pressure	$p_{in} = 1.5 \times 10^{+4}$
Perimeter scaling factor	$w_{\mathcal{P}} = 0.1$
Outlet requirement error	$\tau = 0.005$
Nitsche velocity parameter	$\alpha_{N,\boldsymbol{u}} = 10$
Viscous ghost-penalty	$\alpha_{GP,\mu} = 5 \times 10^{+0}$
Pressure ghost-penalty	$\alpha_{GP,p} = 5 \times 10^{-1}$
Convective ghost-penalty	$\alpha_{GP,\boldsymbol{u}} = 5 \times 10^{-1}$
Relative Optimization Step	$\Delta s = 0.01$
Design variable bounds	$s_i^L = -0.03226L, s_i^U = +0.03226L$
Smoothing radius	$r_\phi = 2.4h$
Number of design variables	$1,849$ (half-domain)

Table IV: Parameters for the splitting manifold problem.

where the fluid volume inside the design domain is defined as:

$$\mathcal{V}^{fd} = \int_{\Omega^f \cap \Omega^d} \mathrm{d}\Omega. \tag{44}$$

Further, we wish to specify the ratio of the outlet mass flow rates. Given that the GCMMA algorithm does not allow equality constraints, we recourse to imposing inequality constraints with lower and upper limits on the mass flow rates. The lower and upper inequality constraint on the i-th outlet are given as in [39]:

$$g_{i+1} = \frac{(1-\tau) f_i \dot{m}_{in} - \dot{m}_{out,i}}{\dot{m}_{in}^0} \tag{45}$$

$$g_{i+5} = \frac{-(1+\tau) f_i \dot{m}_{in} + \dot{m}_{out,i}}{\dot{m}_{in}^0} \tag{46}$$

where τ is a small tolerance value, f_i is the desired fraction of the total mass flow rate through outlet i, and $\sum f_i = 1$. Unless otherwise stated, $\tau = 0.005$. In this paper, we study three constraint configurations, summarized in Table III: (i) the flow rate through the horizontal outlets is twice that of the vertical outlets,

(ii) the outlets have equal flow rates, and (iii) the flow rate through the vertical outlets is twice that of the horizontal outlets. The remaining parameters for the fluid and optimization problem are given in Table IV. Since an outlet cannot simultaneously violate both its minimum and maximum constraints, when reporting whether constraints are violated, we will report the deviation from the target mass flow rate fraction:

$$h_i = \frac{1}{f_i}\left|\frac{\dot{m}_{out,i}}{\sum \dot{m}_{out,i}} - f_i\right| \tag{47}$$

such that $h_i < \tau$ if outlet i satisfies both its constraints or $h_i > \tau$ if one of its constraints is violated.

Since sensitivities only exist near the fluid-solid interface, the LSM-XFEM restricts the topology optimization problem to a general shape optimization problem, no solid inclusions can be created within the fluid phase but only merge. To mitigate this issue, the design is initially seeded with an array of inclusions. In this example, the design domain is initialized with 6×6 circular solid inclusions of radii $0.09L$, as shown in Figure 6. In our experience, the flow topology optimization problems studied here are rather insensitive to the initial design as long as the number of inclusions is sufficiently large.

We consider two problems with different Kn numbers but choose the other flow parameters such that the problems have the same nondimensional inlet pressure. For each of these problems, we will study the differences in design and performance if the Kn-slip boundary condition is ignored. Two problems with different finite Kn numbers but the same nondimensional inlet pressure have the same nondimensional solution, if the Kn-slip boundary condition is ignored and the no-slip condition is used. Thus, we consider the same nondimensional setup with various boundary conditions: (a) no-slip, which is equivalent to ignoring the Kn-slip boundary condition despite a finite Kn number, and the Kn-slip boundary condition with (b) $Kn = 0.01$ or (c) $Kn = 0.02$, as summarized in Table II. The "no-slip" case in Table II represents any problem in which the Kn-slip boundary condition is ignore regardless of whether the Kn is finite or negligible.

5.3.1 Effect of the Kn-slip boundary condition

We study the influence of the boundary condition on the optimum design. When model Kn-slip, the $\boldsymbol{J}_{\{n,t\}}$ terms are included. We find the optimal design for each case in Table II and each configuration in Table III. Figure 7 shows the convergence plots of the objective and the volume and mass flow rate constraints for the no-slip problem in Configuration (i). The initial design violates the volume and some of the mass flow rate constraints; in the process of satisfying these constraints, the objective increases. After the constraints are satisfied, the objective reaches a feasible minimum. The convergence behavior for the other cases and configurations is similar.

The velocity magnitude through the converged designs for constraint configuration (i)-(iii) are shown

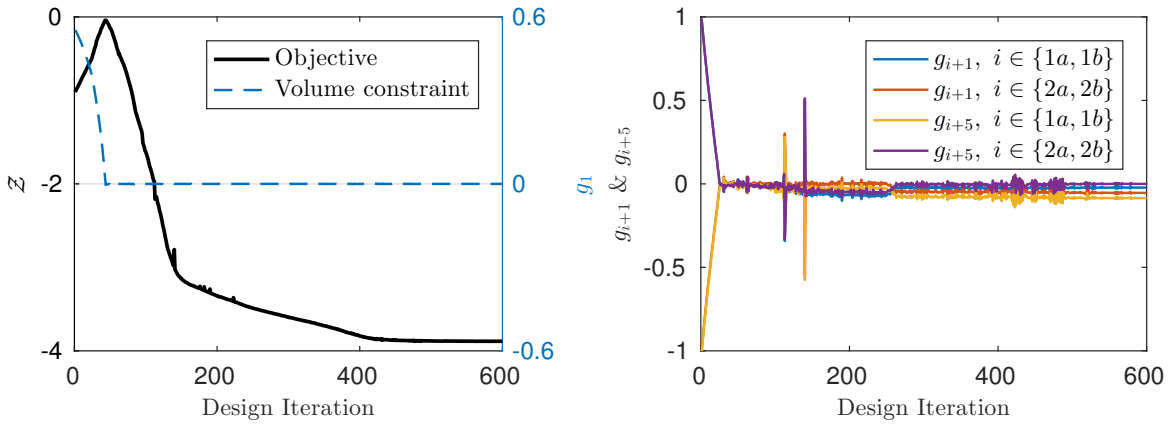

(a) Objective and volume constraint

(b) Lower and upper mass flow rate constraints

Figure 7: Convergence plots of the objective and constraints for Configuration (i) with the no-slip boundary condition.

in Figure 8. The inlet and outlet ports are not shown for brevity. Figure 9 overlays the designs for each Configuration. When the Kn-slip boundary condition is active, the flow has an increased horizontal inertia. Thus, to satisfy the outlet constraints, the design constricts the horizontal outlets and redirects the flow vertically with the changing inclines ahead of the horizontal outlets, compared to the case where the Kn-slip boundary condition is ignored. This difference in design becomes more pronounced for larger Kn numbers, e.g. compare (a) and (d).

To verify that each design is indeed optimal for its flow state, we perform a cross-comparison between the results. Within each constraint configuration, each design is analyzed with the other two boundary conditions. For example, analyzing the design of Case (b) with the flow state in Case (c) corresponds to using a design obtained with $Kn = 0.01$ and for a different problem with $Kn = 0.02$. This comparison is summarized in Table V, which shows the total mass flow and constraint violations for each design. Values for h_i greater than 0.5% constitute a constraint violation.

Table V should only be read row-wise. In each row, i.e. for each boundary condition case, the design with the optimal performance, disregarding instances of constraint violations, is highlighted in boldface. A column-wise reading only reveals that, in general, the (nondimensional) mass flow rate increases with the Kn number, which is not relevant in this study.

If the no-slip design is used instead of the proper Kn-slip design, i.e. design (b) if $Kn = 0.01$ or design (c) if $Kn = 0.02$, the flow will perform suboptimally, though the differences in performance are small. The most noticeable results of this comparison are the mass flow rate violations, which at worst are approximately three times the tolerance set during the optimization process. While the differences in mass flow are small, the constraint violations suggest that it is not ideal to design the manifold with the no-slip boundary condition

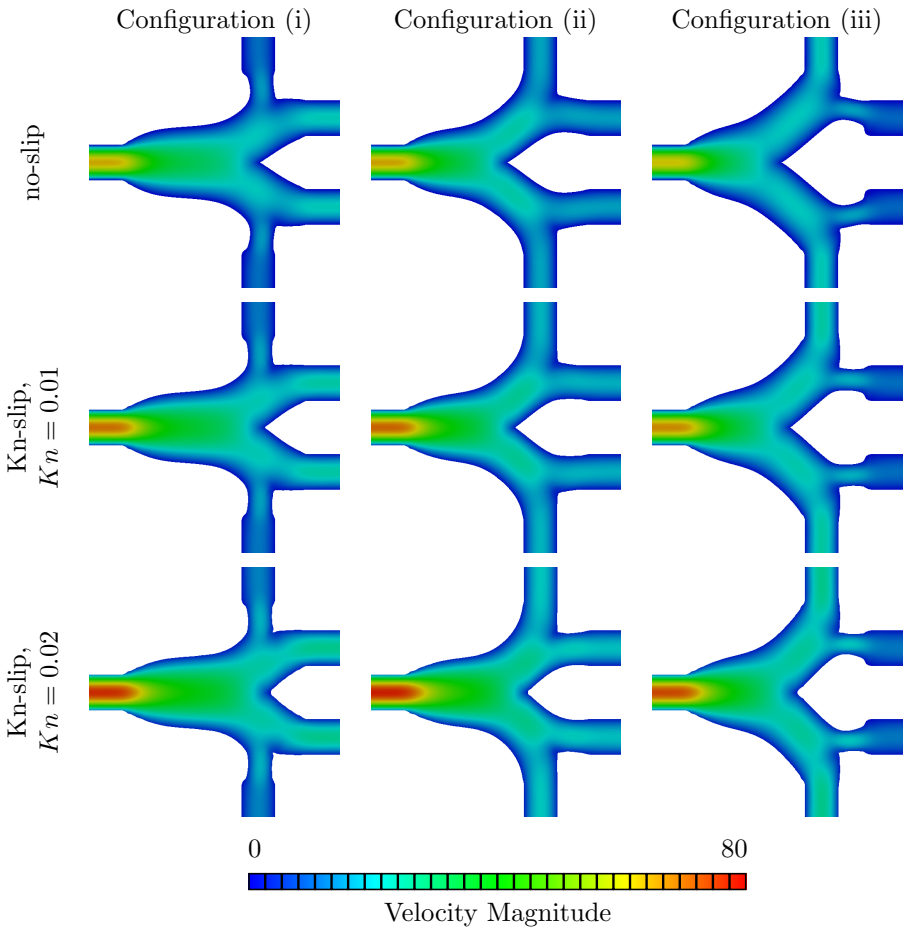

Figure 8: Velocity magnitude of the optimized designs for the splitting manifold problem.

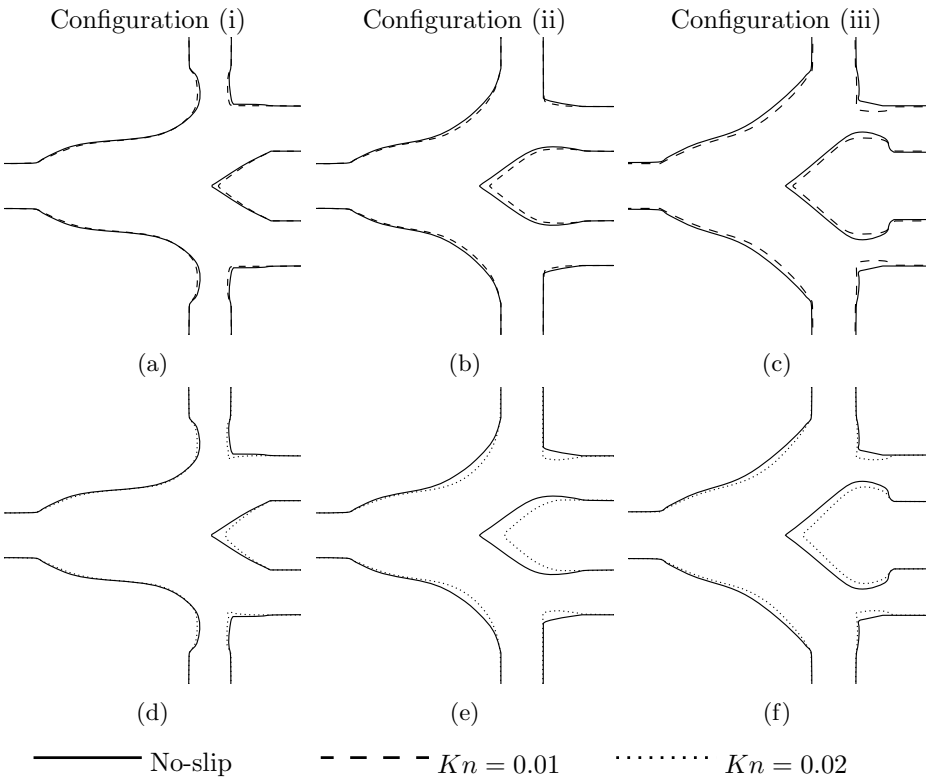

Figure 9: Overlay of no-slip and Kn-slip designs for each Kn and Configuration of the splitting manifold problem.

$\sum \dot{m}_{out,i}$, (h_1, h_2)		Design in Configuration (i)		
		(a)	(b)	(c)
Case	(a)	**3.397**, (**0.28**%, **0.48**%)	3.403, (0.94%, 1.80%)	3.393, (0.11%, 0.29%)
	(b)	3.838, (0.16%, 0.39%)	**3.854**, (**0.27**%, **0.46**%)	3.844, (0.60%, 1.30%)
	(c)	4.344, (0.25%, 0.43%)	4.372, (0.78%, 1.50%)	**4.368**, (**0.05**%, **0.16**%)

$\sum \dot{m}_{out,i}$, (h_1, h_2)		Design in Configuration (ii)		
		(a)	(b)	(c)
Case	(a)	**3.449**, (**0.19 0.25**%)	3.444, (0.88%, 0.92%)	3.443, (0.24%, 0.30%)
	(b)	3.896, (0.23%, 0.27%)	**3.921**, (**0.43**%, **0.48**%)	3.918, (0.02%, 0.06%)
	(c)	4.415, (0.05%, 0.09%)	4.441, (0.31%, 0.35%)	**4.448**, (**0.02**%, **0.021**%)

$\sum \dot{m}_{out,i}$, (h_1, h_2)		Design in Configuration (iii)		
		(a)	(b)	(c)
Case	(a)	**3.262**, (**0.499**%, **0.30**%)	3.267, (0.90%, 0.50%)	3.257, (1.32%, 0.61%)
	(b)	3.690, (0.06%, 0.07%)	**3.705**, (**0.47**%, **0.28**%)	3.698, (1.43%, 0.67%)
	(c)	4.180, (1.58%, 0.83%)	4.202, (1.77%, 0.92%)	**4.196**, (**0.05**%, **0.01**%)

Table V: Total mass flow rate and constraint violations for each case analyzed with each design for each Configuration.

when the physical and fluid characteristics of the problem lead to a finite Kn number.

5.3.2 Critical Kn number

In Section 5.2, we showed that for $Kn < 10^{-3}$, the Kn-slip boundary condition begins to have an impact on the flow in the rotating cylinders problem. To identify the critical Kn number at which the Kn-slip boundary condition should be accounted for in a topology optimization process, we consider constraint configuration (iii) and determine the optimum design for different Knudsen numbers, for $10^{-5} \leq Kn \leq 10^{-2}$.

Figure 10a shows the performance of the no-slip design and design optimized for various Kn numbers. Figure 10b shows the relative difference between the two curves in Figure 10a. For $Kn < 10^{-3}$, there is little difference between the no-slip design and the design optimized for Kn-slip. Near $Kn = 10^{-3}$, the difference then starts increasing rapidly. Figure 11 overlays the optimal designs for the no-slip (dotted black line), and the Kn-slip boundary condition with $Kn = 0.01$ (solid black line) and the various transitional Kn numbers (shades of red). The Kn-slip designs agree with the no-slip design when $Kn < 10^{-3}$. The design with $Kn = 5 \times 10^{-3}$ begins the transition from the no-slip design to the design with $Kn = 10^{-2}$. These results agree well with the one of Section 5.2: when $Kn > 10^{-3}$, the Kn-slip boundary condition will lead to differences, however small, in the design.

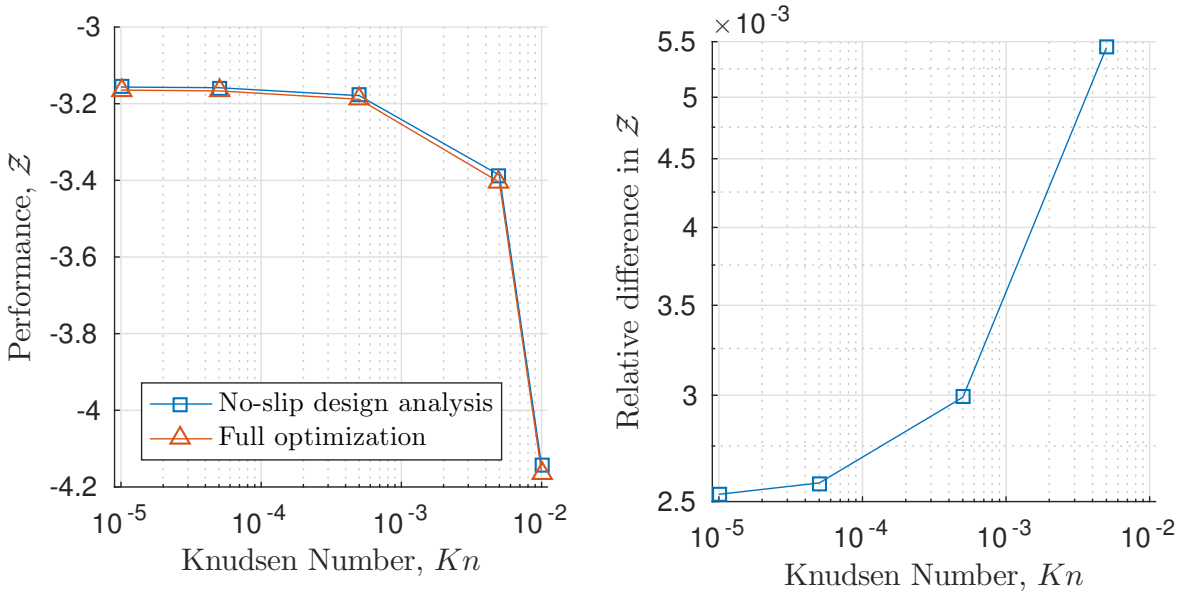

(a) Performance of the no-slip design and optimized design, at various Kn numbers.

(b) Relative difference in performance.

Figure 10: Performance difference study for Configuration (iii) of the splitting manifold problem.

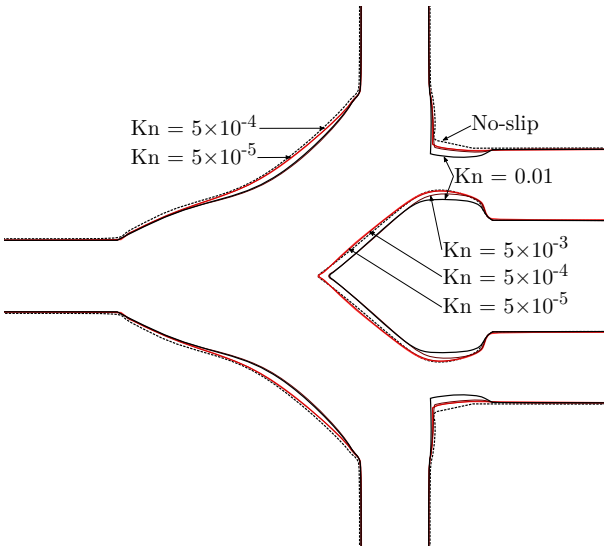

Figure 11: Optimal design for Configuration (iii) for various Kn numbers.

$\sum \dot{m}_{out,i},\ (h_1, h_2)$		Design	
		w/ the $\boldsymbol{J}_{\{n,t\}}$ terms	w/o the $\boldsymbol{J}_{\{n,t\}}$ terms
Case	$Kn = 0.01$	**3.854**, (**0.265**%, **0.456**%)	3.850, (0.397%, 0.869%)
	$Kn = 0.02$	**4.368**, (**0.047**%, **0.161**%)	4.358, (0.693%, 1.453%)

Table VI: Performance of designs in Configuration (i) when analyzed with the $\boldsymbol{J}_{\{n,t\}}$ terms.

5.3.3 Effect of the normal and tangential vector gradients

In Section 5.2, we showed that the $\boldsymbol{J}_{\{n,t\}}$ terms are necessary to fully recover an analytical solution, but that their omission results in only a small error for small Kn numbers. Having shown that design differences arise when the Kn-slip boundary condition is ignored for $Kn > 10^{-3}$, we now study the effect of omitting the $\boldsymbol{J}_{\{n,t\}}$ terms during the optimization process. Recall that including the $\boldsymbol{J}_{\{n,t\}}$ terms requires projecting the gradients of the level set field when low-order elements are used.

We optimize each of the Kn-slip problems, i.e. Cases (b) and (c) within constraint configuration (i), with and without the $\boldsymbol{J}_{\{n,t\}}$ terms, and compare the results. Figure 12 shows the designs for each Kn number; for compactness, we do not display the part of the design below the symmetry plane. Table VI shows the total mass flow rate through both designs when analyzed with the $\boldsymbol{J}_{\{n,t\}}$ terms, for $Kn = 0.01$ and $Kn = 0.02$, as well as the constraint violations. When the designs obtained without the $\boldsymbol{J}_{\{n,t\}}$ terms are analyzed with those terms in place, they violate the outflow constraints and have worse performance in terms of the objective. The differences in performance are admittedly small, but the largest violation is close to three times the tolerance allowed during the optimization process.

We further consider constraint configurations (ii) and (iii). In the worst case scenario, Configuration (iii) with $Kn = 0.02$, the difference in design with and without the $\boldsymbol{J}_{\{n,t\}}$ terms is most noticeable. For brevity, we do not show the resulting designs in constraint configuration (ii). Figure 13 shows an overlay of the designs obtained with and without the $\boldsymbol{J}_{\{n,t\}}$ terms; note that the constriction on the horizontal outlet moves upward to more accurately redirect the flow. Table VII shows the performance and mass constraint violations for these designs when analyzed with the $\boldsymbol{J}_{\{n,t\}}$ terms as part of the Kn-slip boundary condition. While the difference in performance are again small, $< 1\%$, the violation on the mass flow rate constraint is more noticeable at approximately 2%, which is four times the tolerance set during the optimization process. This study shows that the differences in performance or constraint violations resulting from the omission of the $\boldsymbol{J}_{\{n,t\}}$ terms are of the same order as the differences resulting from ignoring the Kn-slip boundary condition altogether. Thus, we suggest that for problems where the Kn-slip boundary condition leads to important differences in design, the $\boldsymbol{J}_{\{n,t\}}$ terms should also be considered.

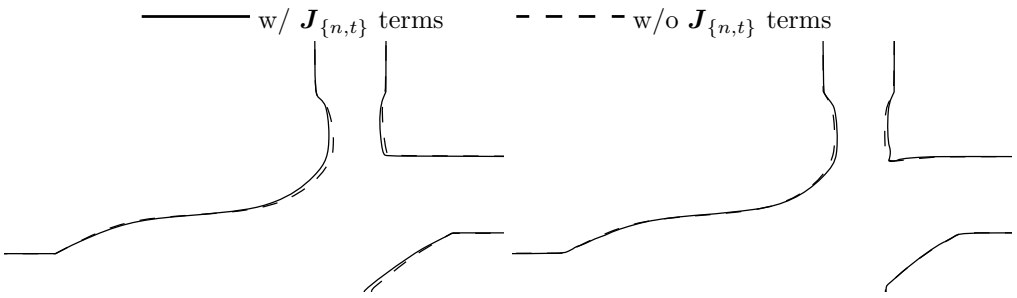

(a) $Kn = 0.01$ (b) $Kn = 0.02$

Figure 12: Designs obtained with and without $\boldsymbol{J}_{\{n,t\}}$ in Configuration (i).

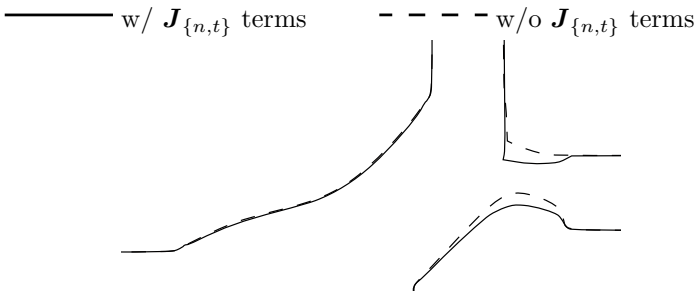

Figure 13: Designs obtained with and without $\boldsymbol{J}_{\{n,t\}}$ in Configuration (iii) with $Kn = 0.02$.

$\sum \dot{m}_{out,i},\ (h_1, h_2)$		Design	
		w/ the $\boldsymbol{J}_{\{n,t\}}$ terms	w/o the $\boldsymbol{J}_{\{n,t\}}$ terms
Case	$Kn = 0.02$	**4.196**, (**0.047**%, **0.014**%)	4.162, (2.045%, 0.869%)

Table VII: Performance of designs in Configuration (iii) when analyzed with the $\boldsymbol{J}_{\{n,t\}}$ terms.

5.4 Design of a fixed-valve fluid diode

Having shown the effect of the Kn-slip boundary condition on the manifold problem, we now seek to study its effect on the design of a fixed-valve fluid diode, commonly referred to as a Tesla valve. A Tesla valve has the property of allowing flow in one direction but restricting it when reversed. For a shape optimization study of the traditional Tesla valve, the reader is referred to [62]. Alternatively, a Tesla valve can have axially aligned ports, which was studied for small Re in [63] and for large Re in [64]. Finally, it is also possible to consider valves with axially aligned but offset ports, as depicted in Figure 16. The example in this paper is similar to the one previously used for flow topology optimization by Pingen *et al* [65].

The difference in the required pressure drop to realize the same mass flow rate in forward and reverse directions is captured in the valve's diodicity, which is defined as:

$$Di = \frac{\Delta \mathcal{T}^{fwd}}{\Delta \mathcal{T}^{rev}} = \frac{\mathcal{T}^{fwd}_{\Gamma^f_1} - \mathcal{T}^{fwd}_{\Gamma^f_2}}{\mathcal{T}^{rev}_{\Gamma^f_2} - \mathcal{T}^{rev}_{\Gamma^f_1}}, \tag{48}$$

where $\mathcal{T}^{fwd}_{\Gamma^f_i}$ is the total pressure at port i with flow in the forward direction and similarly for $\mathcal{T}^{rev}_{\Gamma^f_i}$ in the reverse direction, and Γ^f_1 and Γ^f_2 are the external surfaces of the two ports, e.g. in Figure 14a. The total pressure on a port surface is defined as:

$$\mathcal{T}_i = \int_{\Gamma^f_i} \left(p^f + \frac{\rho^f |\boldsymbol{u}^f|^2}{2} \right) \mathrm{d}\Gamma. \tag{49}$$

We enforce a parabolic inlet velocity, which can be generalized for the Kn-slip boundary condition as:

$$\hat{u}(y) = U_c \left(1 - \left(\frac{y}{r_c} \right)^2 + \frac{2}{r_c} \frac{Kn}{1 + Kn} \right), \tag{50}$$

where r_c is the radius of the port and U_c is the characteristic velocity. The outlet in each flow direction has a traction-free boundary condition. To achieve the desired valve effect, the diodicity is less than one; smaller values of Di indicate valves that better restrict the reverse flow. Figure 14aa shows a typical design for a Tesla valve.

5.4.1 Analysis of a Traditional Valve

Before considering topology optimization, we illustrate the characteristics of a traditional Tesla valve for various Reynolds numbers and use this insight to setup your optimization problem. The traditional Tesla valve, shown in Figure 14a, features a 45°-bend and a redirecting manifold. The radii of the redirection manifold are given with respect to the reference length, $r = 0.2L$ and $R = 0.4L$. We analyze this design

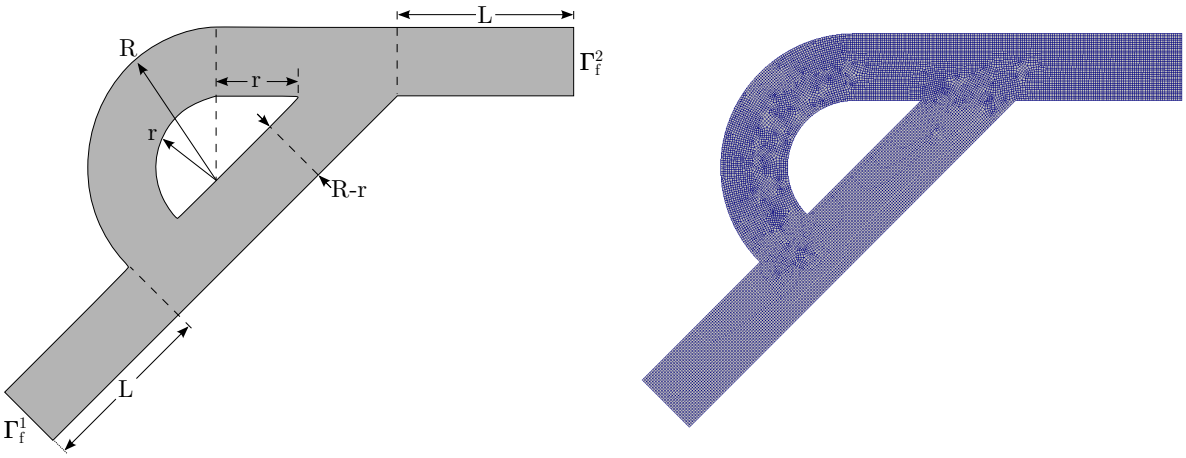

(a) Problem setup (b) Body-fitted mesh

Figure 14: Problem setup (a) and body-fitted unstructured mesh (b) for the traditional Tesla valve.

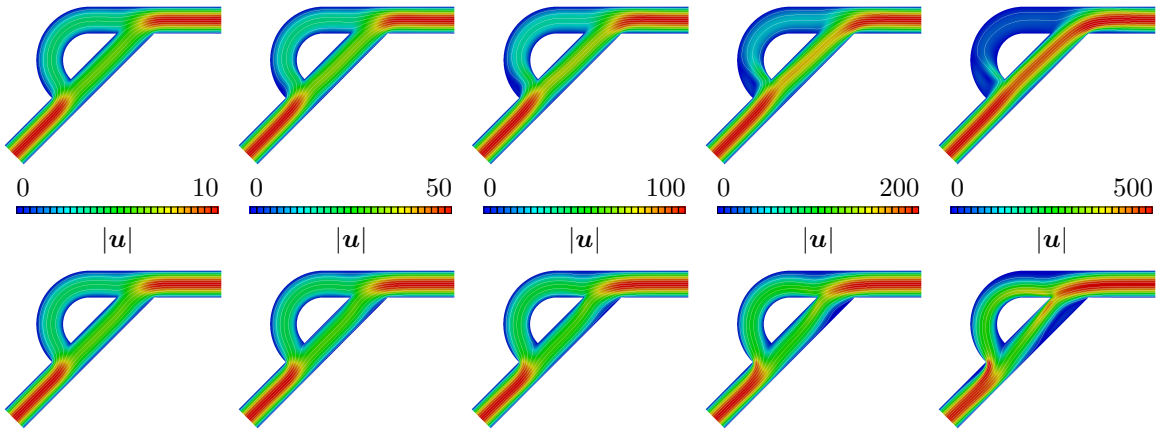

(a) $Re = 10$ (b) $Re = 50$ (c) $Re = 100$ (d) $Re = 200$ (e) $Re = 500$

Figure 15: Forward (top) and reverse (bottom) flows through the traditional Tesla valve for various Re numbers.

using a body-fitted, unstructured mesh, shown in Figure 14b, with 14526 elements, where $h \approx 0.013$ is the average width of each element.

Figure 15 show the flow solution for the forward and reverse flows through the traditional Tesla valve. For small Re numbers, there is no appreciable difference in the forward and reverse flow, aside from flow direction; however, for $Re > 100$, the manifold begins to truly hamper the reverse flow. The diodicity of this design at each Re number is given in Table VIII; these agree with those reported in [63]. For large Re numbers, the traditional Tesla valve offers considerably favorable diodicities; however, recalling the discussion in Sec5.1, for smaller Re numbers in the range that would also have finite Kn numbers (33), the diodicity is very near unity. Thus, a new design is needed for low Re numbers.

Re	Di
1	0.999994
10	0.999993
50	0.999831
100	0.996436
200	0.967686
500	0.816144

Table VIII: Diodicity of the traditional Tesla valve for various Re numbers.

5.4.2 Optimization

The problem setup is shown in Figure 16. The design domain is defined as the space between the two ports, i.e. $\Omega^d = \{(x, y)|0 \leq x \leq L_c, 0 \leq y \leq 2L_c\}$, for some characteristic length scale, L_c. In this work, we formulate the optimization problem (3) as:

$$\mathcal{Z} = \frac{\Delta\mathcal{T}^{fwd}}{\Delta\mathcal{T}^0} + w_{\mathcal{P}}\frac{\mathcal{P}}{\mathcal{P}^0} \tag{51}$$

where the superscript "0" denotes the values of the initial design and $w_{\mathcal{P}}$ is a constant scaling factor. This objective is equivalent to maximizing the mass flow rate when the pressure difference through the fluidic device is prescribed. A constraint on the diodicity is given by:

$$g_1 = \frac{\Delta\mathcal{T}^{fwd}}{\Delta\mathcal{T}^{rev}} - Di^* \tag{52}$$

where Di^* is a chosen target diodicity. We seek to reproduce the diodicity at $Re = 200$ of the traditional Tesla valve but at $Re = 40$, where the incompressibility condition, (33), allows for $Kn = 0.01$; thus, the target diodicity is set to $Di^* = 0.97$. Finally, a volume constraint (43) may be included to discourage trivial solutions. While the optimization problem can alternatively be defined to minimize the valve's diodicity, e.g. [64], this paper follows the formulation found in [63], which performed a topology optimization using density methods for low Re number flows with no-slip boundary conditions.

We perform a topology optimization for the cases of (i) $f_{\mathcal{V}} = 1$, i.e. no volume constraint, (ii) $f_{\mathcal{V}} = 0.6$, and (iii) $f_{\mathcal{V}} = 0.4$, all with the (a) no-slip and (b) Kn-slip with $Kn = 0.01$ boundary conditions. In all cases, $U_c = 40$ in the parabolic velocity distribution (50) at the inlet and the outlet has a traction-free boundary condition, in both the forward and reverse flows. The remaining parameters for this problem are shown in Table IX. The design is initialized with a 6×3 array of circular inclusions of radii $0.09L$, as shown in Figure 16.

Figure 17 shows the velocity magnitude in the forward and reverse flows through the optimized designs,

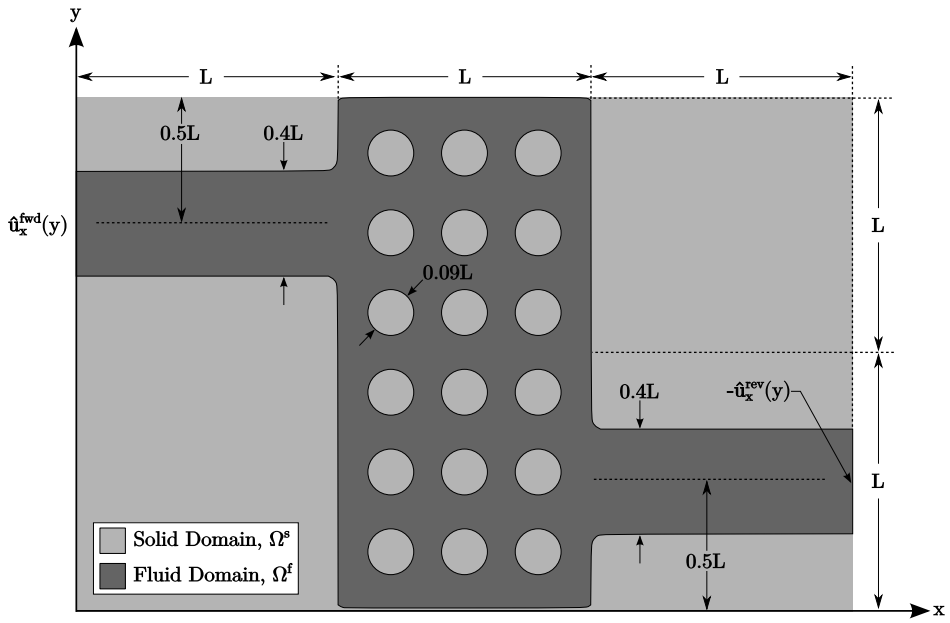

Figure 16: Problem setup and initial design for the Tesla valve example.

	Value
Mesh size	123×82
Element size	$h = 0.0244L$
Characteristic length	$L = 1$
Fluid density	$\rho^f = 1$
Fluid viscosity	$\mu^f = 1$
Characteristic speed	$U_c = 40$
Port radius	$r_c = 0.2L$
Perimeter scaling factor	$w_{\mathcal{P}} = 0.1$
Target diodicity	$Di^* = 0.97$
Volume constraint factor	$f_{\mathcal{V}} = \{1, 0.6, 0.4\}$
Nitsche velocity parameter	$\alpha_{N,\boldsymbol{u}} = 1$
Viscous ghost-penalty	$\alpha_{GP,\mu} = 5 \times 10^{+0}$
Pressure ghost-penalty	$\alpha_{GP,p} = 5 \times 10^{-1}$
Relative Optimization Step	$\Delta s = 0.05$
Design variable bounds	$s_i^L = -0.0244L, s_i^U = +0.0244L$
Smoothing radius	$r_\phi = 2.4h$
Number of design variables	$3,176$

Table IX: Parameters for the fixed-valve problem.

for each boundary condition and volume constraint configuration. The inlet and outlet ports are not shown for brevity. Without a constraint on the fluid volume, the reservoir in the no-slip design mostly retains its rectangular shape with some minimal constrictions (see circles marked by A) in the main body of the valve to create a large vortex in the reverse flow. Further, there is a pronounced vertical constriction (B) on the bottom port. In contrast, the Kn-slip design naturally reduces the volume of the reservoir, favoring a narrower channel (C) in the main body without a constriction near the bottom port, resulting in smaller vortices to redirect the flow through the valve.

With a 60% volume constraint, the design differences are more pronounced. Again, the design with the no-slip condition relies on a constriction on the bottom port (D), whereas the design with the Kn-slip condition uses small vortices (E) to achieve the target diodicity.

In the case of a 40% volume constraint, the design with the no-slip condition introduces a narrow horizontal constriction (F) and brings the second constriction (G) closer to the top port. The design with the Kn-slip is similar in this respect, but the two constrictions (H) are further apart, one near each port. The recirculation region near the top port is larger in the no-slip design (I). While the two designs have similar features, their relative placements and orientations vary to a greater extent than in the splitting manifold problem. Figure 18 overlays the design contours for each volume constraint case for a more direct comparison.

Table X summarizes a comparison study, similar to that in Section 5.3.1, where, within each volume constraint configuration, we analyze each design with the other boundary condition. We find that, for all Configurations, the Kn-slip design performs better than the no-slip design regardless of which boundary condition is used to analyze it. However, the Kn-slip design fails to reach the target diodicity when analyzed with the no-slip condition. Similarly, we find that the no-slip design offers a better diodicity than the Kn-slip design; however, this comes at a worse performance in terms of the objective and is *not* the goal of the optimization problem.

Further, it is important to note that this paper is not meant to provide strict design guidelines for a fixed-valve; rather, this study suggests that, for a given target diodicity, the Kn-slip boundary condition should be included during the design optimization process if the geometric and fluid characteristics lead to a finite Kn number. while the differences in design and performance where small for the splitting manifold problem, they are more noticeable in this example. In Configuration (i), there is a 23% increase in the objective value when using the no-slip design instead of the proper Kn-slip design. Similarly, there is a 15% and 23% increase in the objective value for Configurations (ii) and (iii), respectively.

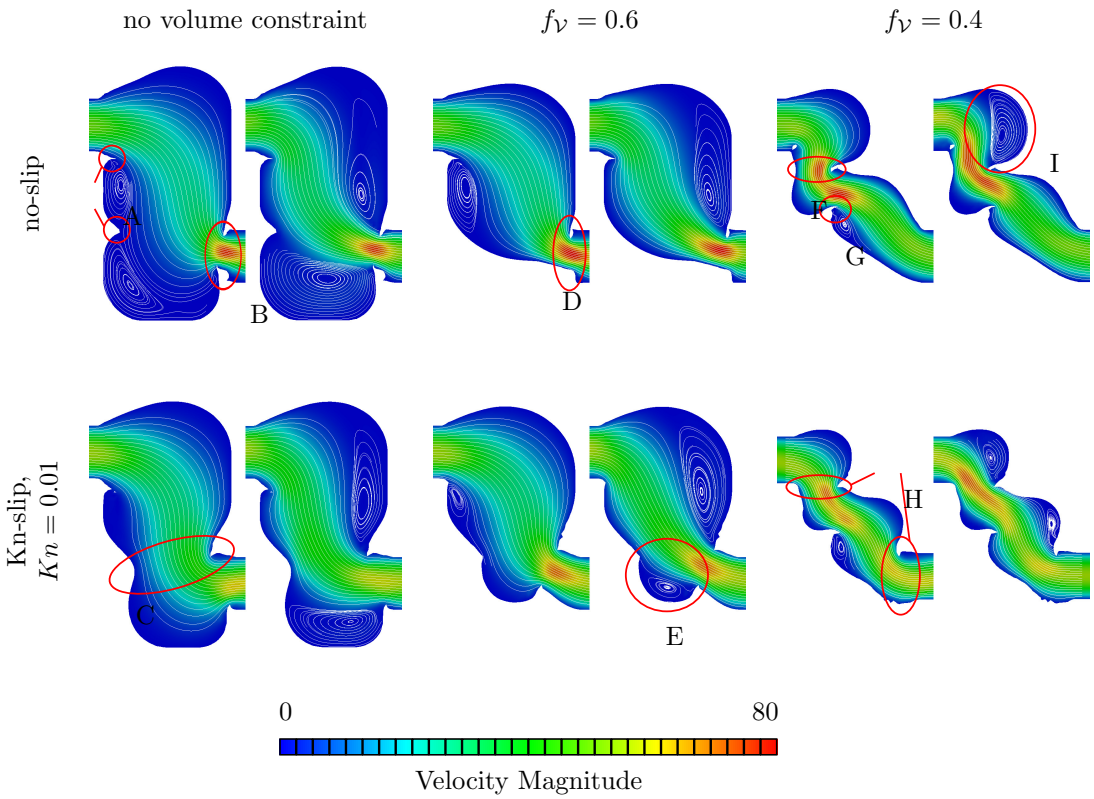

Figure 17: Velocity magnitude with streamlines for forward (left) and reverse (right) flows.

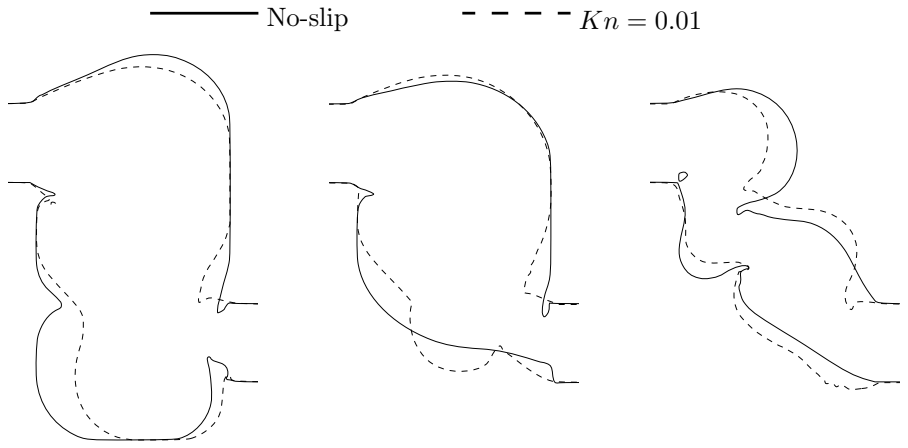

(a) no volume constraint (b) $f_\mathcal{V} = 0.6$ (c) $f_\mathcal{V} = 0.4$

Figure 18: Overlaid designs of the fixed-valve problem for each volume constraint case.

$\mathcal{Z}$, Di		Design in Configuration (i): $f_{\mathcal{V}} = 1.0$	
		(a) No-slip	(b) Kn-slip
Case:	no-slip	**0.306**, **0.968**	0.249, 0.986
	Kn-slip	0.340, 0.953	**0.262**, **0.970**

		Design in Configuration (ii): $f_{\mathcal{V}} = 0.6$	
		(a)	(b)
Case:	no-slip	**0.328**, **0.970**	0.266, 0.989
	Kn-slip	0.342, 0.959	**0.291**, **0.970**

		Design in Configuration (iii): $f_{\mathcal{V}} = 0.4$	
		(a)	(b)
Case:	no-slip	**0.444**, **0.969**	0.343, 0.988
	Kn-slip	0.482, 0.956	**0.370**, **0.967**

Table X: Objective value and diodicity in the comparison study for each configuration in the fixed-valve problem.

6 Conclusion

Full topology optimization for fluidic devices has been limited to problems in the continuum regime. In this work, we consider problems in the slip regime by introducing a slip boundary to model the non-zero fluid velocity at solid walls. The fluid model is the incompressible Navier-Stokes with slip boundary condition that replace the traditional no-slip conditions in the continuum regime. The Kn-slip boundary model relies on the precise position and orientation of the fluid-solid interface, which cannot be recovered using density methods traditionally used for flow topology optimization. We introduce a LSM approach to allow for a precise description of the interface. The level set field is discretized with bilinear elements. The XFEM discretizes the flow model using the LSM geometry description. We project the normal vectors to be able to compute curvature information when low-order elements are used to discretize the level set field. We consider optimization problems with 2D steady incompressible flow. The optimization problems are solved using a nonlinear programming method.

The proposed framework for the Kn-slip boundary condition is validated against an analytical solution for the flow between rotating cylinders. This study suggests that the Kn-slip boundary condition becomes important around $Kn = 10^{-3}$ and that the $\boldsymbol{J}_{\{n,t\}}$ terms are necessary to fully recover the analytical solution.

We consider the effect of the Kn-slip boundary condition on a splitting manifold. The examples in Section 5.3 suggest that, for flows with $Kn > 10^{-3}$, the Kn-slip boundary condition begins to impact the performance of an optimized design in terms of the objective and flow rate constraints. While the differences in design and performance are small for the problems presented, we expect that the effect of the Kn-slip boundary condition compounds for larger Kn numbers. This study further suggests that when the Kn-slip

boundary condition is used, the $\boldsymbol{J}_{\{n,t\}}$ terms should be included for the most optimal design. The differences in omitting these terms are largest when the design needs to primarily redirect the flow, e.g. in constraint configuration (iii).

Finally, we consider the design of a fixed-valve in Section 5.4. While the differences in design and performance are small in the splitting manifold problem, they are considerably larger in the fixed-valve problem. We note that this paper is not meant to provide strict design guidelines for a fixed-valve; rather, this study suggests that, for a given target diodicity, the Kn-slip boundary condition should be accounted for during the design optimization process for finite Kn number flows. With no volume constraint, there is a 23% increase in the objective value when using the no-slip design instead of the proper Kn-slip design. Similarly, there is a 15% and 23% increase in the objective value in the cases of a 40% and 60% volume constraint, respectively.

We recognize that the topology optimization results in this paper reduce to shape optimization for the simple manifold problem; however, we note that the fixed-valve problem introduces various features, including constrictions and recirculation regions, that are not necessarily realizable in a shape optimization setting. The LSM-XFEM framework presented here allows for the enforcement of the Kn-slip boundary condition along an arbitrary fluid-solid interface, which would not be possible with density methods. This framework allows for a design optimization procedure that does not require expensive remeshing after each design update.

In future work, we plan to further investigate these effects in 3D, as well as investigate the effect of the analogous temperature jump condition on the optimum design in temperature-dependent problems. A compressible fluid model should be used to overcome the small Mach number restriction imposed by the incompressible Navier-Stokes model.

References

[1] Robert W Barber and David R Emerson. Challenges in modeling gas-phase flow in microchannels: from slip to transition. *Heat Transfer Engineering*, 27(4):3–12, 2006.

[2] Gui-Hua Tang, Yong-Hao Zhang, and David R Emerson. Lattice boltzmann models for nonequilibrium gas flows. *Physical Review E*, 77(4):046701, 2008.

[3] Bing-Yang Cao, Min Chen, and Zeng-Yuan Guo. Effect of surface roughness on gas flow in microchannels by molecular dynamics simulation. *International Journal of Engineering Science*, 44(13):927–937, 2006.

[4] Lynne O Hare, Duncan A Lockerby, Jason M Reese, and David R Emerson. Near-wall effects in rarefied gas micro-flows: some modern hydrodynamic approaches. *International Journal of Heat and Fluid Flow*, 28(1):37–43, 2007.

[5] Vlasios Leontidis, Jie Chen, Lucien Baldas, and Stéphane Colin. Numerical design of a knudsen pump with curved channels operating in the slip flow regime. *Heat and Mass Transfer*, 50(8):1065–1080, 2014.

[6] Matthew J. McNenly, Michael A. Gallis, and Iain D. Boyd. Empirical slip and viscosity model performance for microscale gas flow. *International Journal for Numerical Methods in Fluids*, 49(11):1169–1191, 2005.

[7] J Van Rij, T Ameel, and T Harman. An evaluation of secondary effects on microchannel frictional and convective heat transfer characteristics. *International Journal of Heat and Mass Transfer*, 52(11):2792–2801, 2009.

[8] J Van Rij, T Harman, and T Ameel. Slip flow fluid-structure-interaction. *International Journal of Thermal Sciences*, 58:9–19, 2012.

[9] Samuel A Schaaf and Paul L Chambre. *Flow of rarefied gases*. Princeton University Press, Princenton, 1961.

[10] Mohamed Gad el Hak. The fluid mechanics of microdevices-the freeman scholar lecture. *ASME Journal of Fluid Engineering*, 121:5–33, 1999.

[11] Wen-Ming Zhang, Guang Meng, and Xueyong Wei. A review of slip models for gas microflows. *Microfluidics and nanofluidics*, 13(6):845–882, 2012.

[12] Xiaolin Zhong, Robert W MacCormack, and Dean R Chapman. Stabilization of the burnett equations and application to hypersonic flows. *AIAA journal*, 31(6):1036–1043, 1993.

[13] Shi Jin and Marshall Slemrod. Regularization of the burnett equations via relaxation. *Journal of Statistical Physics*, 103(5-6):1009–1033, 2001.

[14] Henning Struchtrup and Manuel Torrilhon. Regularization of grads 13 moment equations: derivation and linear analysis. *Physics of Fluids*, 15(9):2668–2680, 2003.

[15] Ramesh Balakrishnan. An approach to entropy consistency in second-order hydrodynamic equations. *Journal of Fluid Mechanics*, 503:201–245, 2004.

[16] Martin P Bendsøe. Optimal shape design as a material distribution problem. *Structural optimization*, 1(4):193–202, 1989.

[17] M Zhou and G I N Rozvany. The coc algorithm, part ii: topological, geometrical and generalized shape optimization. *Computer Methods in Applied Mechanics and Engineering*, 89(1-3):309–336, 1991.

[18] Thomas Borrvall and Joakim Petersson. Topology optimization of fluids in stokes flow. *International journal for numerical methods in fluids*, 41(1):77–107, 2003.

[19] Allan Gersborg-Hansen, Ole Sigmund, and Robert B Haber. Topology optimization of channel flow problems. *Structural and Multidisciplinary Optimization*, 30(3):181–192, 2005.

[20] Fridolin Okkels, Laurits H Olesen, and Henrik Bruus. Applications of topology optimization in the design of micro-and nanofluidic systems. In *Technical Proceedings of the 2005 NSTI Nanotechnology Conference and Trade Show*, pages 575–578, 2005.

[21] Laurits Højgaard Olesen, Fridolin Okkels, and Henrik Bruus. A high-level programming-language implementation of topology optimization applied to steady-state navier-stokes flow. *Int. J. Numer. Meth. Engng*, 65:975–1001, 2006.

[22] Anton Evgrafov, Georg Pingen, and Kurt Maute. Topology optimization of fluid domains: kinetic theory approach. *ZAMM-Journal of Applied Mathematics and Mechanics/Zeitschrift für Angewandte Mathematik und Mechanik*, 88(2):129–141, 2008.

[23] Aycan Erentok and Ole Sigmund. Topology optimization of sub-wavelength antennas. *IEEE transactions on antennas and propagation*, 59(1):58–69, 2011.

[24] Shintaro Yamasaki, Tsuyoshi Nomura, Atsushi Kawamoto, Kazuo Sato, and Shinji Nishiwaki. A level set-based topology optimization method targeting metallic waveguide design problems. *International Journal for Numerical Methods in Engineering*, 87(9):844–868, 2011.

[25] James A Sethian and Andreas Wiegmann. Structural boundary design via level set and immersed interface methods. *Journal of computational physics*, 163(2):489–528, 2000.

[26] Michael Yu Wang, Xiaoming Wang, and Dongming Guo. A level set method for structural topology optimization. *Computer methods in applied mechanics and engineering*, 192(1):227–246, 2003.

[27] Grégoire Allaire, François Jouve, and Anca-Maria Toader. Structural optimization using sensitivity analysis and a level-set method. *Journal of computational physics*, 194(1):363–393, 2004.

[28] Nico P van Dijk, Kurt Maute, M Langelaar, and F Van Keulen. Level-set methods for structural topology optimization: a review. *Structural and Multidisciplinary Optimization*, 48(3):437–472, 2013.

[29] Arun L Gain and Glaucio H Paulino. A critical comparative assessment of differential equation-driven methods for structural topology optimization. *Structural and Multidisciplinary Optimization*, 48(4):685–710, 2013.

[30] Ivo Babuška and Jens M Melenk. The partition of unity method. *International journal for numerical methods in engineering*, 40(4):727–758, 1997.

[31] Ted Belytschko and Tom Black. Elastic crack growth in finite elements with minimal remeshing. *International journal for numerical methods in engineering*, 45(5):601–620, 1999.

[32] Christopher Lang, David Makhija, Alireza Doostan, and Kurt Maute. A simple and efficient preconditioning scheme for heaviside enriched xfem. *Computational mechanics*, 54(5):1357–1374, 2013.

[33] Henning Sauerland and Thomas-Peter FriesFries. The stable xfem for two-phase flows. *Computers & Fluids*, 87:41–49, 2013.

[34] Éric Béchet, Hans Minnebo, Nicolas Moës, and B Burgardt. Improved implementation and robustness study of the xfem for stress analysis around cracks. *International Journal for Numerical Methods in Engineering*, 64(8):1033–1056, 2005.

[35] Alexander Menk and Stéphane Bordas. A robust preconditioning technique for the extended finite element method. *International Journal for Numerical Methods in Engineering*, 85(13):1609–1632, 2011.

[36] Erick Burman, Miguel A Fernández, and Peter Hansbo. Continuous interior penalty finite element method for oseen's equations. *SIAM journal on numerical analysis*, 44(3):1248–1274, 2006.

[37] B Schott, U Rasthofer, V Gravemeier, and W Wall. A face-oriented stabilized nitsche-type extended variational multiscale method for incompressible two-phase flow. *International journal for numerical methods in engineering*, 104(7), 2014.

[38] Yuri Bazilevs and Thomas J R Hughes. Weak imposition of dirichlet boundary conditions in fluid mechanics. *Computers & Fluids*, 36(1):12–26, 2007.

[39] Carlos H Villanueva and Kurt Maute. Cutfem topology optimization of 3d laminar incompressible flow problems. *Computer Methods in Applied Mechanics and Engineering*, 320:444–473, 2017.

[40] Sebastian Kreissl and Kurt Maute. Levelset based fluid topology optimization using the extended finite element method. *Structural and Multidisciplinary Optimization*, 46(3):311–326, 2012.

[41] David Makhija and Kurt Maute. Level set topology optimization of scalar transport problems. *Structural and Multidisciplinary Optimization*, 51(2):267–285, 2015.

[42] Tayfun E Tezduyar, Sanjay Mittal, S E Ray, and R Shih. Incompressible flow computations with stabilized bilinear and linear equal-order-interpolation velocity-pressure elements. *Computer Methods in Applied Mechanics and Engineering*, 95(2):221–242, 1992.

[43] Erick Burman and Peter Hansbo. Fictitious domain methods using cut elements: Iii. a stabilized nitsche method for stokes problems. *ESAIM: Mathematical modeling and numerical analysis*, 48(3):859–874, 2014.

[44] Carlos Hernan Villanueva and Kurt Maute. Density and level set-xfem schemes for topology optimization of 3-d structures. *Computational Mechanics*, 54(1):133–150, 2014.

[45] Ali Beskok and George Em Karniadakis. Report: A model for flows in channels, pipes, and ducts at micro and nano scales. *Microscale Thermophysical Engineering*, 3(1):43–77, 1999.

[46] J Clerk Maxwell. On stresses in rarefied gases arising from inequalities of temperature. *Phil. Trans. R. Soc. Lond.*, 170:231–256, 1879.

[47] Erik Burman. A penalty-free nonsymmetric nitsche-type method for the weak imposition of boundary conditions. *SIAM Journal on Numerical Analysis*, 50(4):1959–1981, 2012.

[48] Y Bazilevs, Christian Michler, VM Calo, and TJR Hughes. Isogeometric variational multiscale modeling of wall-bounded turbulent flows with weakly enforced boundary conditions on unstretched meshes. *Computer Methods in Applied Mechanics and Engineering*, 199(13):780–790, 2010.

[49] Anita Hansbo and Peter Hansbo. A finite element method for the simulation of strong and weak discontinuities in solid mechanics. *Computer Methods in Aplied Mechanics and Engineering*, 193(33-35):3523–3540, 2004.

[50] David Makhija and Kurt Maute. Numerical instabilities in level set topology optimization with the extended finite element method. *Structural and multidisciplinary optimization*, 49(2):185–197, 2014.

[51] Kenjiro Terada, Mitsuteru Asai, and Michihiro Yamagishi. Finite cover method for linear and non-linear analyses of heterogeneous solids. *International joournal for numerical methods in engineering*, 58(9):1321–1646, 2003.

[52] T Q N Tran, H P Lee, and S P Lim. Modeling porous structures by penalty approach in the extended finite element method. *Computer Methods in Biomechanics and Biomedical Engineering*, 16(4):347–357, 2013.

[53] Young Joon Choi, Martien A Hulsen, and Han E H Meijer. Simulation of the flow of a viscoelastic fluid around a stationary cylinder using an extended finite element method. *Computers & Fluids*, 57:183–194, 2012.

[54] Ashesh Sharma, Carlos H Villanueva, and Kurt Maute. On shape sensitivities with heaviside-enriched xfem. *Structural and Multidisciplinary Optimization*, 55(2):385–408, 2017.

[55] Youcef Saad and Martin H schultz. Gmres: a generalized minimal residual algorithm for solving nonsymmetric linear systems. *SIAM Jounral on scientific and statistical computing*, 7(3):856–869, 1986.

[56] Youcef Saad. Ilut: A dual threshold incomplete lu factorization. *Numerical Linear Algebra with Applications*, 1(4):387–402, 1994.

[57] Sebastian Kreissl, Georg Pingen, and Kurt Maute. Topology optimization for unsteady flow. *Topology optimization for unsteady flow*, 87(13):1229–1253, 2011.

[58] Stephanie Golmon, Kurt Maute, and Martin L Dunn. Multiscale design optimization of lithium ion batteries using adjoint sensitivity analysis. *International Journal for Numerical Methods in Engineering*, 92(5):475–494, 2012.

[59] Krister Svanberg. A globally convergent version of mma without line search. In *Proceedings of the first world congress of structural and multidisciplinary optimization*, volume 28, pages 9–16. Goslar, Germany, 1995.

[60] Stéphane Colin. Rarefaction and compressibility effects on steady and transient gas flows in microchannels. *Microfluidics and Nanofluidics*, 1(3):268–279, 2005.

[61] Georg Pingen, Matthias Waidmann, Anton Evgrafov, and Kurt Maute. A parametric level-set approach for topology optimization of flow domains. *Structural and Multidisciplinary Optimization*, 41(1):117–131, 2010.

[62] Adrian R Gamboa, Christopher J Morris, and Fred K Forster. Improvements in fixed-valve micropump performance through shape optimization of valves. *Journal of Fluids Engineering*, 127(2):339–346, 2005.

[63] Yongbo Deng, Zhenyu Liu, Ping Zhang, Yihui Wu, and Jan G Korvink. Optimization of no-moving-part fluidic resistance microvalves with low reynolds number. In *Proceedings IEEE international conference on Micro Electro MechanicalSystems (MEMS)*, pages 67–70, 2010.

[64] Sen Lin, Longyu Zhao, James K Guest, Timothy P Weihs, and Zhenyu Lui. Topology optimization of fixed-geometry fluid diodes. *Journal of Mechanical Design*, 137(8):081402, 2015.

[65] Georg Pingen, Anton Evgrafov, and Kurt Maute. A parallel schur complement solver for the solution of the adjoint steady-state lattice boltzmann equations: application to design optimization. *International Journal of Computational Fluid Dynamics*, 22(7):457–464, 2008.